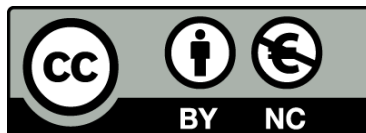




UNIVERSITAT DE
BARCELONA

Out-of-equilibrium dynamics in driven and active magnetic colloids

Helena Massana-Cid



Aquesta tesi doctoral està subjecta a la llicència [Reconeixement- NoComercial 4.0. Espanya de Creative Commons](#).

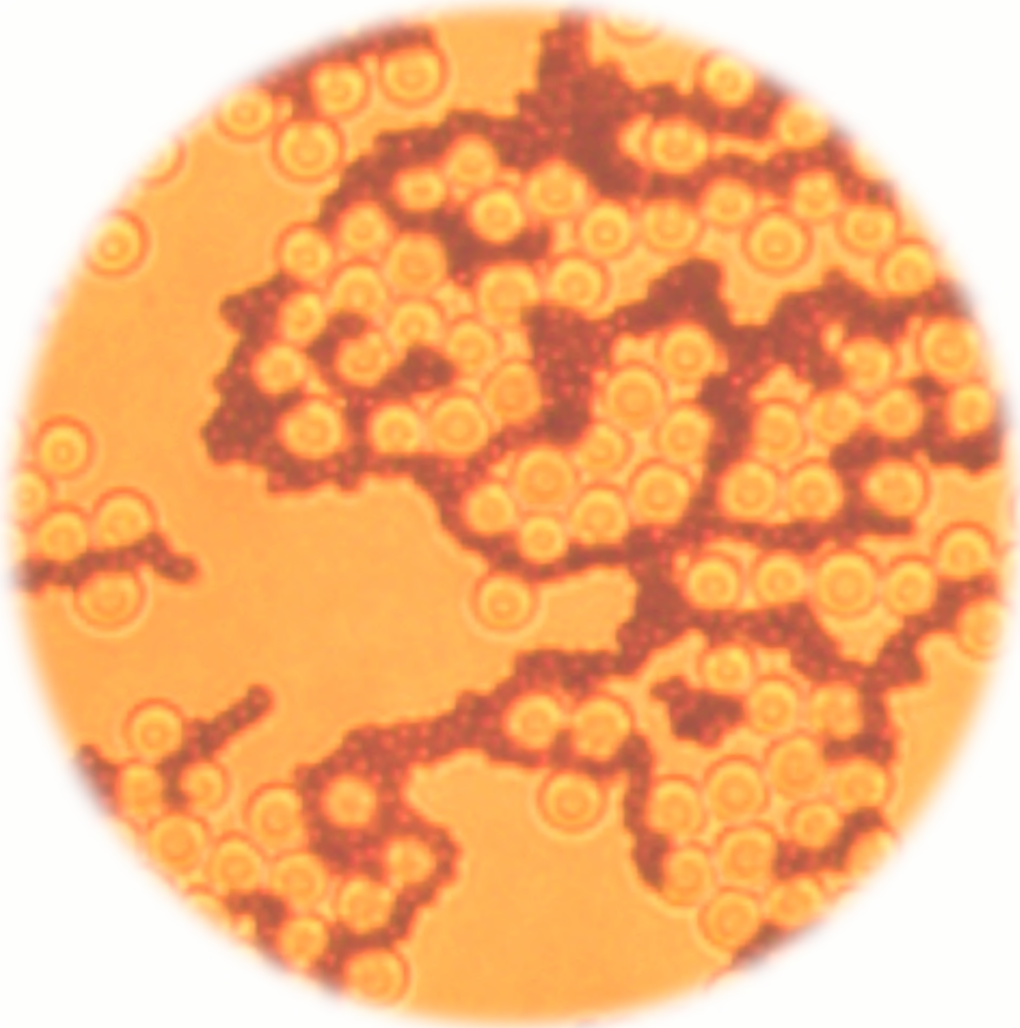
Esta tesis doctoral está sujeta a la licencia [Reconocimiento - NoComercial 4.0. España de Creative Commons](#).

This doctoral thesis is licensed under the [Creative Commons Attribution-NonCommercial 4.0. Spain License](#).

PH.D. THESIS

OUT-OF-EQUILIBRIUM DYNAMICS IN
DRIVEN AND ACTIVE MAGNETIC
COLLOIDS

Helena MASSANA-CID



UNIVERSITAT DE
BARCELONA

OUT-OF-EQUILIBRIUM DYNAMICS IN DRIVEN AND ACTIVE MAGNETIC COLLOIDS

Helena MASSANA-CID

— Ph.D. Thesis —

Ph.D. advisor: Pietro TIERNO

Tutor: Antoni Planes

Programa de doctorat en Física

Departament de Física de la Matèria Condensada

Facultat de Física

Barcelona, September 2019



UNIVERSITAT_{DE}
BARCELONA

Helena Massana-Cid

Departament de Física de la Matèria Condensada

Facultat de Física

Universitat de Barcelona

Barcelona, 08028 (Spain)

massana@ecm.ub.edu

Cover: Microscope image of a colloidal gel assembled by active apolar doping.

This work has received financial support from the European Research Council (Project No. 335040).

CONTENTS

Preface	vii
Abstract	ix
I Introduction	1
1 General introduction	3
1.1 Thesis aims and structure	3
1.2 Soft condensed matter and colloids	4
II Fundamentals	5
2 Colloidal science	7
2.1 Colloids as a model for atoms	7
2.2 Visualisation and characterization of colloids	8
2.3 Brownian motion	9
2.4 Interactions between colloids	10
2.5 Examples of colloids	12
2.6 Colloidal crystals and gels	13
3 Magnetic particles	15
3.1 Magnetic materials	15
3.2 Size effects in magnetic nanoparticles	17
3.3 Magnetic interactions in a fluid suspension	18
4 Fluid dynamics at low Reynolds number	21
4.1 Swimming at low Reynolds number	21
4.2 Magnetic micropropellers	24
4.3 Synthetic active Brownian particles	25

III	Materials and Methods	31
5	Sample Preparation	33
5.1	Ferromagnetic Colloids	33
5.2	Paramagnetic Colloids	35
5.3	Ferrite Garnet Films	36
5.4	Final solution preparation	37
6	Experimental set-up	39
6.1	Magnetic coils system	39
6.2	Observation of the system and illumination set-up	40
6.3	Image and data analysis	40
IV	Results	43
7	Summary of results	45
8	Publications	51
8.1	Publication 1: Orientational dynamics of fluctuating dipolar particles assembled in a mesoscopic colloidal ribbon	51
8.2	Publication 2: Propulsion and hydrodynamic particle transport of magnetically twisted colloidal ribbons	59
8.3	Publication 3: Leap-frog transport of magnetically driven anisotropic colloidal rotors	75
8.4	Publication 4: Tunable self-healing of magnetically propelling colloidal carpets	85
8.5	Publication 5: Bidirectional particle transport and size selective sorting of Brownian particles in a flashing spatially periodic energy landscape	103
8.6	Publication 6: Assembly and Transport of Microscopic Cargos via Reconfigurable Photoactivated Magnetic Microdockers	113
8.7	Publication 7: Active apolar doping determines routes to colloidal clusters and gels	131
V	Conclusions	145
9	Conclusions and perspectives	147
	Bibliography	149
	List of publications	163

Resum en català	165
List of figures	169
List of symbols and abbreviations	171

PREFACE

This thesis presents my Ph.D. research in soft condensed matter physics, performed under the supervision of Prof. Pietro Tierno at the University of Barcelona between March 2016 and September 2019 in the Magnetic Soft Matter Group.

It is a compendium of publications including exclusively the published projects joined by a common introduction and discussion. During my Ph.D., I did a three-month stay at the University of Bayreuth under the supervision of Prof. Thomas M. Fisher. The results of this collaboration were published in a separate paper, which is not included in this thesis in view of the fact that it was on a different subject.

ABSTRACT

In this thesis we investigate the structure formation and the out-of-equilibrium dynamics of driven and active magnetic colloids. The interactions in our system were tuned in situ by using external fields, with the aim of finding novel approaches to drive and engineer these microparticles into a rich variety of microstructures. The colloids formed chains and clusters able to transport cargos, space-filling gels and self-healing crystals. Moreover, we demonstrated the bidirectional transport of paramagnetic particles on top of a structured magnetic substrate. Because of their associated length-scale, colloids are experimentally accessible with traditional optical microscope techniques. We analysed the data extracted from digital video microscopy and used such information to infer the particle dynamics. Colloids have been proven to be excellent model systems for structures across different length scales that are more difficult to observe, such as collections of atoms and molecules. Furthermore, they can be helpful test-beds to investigate fluid dynamics at low Reynolds number and can form artificial micromachines that are essential for the realization of disparate functional tasks at the microscale.

PART I

INTRODUCTION

CHAPTER 1

GENERAL INTRODUCTION

Colloidal particles containing magnetic materials can be manipulated by external fields and their interactions tuned from short to long-range, giving rise to captivating collective phenomena. Because colloids are characterized by experimentally accessible length and time scales, they are used as model systems to investigate similar effects arising in atomic, molecular or granular assemblies. Moreover, colloids are useful probes that help to understand the principles that govern the hydrodynamics at the microscale, where swimming by reciprocal motion does not lead to net translation. Finding ways to realize propelling microdevices is essential for the miniaturization of numerous processes in physics, biology and analytical science. Thus, magnetic colloids are fascinating for both fundamental and technological reasons.

1.1 Thesis aims and structure

The main objective of this thesis is to investigate soft condensed matter systems using the manipulation of magnetic colloids in an effort of realizing propelling microdevices and assembling large and complex structures. In this context, we tuned the interactions between collections of particles by using external magnetic fields, magnetic substrates and the photoactivity of specially synthesised hematite particles. With this control, we want to understand the fundamental properties of these microscopic systems and find numerous applications in emerging technologies as microfluidics and lab-on-a-chip.

This thesis is structured into five parts. After a first introduction ([Part I](#)), I will define some fundamental concepts in order to better understand the basic principles of magnetic colloidal systems ([Part II](#)). [Chapter 2](#) explains why colloids can be used as model systems, lists some common techniques employed to visualize and characterize colloids, describes their main interactions and mentions some of the structures that these particles can form. In [Chapter 3](#) I will talk about magnetic micro and nanoparticles, illustrating some of the interactions that play a role when magnetic colloids are subjected to external fields. [Chapter 4](#) deals with the peculiarities of fluid dynamics at low Reynolds number, introducing

some of the latest developments in active particle suspensions and magnetic micropropellers. In [Part III](#) I will report the materials and methods used in this work. In [Chapter 5](#) I will detail the colloids we used and how we prepared our samples. [Chapter 6](#) describes our experimental set-up and data analysis processes. In [Part IV](#) I will summarize all the results we obtained ([Chapter 7](#)) and include all the publications ([Chapter 8](#)). Finally, in [Part V](#) I will recapitulate the conclusions and give some future perspectives.

1.2 Soft condensed matter and colloids

The work described in this thesis is done in the context of soft condensed matter, which is a very broad area of research. Condensed matter physics mainly deals with the properties of solid and liquid matter in macroscopic or microscopic states. Soft condensed matter is the part of condensed matter that studies soft materials, i.e. materials that can easily withstand deformations. In these systems, interactions have often the strength of the order of the thermal energy $k_B T$. Soft condensed matter materials have essentially slow dynamics and experimentally accessible time and length scales. They include a wide variety of substances ranging from liquid crystals, granular materials and polymers to biological matter. Thus, this research field is rather multidisciplinary, as it embraces different disciplines spanning from physics to chemistry and chemical engineering [1].

Colloids are also a class of soft condensed matter systems. According to the Encyclopaedia Britannica, a colloid is any substance consisting of particles substantially larger than atoms or ordinary molecules but too small to be visible to the unaided eye. More specifically, a colloidal suspension is a mixture of insoluble particles between approximately one nanometer and a few micrometers dispersed in another medium such as a fluid. There are many examples of colloids in everyday life, such as toothpaste, milk and paint.

The name colloid was first used by Thomas Graham in the 1860s to describe a naturally occurring gum. It comes from the greek "glue" (kolla) [2–5]. Thanks to Perrin's experiments in 1910 [6] and Einstein's theory of Brownian motion in 1905 [7, 8] colloids helped prove the molecular composition of matter. Colloidal science started to develop more quantitative theories in the 1940s with the derivation of the effective pair potential of charged colloidal particles by Derjaguin, Landau, Verwey and Overbeek [9]. In the same decade, the first synthetic colloidal spheres were made [10]. In the following years, colloidal science attracted more attention to both experimentalists and theorists. Nowadays, colloids are a widely used system in soft condensed matter studies.

PART II

FUNDAMENTALS

CHAPTER 2

COLLOIDAL SCIENCE

Colloidal science has gained more attention over the past decades thanks to the development of experimental techniques and tools that allow the fabrication, manipulation and visualization of microscopic and nanoscopic particles with high precision. Furthermore, colloids have become a useful model system since, on a collective level, they behave similarly to a collection of atoms and other systems across different length scales.

The colloids involved in the present work are specifically solid microparticles dispersed in a liquid solution. In this chapter, I will only briefly introduce some concepts relevant to this thesis. For further reading, Peter Pusey's lectures [11, 12] are one of the basics of modern colloid physics. Numerous books explain colloids from different interesting perspectives, ranging from applied to more fundamental ones [13–15].

2.1 Colloids as a model for atoms

A dilute suspension of colloidal particles, from a thermodynamic point of view, can behave like a collection of "large atoms": the particles can have the same equation of state at equilibrium and show the same sedimentation processes as a classical ideal atomic gas [11]. This analogy enforces the use of colloids as model systems for condensed matter physics. For instance, colloids have been widely used to study phenomena such as crystallization [16, 17] and glassy arrest [18–20] (Figure 2.1). One of the advantages of using these microscopic particles is that they have accessible experimental length and time scales. However, at the level of individual units, atoms and colloids present many differences. Atoms need a quantum description and present very different types of interactions, while colloids are also affected by Brownian motion and usually present polydispersity. Therefore, it is important to carefully choose the particles used and understand the interactions involved in the suspensions in order to properly describe them.



FIGURE 2.1: Colloidal phases. (a) Photography of suspensions of colloidal spheres with different concentrations illuminated with white light. Concentration increases from right to left: the phases go from colloidal fluids to the appearance of polycrystalline states. The samples with larger concentrations present glassy phases. From Ref. [21]. (b) Confocal microscope image of a colloidal glass. Scale bar is 10 μm . From Ref. [22].

2.2 Visualisation and characterization of colloids

In the last century, the main technique that was used to study colloids was light scattering. In general, *scattering* is the process where the incident radiation on a sample deflects from its initial trajectory. Because this process averages over large ensembles of the system's configurations, it provides highly accurate measurements of both structure and dynamics, but it can not probe its local properties. For example, light scattering can accurately measure the fraction of a colloidal sample which is in a crystalline state, but it can not determine the exact domain shape. Scattering is useful, for instance, to study the kinetics of crystallization [23].

Rheology is the study of the deformation and flow of a material in response to an external perturbation, as an applied force. It can reveal interesting properties regarding the particular microstructure and the forces involved in colloidal suspensions [24]. Since these measurements are macroscopic in nature, the structure and dynamics at short length scales can only be indirectly studied. Understanding the rheology of colloidal suspensions, how the flow is affected and can be manipulated by external stresses, is necessary especially when engineering industrial products made of colloids such as paint and pharmaceuticals [25].

In the last decades, the developments of *optical and video microscopy* techniques have enabled to study the dynamics of colloids in real space [26, 27], since they have a size of the order of the wavelength of visible light and relatively slow dynamics. These are easy and cost-effective techniques, but they do not allow three-dimensional imaging. This can be solved by *confocal laser scanning microscopy*, whose functioning lies in the illumination of a small sample volume and the rejection of out-of-focus light. It allows for high-quality

direct imaging of a sample both in two or three-dimensions [28]. However, it has a higher cost and a lower time resolution than an optical microscope. Thus, an optical microscope coupled with a camera with a high repetition rate is an excellent tool to investigate the dynamics and local properties of colloidal particles, even if its observation capability is constrained to two-dimensional or quasi-two-dimensional systems. All of our experiments were performed with this technique (Chapter 6). We also used *Scanning electron microscopy* (SEM) as a complementary tool to characterise the size and shape of our particles, since it allows the imaging of dried samples of colloids in vacuum with extremely high resolution.

2.3 Brownian motion

When microscopic or nanoscopic particles are suspended in a fluid they display Brownian motion due to the continuous collision with the surrounding solvent molecules [7, 8]. The Brownian motion of colloids, in fact, played an important role in proving the granular nature of matter [29, 30]. This type of motion is random and erratic and, on average, it does not result in a net displacement. Thus, to measure the extent of the diffusion process of a particle, the mean square displacement $\langle \Delta r^2 \rangle$ is used. For an isolated free particle which has diffused a time t , that can be written as [2]:

$$\langle \Delta r^2 \rangle = 2nDt \quad (2.1)$$

This is the Einstein-Smoluchowski equation, where D is the diffusion coefficient and n is the dimensionality of the system. To characterise D for particles in a low Reynolds number fluid, the Stokes-Einstein relationship is often used [31, 32]:

$$D = \frac{k_B T}{\gamma} \quad (2.2)$$

Where k_B is the Boltzmann constant, T is the temperature and γ is the drag coefficient of the particle, which depends on its shape and size and on the viscosity of the medium η . This is related to a characteristic time called the *Brownian time* (τ_B), which is the time that a particle takes to diffuse its own radius [33]. Using Equations (2.1) and (2.2) for a particle with radius R , that is:

$$\tau_B = \frac{\gamma R^2}{2nk_B T} \quad (2.3)$$

For a colloid that has a size of the order of a few micrometers, τ_B is of the order of seconds, which can be easily captured using video microscopy.

It is important to note that Eq. (2.1) is true for a single isolated passive particle not diffusing in a complex environment, i.e. a medium where there are no geometrical confinements, external flows, obstacles or heterogeneities that could affect the random walk in

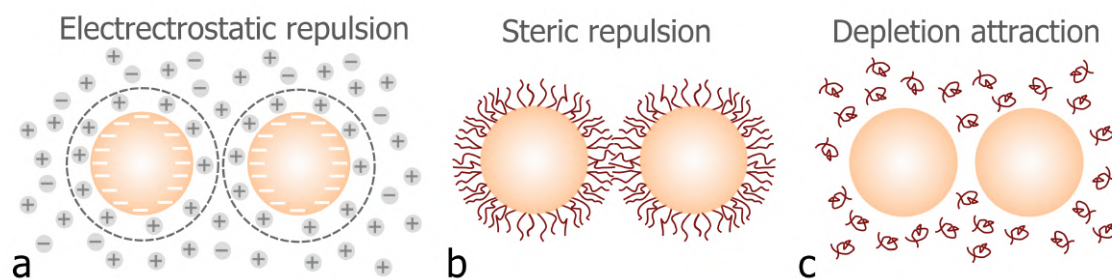


FIGURE 2.2: Schematic showing different interactions between colloids. (a) Electrostatic repulsion by the electrical double layer of negatively charged particles in an electrolyte solution. (b) Steric repulsion of particles coated with polymers. (c) Depletion attraction by random-coil polymers.

any direction. This type of transport where the mean square displacement is a linear function of time is called normal diffusion [34]. Otherwise, there is anomalous particle transport, which can be observed for instance in active self-propelled particles (Chapter 4.3). Furthermore, even the diffusion of isolated particles has a ballistic behaviour ($\langle \Delta r^2 \rangle \propto t^2$) at very short time scales because of the particle's inertia [35, 36]. Anisotropic particles such as ellipsoids have also a different diffusive behaviour because of their shape and are characterized by distinct friction coefficients related to their translational and rotational motion [37–41].

2.4 Interactions between colloids

When studying dense suspensions of colloidal particles it is important to understand their interactions, which have distinctive origins, as described below.

Firstly, colloids experience a *Van der Waals attraction*, which is a purely attractive force caused by the interaction between the electromagnetic fields of the particles associated with their electric polarisabilities. This attraction depends on the properties of the materials which the particles are made of and on the suspension medium. With the correct solvent, the Van der Waals interactions can become very small [42]. Otherwise, stabilization is necessary to avoid aggregation. One common strategy is to have either ionizable moieties or short polymer chains present on the surface of the colloids, which gives rise to additional repulsive interactions, as follows.

If the particles are ionizable, they experience repulsion due to their *electric double layers* (EDL), which in general form when a charged interface is in contact with an electrolyte [43]. The ionizable groups on the surface of the colloids dissociate, the particles acquire a net charge and attract counterions from the liquid. The result is an electrical double layer surrounding the particle, where the concentration profile of ions is different from its bulk value. When charged colloids approach each other, the overlap of their EDL causes a

repulsive force which helps to avoid aggregation (Figure 2.2a). The interaction energy of charged colloidal particles in an electrolyte can be described by the *DLVO potential*, which is an effective pair potential derived by Derjaguin, Landau, Verwey and Overbeek [44]. It includes the EDL repulsion and the Van der Waals attraction (Figure 2.3). However, this represents a simplified picture and other more detailed theories have been developed [42].

If the colloids are coated with polymers, they experience *steric repulsion*. When two coated particles approach too closely there is compression of their interpenetrating polymer layers, which results in a strong repulsion (Figure 2.2b). However, this interaction depends on the coating polymers and it is difficult to generalize. In the solvents where the Van der Waals attractions can be neglected, the effective pair potential of coated colloids can be approximated to that of hard spheres. Minimizing the inter-particle interactions can be useful to investigate excluded volume effects, which represent a simple system mathematically where the only relevant thermodynamic variable is the volume fraction ϕ . For a system of volume V with N spheres of radius R that is given by:

$$\phi = \frac{4\pi R^3 N}{3 V} \quad (2.4)$$

However, measuring ϕ in colloidal systems is not completely straightforward, due to the particles' polydispersity and the fact there is always some softness in the interparticle potential [45].

The interactions in colloidal suspensions can also be modified by tuning the properties

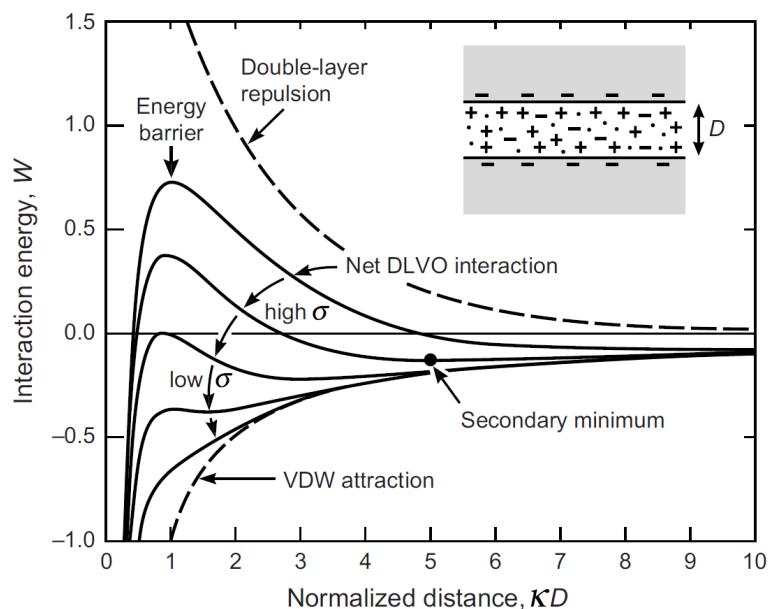


FIGURE 2.3: DLVO interaction energy versus distance between two surfaces with charges σ and the inverse of the Debye screening length κ in a 1:1 electrolyte solution. From Ref. [42].

of the dispersing medium. When smaller solutes are added to the suspension, for instance free random-coil polymers, particles experience an attractive force of entropic origin (*depletion attraction* in Figure 2.2c).

2.5 Examples of colloids

When choosing a colloidal suspension to use as a model system, it is important that its constituent particles are monodisperse in size and uniform in shape such that the inter-particle interactions are similar. In this context, there are a number of very well-characterised types of spherical colloids.

Polystyrene (PS) spheres [47, 48] (Figure 2.4), composed of polystyrene molecules, are one of the most used colloids and they were one of the first to be synthesised. At the particles' surface there are hydrophilic groups that in water and other polar liquids acquire a negative charge such that the particles do not aggregate irreversibly. *Polymethylmethacrylate* (PMMA) spheres sterically stabilised are also often employed since they can behave as nearly-perfect hard spheres in solvents that match the particle density and refractive index [33]. *Silica* (SiO_2) particles are widely used as well. They acquire a negative charge when in contact with a solvent like water [49] and can be sterically stabilised by a variety of polymers.

In this work we used silica particles mixed with magnetic colloids, both commercial and synthesised. As I discuss in Chapter 3, the latter present additional interactions because of their magnetic properties. Furthermore, they can be manipulated by external fields.

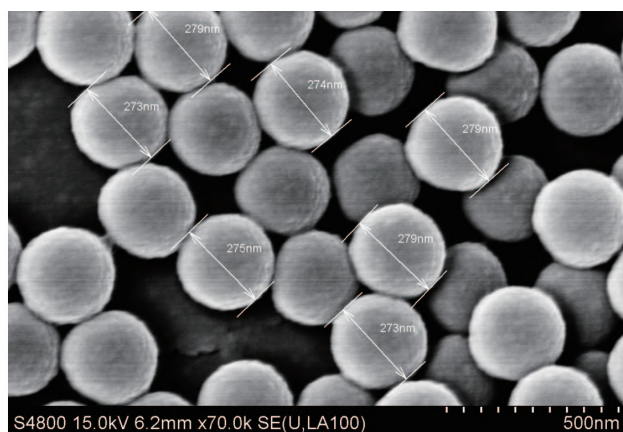


FIGURE 2.4: Electronic microscope images of polystyrene microspheres with a diameter of 270 nm. From Ref. [46].

2.6 Colloidal crystals and gels

The fact that inter-particle interactions can be tuned in colloidal suspensions opens up the possibility to engineer different microscale materials. Here I will describe colloidal crystals and gels [52], although glasses have been also widely studied [22].

Colloidal crystals are highly ordered periodic structures formed by monodisperse particles [53] with a surface charge to avoid random aggregation but not large enough to prevent close packing [54]. A crystalline order can be achieved by equilibrium self-assembly or by dynamic self-assembly processes [55]. In general, self-assembly is the autonomous organization of components into patterns or structures. Systems formed through static self-assembly are at global or local equilibrium and do not dissipate energy. For instance, monodisperse colloidal particles can spontaneously organize into equilibrium periodic crystals in three dimensions. When left undisturbed, most colloidal particles settle to the bottom of their container where their concentration can become high enough for crystallization [50] (Figure 2.5a). On the other hand, colloidal crystals can also be formed through dynamic self-assembly. This process involves the continuous injection of energy that produces dissipation. As an example, two-dimensional colloidal crystals can be assembled by rotating magnetic fields (Figure 2.5b). Furthermore, self-propelled active particles can also form crystals (Chapter 4.3). Stable three-dimensional ordered colloidal systems with lattice constants comparable to the wavelength of visible light can find applications as photonic crystals [56], optical switches [57] or sensors [58]. Additionally, periodic structures formed in systems driven out-of-equilibrium by external fields or forces have been

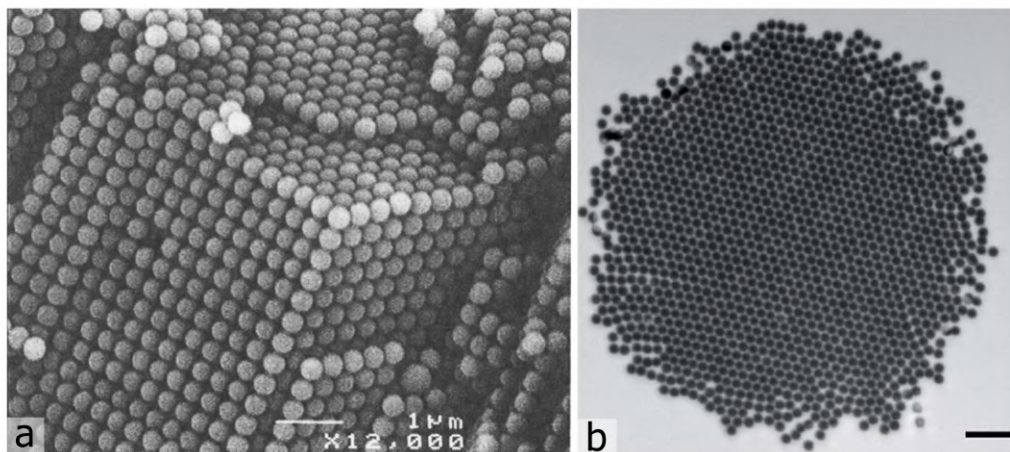


FIGURE 2.5: Colloidal crystals. (a) Scanning electron micrograph of a polystyrene colloidal crystal formed by equilibrium self-assembly from Ref. [50]. (b) Optical microscopy image of a 2D colloidal crystal made of magnetic colloids dynamically self-assembled with rotating magnetic fields. Scale bar is $10 \mu\text{m}$. From Ref. [51].

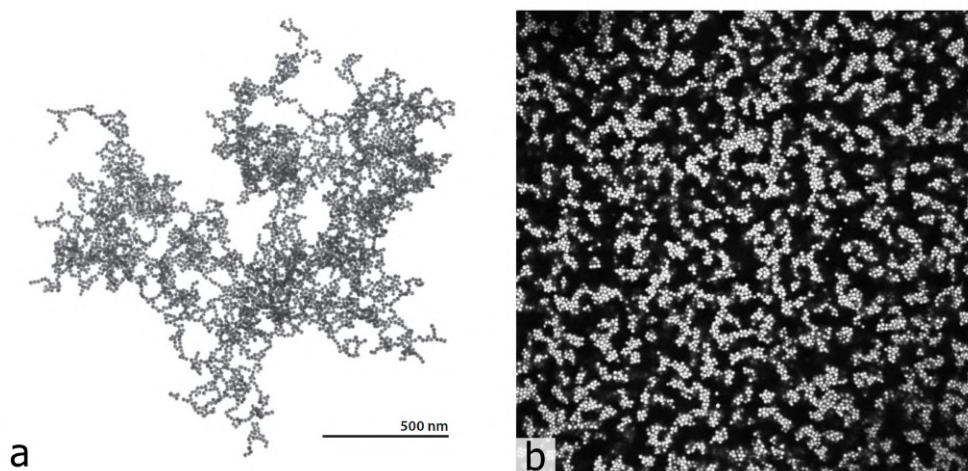


FIGURE 2.6: Colloidal gels. (a) Transmission electron micrograph of a gold colloid aggregate formed by diffusion-limited cluster aggregation. From Ref. [52]. (b) Confocal micrographs of a gel network of charged PMMA particles in suspension with non-adsorbing polymers. From Ref. [63].

the subject of much attention over the last few years because of their richness and complexity [51, 59, 60]. They have also fundamental interest in investigations of different processes such as melting and crystallisation [61, 62].

Colloidal gels have also been investigated as model systems. In general, a gel is a system that aggregates in a low-density disordered percolating network that does not flow but possesses solid-like properties. There are different routes to gelation, both non-equilibrium and equilibrium ones [64]. A colloidal gel can be formed, for instance, when the attraction between particles is strong and short-ranged. If colloids stick irreversibly to each other upon contact, particles diffusing in a fluid aggregate to form clusters that percolate in a gel [52] (Figure 2.6a). Charged PMMA spheres in solutions with non-adsorbing polymers can also be assembled into gel networks [63] (Figure 2.6b).

In this thesis, we will show the magnetic field assembly of large-scale two-dimensional propelling clusters that are able to crystallise and self-heal (Publication 4). Furthermore, using interactions activated by light, we found a new out-of-equilibrium route towards the formation of two-dimensional colloidal space-filling gels, clusters, and bicontinuous structures (Publication 7).

CHAPTER 3

MAGNETIC PARTICLES

Magnetic colloids exhibit a wide range of functionalities because they can be easily manipulated with magnetic fields. With the correct strategy, they can be transported in a microfluidic environment and carry or deliver drugs previously attached to their surfaces. Furthermore, magnetic fields can be used to induce interactions in a collection of magnetic particles: while the amplitude of the external magnetic field can tune the strength of the pair interaction, its direction can control the sign of the interaction potential, from attractive to repulsive. This gives rise to the formation of different types of structures and to the appearance of a broad variety of phenomena [65–67].

In general, magnetic materials can be used in a wide range of applications, from microelectronics to motors [68]. Magnetic colloids specifically, besides being used as microfluidic probes, can be used for functions such as biomedical imaging [69].

3.1 Magnetic materials

Magnetic materials can be classified as diamagnetic, paramagnetic or ferromagnetic. The origin of this behaviour lies in the orbital motion, spin and interactions between the electrons [68].

Diamagnetic materials exhibit a weak magnetisation in the direction opposite to the applied field (Figure 3.1). In the absence of a magnetic field, they have no net moment. On the other hand, *paramagnetic* materials have moments that align parallel to the external field. If there is no magnetic field, they have randomly oriented dipoles and no net magnetisation.

Typically, paramagnets and diamagnets have very weak magnetic interactions, which gives rise to low magnetisations. What we traditionally understand as magnetic materials are the ones with *ferromagnetic* behaviour, which can have a net magnetisation even in the absence of an external field, and have atoms with strongly interacting magnetic moments. The maximum magnetisation of a ferromagnet is called the saturation magnetisation M_S , and it occurs when all of the spins of the material are oriented along the same direction.

The magnetisation M as a function of the applied field H for these materials describes a hysteresis loop (Figure 3.2a). The remanence magnetisation M_r is the magnetisation that remains when there is no applied field. To reduce the magnetisation to zero, an external field H_c , called coercivity field, is required.

Materials with ferromagnetic behaviour can have a ferromagnetic, ferrimagnetic or antiferromagnetic coupling of their adjacent magnetic moments (Figure 3.1), depending on their crystal structure. Strictly ferromagnetic materials present parallel coupling, while antiferromagnetic and ferrimagnetic have antiparallel coupling. In ferrimagnetic materials the moment in one direction is weaker than that in the other direction, resulting in a finite net magnetisation. In most antiferromagnetic materials, the net magnetisation is zero. Nevertheless, sometimes the magnetic moments in antiferromagnets can be canted, which gives rise to a non-zero net magnetisation. In this work we will use hematite particles, which have a permanent moment because of their canted antiferromagnetic coupling.

Magnetic materials can be characterised by their volumetric magnetic susceptibility χ . In an applied field of strength H , the magnetisation induced in a material is [68]:

$$M = \chi H \quad (3.1)$$

The magnetisation depends on the magnetic moment m of a volume V of the material as $M = m/V$. The susceptibility χ in ferromagnetic materials depends on the temperature and also on H , which causes the hysteresis curve.

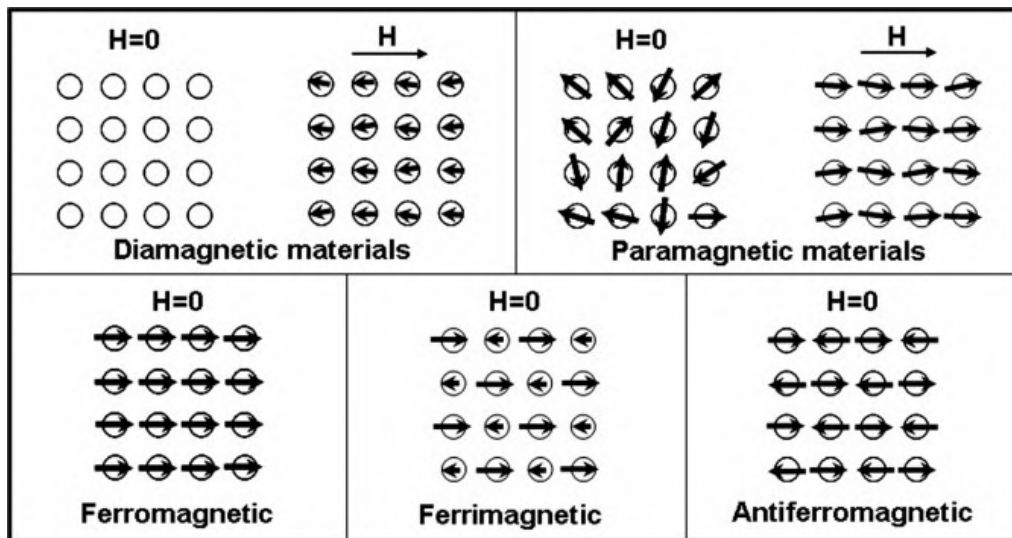


FIGURE 3.1: Schematic illustrating the arrangements of magnetic dipoles for five different types of magnetic materials in the absence or presence of an external magnetic field (H).
From Ref. [69].

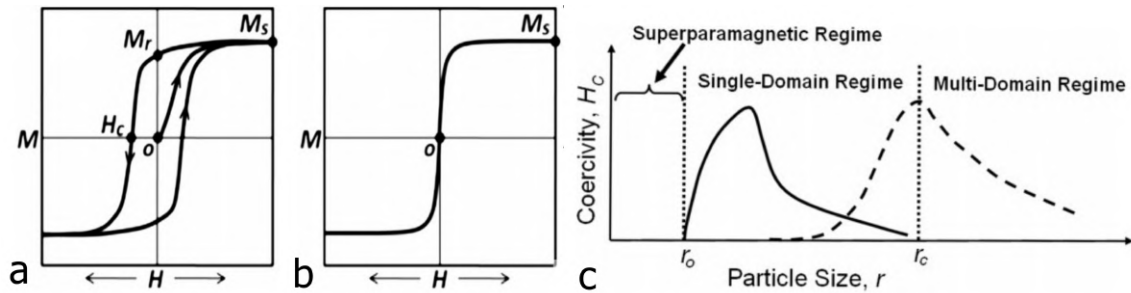


FIGURE 3.2: (a) Typical magnetisation curve for a ferromagnetic material. From Ref. [73]. (b) Typical curve for a superparamagnetic material. From Ref. [73]. (c) Dependence of the magnetic coercivity on the particle size. For a superparamagnetic particle $H_c = 0$. In the single domain regime, the coercivity can follow either curve depending on whether the particles have coupling between them. From Ref. [69].

3.2 Size effects in magnetic nanoparticles

The magnetic properties of nano- and micron-sized magnetic particles differ from those of the corresponding bulk magnetic materials due to their size [70]. Large particles have different magnetic domains, which are groups of spins pointing along the same direction, acting cooperatively and separated by domain walls. When a magnetic field is applied, there is nucleation and motion of these domain walls. However, if the size of the particle is lower than a critical value, the formation of domain walls is no longer energetically favourable. These are *single-domain particles*. If the radius of the particles is decreased further, the thermal energy $k_B T$ can be enough to flip the direction of a spin, which leads to a randomization of the magnetic moments. In these nanoparticles, if $H = 0$ the measured magnetization is zero. They are called superparamagnetic [71] because they behave like a paramagnetic spin with a very large moment. The *blocking temperature* is the temperature above which the thermal energy is comparable to the energy barrier for spin reorientation. For superparamagnetic particles above the blocking temperature, the $M-H$ curve does not show any hysteresis, i.e. the coercivity is zero (Figure 3.2b,c). For example, at room temperature, the maximum radius for a superparamagnetic spherical particle of iron is 6 nm. Iron oxide (Fe_3O_4) particles with diameters in the range of 5-100 nm are also superparamagnetic [72].

Magnetic nanoparticles have been widely studied over the last decades since they have applications ranging from biomedicine [74] to high-density data storage [73, 75]. There are numerous methods to synthesize microscopic magnetic particles, which are beyond the scope of the present work [69, 76–79].

In this work we used microscopic (1-2.8 μm) paramagnetic colloids in Publications 4 and 5. These particles are formed by a matrix of mono-domain superparamagnetic nanoparticles embedded in a polymer. The nanoparticles are dispersed enough to avoid

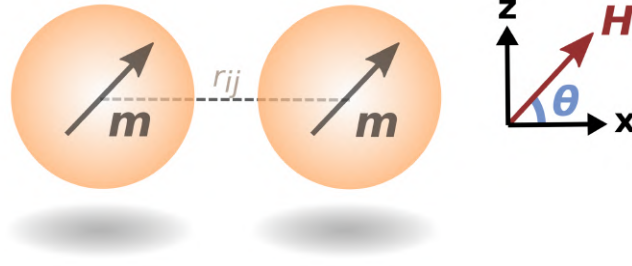


FIGURE 3.3: Schematic illustrating two magnetic particles with the same moment m aligned with an external field H .

interaction, causing superparamagnetic behaviour in these relatively large particles. We also used polycrystalline ferromagnetic particles in Publications 1, 2, 3, 6 and 7, which will be explained more in detail in Chapter 5.

3.3 Magnetic interactions in a fluid suspension

In general, when there is a collection of particles with magnetic moments, each particle experiences interaction with the others because of the local field generated by each dipole. The dipolar interaction U_d between two point particles i and j separated a distance r_{ij} is given by [68]:

$$U_d = \frac{\mu_m}{4\pi} \left[\frac{\mathbf{m}_i \cdot \mathbf{m}_j}{r_{ij}^3} - \frac{3(\mathbf{m}_i \cdot \mathbf{r}_{ij})(\mathbf{m}_j \cdot \mathbf{r}_{ij})}{r_{ij}^5} \right] \quad (3.2)$$

Where \mathbf{m}_i and \mathbf{m}_j are their dipole moments and μ_m is the magnetic permeability of the dispersing medium. It is often interesting to consider the particular case where two particles have the same moment \mathbf{m} . The interaction of equation (3.2) reduces to:

$$U_d = -\frac{\mu_m m^2}{2\pi r_{ij}^3} P_2(\cos \theta) \quad (3.3)$$

Where $P_2(x) = (3x^2 - 1)/2$ is the second-order Legendre polynomial and θ is the angle between the dipoles and the vector that connects the particles' centers r_{ij} (Figure 3.3). There is an angle $\theta_m = 54.7^\circ$, called the magic angle [80] where this interaction becomes zero. When $\theta < \theta_m$ the particles are attracted to each other and when $\theta > \theta_m$ they repel. Thus, the orientation of an applied field aligns the magnetic moment and can tune the interactions in collections of magnetic particles, which can be used to assemble a rich variety of structures. For instance, in two-dimensionally confined suspensions of magnetic colloids, triangular lattices of repulsive particles form when $\theta = 0^\circ$ (Figure 3.4a) and chains of attracting spheres assemble for $\theta = 90^\circ$ (Figure 3.4b) [81].

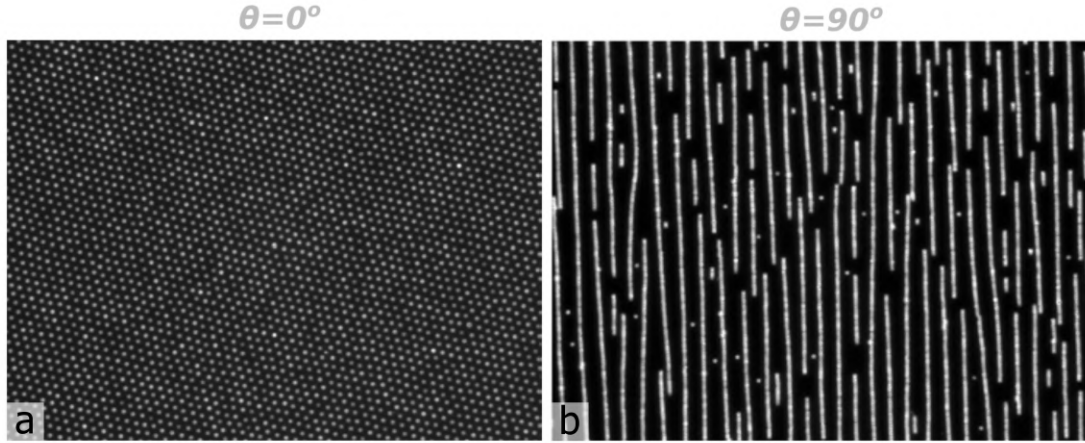


FIGURE 3.4: Optical microscopy images of paramagnetic colloids confined in a air–water interface under an external magnetic field. (a) For a field perpendicular to the particle plane ($\theta = 0^\circ$) a two-dimensional triangular crystal is found. (b) For in-plane fields ($\theta = 90^\circ$) there is chain formation in the direction of the field. From Ref. [81].

Beyond the formation of static structures, colloids can also dynamically rotate in a fluid. For instance, when a static external field \mathbf{H} is applied to a ferromagnetic colloid, there is a reorientation time where the particle rotates at an angular velocity Ω while its moment \mathbf{m} aligns with the field \mathbf{H} . There is a magnetic torque that acts on the particle that is [82]:

$$\mathbf{T}_m = \mu_m (\mathbf{m} \times \mathbf{H}) \quad (3.4)$$

Assuming large enough particles where the thermal fluctuations can be neglected, \mathbf{T}_m is balanced by the viscous torque created by the particle's rotation in a low Reynolds number fluid. The torque balance equation implies:

$$\mathbf{T}_m + \mathbf{T}_v = 0 \quad (3.5)$$

This viscous torque \mathbf{T}_v is:

$$\mathbf{T}_v = -\zeta_r \Omega \quad (3.6)$$

Where Ω is the velocity of rotation and ζ_r the rotational friction coefficient. Equations (3.4), (3.5) and (3.6) for a static field, lead to a reorientation angle between \mathbf{m} and \mathbf{H} after a time t of:

$$\Theta(t) = \tan^{-1} \left[\tan(\Theta_0) \exp\left(\frac{t - t_0}{\tau_r}\right) \right] \quad (3.7)$$

Where Θ_0 is the angle at time $t = t_0$ and $\tau_r = 2\zeta_r/(\mu_m m H)$ is the relaxation time. Additionally, if instead of a static field there is a rotating field acting on the particle, ferromagnetic colloids can continuously rotate [67, 83]. For low enough frequencies, the phase-lag angle between \mathbf{m} and \mathbf{H} is constant and the particle rotates synchronously with the field.

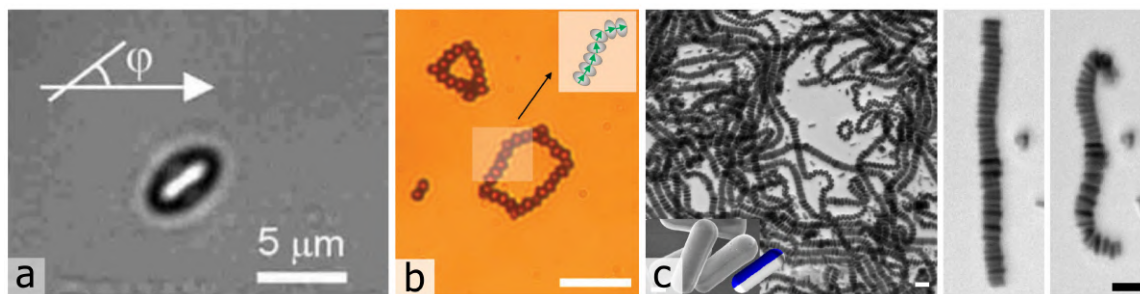


FIGURE 3.5: Anisotropic magnetic colloids. (a) Optical microscope image of a paramagnetic ellipsoid from Ref. [82]. (b) Optical microscope image of rings of dipolar ellipsoids. The schematic shows a section of one ring composed by ellipsoids and the permanent moments. Scale bar is $10 \mu\text{m}$. From Ref. [67]. (c) Optical images of a suspension of dipolar Janus rods. Scale bar is $5 \mu\text{m}$. Inset: scanning electron microscopy image of individual rods with schematic representation. Scale bar is $0.5 \mu\text{m}$. From Ref. [86].

For frequencies that are too large, the phase-lag is no longer constant, the particles are not able to follow the field and show a "back-and-forth" motion, slowing down their rotation frequency.

Paramagnetic particles can also rotate in a fluid medium when there is a circularly or elliptically polarised field because of their *internal relaxation time* τ_{int} [66, 84, 85]. This causes a phase shift between the particle magnetisation and the external magnetic field, which makes the particle experience a time-average non zero magnetic torque $T_m = \mu_m \langle \mathbf{m} \times \mathbf{H} \rangle$ and continuously rotate. This can quantitatively be described with a complex susceptibility which is dependent on the frequency. The fact that colloids can have a tunable rotation frequency can lead to important applications for particle manipulation in microfluidic environments.

Anisotropic magnetic colloids, i.e. particles with a preferred magnetisation direction, can show additional exciting properties [80]. This anisotropy can come from different factors such as crystal or shape anisotropy [87] and it causes a wider variety of collective phenomena. Their magnetic susceptibility becomes a tensor instead of a scalar and it has been shown that this anisotropy also affects fundamental behaviour such as Brownian motion [38]. Moreover, the orientation of the magnetic moment of particles with anisotropic shape can be inferred by visualizing them with simple optical techniques (Figure 3.5). In this work, we used ferromagnetic ellipsoids in Publications 1, 2, 3, 6 and 7.

CHAPTER 4

FLUID DYNAMICS AT LOW REYNOLDS NUMBER

When manipulating driven and active colloidal particles, it is essential to understand the fluid dynamics at the microscale, where the hydrodynamic regime is different than that of the macroscale. The equations regarding the flow become time-reversible and moving by reciprocal motion does not lead to net translation. Realizing propelling microdevices able to move and transport cargos is crucial for the engineering of microfluidic devices, controlled cargo delivery for biomedicine [88–95] and for the fundamental understanding of the physics of motion at such scales [96].

4.1 Swimming at low Reynolds number

The origin of the time-reversibility of microscale flows can be explained as follows. In an incompressible Newtonian fluid ($\nabla \cdot \mathbf{u} = 0$) with viscosity η and density ρ , the flow field \mathbf{u} follows the Navier-Stokes equation [97]:

$$\rho \frac{\partial \mathbf{u}}{\partial t} + \rho(\mathbf{u} \cdot \nabla)\mathbf{u} = -\nabla p + \eta \nabla^2 \mathbf{u} \quad (4.1)$$

Where p is the pressure. These, together with the corresponding boundary conditions, describe the flow field in a system. The *Reynolds number* value (Re) is often used to determine the hydrodynamic regime. Re is a dimensionless quantity and it is defined as the ratio of the inertial to the viscous forces. That is:

$$Re \equiv \frac{\text{inertial forces}}{\text{viscous forces}} \sim \frac{LU\rho}{\eta} \quad (4.2)$$

Where L and U are the characteristic length and velocity scales of the flow, respectively. For large Re the inertial terms in the Navier-Stokes equation are dominant, which is the case for a human swimming in water ($Re \sim 10^4$). On the other hand, for very small objects ($L \ll 1$) or highly viscous fluids ($\eta \gg 1$) the inertial terms are negligible, i.e. Re is very low, which is what happens when a microscopic object swims in water. In that case, the

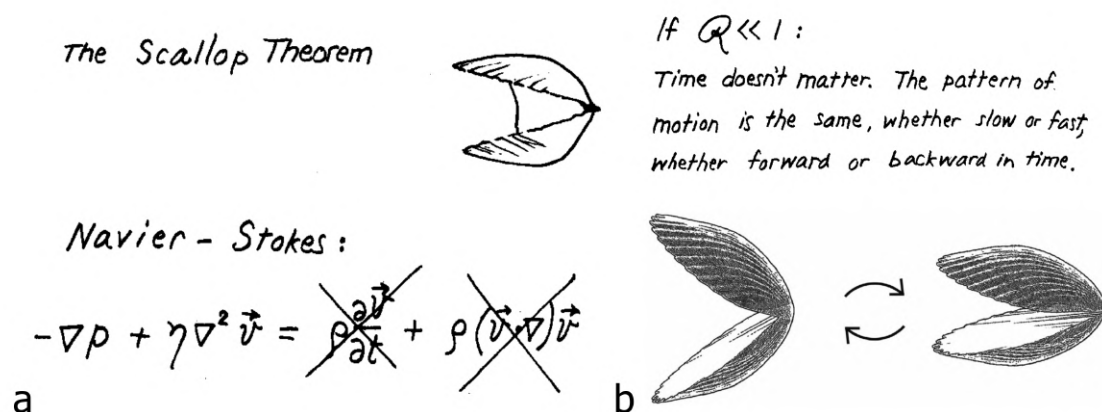


FIGURE 4.1: (a) Illustration of the Scallop theorem from Ref. [99]. (b) Illustration of the reciprocal motion of the Scallop from Ref. [106].

Navier-Stokes equation (4.1) simplifies to the Stokes equation, where the inertial term is neglected:

$$-\nabla p + \eta \nabla^2 \mathbf{u} = 0 \quad (4.3)$$

Equation (4.3) is linear and independent of time, which is why it is time-reversible. In this situation, reciprocal motion does not lead to propulsion [98, 99]. This is explained in the seminal paper *Life at low Reynolds numbers* [99], in which Purcell states that a scallop that moves by opening and closing its valves would not translate in water at the microscale (*The Scallop Theorem*, Figure 4.1). This is why living microorganisms such as bacteria have to perform complex movements that are not reciprocal in order to swim [100, 101] (Figure 4.2). For instance, amoeba deform their bodies, *E. coli* beat flagella, paramecia use ciliary motion and cyanobacteria traveling surface waves [102]. Many studies have been devoted to the understanding of motion in biological systems [103, 104]. Over the last decades, these mechanisms have inspired the design of numerous microdevices and *microwimmers*, i.e. microscopic objects capable of performing self-propelled motion in fluids through converting different types of energies into mechanical movement [96, 105].

There were several attempts to theoretically design simple microwimmers. Purcell's Three-Link Swimmer (Figure 4.3a) consists of three stiff arms and it translates by moving its front and rear parts in a cyclic way [99, 108, 109]. Similarly, the Three-sphere swimmer (Figure 4.3b) is composed of three spheres performing one-dimensional displacements [110, 111]. To obtain net propulsion, it is also possible to use the flexibility or elasticity of the swimmer [112–115] (Figure 4.3c). There have been theoretical models [116] inspired by microorganisms propelled by flagella, e.g. spermatozoa.

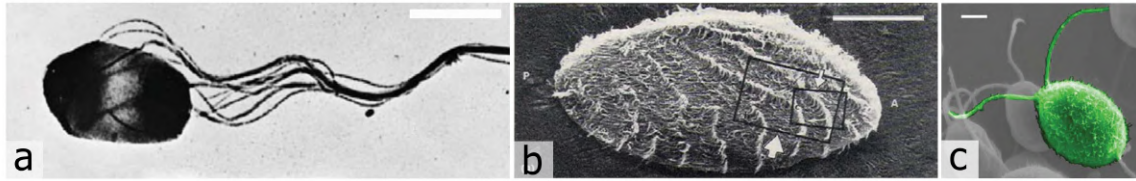


FIGURE 4.2: Examples of biological swimmers. (a) Salmonella swim by a bundle of rotating helical flagella. Scale bar is $1\mu\text{m}$. (b) The surface of Opalina is covered by many hairlike filaments called cilia. Opalina swims by a stroke-like wiggling of the cilia. Scale bar is $100\mu\text{m}$. (c) Chlamydomonas swim by a breast-stroke-like motion of its two flagella. Scale bar is $2\mu\text{m}$. Images from Ref. [107]

Mathematical models such as the *Squirmer* [117, 118] have been useful for the modelling and simulations of some microorganisms such as ciliates (Opalina), colonies of flagellates (Volvox) and Paramecium. These are approximately spherical in shape and swim using beating arrays of cilia or short flagella covering their surfaces. The physical actuation of the microswimmer on the fluid is described as the generation of velocities on a continuous spherical surface [119].

There has also been an extensive effort put into experimentally realizing microscopic synthetic propellers [120]. Because of the focus of this thesis, I will differentiate between the structures propelled by external fields, specifically magnetic fields, and the ones driven by chemical reactions and phoretic effects, i.e. propulsion mechanisms relying on local field gradients [121, 122]. However, there are numerous other ways to achieve propulsion at low Reynolds number. For instance, particles can be moved using external electric fields [123], structured light has been used to control intrabody shape changes in microrobots [124] and strategies to develop hybrid biotic/abiotic swimming microrobots have been investigated [125]. The possible applications of these synthetic motors include their use as practical propelling drug-delivery systems and chemical sensors [126, 127].

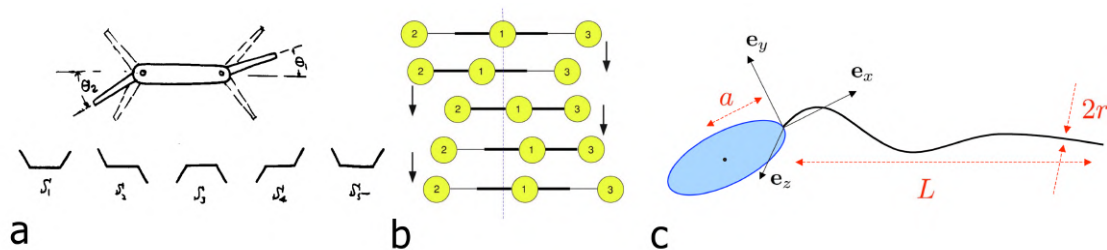


FIGURE 4.3: Examples of theoretical proposals of microswimmers. (a) Three-link swimmer from Ref. [99]. (b) Three-sphere swimmer from Ref. [110]. (c) Elastic swimmer from Ref. [116].

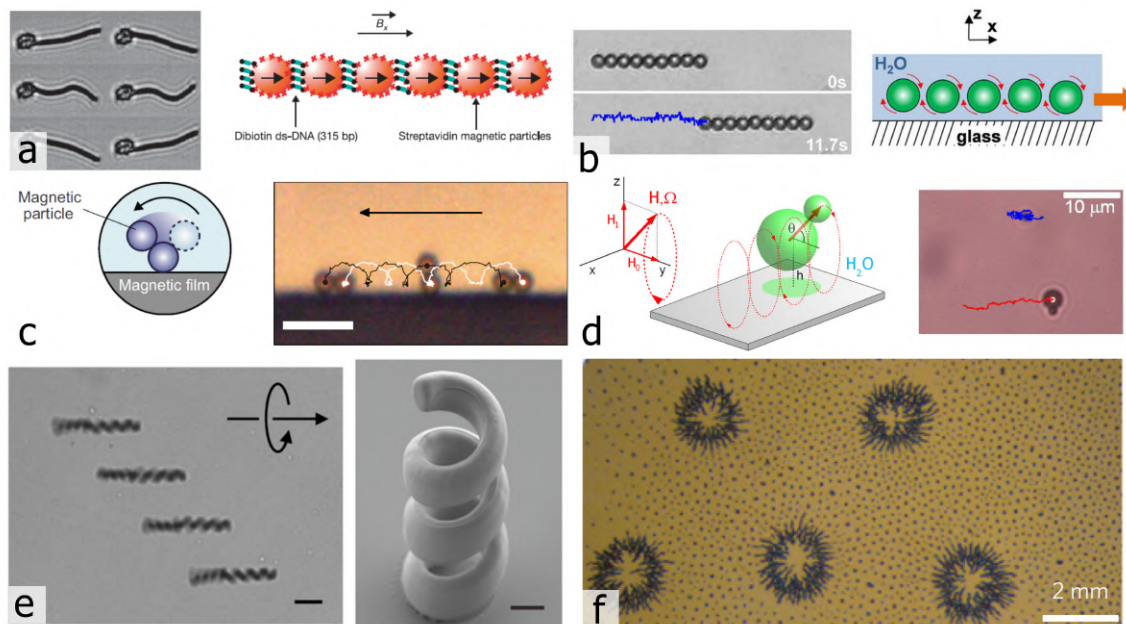


FIGURE 4.4: Examples of magnetic micropellers. (a) Swimming magnetic flexible filament. Illustration and beating pattern when attached to a red blood cell from Ref. [129]. (b) Worm of paramagnetic colloids translating close to a glass plate from Ref. [66]. (c) Tumbling motion of magnetic particles on a magnetic substrate induced by a rotational magnetic field from Ref. [130]. Scale bar is $10\mu\text{m}$. (d) Propelling anisotropic doublet rotors from Ref. [131]. (e) Microscopic magnetic helices are propelled in a rotating magnetic field from Ref. [132]. Scale bars are $20\mu\text{m}$ and $2\mu\text{m}$. (f) Swimming colloidal asters from Ref. [133].

4.2 Magnetic micropellers

External magnetic fields can be used to drive magnetic bodies at low Reynolds number with a high degree of control in direction and speed [128]. Additionally, compared with swimmers powered by chemical reactions, magnetic micropellers do not present efficiency reduction due to fuel shortage. Below I list distinct approaches that have been proven to transport microscopic particles in viscous fluids using magnetic fields.

A red blood cell with an attached flexible tail made of a chain of paramagnetic colloidal particles that imitates a flagellum can be propelled by inducing a beating pattern on the filament with an oscillating magnetic field [129] (Figure 4.4a). Similarly, magnetoelectric filaments [134], flexible nanowire motors [135], DNA-based flagellar bundles [136] and rotating helical shaped structures [132, 137, 138] (Figure 4.4e) can be moved under the command of time-dependent magnetic fields and show translation at low Reynolds number. Magnetic substrates can help to induce propulsion as well. For instance, the tumbling motion of paramagnetic particles on a magnetic substrate under a rotational magnetic field has been reported [130] (Figure 4.4c).

Confinement plays a critical role in microswimmers. If particles are close to a bounding wall, their rotational motion is rectified into net translation [139, 140]. For instance, rotating anisotropic doublet rotors [131] (Figure 4.4d), nickel nanowires [141] and worms of paramagnetic colloids [66] (Figure 4.4b) translate close to a confining wall. Additionally, a collection of ferromagnetic microparticles confined at the interface between two immiscible liquids dynamically self-assemble into asters which exhibit locomotion and shape change by applying an alternating magnetic field [133] (Figure 4.4f). Propulsion under confinement can be exploited for cargo transport in microfluidic channels or narrow pores in biological networks. Furthermore, it can imitate the symmetry breaking in the proximity of a boundary that has been observed for bacteria such as *E. Coli*, which perform circular trajectories instead of straight runs when swimming close to a solid surface [142]. In the present work we used confinement in order to propel structures made of paramagnetic and ferromagnetic particles.

4.3 Synthetic active Brownian particles

Synthetic active particles are able to take up energy from their environment and to convert it into directed motion [143]. Therefore, they are excellent candidates for propulsion at low Reynolds number. Moreover, because of their interactions with each other and with the dispersing medium, active particles can present very interesting and diverse collective phenomena while reproducing the behaviour observed in collections of living active systems, with the advantage that their interactions can be tuned on command [122]. Complex living systems present phenomena across different length scales and some examples include birds that form flocks, land animals that assemble into herds, fish that organize into schools and bacteria that form clusters [101].

Propulsion in active Brownian particles can be achieved by different techniques. One of them is phoretic motion [144], which is caused by local field gradients around the swimming body. The particle interacts with this field, is driven out-of-equilibrium, and converts energy into directed motion. Because of this constant flow of energy, their behavior can be explained and understood only within the framework of non-equilibrium physics [145]. In self-phoretic particles, the field gradient is caused by the particle's own asymmetries [121]. The gradient driving the particle can also be imposed externally, e.g. a temperature gradient. There are different types of phoresis depending on the type of field that presents local inhomogeneities. Below I list some examples.

Electrophoretic swimmers move because of an electric field gradient. This effect seems to cause the propulsion of bimetallic nanorods in a hydrogen peroxide solution (Figure 4.5a,b) [146, 147], which was one of the first realizations of a synthetic micromotor. Half of the rod is made of platinum, which catalyses the oxidation of the hydrogen peroxide and produces electrons and protons. These are consumed on the other side of the

rod, which is made of gold, by the reduction of hydrogen peroxide. As a consequence, an electron current in the rod and a proton current in its surface create a flow field that results in propulsion (Figure 4.5b). However, in this particular case, the possibility for other phenomena contributing to the rod propulsion have also been considered [149]. Electrophoresis has been used to propel other systems, for instance by applying an external alternating electric field to microdroplets in anisotropic fluids [150].

In *thermophoresis*, a local gradient of temperature is what causes the directed motion (Figure 4.5c). For example, silica particles half-coated with gold propel when irradiated with a laser beam. This is because the gold-coated side of the particle absorbs more light than the silica side, causing a local asymmetry of temperature [151, 152]. In a similar approach, a time-dependent magnetic field can be used to heat an object with a ferromagnetic cap, inducing its thermophoretic motion, while an additional constant magnetic field can orient and guide the synthetic particle [153].

In *diffusophoresis* [154], the particle moves because of a gradient of concentration of one type of molecules (Figure 4.5d). It is often caused by a chemical reaction on one part of the particle, but it can also be the result of the local demixing of a critical mixture in one half of a sphere when it is illuminated by light [155] (Figure 4.6a). Figure 4.5d shows a common self-diffusophoresis example: a polystyrene-platinum Janus particle dispersed in a solution of water and hydrogen peroxide (H_2O_2) [156, 157]. Due to the presence of H_2O_2 , its molecules are decomposed into oxygen and water at the platinum side of the

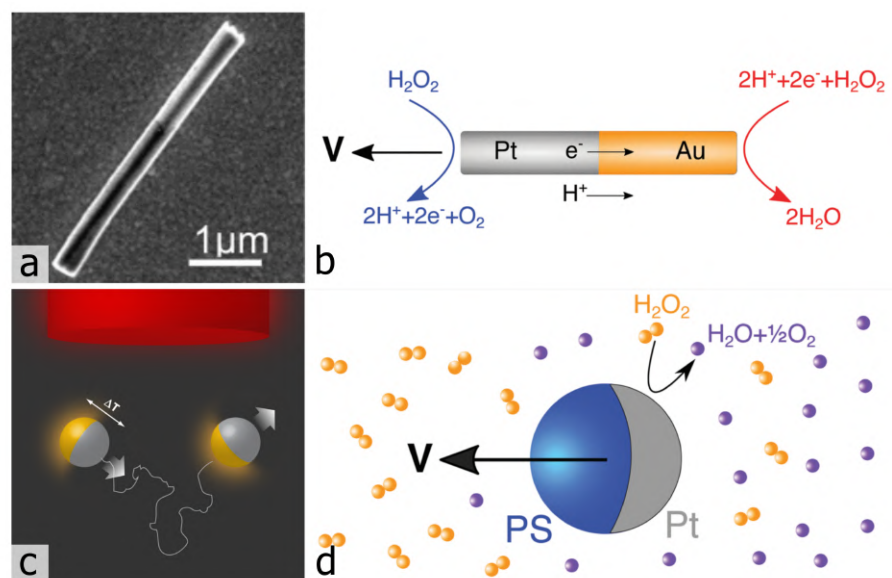


FIGURE 4.5: Examples of phoretic swimmers. (a) Bimetallic nanorod from Ref. [146]. (b) Representation of a bimetallic Pt–Au nanorod powered by the catalytic decomposition of hydrogen peroxide of [147] from Ref. [121]. (c) Illustration of self-thermophoresis from Ref. [148]. (d) Illustration of self-diffusophoresis from Ref. [121].

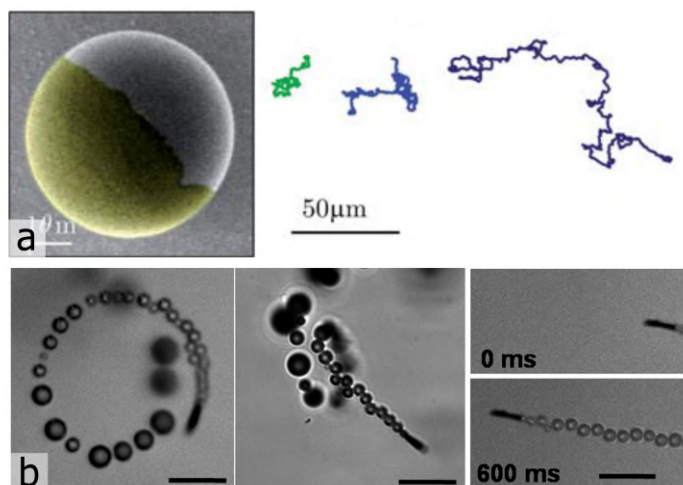


FIGURE 4.6: Examples of self-propelled bodies. (a) Self-propulsion of Janus particles in critical mixtures. Scanning electron microscopy image of a colloidal particle with gold cap and 2D trajectories of a Janus particle for different illumination intensities. From Ref. [155]. (b) Microtubular catalytic engine from Ref. [159]. Scale bars are 20 μm .

colloid with the reaction:



This decomposition can be catalysed by platinum, but it is also catalysed by hematite under blue light. This provides an extra degree of control to the system, since the interaction that causes the propulsion can be deactivated by switching off the light. Diffusophoresis can also cause the reversible docking of chemically active particles to passive bodies [158]. In this case, the symmetry of the chemical gradient surrounding an activated particle is broken by the presence of passive colloids in the solution.

Self-propulsion has also been seen in systems where the decomposition of hydrogen peroxide causes bubble nucleation. In that case, motion does not result from phoresis but from momentum transfer due to the bubbles growing and detaching from the surface. This propels particles to ultrafast speeds, e.g. 305 body lengths per second [159–162] (Figure 4.6b).

However, the requirement of high concentration of hydrogen peroxide fuel, which is toxic for biological systems, has complicated practical applications. In the last few years, other reaction schemes have been studied in order to solve this problem. The catalytic decomposition of hydrazine in very low concentrations has proven to be very efficient [163]. Acid-driven hydrogen-bubble-propelled microrockets characterised by a spontaneous redox reaction occurring at the surface [164] and polymerization-driven motors have also been investigated [165].

I have listed so far several methods that propel synthetic particles using magnetism and diffusophoresis. It is also very interesting when both approaches are combined. The

applied magnetic field can be used to steer the swimmer, or a chemically bound dimer can be propelled by an external magnetic field [158, 166].

There are very interesting *collective effects* that can be observed in assemblies of active particles [167]. The interactions responsible for these phenomena can be very different and include excluded-volume interactions, hydrodynamic interactions, or interactions mediated by the field responsible for the phoretic motion.

For instance, dense solutions of self-propelled particles can accumulate into clusters separated by gas-like dilute regions [121, 143]. This is a consequence of the out-of-equilibrium dynamics [171] and, qualitatively, it can be explained as follows. When particles collide, their orientations have to change for them to become free. If more particles collide before this happens, a cluster starts to form (Figure 4.7b). This mechanism depends on several parameters such as the rotational diffusion time. Theoretical work has introduced the concept of Motility Induced Phase Separation (MIPS) to explain this phenomenon [172]. In experimental systems, the cluster formation is often also promoted by

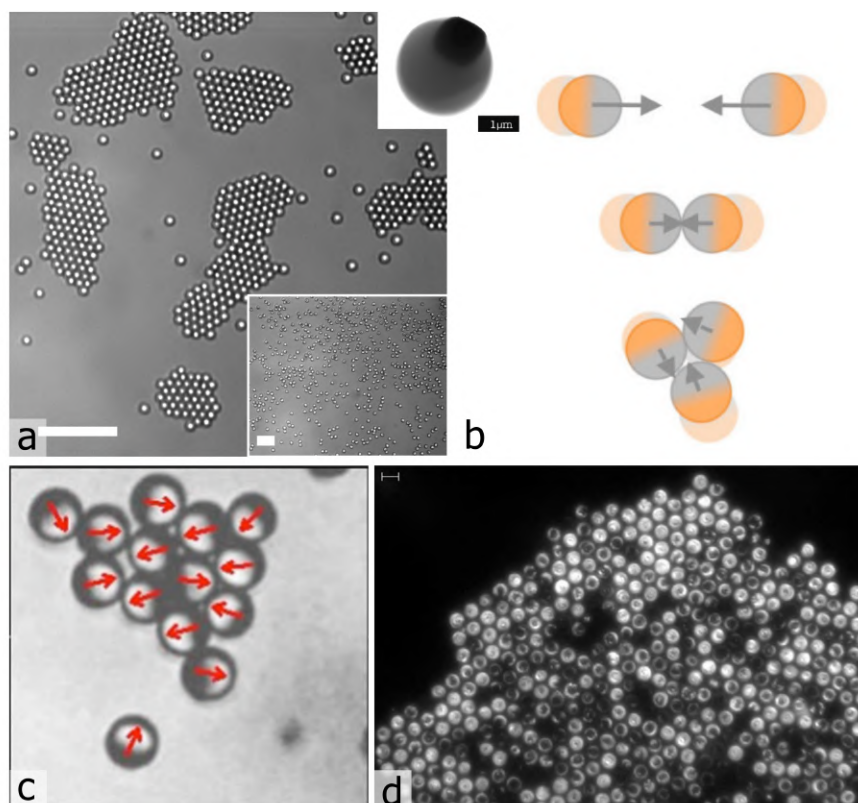


FIGURE 4.7: Examples of clusters formed in active systems. (a) Living active crystals and scanning electron microscopy image (SEM) of the constituent: a colloidal sphere with protruding hematite cube. Scale bar is $10\mu\text{m}$. Inset is the initial configuration. From Ref. [168]. (b) Illustration of the clustering process from Ref. [143]. (c) Cluster of self-propelled diffusiophoretic Janus particles from Ref. [169]. (d) Bacterial crystal from Ref. [170]. Scale bar is $10\mu\text{m}$.

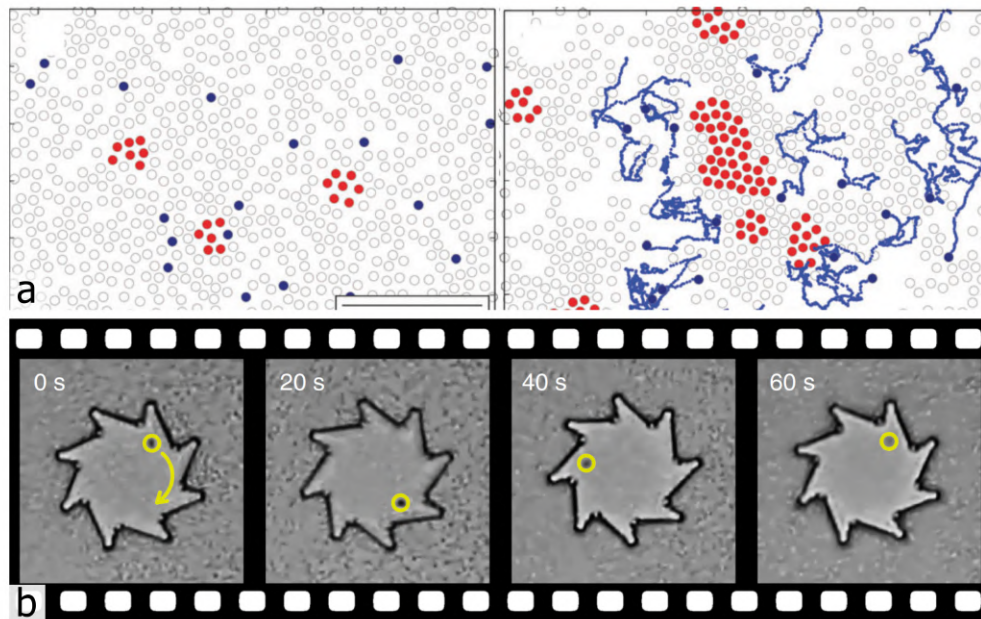


FIGURE 4.8: Examples of collective phenomena in a mixture of active and passive particles. (a) Crystallisation of passive particles promoted by active particles. Experimental snapshots of the temporal evolution of a mixture of passive (red and grey) and active (blue) particles at 0s and 1200s. Scale bar is $50\ \mu\text{m}$. From Ref. [176]. (b) Asymmetric gear ($48\ \mu\text{m}$ external diameter, $10\ \mu\text{m}$ thickness) rotates when immersed in an active bath of motile *E. coli* cells. From Ref. [177].

an attraction between the particles caused by the same phoretic interactions that produce self-propulsion [168]. In most of the cases, the formed clusters are dynamic, i.e. as they move, they accumulate new particles, expel some of them, rotate and merge with other clusters [169, 173–175] (Figure 4.7a,c). Active clusters have also been seen in living systems such as fast swimming bacteria [170] (Figure 4.7d), where the dynamics are caused by the hydrodynamic and steric interactions between the cells.

A mixture of active and passive particles also undergoes interesting collective effects [107, 143]. For instance, few active particles can promote the crystallization of passive particles [176, 178, 179] (Figure 4.8a). If the number of active particles increases, there can be turbulence [180], phase separation [181] and the passive particles can present non-thermal fluctuations caused by the active suspension. Additionally, a passive particle in an active bath can behave like an active particle [182] and it can even present directed motion (or rotation) if it has an asymmetric geometry. For example, an asymmetric gear rotates in an active bath of motile *E. coli* cells [177].

It is often interesting to study collective effects in collections of active particles when there are interactions beyond phoresis [183, 184]. For instance, if there are interactions that align the particles, there can be phase separation and swarming. This was shown by the Vicsek model [185, 186] and it can be very useful as a model system to understand

biological living systems such as schools of fish, flocks of birds, or groups of migrating bacteria [101].

In this thesis, we used light-activated hematite colloids to dock passive particles through diffusophoretic mechanisms and transported them using an external magnetic field (Publication 6). We also found a non-equilibrium diffusiophoresis route to form two-dimensional arrested structures in collections of active hematite colloids and passive particles (Publication 7).

PART III

MATERIALS AND METHODS

CHAPTER 5

SAMPLE PREPARATION

In this work we have mainly used paramagnetic and ferromagnetic colloids. We also mixed them with non-magnetic colloids and used magnetized substrates in order to transport them or tune their interactions. Below I describe the particles and substrates we employed and explain how we prepared the samples.

5.1 Ferromagnetic Colloids

We synthesised ferromagnetic hematite (α -Fe₂O₃) ellipsoids with two different sizes using a sol-gel method developed by Sugimoto and co-workers [187]. This is an efficient procedure since it results in large quantities of monodisperse particles. Also, different shapes can be obtained, such as cubes, peanuts or ellipsoids.

For the work described in this thesis, we used ellipsoids of two sizes. The smaller ellipsoids have an average major and minor axes of length $a_1 = 1.80 \pm 0.11 \mu\text{m}$ and $b_1 = 1.31 \pm 0.12 \mu\text{m}$, respectively (Figure 5.1a). The larger ellipsoids have a subtle peanut-like shape and axes of length $a_2 = 2.5 \pm 0.12 \mu\text{m}$ and $b_2 = 1.4 \pm 0.13 \mu\text{m}$ (Figure 5.1b).

The preparation for the small ellipsoids was as follows. A sodium hydroxide solution (21.64 g of NaOH in 90 ml of high deionized water) was slowly mixed with an iron chloride hexahydrate solution (54.0 g FeCl₃ · 6H₂O in 100 ml of high deionized water) at room temperature. During the mixing process, which lasted 5 minutes, both solutions were vigorously stirred. Then, a solution containing potassium sulfate (0.285 g K₂SO₄ in 10ml of high deionized water) was poured and the resulting dark brown mixture was stirred for another 5 minutes. The resulting liquid was transferred to a Pyrex bottle and left unperturbed in an oven at 100°C for 8 days. For the bigger ellipsoids, the preparation procedure was identical but a different quantity of sodium hydroxide was added: 19.48 g of NaOH in 90 ml of high deionized water. In both cases, a dense aqueous suspension composed of microscopic ellipsoids together with rod-like nanoparticles made of akaganeite (β -FeOOOH) was obtained after 8 days. This is because the particles are formed through a two-step phase transformation and β -FeOOOH is a secondary product and a precursor

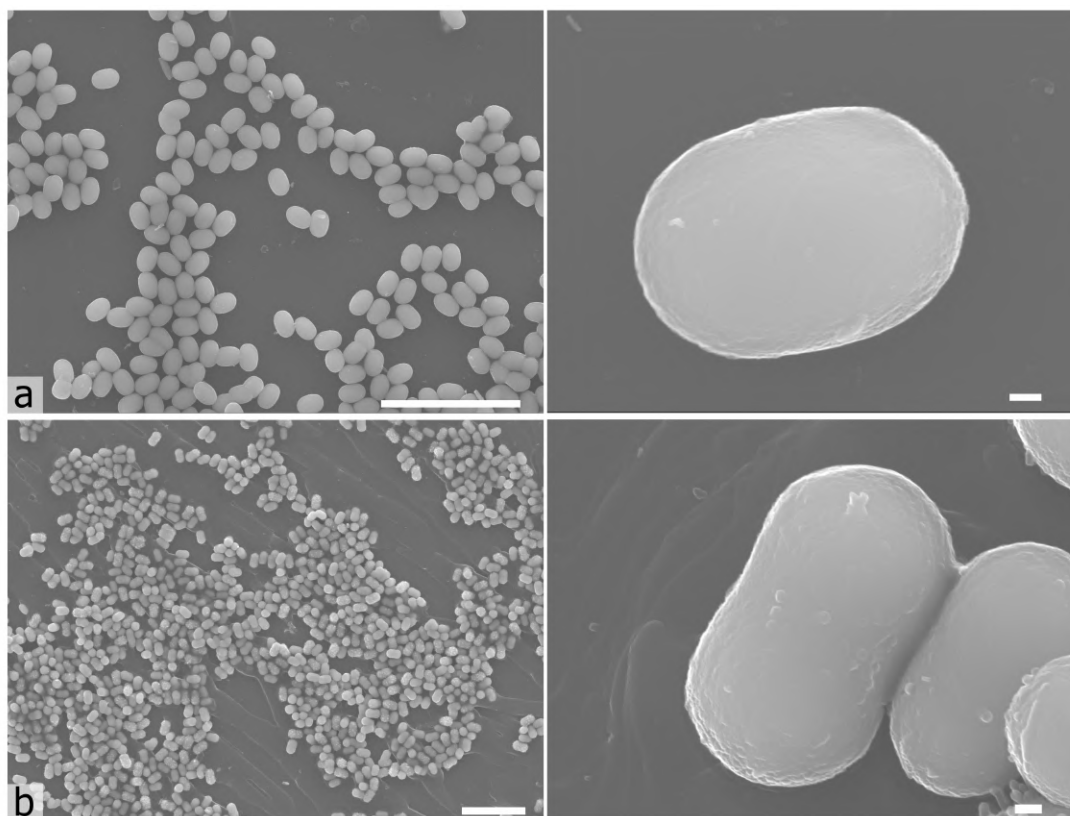


FIGURE 5.1: Scanning electron microscopy (SEM) image of the hematite ellipsoids. (a) Small ellipsoids. Scale bars are 10 μm and 200nm. (b) Big ellipsoids. Scale bars are 10 μm and 200nm.

of the hematite in the synthesis [188]. The akaganeite could be easily removed by diluting the suspension with high deionized water, letting the particles sediment and removing the resulting yellowish supernatant. This procedure was repeated several times until a clear supernatant appeared.

The hematite ellipsoids were functionalized with the surfactant sodium dodecyl sulfate (SDS, 0.12g of SDS in 80ml of high deionized water). SDS consists of a single negatively charged sulfate group with a hydrophobic alkyl chain. The surfactant grafts on the particle surface and it disperses the ellipsoids in the solution, avoiding the irreversible sticking between the particles [189].

Finally, the pH of the resulting solution was adjusted to 8.5-9.5 by adding Tetramethylammonium Hydroxide (TMAH). We used TMAH since in basic conditions the hematite particles display a negative phoresis, i.e. they are able to attract colloidal particles made by polystyrene or silica, as previously reported [158]. This was taken advantage of in Publications 6 and 7. Furthermore, adjusting a basic pH in the solution of these iron oxide particles seemed to increase their stability and reduce permanent aggregation [190].

With this method, we obtained monodisperse hematite particles with a prolate shape.

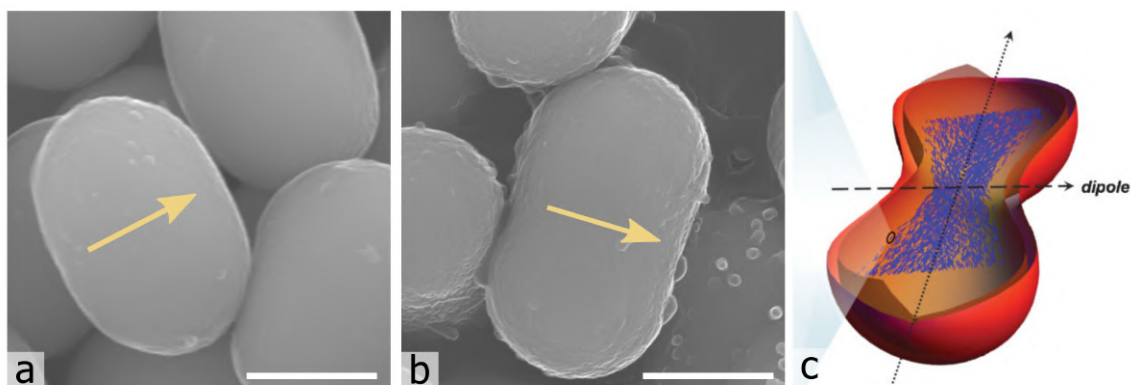


FIGURE 5.2: Schematic showing the permanent magnetic moment orientation in the SEM images of the (a) small and (b) big hematite ellipsoids, which is perpendicular to their long axis. Scale bar is $1\mu\text{m}$. (c) Schematic showing the particle's microstructure derived from aggregates of crystallites (blue spindles). From Ref. [192].

Particle size and shape were analyzed by scanning electron microscopy (SEM, Quanta 200 FEI, XTE 325/D8395). The particles acquired a permanent moment perpendicular to their long axis (Figure 5.2), which is a consequence of the hematite shape and microstructure. These particles are polycrystals consisting of much smaller elongated monocrystals in the direction parallel to the particle's long axis [188, 191] (Figure 5.2c). At room temperature, hematite presents the coupling of a canted antiferromagnet and it exhibits a non-zero spontaneous magnetization. Because of how the iron cations are aligned, the permanent dipole moment is perpendicular to the monocrystals' and the particles' long axis [192].

The resulting permanent magnetic moment of the small and big particles was $m_1 = 2 \cdot 10^{-16} \text{Am}^2$ and $m_2 = 9 \cdot 10^{-16} \text{Am}^2$, respectively. Furthermore, from SQUID (Superconducting Quantum Interference Devices) measurements, we find that, in the range of field used, the induced magnetization is negligible compared with the permanent magnetization (Supporting Information in Publication 6).

In the right conditions, these hematite particles can also show chemical activity. When exposed to blue light, they catalyse the decomposition of hydrogen peroxide in solution, which, together with their magnetic properties, makes these particles very useful for a wide variety of studies.

5.2 Paramagnetic Colloids

We used commercial spherical monodisperse paramagnetic colloids. Smaller particles with a diameter $d = 1.0 \mu\text{m}$ (Dynabeads Myone, Dynal) and larger ones with $d_L = 2.8 \mu\text{m}$ (Dynabeads M-270, Dynal) (Figure 5.3a,b). These particles have been widely used and studied in the literature [193, 194] because of their wide range of applications, for instance, in biomedical analysis [74].

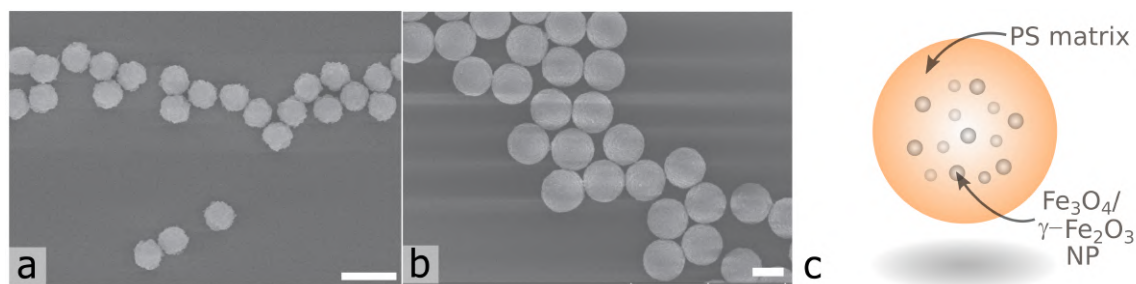


FIGURE 5.3: SEM images of the (a) MyOne and (b) M270 Dynabeads from Ref. [194]. (c) Schematic illustrating the dispersion of nanosized magnetic particles distributed in a polymer spherical host matrix.

These magnetic microspheres are composed of a dispersion of superparamagnetic nanoparticles (NP) made from iron oxides (Fe_3O_4 or $\gamma\text{-Fe}_2\text{O}_3$), which are uniformly and randomly distributed within a spherical porous host matrix (Figure 5.3c). They are separated enough to not interact and to show superparamagnetic behavior (Chapter 3). The small and large particles have magnetic volume susceptibilities of approximately $\chi_s = 1$ and $\chi_L = 0.4$, respectively [195, 196]. Furthermore, these particles are functionalized with surface carboxylic acid groups, which increases dispersion in the solution due to their electrostatic double layer and avoids aggregation.

5.3 Ferrite Garnet Films

We used complex magnetic substrates to manipulate the colloids, specifically ferrite garnet films (FGFs). The FGFs were grown by dipping phase epitaxy in the group of Tom H. Johansen at the University of Oslo and have a composition of $\text{Y}_{2-5}\text{Bi}_{0-5}\text{Fe}_{5-q}\text{Ga}_q\text{O}_{12}$ where $q = 0.5 - 1$ [197]. These films present magnetic domains which have a magnetization perpendicular to their surface. The domains are each magnetized oppositely to their adjacent ("up" or "down") and are organized into lattices of stripes (Figure 5.4) or bubbles, with a spatial periodicity λ of the order of a few microns. In the boundaries of the magnetic domains there are Bloch walls (BWs), which are narrow transition regions where the magnetization vector rotates by 180 degrees. These domains can be easily modulated in size by applying magnetic fields with a perpendicular component to the substrate.

The FGFs have been used to transport paramagnetic colloidal particles [198–200] (Figure 5.4c,d). The mechanism is as follows. When an aqueous solution of the particles is deposited over the film, the colloids pin to the BWs due to the intense field generated. To avoid particle sticking and reduce the strong attraction of the FGF, we coat the film with a uniform layer of a positive photoresist AZ-1512 (Microchem, Newton, MA) by standard spin coating. Due to electrostatic repulsive interaction, the particles float a few nanometers above the coating layer without touching it. Under no applied field, a FGF with stripe

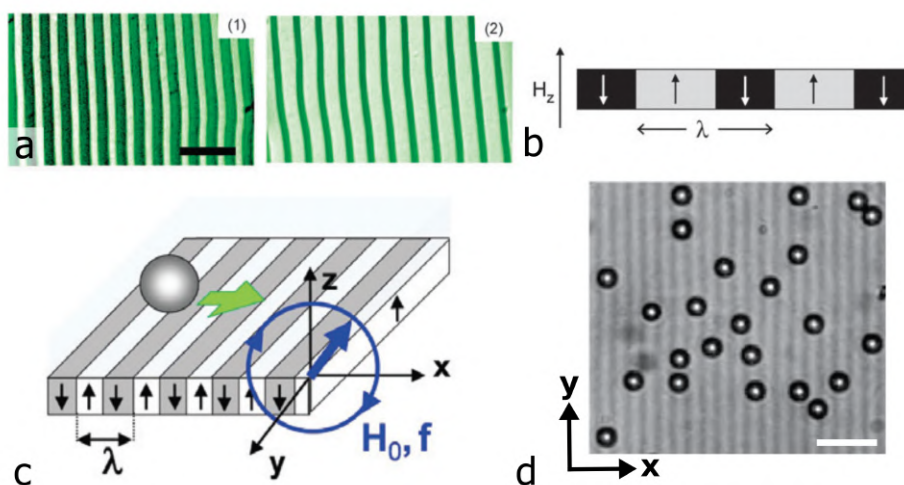


FIGURE 5.4: Ferrite garnet films (FGFs). (a) Magneto-optical images of domains in a stripe patterned FGF in different magnetic fields H_z , applied perpendicular to the film. The first image is for $H_z = 0$. The scale bar is $30\mu\text{m}$. (b) Side view of the domain configuration. From Ref. [197]. (c) Schematic of a paramagnetic colloidal particle on top of a FGF subjected to a rotating magnetic field. (d) Optical microscope image showing a diluted sample of particles and the magnetic pattern of the FGF. Scale bar is $10\mu\text{m}$. From Ref. [199].

domains causes a one-dimensional $\lambda/2$ -periodic magnetic landscape. If an external time-dependent rotating magnetic field is applied, it generates a travelling wave potential that translates at a constant speed. Thus, the particles are trapped in the minima of the traveling wave and can translate on the FGF surface. This method can be used to achieve directed transport with particle speeds up to $200\mu\text{m/s}$ [197]. We used this strategy in [Publication 5](#) to transport paramagnetic colloidal particles on the surface of FGFs with parallel stripe domains.

5.4 Final solution preparation

In the different publications, we used similar strategies to prepare the samples that are placed in the magnetic coil stage and observed under the light microscope. They were as follows.

First, we prepared the solution. In [Publication 1](#) and [3](#), the solution consisted of the magnetic ellipsoids with surfactant and adjusted pH. In [Publication 2](#), non-magnetic particles, specifically commercial aqueous suspensions of monodisperse silicon dioxide particles (44054 Sigma-Micro, Sigma-Aldrich) of diameter $4\mu\text{m}$, were added to the solution of magnetic ellipsoids. In [Publication 4](#) the solution contained paramagnetic particles of diameter $2.8\mu\text{m}$ (Dynabeads M-270, Dynal). In [Publication 5](#) the solution contained paramagnetic particles of diameter $2.8\mu\text{m}$ and also smaller ones of $1\mu\text{m}$ (Dynabeads MyOne, Dynal).

In [Publication 6](#) and [7](#) hydrogen peroxide was added (H_2O_2 , 9 vol%) to the solution of ellipsoidal particles. The non-magnetic samples employed in [Publication 6](#) were commercial aqueous suspensions of monodisperse particles based on silicon dioxide (44054 Sigma-Micro), which have diameters in the range of 1-5 μm . In [Publication 7](#) silicon dioxide particles (44054 Sigma-Micro, Sigma-Aldrich), having 4 μm were added.

In [Publication 1](#), [2](#), [3](#), [4](#), [6](#) and [7](#) the solution was introduced in a sealed capillary chamber (inner dimensions 0.1–2.00mm, CMC Scientific). The colloids sedimented and each particle floated at a certain distance from the glass bottom plate due to the balance between gravity and electrostatic interactions with the negatively charged substrate. The glass surface has a negative charge caused by the dissociation of silanol groups [49]. The particles, at room temperature, displayed small Brownian motion above the substrate and negligible out-of-plane fluctuations. In our experiments, particles remained quasi-two-dimensional confined due to gravity. In [Publication 5](#) the solution containing paramagnetic particles of different sizes was deposited above the coated FGF surface, where the particles sedimented on top of the photoresist and were also confined to the horizontal plane.

CHAPTER 6

EXPERIMENTAL SET-UP

The experimental set-up allowed us to apply external constant and time-dependant magnetic fields in situ while observing the evolution of the sample in real-time with video microscopy techniques. We analysed the resulting videos and obtained information about the out-of-equilibrium dynamics of our systems.

6.1 Magnetic coils system

A set of *magnetic coils* were used to apply different magnetic fields in the three directions of space. It consists of a triaxial magnetic coil system connected to a waveform generator (TGA1244, TTI) feeding a power amplifier (AMP-1800, AKIYAMA or BOP 20-10M, Kepco) or a direct current power supply (EL 302RT, TTI).

The three sets of coils have their main axis aligned along with the three orthogonal directions (x, y, z) . These coils were custom-made and are composed each by $N = 1100$ turns of a 0.4 mm copper wires. They are able to generate a uniform magnetic field on the sample plane. The solution of colloids was placed in the center of the (x, y) plane which is aligned with the fifth coil (Figure 6.1a).

This set-up allowed to apply both time-dependent fields generated by an alternating current (AC) passing through the coils, as well as constant fields generated by a direct current (DC). Rotating fields in a given plane, such as (x, z) or (x, y) , can be applied by passing through two perpendicular coils two sinusoidal currents with a ninety degrees phase shift. The field in the center of the coil configuration for each direction (x, y, z) was calibrated using a Teslameter (FM 205, Projekt Elektronik GmbH). Under time-dependent fields the calibration was done for all the measuring frequencies. Due to the inductance of the coils, keeping the field constant when increasing the driving frequency requires an increase of the applied voltage.

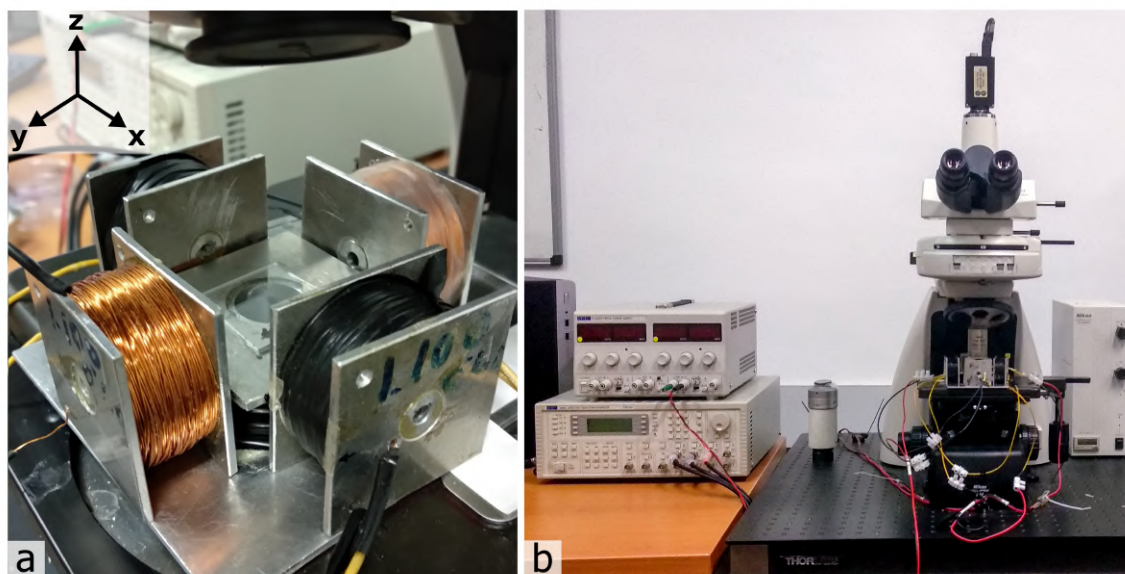


FIGURE 6.1: Experimental set-up. (a) Image of the set-up including the magnetic coils and the set of chosen coordinates. The sample is in the center. (b) Full experimental set-up including the light microscope, the waveform generator, the DC power supply and the mercury-fiber illuminator system.

6.2 Observation of the system and illumination set-up

The magnetic coils were arranged on the stage of a light microscope (Eclipse Ni, Nikon), equipped with high magnification objectives (Figure 6.1b). The objectives used were 100x, 1.30 NA (Nikon) and 40x, 0.60 NA (Nikon). We sometimes also used a TV lens of magnification of 0.45x. The dynamics were investigated by determining the motion of the colloidal particles with a CCD camera (Basler Scout scaA640-74f, Basler), at a frame rate of up to 75 fps, mounted on top of the microscope.

Illumination of a chosen wavelength can be applied to the sample using a commercial mercury-fiber illuminator system (C-HGFI Intensilight Nikon) connected to the optical microscope through an epifluorescent tower. Blue light was obtained using a fluorescent filter with an excitation wavelength between 450nm and 490nm. The optical power was measured at the sample plane with a power meter (PM200, Thorlabs) equipped with a photodiode sensor (400 - 1100 nm, S121C, Thorlabs).

6.3 Image and data analysis

The positions of the particles were obtained from the movies recorded by the commercial software (STREAMPIX) and later on analyzed using a MATLAB adaptation of the particle tracking software developed by Grier, Crocker, and Weeks [201, 202], in which the centres

of particles are found by computing the brightness-weighted centroid of each particle in the image. Using this method, the particle positions can be determined with sub-pixel resolution [26]. The images and videos captured were also analysed using the software packages ImageJ.

PART IV

RESULTS

CHAPTER 7

SUMMARY OF RESULTS

Colloidal microparticles made of magnetic materials were manipulated by external fields. In Publications 1-5 we used magnetic fields to assemble and drive magnetic particles and we analysed the structures they form. We assembled chains and clusters that were able to propel at a constant speed above the sample plane. Furthermore, we observed the bidirectional transport of colloids over a magnetic patterned substrate. In Publications 6 and 7 we introduced activity to our system. The latter was formed by a mixture of active colloidal particles and passive microspheres. This activity induced diffusophoretic mechanisms that allowed the docking of cargos to the magnetic active particles, which were transported using an external field. Furthermore, the same particles were used as active dopants towards the formation of two-dimensional clusters and gels.

In dense solutions, our hematite ellipsoids with axes of length $a_1 = 1.80 \pm 0.11 \mu\text{m}$ and $b_1 = 1.31 \pm 0.12 \mu\text{m}$ self-assembled into elongated ribbon-like structures due to their permanent magnetic moment (Figure 7.1). In Publication 1 we studied how the magnetic interactions between the particles affect the stability of the ribbon. These structures aligned parallel to the direction of an applied static field, while the thermal fluctuations caused the ellipsoids to have a certain orientational motion which depended on the field amplitude. We characterised the orientational dynamics of these structures experimentally and compared it to an analytical expression derived from theoretical arguments. We measured

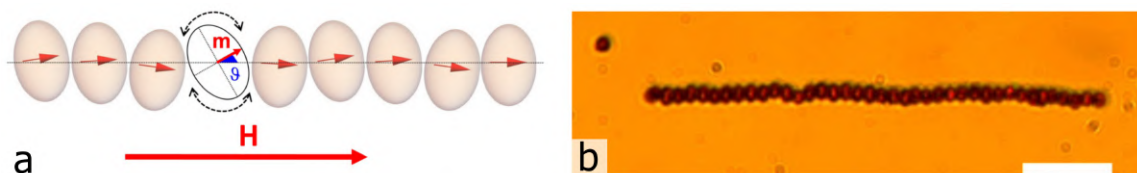


FIGURE 7.1: (a) Schematic showing a chain of ferromagnetic ellipsoids subjected to an external static magnetic field H . (b) Optical microscope image of a ribbon under a field of strength $H = 1600 \text{ A/m}$. Scale bar is $10 \mu\text{m}$. From Publication 1.

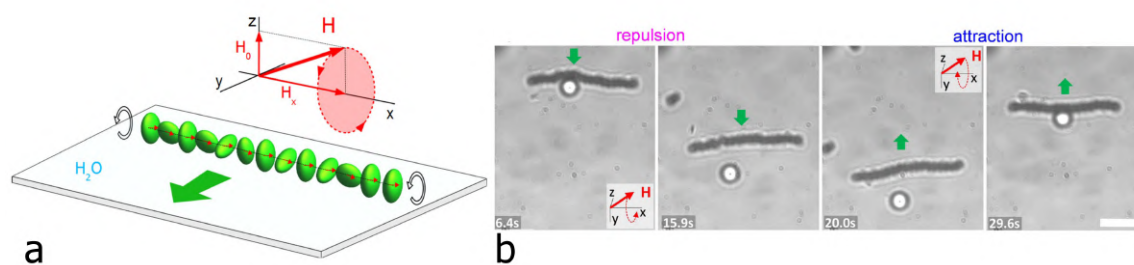


FIGURE 7.2: (a) Schematic illustrating a magnetic ribbon propelling due to a precessing magnetic field \mathbf{H} . (b) Sequence of microscope images showing how the motion of one silica particle is controlled by the propelling ribbon. Scale bar is $10\ \mu\text{m}$. From [Publication 2](#).

the average angle ϑ between the permanent dipoles in the chain with respect to the applied external field \mathbf{H} (Figure 7.1a) and found that increasing \mathbf{H} reduced the amplitude of the orientational fluctuations, centering the angular distribution at $\vartheta=0^\circ$. The study of the fluctuations in these chains of dipolar particles is interesting from a fundamental point of view and it also serves to understand and characterise the stability of similar magnetic chains that can be used for microfluidic applications.

Additionally, these ribbons can be propelled using an external elliptically polarised field (Figure 7.2a), which torques the particles forming the ribbon and makes them rotate. Differently than in [Publication 1](#), the ribbons reorient perpendicular to the field direction [67]. Because of the confining wall, this rotation causes propulsion of the entire structure. We further strengthen the ribbon along a defined direction by adding also a static magnetic field. In [Publication 2](#) we demonstrated a method that uses the hydrodynamic flow

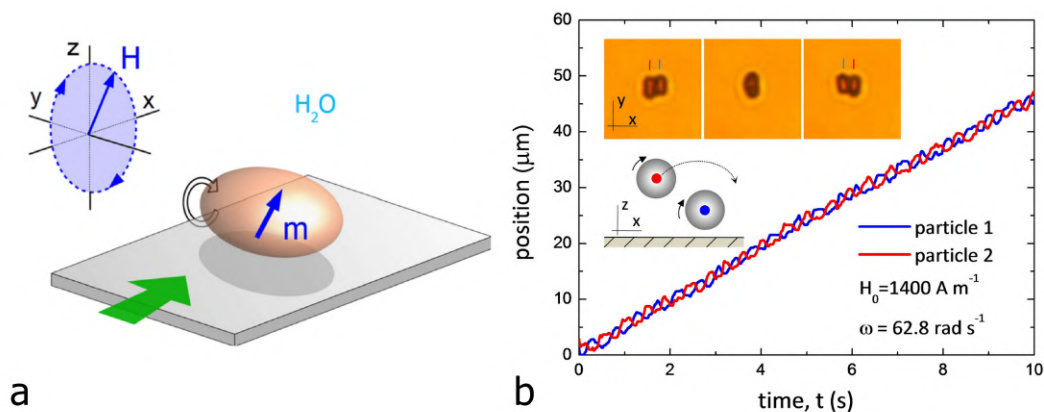


FIGURE 7.3: (a) Schematic illustrating a ferromagnetic hematite ellipsoidal particle propelling due to the application of a rotating magnetic field \mathbf{H} . (b) Position vs. time of two particles performing the leap-frog dynamics. Insets show experimental images and a schematic of the motion. From [Publication 3](#).

field created by these propelling ribbons to trap, transport and release microscopic particles. We varied the amplitudes of the external field in order to determine the range of experimental values where the propelling ribbons are observed. For very high amplitudes of the rotating field, the ribbon breaks. This results from the fact that the magnetic torque is able to spin the entire structure, and the ribbon behaves as a compact rod that tries to follow the rotation of the field, but it ruptures when standing up due to the presence of the solid substrate and the action of gravity. Furthermore, the ribbon does not propel for very low field amplitudes. We also found that these chains have a twisted conformation, with groups of particles rotating together. The ellipsoidal shape of the particles allowed to characterize this distortion. On the other hand, we characterised the propulsion speed and direction in terms of frequency and amplitude of the applied field. We propelled the ribbon next to a silica particle of $4\ \mu\text{m}$ of diameter (Figure 7.2b) and found that the non-magnetic colloid can be either repelled or attracted when located in front or behind the translating chain, respectively. We measured the average speed of the non-magnetic tracer particles as a function of the distance from the center of a ribbon and compared it to a theoretical model of the flow field generated by the chain. Our magnetic ribbons may be used in channel-free microfluidic applications, where the precise trapping and transport of particles is required.

When the ribbon ruptures, it breaks apart into individual ellipsoids that rotate following the direction of the applied field. We explored this regime for ellipsoids with axes

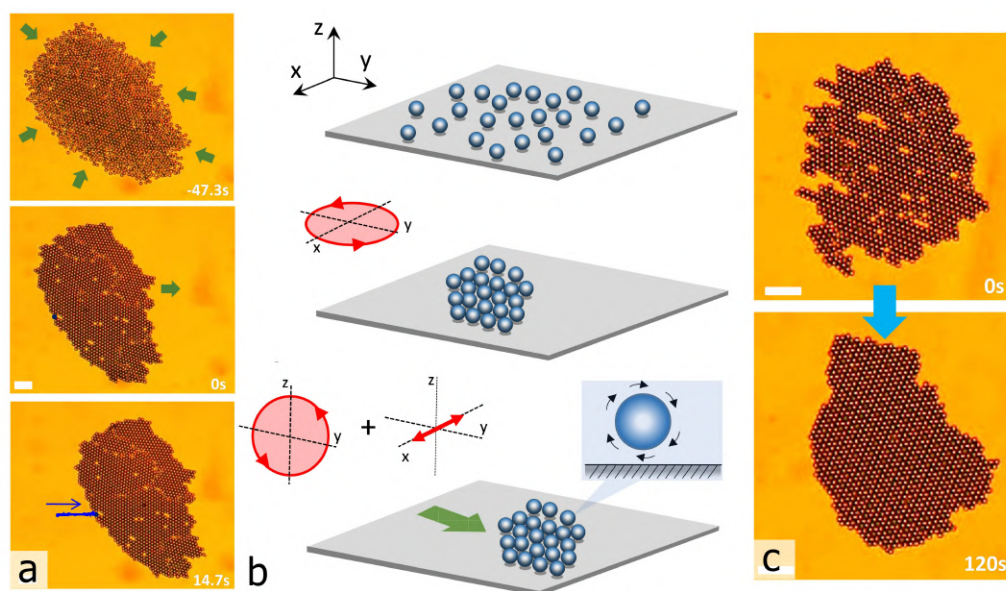


FIGURE 7.4: (a) Sequence of microscope images and (b) schematics showing the formation and propulsion of a carpet. (c) Self-healing of the magnetic carpet. Experimental images showing an initial polycrystalline carpet and a monocrystalline carpet obtained after propulsion. The scale bars are $20\ \mu\text{m}$. From [Publication 4](#).

of length $a_2 = 2.5 \pm 0.12 \mu\text{m}$ and $b_2 = 1.4 \pm 0.13 \mu\text{m}$ in [Publication 3](#). We described first the motion of a single rotor, propelled by applying a rotating magnetic field circularly polarized. For low frequencies, the ellipsoid rotates synchronously with the field, while for frequencies beyond a critical value the motion becomes asynchronous and there is a reduction of the average rotational motion. When these hematite rotors propel very close to each other, they may couple their motion forming bound states, dynamically assembling into translating three-dimensional stable clusters that perform a periodic leap-frog type dynamics and propel at a faster speed ([Figure 7.3](#)). We observed that this bound state can be formed by two or more rotors. We experimentally analysed the cluster formation and its lifetime. We described a theoretical model that qualitatively explains the observed phenomena and the role of particle shape in the propulsion speed and stability. These clusters of rotors could be used to transport a biological cargo by entrapping it in their vortical flow. From a more fundamental perspective, it is interesting to investigate the role of hydrodynamic interactions in synchronization phenomena between actuated magnetic colloids.

On the other hand, we made experiments using paramagnetic particles. We assembled these colloids into two-dimensional colloidal clusters (carpets) by inducing attraction using an in-plane rotating magnetic field ([Figure 7.4a](#)). The particles are torqued by the magnetic field because of their finite internal relaxation time. Furthermore, these structures can be steered in any direction of the plane by adding a perpendicular component to the field [[203](#)]. In [Publication 4](#) we analysed the different dynamic states of these structures by changing the parameters of the external field. We found a stationary phase where particles can detach from the rear end of the propelling cluster and transport above the carpet, while the entire structure continues to propel close to the plane. These particles travelling above the carpet surface follow its crystallographic direction. During their

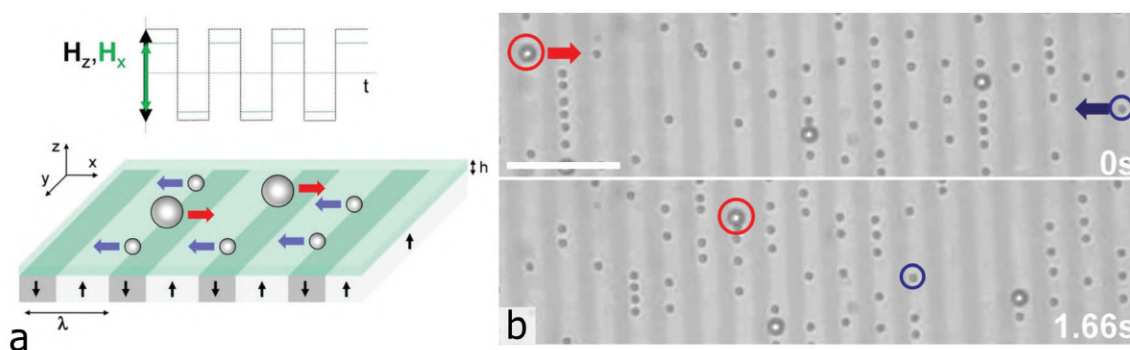


FIGURE 7.5: (a) Schematic showing a binary mixture of paramagnetic colloids deposited above a ferrite garnet film, characterised by parallel stripes. (b) Sequence of microscope images showing the bidirectional transport of a large particle (moving to the right, red circle) and a small particle (moving to the left, blue circle). From [Publication 5](#).

path, they can either fill vacancies or reach and rejoin the leading edge of the structure. We showed that with this mechanism, large-scale propelling disordered carpets can continuously transform into a perfect crystalline lattice (Figure 7.4b). We combined experiments with a theoretical model and simulations. This out-of-equilibrium colloidal model system allowed us to investigate crystallization in transported systems and could thus provide deep insight for similar processes occurring in systems at different length and time scales.

The high-velocity transport of paramagnetic particles on top of a substrate can be achieved by using the cooperative motion of clusters (Publication 4). Alternatively, magnetic substrates can also induce large particle velocities [197]. In Publication 5 we propelled paramagnetic colloids on top of Ferrite Garnet Films (FGFs) with parallel ferromagnetic domains. Two types of particles with different sizes were proven to be simultaneously transported in opposite directions when subjected to a square-wave modulation of an externally applied oscillating magnetic field (Figure 7.5). This is due to the fact they are located at distinct elevations from the surface (because of their size) and are subjected to different energy landscapes. This system allowed remote control over the particle motion, speed and trajectory, by using relatively low intense magnetic fields. We also explored the sorting capability of our system by depositing on the FGF a polydisperse suspension composed of paramagnetic colloids with seven different sizes, from 270 nm to 10 μm . We found that the particles with a diameter equal or smaller than 1 μm moved in a certain direction, while larger particles transported in the opposite one. Regarding applications, this work could provide a method to separate magnetic microspheres in a channel-free microfluidic environment.

Separately, in Publications 6 and 7 we exploited the activity of our hematite ellipsoids. When exposed to blue light, they start the decomposition of hydrogen peroxide in solution. This reaction produces a gradient in the chemical concentration around the particle. Because of its symmetry, if the ellipsoid is isolated it does not self-propel, i.e. it is an active *apolar* colloid. However, the generated diffusiphoretic flow can attract and bind other

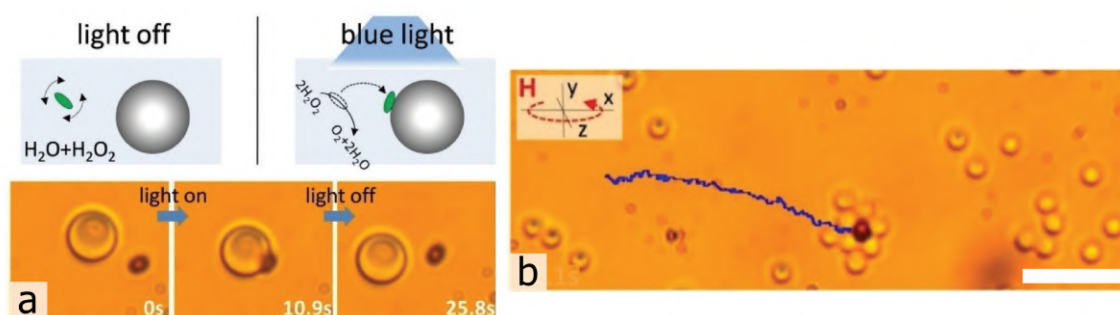


FIGURE 7.6: (a) Schematics showing the attraction induced by blue light and snapshots illustrating the binding and unbinding of one hematite ellipsoid close to a silica particle. (b) Images showing the transport of the cargo cluster. Scale bar is 10 μm . From Publication 6.

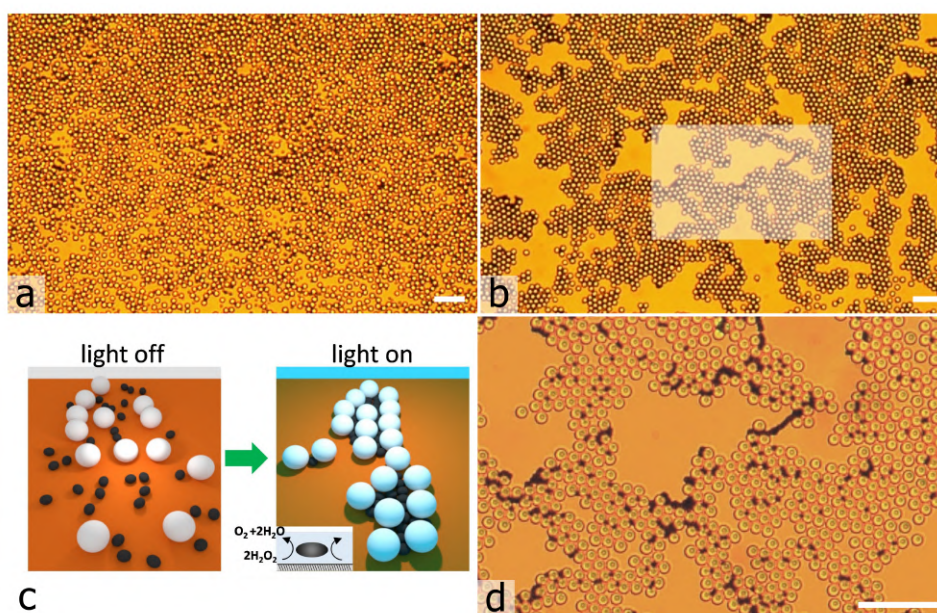


FIGURE 7.7: Colloidal gel assembled from doping a bath of silica spheres with a few hematite ellipsoids in a water solution containing H_2O_2 (a) before and (b) after application of blue light ($t=165s$). (c) Schematic of the assembly of clusters due to photoactivated dopants. (d) Enlargement of the region shown in the box in (b). Scale bars are $20 \mu m$. From [Publication 7](#).

particles that are close enough to its surface. In [Publication 6](#) we used external magnetic fields to transport a light-activated hematite particle attached to passive particles to any location of the experimental platform. The binding–unbinding is completely reversible since, when switching off the illumination, the ellipsoids immediately detach from the cargo’s surface due to their diffusive motion. This allowed to precisely dock, transport and release microscopic objects on external command (Figure 7.6). Furthermore, the transported active colloidal clusters were of various sizes. We demonstrated the possibility to easily reconfigure the location of the docker above the cargo, which enabled to optimize transport and cargo release operations. This work has direct applications regarding the delivery of drugs, chemicals and other cargos in small channels and pores.

Finally, in [Publication 7](#) we showed that, only with the light activation and without the presence of a magnetic field, a mixture of passive and active colloidal particles can assemble into two-dimensional colloidal clusters and gels by non-equilibrium diffusio-phoresis (Figure 7.7). By varying the relative fraction of active and passive particles, we found a rich phase diagram including ordered and disordered clusters, space-filling gels, and structures formed by filamentary dockers percolating through a solid network of silica spheres. We compared experimental results with numerical simulations and characterised the slow relaxation and dynamic arrest of the different phases. This work has applications towards the engineering of mesoscopic gels and clusters using active colloidal doping.

PUBLICATION 1

Orientational dynamics of fluctuating dipolar particles assembled in a mesoscopic colloidal ribbon

Physical Review E **96**, 012607 (2017)

Helena Massana-Cid¹, Fernando Martinez-Pedrero², Andrejs Cebers³,
and Pietro Tierno^{1,4,5}

¹ Departament de Física de la Matèria Condensada,
Universitat de Barcelona, 08028 Barcelona, Spain

² Departamento de Química Física I, Universidad Complutense
de Madrid, Ciudad Universitaria, 28040, Madrid, Spain

³ Faculty of Physics and Mathematics, University of
Latvia, Zellu 23, LV-1002

⁴ Universitat de Barcelona Institute of Complex Systems
(UBICS), Universitat de Barcelona, 08028 Barcelona, Spain

⁵ Institut de Nanociència i Nanotecnologia, IN²UB,
Universitat de Barcelona, 08028 Barcelona, Spain

Orientational dynamics of fluctuating dipolar particles assembled in a mesoscopic colloidal ribbonHelena Massana-Cid,¹ Fernando Martinez-Pedrero,² Andrejs Cebers,³ and Pietro Tierno^{1,4,5,*}¹*Departament de Física de la Matèria Condensada, Universitat de Barcelona, 08028 Barcelona, Spain*²*Departamento de Química Física I, Universidad Complutense de Madrid, Ciudad Universitaria, 28040, Madrid, Spain*³*Faculty of Physics and Mathematics, University of Latvia, Zellu 23, LV-1002*⁴*Universitat de Barcelona Institute of Complex Systems (UBICS), Universitat de Barcelona, 08028 Barcelona, Spain*⁵*Institut de Nanociència i Nanotecnologia, IN² UB, Universitat de Barcelona, 08028 Barcelona, Spain*

(Received 13 June 2017; published 24 July 2017)

We combine experiments and theory to investigate the dynamics and orientational fluctuations of ferromagnetic microellipsoids that form a ribbonlike structure due to attractive dipolar forces. When assembled in the ribbon, the ellipsoids display orientational thermal fluctuations with an amplitude that can be controlled via application of an in-plane magnetic field. We use video microscopy to investigate the orientational dynamics in real time and space. Theoretical arguments are used to derive an analytical expression that describes how the distribution of the different angular configurations depends on the strength of the applied field. The experimental data are in good agreement with the developed model for all the range of field parameters explored. Understanding the role of fluctuations in chains composed of dipolar particles is important not only from a fundamental point of view, but it may also help understanding the stability of such structures against thermal noise, which is relevant in microfluidics and laboratory-on-a-chip applications.

DOI: [10.1103/PhysRevE.96.012607](https://doi.org/10.1103/PhysRevE.96.012607)**I. INTRODUCTION**

Brownian particles assembled into a linear chain due to anisotropic interactions, as the ones arising from dipolar forces, represent an accessible and thus appealing model system to study the role of noise in simple polymerlike structures [1]. When the linkage between the particles is not provided by a strong chemical bond [2–6], but it results from a weak attractive interaction [7,8], then the fluctuations of the single particles may significantly influence the chain dynamics, producing torsions, bending, or even irreversible breakage. Investigating the role of thermal noise in such systems, and how the single-particle fluctuations affect the chain dynamics, is thus necessary to understand the behavior and the stability of the whole structure.

There are different works that explored the deformations and the dynamics of chains composed by spherical microspheres [9–12]. More recently, experiments with magnetic dumbbells [13], Janus rods [14], and hematite ellipsoids [15] have shown the possibility to realize and manipulate elongated structures composed by anisotropic colloids via external fields. In contrast to spherical colloids, anisotropic particles such as ellipsoids introduce an additional rotational degree of freedom that complicates their dynamics, giving rise to a richer physical behavior. However, the role of thermal fluctuations in the orientation of the anisotropic elements when assembled into linear chains has not been addressed yet.

In this article, we study the dynamics of ferromagnetic microellipsoids around the direction determined by an external field, both alone and when assembled into a ribbon. In the latter case, the orientational fluctuations are described by formulating a theoretical framework based on a modified version of the wormlike model [1]. The model allows capturing the fundamental physics of the process and deriving an analytic

expression for the distribution of the particle orientations within the ribbon.

II. EXPERIMENTAL SYSTEM AND PROCEDURES

The anisotropic ferromagnetic ellipsoids are synthesized following a well-established procedure developed by Sugimoto and coworkers [16] and described in detail in several previous works [17–20]. With this method, we obtain monodisperse hematite particles with prolate shape and a major (minor) axis equal to $a = 1.80 \pm 0.11 \mu\text{m}$ ($b = 1.31 \pm 0.12 \mu\text{m}$, respectively). From the analysis of scanning electron microscopy images, we measure a polydispersity index equal to $\sigma_a = 0.022$ and $\sigma_b = 0.023$, for the long and short axis of the synthesized particles, respectively. After synthesis, the particles have a small permanent moment $m \simeq 2 \times 10^{-16} \text{Am}^2$, perpendicular to their long axis, as depicted in Fig. 1(a). The peculiar orientation of this moment, as compared to other anisotropic magnetic particles [21], is caused by the magnetic structure of hematite, which crystallizes in the corundum form [22]. The value of m was obtained by measuring the reorientational motion of individual hematite particles subjected to a static magnetic field [15]. The permanent moment of the particles allows us to estimate a dipolar coupling constant $\lambda = \mu_0 m^2 / (4\pi k_B T b^3) = 0.44$ and a Langevin parameter equal to $\Lambda = \mu_0 m H / (k_B T) = 93.2$, for an external field $H = 1500 \text{Am}^{-1}$ [23]. Here, $\mu_0 = 4\pi 10^{-7} \text{Hm}^{-1}$ is the magnetic permeability, $T \sim 293 \text{K}$ is the room temperature, and k_B is the Boltzmann constant. Moreover, from the superconducting quantum interference devices measurements (data not shown here), we find that the particle permanent moment is one order of magnitude larger than the induced moment in all the range of explored field strengths [24].

After synthesis, the particles are dispersed in highly deionized water (purified using a Milli-Q system, Millipore), stabilized with a surfactant by adding 0.11 g of sodium dodecyl sulfate for 80 ml of water, and finally the pH of the solution

*ptierno@ub.edu

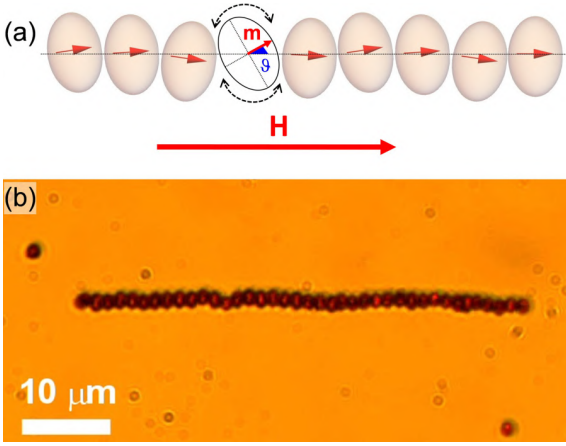


FIG. 1. (a) Schematic showing a chain of ferromagnetic ellipsoids subjected to an external magnetic field H , being ϑ the angle between the particle moment and the x axis, that coincides with the direction of the applied field. Each particle displays orientational thermal fluctuations around this axis. (b) Optical microscope image of a chain composed by 39 ellipsoids under a constant field $H = 1600 \text{ Am}^{-1}$, applied along the same direction as shown in the schematic at the top.

is adjusted to 9.5 by adding tetramethylammonium hydroxide. These procedures are used to create a protective steric layer around the particles that avoids the irreversible sticking due to attractive Van der Waals interactions. The particles sediment close to a glass plate, where they remain quasi-two-dimensionally confined due to the balance between gravity and the electrostatic repulsion with the glass surface. The particle dynamics are visualized using an optical microscope (Eclipse Ni, Nikon), and their positions and orientations are recorded with a CCD camera (Scout scA640-74f, Basler) working at 50 fps. The anisotropic shape of the particles allows for monitoring the instantaneous direction of their permanent moment. The external magnetic field is generated with a custom-made coil system connected to a direct current power supply (EL 302RT, TTi).

III. SINGLE-PARTICLE DYNAMICS

Before analyzing the orientational fluctuations in the ribbon, we have first characterized the thermal motion of a single ellipsoid in absence and in presence of an external field. The dynamics of an individual ellipsoid in water has been treated in different works [25–29], and thus here will be only briefly described. In the absence of a magnetic field, the anisotropic shape of the particle causes a nontrivial coupling between its rotational and translational motion. In particular, the particle translational diffusion is anisotropic at short times, $t \sim 0 \text{ s}$, t being the time interval defined with respect to the initial measured position of the ellipsoid. Thus, the dynamics can be described by two different diffusion coefficients, D_{\parallel} and D_{\perp} , characterizing the translational dynamics parallel and perpendicular to the particle long axis, respectively. This behavior arises from the fact that the ellipsoid has two different friction coefficients, γ_{\parallel} and γ_{\perp} , along the direction parallel and perpendicular to its long axis, respectively. Since $\gamma_{\perp} > \gamma_{\parallel}$ and $D = k_B T / \gamma$, one obtains that $D_{\perp} < D_{\parallel}$. In contrast, after

a long time the diffusion becomes isotropic, and the two diffusion coefficients coincide $D_{\perp} = D_{\parallel}$. The crossover time between both behaviors is given by the rotational diffusion time, $\tau_{\vartheta} = 1/(2D_{\vartheta})$, D_{ϑ} being the rotational diffusion coefficient. Thus, for time $t < \tau_{\vartheta}$, one has that $D_{\parallel} \neq D_{\perp}$, since the rotational motion still needs to become important in the particle dynamics. When $t > \tau_{\vartheta}$, the rotational movement erases the directional memory of the particle, and the two diffusion coefficients approach a common value. To determine the characteristic time τ_{ϑ} for our particles, we record the motion of several individual ellipsoids ($i = 1 \dots N$) and extract the particle positions and orientations, $(x_i(t), y_i(t), \vartheta_i(t))$, $\vartheta_i(t)$ being the angle between the x axis and the particle minor axis. We then determine the corresponding diffusion coefficients from the mean-square displacement (MSD). For the angular variable, the MSD can be written as

$$D_{\vartheta}(t) = \frac{1}{2Nt} \left\langle \sum_{i=1}^N [\vartheta_i(t) - \vartheta_i(0)]^2 \right\rangle. \quad (1)$$

From these data, we measure $D_{\vartheta} = 0.08 \text{ rad}^2 \text{ s}^{-1}$ that corresponds to $\tau_{\vartheta} = 6.2 \text{ s}$. We note that this value is larger than what was found for nonmagnetic ellipsoids ($\tau_{\vartheta} = 3.1 \text{ s}$ [26]), probably due to the different aspect ratio and the higher density of the hematite ellipsoids that could hinder diffusion by forcing the particle to stay closer to the substrate, thus increasing the values of the translational and the rotational friction coefficients. For time $t > \tau_{\vartheta}$, we measure a common diffusion coefficient, $D_{\parallel} = D_{\perp} = 0.074 \mu\text{m}^2 \text{ s}^{-1}$.

An external magnetic field can be used to impede the rotational motion, separating the diffusion coefficients along the directions parallel and perpendicular to the particle's long axis. In this situation, the particle aligns with its short axis (long axis) parallel (perpendicular) to the field direction. Thus, there is no transition toward the isotropic diffusion, and the hematite ellipsoids present an anisotropic motion with two different diffusion coefficients, even at long times. In particular, for a field amplitude of $H = 1500 \text{ Am}^{-1}$, we find that the diffusion is totally anisotropic, with $D_{\parallel} = 0.112 \mu\text{m}^2 \text{ s}^{-1}$ and $D_{\perp} = 0.037 \mu\text{m}^2 \text{ s}^{-1}$. We next analyze, first theoretically and later via experiments, the dynamics of a chain of interacting hematite ellipsoids.

IV. THEORETICAL MODEL

We consider a chain of permanent dipoles aligned along the direction imposed by a constant field H and subjected to thermal fluctuations that disorder the particle orientations by increasing the angle ϑ , Fig. 1(a). We describe this situation by using a modified version of the stretched wormlike model [1,30,31]. In our model the energy of the chain is given by

$$E = \frac{K_b}{2} \int_0^L \left(\frac{d\vartheta}{dl} \right)^2 dl - MH \int_0^L \cos(\vartheta) dl, \quad (2)$$

where K_b is the bending constant that takes into account the dipolar interactions between the ellipsoids and can be written as $K_b = m^2/2b^2$, b being the ellipsoid minor axis. Further, M is the particle magnetization per unit length and L is the length of the chain. Our analysis of the chain thermal fluctuations is based on the relation between the propagator of

the orientation angles of the dipoles and the chain free energy. The orientational distribution function of the system can be written as

$$P(\vartheta, l) = \int_0^{2\pi} G(\vartheta, l | \vartheta', l') P(\vartheta', l') d\vartheta', \quad (3)$$

where the function G in the limit $l - l' \rightarrow 0$ is given by the Boltzmann distribution:

$$G(\vartheta, l + \Delta l | \vartheta', l) = \sqrt{\frac{K_b}{2\pi k_B T \Delta l}} e^{\left(-\frac{K_b(\vartheta - \vartheta')^2}{2k_B T \Delta l} + \frac{MH \cos(\vartheta) \Delta l}{k_B T}\right)}. \quad (4)$$

In the limit $l \rightarrow l'$, we may derive the following differential equation for P [31]:

$$\frac{\partial P}{\partial l} = \frac{1}{2l_p} \frac{\partial^2 P}{\partial \vartheta^2} + \frac{MH \cos(\vartheta)}{k_B T} P = \hat{H} P, \quad (5)$$

where $l_p = K_b/k_B T$ is the persistence length of the chain. As a result, G may be expressed through the eigenfunctions ψ_k and the eigenvalues λ_k of the operator \hat{H} as follows:

$$G = \sum_k \exp[\lambda_k(l - l')] \psi_k(\vartheta) \psi_k(\vartheta'). \quad (6)$$

For infinitely long chains, $L \rightarrow \infty$ ($l = L; l' = 0$), only the largest eigenvalue λ_1 will contribute in Eq. (6), and

$$G(\vartheta, L | \vartheta', 0) = \exp(\lambda_1 L) \psi_1(\vartheta) \psi_1(\vartheta'). \quad (7)$$

Since

$$G(\vartheta, L | \vartheta', 0) = \int \dots \int G(\vartheta, \vartheta_{n-1} | \Delta l) \dots G(\vartheta_1, \vartheta' | \Delta l) \times d\vartheta_1 \dots d\vartheta_{n-1}, \quad (8)$$

we thus obtain

$$\int G(\vartheta, L | \vartheta', 0) d\vartheta d\vartheta' = Z, \quad (9)$$

where Z is a statistical sum done over all the ellipsoids that form the magnetic chain. Thus, the total free energy can be expressed as

$$F = -k_B T \ln Z = -k_B T \lambda_1 L. \quad (10)$$

For large values of L , the orientation distribution function can be determined by the eigenfunction of \hat{H} corresponding to the largest eigenvalue λ_1 :

$$P(\vartheta) \sim \psi_1(\vartheta). \quad (11)$$

Now we present the results for the two limiting regimes characterized by the amplitude of the applied field.

V. LARGE APPLIED FIELDS

Let us consider a magnetic chain with length L under periodic conditions, $\vartheta(l + L) = \vartheta(l)$. We can write the angle ϑ as

$$\vartheta = \sum_k \vartheta_k \exp(ikl); k = \frac{2\pi n}{L}. \quad (12)$$

For small thermal fluctuations, the energy of the system may be expressed as

$$E = \frac{L}{2} \sum_k (K_b k^2 + MH) |\vartheta_k|^2. \quad (13)$$

According to the Boltzmann principle, we can write the probability density of the amplitude of the fluctuations as

$$\varrho \approx \exp\left(-L \sum_{k>0} (K_b k^2 + MH) |\vartheta_k|^2 / k_B T\right), \quad (14)$$

and the spectral amplitude as

$$\langle |\vartheta_k|^2 \rangle = \frac{k_B T}{L(K_b k^2 + MH)}, \quad (15)$$

and

$$\left\langle \int_0^L \cos(\vartheta) dl \right\rangle = L - L \sum_{k>0} |\vartheta_k|^2. \quad (16)$$

The sum in Eq. (16) can be calculated upon direct integration,

$$\left\langle \int_0^L \cos(\vartheta) dl \right\rangle = L \left(1 - \frac{1}{4} \frac{1}{\sqrt{MH K_b / (k_B T)^2}}\right). \quad (17)$$

At equilibrium, the variation of the chain free energy with the magnetic field may be expressed as

$$\frac{\partial F}{\partial H} = -M \left\langle \int_0^L \cos(\vartheta) dl \right\rangle, \quad (18)$$

where the right member in Eq. (18) is the total magnetic moment of the chain. From Eqs. (10), (17), and (18), we derive the following relationship:

$$k_B T L \frac{\partial \lambda_1}{\partial H} = ML \left(1 - \frac{1}{2\sqrt{2}\sqrt{\xi}}\right), \quad (19)$$

which can be used to test our variational approach, $\xi = MH 2l_p / k_B T$ being the dimensionless magnetic energy. By defining the dimensionless variable $\tilde{\lambda}_1 = \lambda_1 2l_p$, we have

$$\frac{\partial \tilde{\lambda}_1}{\partial \xi} = 1 - \frac{1}{2\sqrt{2}\sqrt{\xi}} \quad (20)$$

or

$$\tilde{\lambda}_1 \simeq \xi - \frac{1}{\sqrt{2}} \sqrt{\xi}. \quad (21)$$

VI. SMALL APPLIED FIELDS

In the limit of small applied fields, and according to the perturbation theory, the magnetization is given by

$$\begin{aligned} & \left\langle \int_0^L \cos(\vartheta) dl \right\rangle \\ &= Z^{-1} \int D(\vartheta) \int_0^L \cos[\vartheta(l)] dl \exp(-E/k_B T) \\ &\simeq \frac{MH}{k_B T} \left\langle \int_0^L \cos[\vartheta(l)] dl \int_0^L \cos(\vartheta(l')) dl' \right\rangle. \end{aligned} \quad (22)$$

From Eq. (5), it follows that in the absence of a magnetic field

$$\langle \cos[\vartheta(l)] \cos[\vartheta(l')] \rangle = \frac{1}{2} \exp[-|l - l'| / (2l_p)]. \quad (23)$$

Integrating the previous equation, one obtains

$$\int_0^L \int_0^L \frac{1}{2} \exp[-|l-l'|/(2l_p)] dl dl' \simeq 2l_p L. \quad (24)$$

From Eqs. (22), (23), and (24), the magnetic moment is given by

$$M \left\langle \int_0^L \cos(\vartheta) dl \right\rangle = M \frac{MH}{k_B T} 2l_p L, \quad (25)$$

and from Eq. (18),

$$k_B T \frac{\partial \lambda_1}{\partial H} = M \frac{MH}{k_B T} 2l_p. \quad (26)$$

Finally, we arrive to another relationship that is valid for large thermal fluctuations,

$$\frac{\partial \tilde{\lambda}_1}{\partial \xi} = \xi; \quad \tilde{\lambda}_1 = \frac{1}{2} \xi^2, \quad (27)$$

and its validity can be demonstrated by using a variational method, as described in the following section.

VII. VARIATIONAL SOLUTION

By defining the dimensionless length $l/2l_p$, Eq. (5) follows from the variation of the functional

$$W = \int_0^{2\pi} \left[- \left(\frac{\partial P}{\partial \vartheta} \right)^2 + \xi \cos(\vartheta) P^2 \right] d\vartheta / \int_0^{2\pi} P^2 d\vartheta. \quad (28)$$

From this equation, we have

$$\frac{d^2 P}{d\vartheta^2} + \xi \cos(\vartheta) P = W P, \quad (29)$$

and the largest eigenvalue of the operator \hat{H} corresponds to the maximal value of the functional W . To find this value, we use the following trial function for the probability density distribution:

$$P = \frac{\exp[\alpha \cos(\vartheta)]}{\sqrt{2\pi} I_0(2\alpha)}, \quad (30)$$

where $I_n(x)$, ($n = 0, 1, 2, \dots$) are the modified Bessel functions of the first kind. This function is normalized as $\int_0^{2\pi} P^2 d\vartheta = 1$, and it is proportional to $\exp(\alpha \cos \vartheta)$. Using this expression, the functional in Eq. (28) can be written as

$$W = \frac{1}{I_0(2\alpha)} \left[-\frac{1}{2} F_{01}(2, \alpha^2) + \xi I_1(2\alpha) \right], \quad (31)$$

where $F_{01}(2, z)$ is the confluent hypergeometric function. To justify the selection of the trial function, we calculated the values of the parameter α that maximize the functional in Eq. (31) for both small ($\xi \in [0; 0.1]$) and large ($\xi \in [10; 100]$) values of ξ . The data resulting from these calculations are plotted versus ξ in Figs. 2(a) and 2(b). From these images, it follows indeed that the numerical data are in excellent agreement with the theoretical expressions derived from small [Eq. (21)] and large [Eq. (27)] thermal fluctuations.

VIII. FLUCTUATIONS IN THE COLLOIDAL RIBBON

To validate our model, we perform different experiments by measuring the average angle ϑ as a function of the applied field. Thermally induced torsions, which cause the rotation of the ellipsoids around the main axis of the chain, are hindered by the presence of the glass surface, and almost all the ellipsoids rest on the surface with their long axis parallel to the horizontal plane. In this study, we have also neglected the weak out-of-plane fluctuations of the magnetic moments. Further, we find that during the measurements the magnetic ribbons are sensitive to the Earth's magnetic field, $H_e \sim 40 \text{ Am}^{-1}$, and thus they orient along H_e even in the absence of any extra applied field. To cancel H_e , we balance the latter by applying a small DC field in the opposite direction. Under this condition, the particles in the chain do not present any preferential orientation, as shown by the empty circles in Fig. 3,

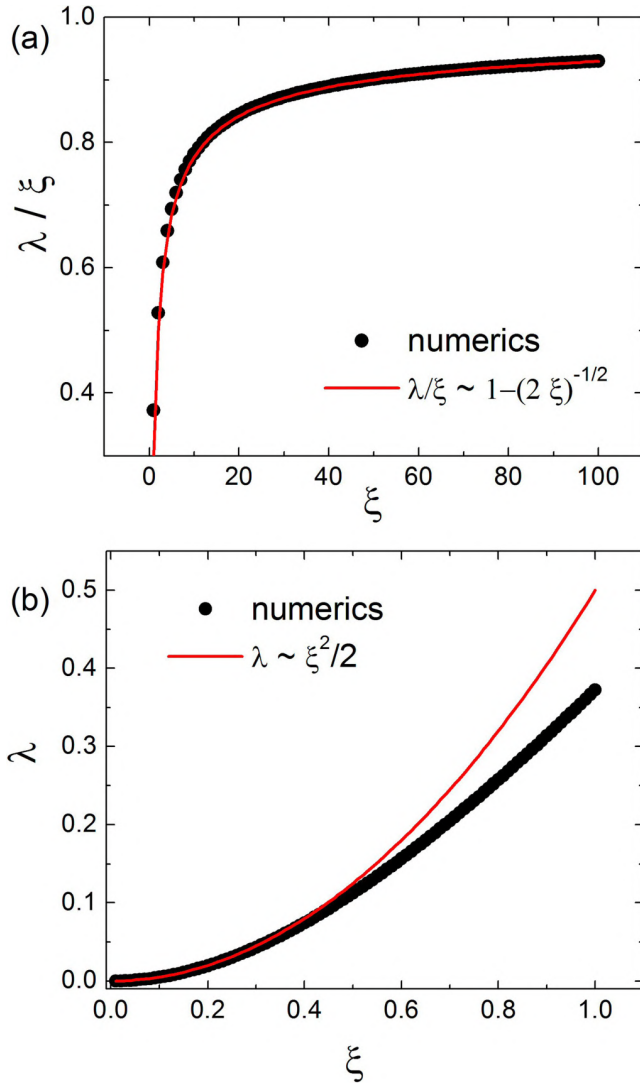


FIG. 2. (a) Ratio λ/ξ versus ξ , λ being the eigenvalues corresponding to the maximum of the functional W . The continuous red line is a fit corresponding to Eq. (21), where the numerical data are obtained for large values of ξ . (b) Eigenvalues λ calculated for small values of $\xi \in [0 \dots 1]$. The continuous red line corresponds to Eq. (27) in the text.

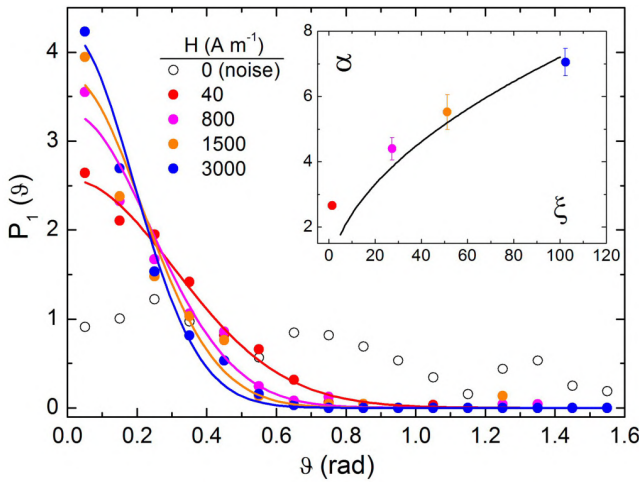


FIG. 3. Distribution of the particle orientation, $P_1(\vartheta)$, for different amplitudes of the applied field H . Symbols denote experimental data, continuous lines starting from $H = 40 \text{ Am}^{-1}$ are theoretical curves calculated following the equation of $P_1(\vartheta)$ in the text. The obtained values of the fitted dimensionless parameter $\alpha = \tilde{\alpha}/2$ for all the curves are shown as a function of $\xi = mHl_p/bk_B T$ in the top inset. Here we use $l_p = 0.3 \mu\text{m}$ and $m = 2.3 \times 10^{-16} \text{ Am}^2$. The continuous line results from the functional W in Eq. (31).

and the ribbons form rings [14,20,32] or break due to thermal fluctuations.

The distribution of the angles $P_1(\vartheta)$ are shown in Fig. 3, where the experimental data are scattered points, while the continuous lines are fit to the theoretical model. Due to the geometry of our experimental system, we have assumed that the distribution is symmetric around the x axis, $P_1(\vartheta) = P_1(-\vartheta)$, and that $P_1(\vartheta > \pi/2) \sim 0$. Thus, we normalize the experimental data as $\int_0^{\pi/2} P_1(\vartheta) d\vartheta = 1$ and use the expression $P_1(\vartheta) = \exp[\tilde{\alpha} \cos(\vartheta)] / [\pi I_0(\tilde{\alpha})]$. We note that this distribution reduces to Eq. (30) of the model $P_1(\vartheta) = P(\vartheta)$ for $\alpha = \tilde{\alpha}/2$ and large values of the parameter α . The application of an external field reduces the amplitude of the orientational fluctuations, centering the angular distribution about $\vartheta = 0$ rad. The half width of the distribution decreases with the field, in agreement with the prediction of Eq. (30). The good agreement between the experimental data and the theoretical expression is also proved by the small inset in Fig. 3. Here we show the fitting parameters $\alpha = \tilde{\alpha}/2$ obtained from the main graph as a function of the normalized magnetic

energy ξ . To determine ξ , we use as persistence length of the chain the value $l_p \sim 0.3 \mu\text{m}$, which was previously determined in a set of independent experiments [20]. The scattered data are in excellent agreement with the continuous line that was independently obtained from the numerical calculation of the maximum of the functional W in Eq. (31).

IX. CONCLUSIONS

We have combined experiments and theory to analyze the orientational fluctuations in a colloidal chain made by ferromagnetic hematite ellipsoids. Our model quantitatively captures the physics of the colloidal system, showing a good agreement with the experimental data. In absence of external field, the chain shows large fluctuations of the individual elements along the whole range of angles $[0, 2\pi]$ and can easily break. When an external field is applied, the amplitude of the fluctuations decreases, becoming limited to a narrow range of angles.

The assembly of magnetic colloids into linear chains is an appealing research subject with both fundamental [33] and technological applications [34]. In the first case, magnetic chains influenced by thermal fluctuations have shown a variety of interesting phenomena, including diffusion limited aggregation [35,36], multiscale kinetics [37], and subdiffusive dynamics [38]. On the application side, magnetic chains have been used in the past as micromechanical sensors [3,39], to measure the growth of actin filaments [40], the rheological properties of the dispersing medium [41,42], or even to realize biomimetic structures, such as actuated magnetic propellers [43,44] and artificial cilia [45,46]. Further, our mesoscopic colloidal system may be also used as a simplified model for magnetic polymer beads, which present exciting applications in targeted drug delivery and in the oil industry [47].

ACKNOWLEDGMENTS

H.M.C., F.M.P., and P.T. acknowledge support from the European Research Council (ERC) starting Grant ‘‘DynaMO’’. P.T. acknowledges support from Ministerio de Economía, Industria y Competitividad (MINECO) (Grant No. FIS2016-78507-C2-2-P) and Agència de Gestió d’Ajuts Universitaris i de Recerca (DURSI) (Grant No. 2014SGR878). A.C. acknowledges support from National Research Programme Grant No. 2014.10-4/VPP-3/21 and from the M-ERA-NET project ‘‘Metrology at the Nanoscale with Diamonds’’ (MyND). F.M.P. acknowledges support from MINECO (Grant No. RYC-2015-18495).

[1] M. Doi and S. F. Edwards, *The Theory of Polymer Dynamics* (Clarendon Press, Oxford, 1988).
 [2] E. M. Furst, C. Suzuki, M. Fermigier, and A. P. Gast, *Langmuir* **14**, 7334 (1998).
 [3] C. Goubault, P. Jop, M. Fermigier, J. Baudry, E. Bertrand, and J. Bibette, *Phys. Rev. Lett.* **91**, 260802 (2003).
 [4] S. L. Biswal and A. P. Gast, *Phys. Rev. E* **68**, 021402 (2003).
 [5] H. R. Vutukuri, A. F. Demirörs, B. Peng, P. D. J. van Oostrum, A. Imhof, and A. van Blaaderen, *Angew. Chem. Int. Ed.* **50**, 3747 (2011).

[6] A. Demortière, A. Snezhko, M. V. Sapozhnikov, N. Becker, T. Proslrier, and I. S. Aranson, *Nat. Commun.* **5**, 3117 (2014).
 [7] A. T. Skjeltorp, *Phys. Rev. Lett.* **51**, 2306 (1983).
 [8] R. Toussaint, G. Helgesen, and E. G. Flekkøy, *Phys. Rev. Lett.* **93**, 108304 (2004).
 [9] A. S. Silva, R. Bond, F. Plouraboué, and D. Wirtz, *Phys. Rev. E* **54**, 5502 (1996).
 [10] S. Cutillas and J. Liu, *Phys. Rev. E* **64**, 011506 (2001).
 [11] L. Hong, S. M. Anthony, and S. Granick, *Langmuir* **22**, 7128 (2006).

- [12] D. Li, N. Fakhri, M. Pasquali, and S. L. Biswal, *Phys. Rev. Lett.* **106**, 188302 (2011).
- [13] D. Zerrouki, J. Baudry, D. Pine, P. Chaikin, and J. Bibette, *Nature* **455**, 380 (2008).
- [14] J. Yan, K. Chaudhary, S. C. Bae, J. A. Lewis, and S. Granick, *Nat. Commun.* **4**, 1516 (2013).
- [15] F. Martinez-Pedrero, A. Cebers, and P. Tierno, *Soft Matter* **12**, 3688 (2016).
- [16] T. Sugimoto, M. M. Khan, and A. Muramatsu, *Colloids Surfaces A—Physicochem. Eng. Aspects* **70**, 167 (1993).
- [17] S. J. Gerbode, S. H. Lee, C. M. Liddell, and I. Cohen, *Phys. Rev. Lett.* **101**, 058302 (2008).
- [18] S. H. Lee and C. M. Liddell, *Small* **5**, 1957 (2009).
- [19] J. Palacci, S. Sacanna, A. Vatchinsky, P. M. Chaikin, and D. J. Pine, *J. Am. Chem. Soc.* **135**, 15978 (2013).
- [20] F. Martinez-Pedrero and P. Tierno, *Phys. Rev. Appl.* **3**, 051003 (2015).
- [21] P. Tierno, *Phys. Chem. Chem. Phys.* **16**, 23515 (2014).
- [22] C. G. Shull, W. A. Strauser, and E. O. Wollan, *Phys. Rev.* **83**, 333 (1951).
- [23] R. E. Rosensweig, *Ferrohydrodynamics* (Cambridge University Press, Cambridge, 1986).
- [24] F. Martinez-Pedrero, H. Massana-Cid, and P. Tierno, *Small* **13**, 1603449 (2017).
- [25] F. Perrin, *J. Phys. Radium* **5**, 497 (1934).
- [26] Y. Han, A. M. Alsayed, M. Nobili, J. Zhang, T. C. Lubensky, and A. G. Yodh, *Science* **314**, 626 (2006).
- [27] R. Grima and S. N. Yaliraki, *J. Chem. Phys.* **127**, 084511 (2007).
- [28] T. P. Güell O. and S. F., *Eur. Phys. J. ST*, **187**, 15 (2010).
- [29] W.-T. Louis Fan, O. S. Pak, and M. Sandoval, *Phys. Rev. E* **95**, 032605 (2017).
- [30] M. Fixman and J. Kovac, *J. Chem. Phys.* **58**, 1564 (1973).
- [31] M. J. F. and E. D. Siggia, *Macromolecules* **28**, 8759 (1995).
- [32] W. Wen, F. Kun, K. F. Pál, D. W. Zheng, and K. N. Tu, *Phys. Rev. E* **59**, R4758(R) (1999).
- [33] K. Butter, P. H. H. Bomans, P. M. Frederik, G. J. Vroege, and A. P. Philipse, *Nat. Mater.* **2**, 88 (2006).
- [34] B. Berkovski and V. B. (eds.), *Magnetic Fluids and Applications Handbook* (Begel House, New York, 1996).
- [35] J. Černák, G. Helgesen, and A. T. Skjeltorp, *Phys. Rev. E* **70**, 031504 (2004).
- [36] R. M. Erb, M. D. Krebs, E. Alsberg, B. Samanta, V. M. Rotello, and B. B. Yellen, *Phys. Rev. E* **80**, 051402 (2009).
- [37] J. W. Swan, P. A. Vasquez, P. A. Whitson, E. M. Fincke, K. Wakata, S. H. Magnus, F. D. Winne, M. R. Barratt, J. H. Agui, R. D. Green, N. R. Hall, D. Y. Bohman, C. T. Bunnell, A. P. Gast, and E. M. Furst, *Proc. Natl. Acad. Sci. USA* **109**, 16023 (2012).
- [38] J. Jordanovic, S. Jäger, and S. H. L. Klapp, *Phys. Rev. Lett.* **106**, 038301 (2011).
- [39] R. Dreyfus, D. Lacoste, J. Bibette, and J. Baudry, *Eur. Phys. J. E* **28**, 113 (2009).
- [40] C. Brangbour, O. du Roure, E. Helfer, D. Démoulin, A. Mazurier, M. Fermigier, M.-F. Carlier, J. Bibette, and J. Baudry, *PLoS Biol.* **9**, e1000613 (2011).
- [41] G. K. Auernhammer, D. Collin, and P. Martinoty, *J. Chem. Phys.* **124**, 204907 (2006).
- [42] S. Huang, G. Pessot, P. Cremer, R. Weeber, C. Holm, J. Nowak, S. Odenbach, A. M. Menzel, and G. K. Auernhammer, *Soft Matter* **12**, 228 (2016).
- [43] R. Dreyfus, J. Baudry, M. L. Roper, M. Fermigier, H. A. Stone, and J. Bibette, *Nature* **437**, 862 (2005).
- [44] F. Martinez-Pedrero, A. Ortiz-Ambriz, I. Pagonabarraga, and P. Tierno, *Phys. Rev. Lett.* **115**, 138301 (2015).
- [45] M. Vilfan, A. Potocnik, B. Kavcic, N. Osterman, I. Poberaj, A. Vilfan, and D. Babic, *Proc. Natl. Acad. Sci. USA* **107**, 1844 (2010).
- [46] N. Coq, A. Bricard, F.-D. Delapierre, L. Malaquin, O. du Roure, M. Fermigier, and D. Bartolo, *Phys. Rev. Lett.* **107**, 014501 (2011).
- [47] S. E. Kushnir, P. E. Kazin, L. A. Trusov, and Y. D. Tretyakov, *Russian Chem. Rev.* **81**, 560 (2012).

PUBLICATION 2

Propulsion and hydrodynamic particle transport of magnetically twisted colloidal ribbons

New Journal of Physics **19**, 103031 (2017)

Helena Massana-Cid¹, Fernando Martinez-Pedrero², Eloy Navarro-Argemí^{1,3},
Ignacio Pagonabarraga^{1,3} and Pietro Tierno^{1,3,4}

¹ Departament de Física de la Matèria Condensada,
Universitat de Barcelona, 08028 Barcelona, Spain

² Departamento de Química Física I, Universidad
Complutense de Madrid, Ciudad Universitaria, 28040, Madrid, Spain

³ Universitat de Barcelona Institute of Complex Systems
(UBICS), Universitat de Barcelona, 08028 Barcelona, Spain

⁴ Institut de Nanociència i Nanotecnologia, IN²UB,
Universitat de Barcelona, 08028 Barcelona, Spain



PAPER

Propulsion and hydrodynamic particle transport of magnetically twisted colloidal ribbons

OPEN ACCESS

RECEIVED

29 May 2017

REVISED

2 August 2017

ACCEPTED FOR PUBLICATION

7 August 2017

PUBLISHED

25 October 2017

Original content from this work may be used under the terms of the [Creative Commons Attribution 3.0 licence](#).

Any further distribution of this work must maintain attribution to the author(s) and the title of the work, journal citation and DOI.

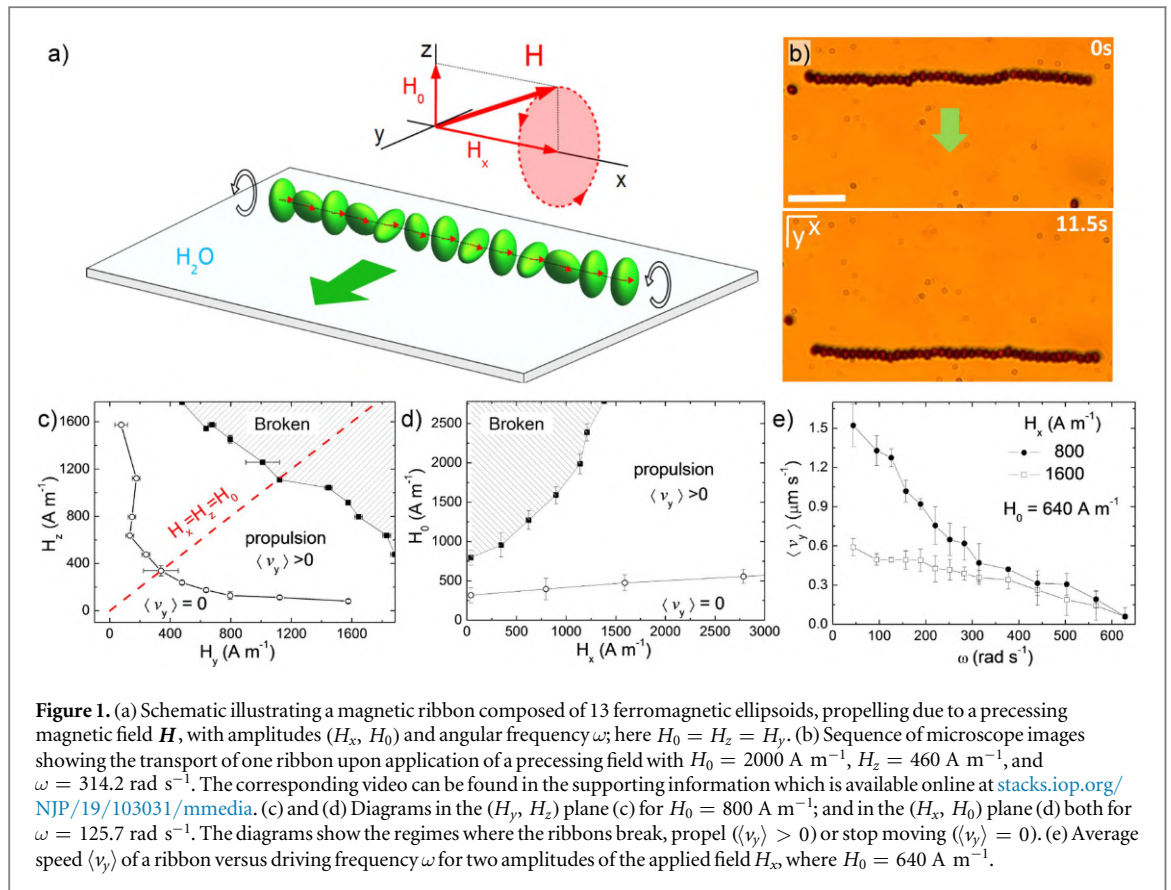
Helena Massana-Cid¹, Fernando Martinez-Pedrero², Eloy Navarro-Argemí^{1,3}, Ignacio Pagonabarraga^{1,3} and Pietro Tierno^{1,3,4}¹ Departament de Física de la Matèria Condensada, Universitat de Barcelona, E-08028, Barcelona, Spain² Departamento de Química Física I, Universidad Complutense de Madrid, Ciudad Universitaria, E-28040, Madrid, Spain³ Universitat de Barcelona Institute of Complex Systems (UBICS), Universitat de Barcelona, E-08028, Barcelona, Spain⁴ Institut de Nanociència i Nanotecnologia, IN²UB, Universitat de Barcelona, E-08028, Barcelona, SpainE-mail: ptierno@ub.edu**Keywords:** low Reynolds number, autonomous actuation, magnetism, fluid-structure interaction, bio-mimeticsSupplementary material for this article is available [online](#)**Abstract**

We describe a method to trap, transport and release microscopic particles in a viscous fluid using the hydrodynamic flow field generated by a magnetically propelled colloidal ribbon. The ribbon is composed of ferromagnetic microellipsoids that arrange with their long axis parallel to each other, a configuration that is energetically favorable due to their permanent magnetic moments. We use an external precessing magnetic field to torque the anisotropic particles forming the ribbon, and to induce propulsion of the entire structure due to the hydrodynamic coupling with the close substrate. The propulsion speed of the ribbon can be controlled by varying the driving frequency, or the amplitude of the precessing field. The latter parameter is also used to reduce the average inter particle distance and to induce the twisting of the ribbon due to the increase in the attraction between the rotating ellipsoids. Furthermore, non magnetic particles are attracted or repelled with the hydrodynamic flow field generated by the propelling ribbon. The proposed method may be used in channel free microfluidic applications, where the precise trapping and transport of functionalized particles via non invasive magnetic fields is required.

1. Introduction

The trapping and transport of microscopic entities via hydrodynamic flow is an emergent field of research that could lead to novel and exciting developments in lab on a chip devices, such as the controlled release and site specific delivery of chemical or biological cargos. In microfluidic systems, where pressure fields are used to displace nanoliter volumes of reagent in $\sim 100 \mu\text{m}$ wide channels, the trapping, assembly and positioning of microspheres via hydrodynamic flow has been demonstrated in different works [1–6]. The time reversal nature of fluid flow at low Reynolds (Re) number [7] allows for realizing precise single particle operations at the microscale, since inverting the fluid current does not lead to the formation of swirls or turbulence that can randomize the motion of the dispersed particles.

An alternative approach that is gaining much attention is the use of externally driven micropropellers capable to drag and transport microscopic objects using the hydrodynamic flow generated by their movement. This strategy does not require lithographic confinement or externally imposed pressure fields, but a suitable actuation scheme that enables net propulsion at low Re number, avoiding reciprocal motion, namely periodic backward and forward body displacements [8]. Recent examples in this direction include the use of magnetically driven nanorods [9], colloidal rotors [10–12], or magnetic particles driven above ferromagnetic structures [13–16]. In contrast to other actuation schemes, for instance the ones based on chemical reactions [17], electric [18], acoustic [19] or optic fields [20], magnetic fields have the advantage of not directly altering the dispersing medium, although they require magnetic parts within the prototypes [21–28].



In this article we demonstrate a method to assemble and propel a colloidal ribbon, which is later used to trap and release non magnetic objects in a viscous fluid by using the hydrodynamic flow that it generates. The ribbon is composed by a collection of hematite microellipsoids assembled and propelled upon application of an external precessing magnetic field. The applied field aligns the particles and forces them to rotate in a plane perpendicular to the close surface. The ribbon translates as a whole at a constant speed due to the collective rotations of the composing particles, generating a net flux with a major component perpendicular to its long axis. This hydrodynamic flow is used to manipulate unbound non magnetic particles in a fluid, by attracting or repelling them depending on the sense of rotation of the ellipsoids forming the ribbon. We develop a theoretical model that allows us to compute the generated hydrodynamic flow by using analytical arguments, and to obtain a good agreement with the experimental data.

2. Experimental

The colloidal ribbon is composed of hematite ($\alpha\text{-Fe}_2\text{O}_3$) microellipsoids, synthesized following the method developed by Sugimoto and coworkers [29]. The realized particles are monodisperse prolate ellipsoids with a major axis (two minor axes) equal to $1.80 \pm 0.11 \mu\text{m}$ ($1.31 \pm 0.12 \mu\text{m}$ resp.). During the synthesis, the particles acquire a permanent moment oriented mainly perpendicular to their long axis, as shown in the schematic in figure 1(a). The non magnetic particles used as a cargo are commercial aqueous suspensions of monodisperse silicon dioxide particles (44054 Sigma-Micro, Sigma-Aldrich), having $4 \mu\text{m}$ in size. Before the experiments, we first disperse the particles in high deionized water (milliQ, Millipore), stabilize them with sodium dodecyl sulfate (0.11 g of SDS for 80 ml of water) and finally adjust the pH of the solution to 9.5, by adding different aliquots of tetramethylammonium hydroxide. This procedure avoids irreversible sticking between the particles and to the glass surface, induce by attractive Van der Waals interactions. The resulting solution is introduced in a sealed capillary chamber (inner dimensions 0.1–2.00 mm, CMC Scientific), where the particles sediment due to density mismatch. After few minutes, the ellipsoids float at a certain distance above the bottom plate due to balance between gravity and electrostatic repulsive interactions with the surface. We visualize the particle dynamics with an upright optical microscope (Eclipse Ni, Nikon) connected to a CCD camera (Balser Scout scA640-74fc) equipped with a $100\times 1.3 \text{ NA}$ oil immersion objective.

The precessing field used to propel the magnetic ribbon is generated with a custom made system composed by three coils with their main axis aligned along the three orthogonal directions (\hat{x} , \hat{y} , \hat{z}). The whole

experimental setup is oriented in such a way that the \hat{x} axis coincides with the direction of the Earth magnetic field. In order to generate a rotating magnetic field in the (\hat{y}, \hat{z}) plane, i.e. perpendicular to the glass substrate, two pairs of coils are connected to a power amplifier (IMG STA-800, Stage Line) that is commanded by an arbitrary waveform generator (TGA1244, TTI). To apply a constant field along the \hat{x} direction, the third coil is connected to a DC power supply (EL 302RT, TTI).

3. Ribbon assembly and propulsion

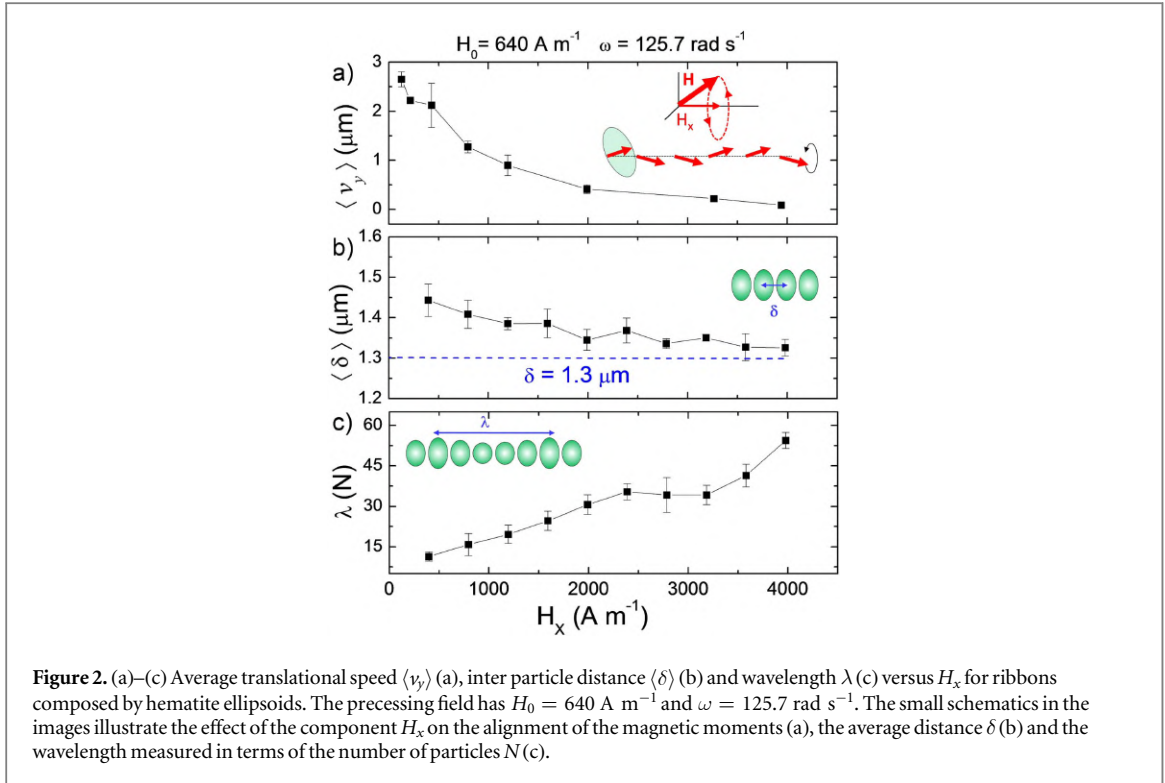
In absence of any external field ($\mathbf{H} = 0$), the hematite ellipsoids spontaneously assemble into chains or rings due to attractive dipolar interactions arising from their permanent magnetic moments [30]. In a previous work [31], we investigated the orientational dynamics of individual ellipsoids under a static external field and measured an average magnetic moment of $m = 2.3 \times 10^{-16}$ A m². Since this moment is perpendicular to the long axis of the ellipsoid, when chaining the particles arrange side by side, forming a ribbon. This configuration is similar to that previously found for ferromagnetic Janus rods, that also showed a magnetization along their short axis [32]. The assembled structure however is rather fragile, and can be easily broken by thermal fluctuations. As a matter of fact, the interaction energy between two isolated ellipsoids at close contact can be estimated as: $U_m = \mu_0 m^2 / (4\pi a^3) \sim 0.4 k_B T$, being $\mu_0 = 4\pi \times 10^{-7}$ H m⁻¹, k_B the Boltzmann constant and $T = 293$ K the room temperature. This interaction may increase within the ribbon due to nearest particles, but still it would be of the order of few $k_B T$.

We strengthen and propel the ribbon along a defined direction, in this particular case the \hat{y} axis, by applying an external precessing magnetic field, composed by a static component of amplitude H_x and aligned along the x -axis, and a rotating one polarized in the perpendicular plane (\hat{y}, \hat{z}) , figure 1(a). The applied field is thus given by: $\mathbf{H} = H_x \hat{x} + H_0 (\cos(\omega t) \hat{y} - \sin(\omega t) \hat{z})$, where $H_0 = \sqrt{(H_y^2 + H_z^2)}/2$ corresponds to the amplitude of the rotating field and ω its angular frequency. This field has different effects on the chain of ellipsoids. First, the component H_x orients the ribbon along the x axis, minimizing the magnetostatic and the effective demagnetizing energy densities [31]. This effect makes the chain stiffer, as it further aligns the particle moments along the ribbon axis. Second, the rotating component applies a net torque to the ellipsoids, $\boldsymbol{\tau}_m = \mu_0 \mathbf{m} \times \mathbf{H}$, forcing them to rotate around their short axis. The existence of this torque is due to the fact that, within each ellipsoid, the permanent moments are not exactly perpendicular to the particles' long axis as in an ideal situation, but they have a narrow tilt angle distribution that arises from imperfections during the chemical growth process. This distribution was assessed for isolated particles by measuring the angles between the long axis of the ellipsoids and the direction of a constant applied field, and it is shown in the supporting information⁵. The rotation of the individual ellipsoids within the ribbon is essential for inducing its net displacement. Since the ellipsoids are close to a surface, their rotational motion is rectified in a rolling dynamics, and the ribbon moves as a whole at a constant average speed and along a direction that is dictated by the chirality of the rotating field, figure 1(b).

We first vary the different amplitudes of the precessing field in order to determine the range of experimental values where the propelling ribbons are observed. In the diagram in figure 1(c), we keep constant the static field H_x while varying the ellipticity of rotating field, defined as $\beta = (H_z^2 - H_y^2) / (H_z^2 + H_y^2)$ [33]. The red line cutting in half the diagram denotes the circularly polarized case where $\beta = 0$ ($H_y = H_z = H_0$). The ribbon is propelled for both positive ($H_z > H_y$) and negative ($H_z < H_y$) values of β , while it breaks for large field amplitudes, $H_0 > 1200$ A m⁻¹. The ribbon rupture results from the fact that the magnetic torque is now able to spin the entire structure, and the ribbon behaves as a compact rod that tries to follow the conical precession of the field. However, the magnetic chain inevitably breaks when standing up due to the presence of the solid substrate and the action of gravity. Below $H_0 \sim 400$ A m⁻¹, the magnetic actuation is too weak to induce any propulsive motion. When considering a rotating field circularly polarized ($\beta = 0$), the propelling ribbons are stable for a wide range of values of H_x , as shown in figure 1(d). The tendency to break or to stop propulsion are found for large and small values of H_0 respectively, in agreement with the previous graph. We note that $\langle v_y \rangle = 0$ was defined as the condition accomplished when the average translational motion of the ribbon cannot be distinguished by the one observed in absence of the precessing field, i.e. when the motion of the ellipsoids is due to sole thermal fluctuations.

The average speed of the ribbon $\langle v_y \rangle$ can be easily tuned by varying two control parameters, namely ω and H_x . We start by measuring the dependence of $\langle v_y \rangle$ with ω , and at constant H_x , figure 1(e). For most of the magnetic propellers that are actuated by time dependent fields, the driving frequency is the natural parameter used to control their speed. The frequency allows for changing the particle dynamics from a synchronous regime, where

⁵ See supporting information for two videos illustrating the propulsion of one individual ribbon and the controlled hydrodynamic trapping on a silica microsphere.



velocity of the propeller is proportional to the driving frequency, to an asynchronous one, where $\langle v_y \rangle$ decreases as ω increases since the propeller is slower than the field rotations. We find that, for our magnetic ribbons, the rotations of the ellipsoids are in the asynchronous regime for all the explored frequencies, $\omega \in [10, 650] \text{ rad s}^{-1}$. In this regime of motion the phase angle ϕ between the direction of the magnetic field and the orientation of the permanent moment follows the Adler equation [34] with $\dot{\phi} = \omega - \omega_c \sin(2\phi)$, being ω_c the critical frequency that separates the synchronous from the asynchronous motion. Solving the previous equation for $\omega > \omega_c$ gives the average rotational speed as $\langle \Omega \rangle = \omega(1 - \sqrt{1 - (\omega_c/\omega)^2})$ [35]. Thus, in the asynchronous regime the hematite ellipsoids rotate with an angular frequency $\langle \Omega \rangle$ smaller than the driving frequency ω , showing characteristic ‘back and forth’ oscillations within the ribbon.

The relative low value of the average speed found, as compared to other magnetic rotors [36–40] results from both, the strongly constrained motion of the particles within the ribbon, and from the small tilt angle of their permanent moments. For $H_x = 800 \text{ A m}^{-1}$, the average speed $\langle v_y \rangle$ decreases with ω , starting from $\langle v_y \rangle = 1.5 \mu\text{m s}^{-1}$ ($\omega = 43.9 \text{ rad s}^{-1}$) and reducing to zero at $\omega = 628.3 \text{ rad s}^{-1}$. From the data in figure 1(e) it also emerges that an increase in the amplitude of the in plane field H_x decreases the particle rotational motion and thus the velocity $\langle v_y \rangle$. However, both curves display similar trends beyond $\omega \sim 300 \text{ rad s}^{-1}$ which could be an indication that a different mechanism such as magnetic relaxation [41] becomes dominant at high frequency.

We next characterize the average speed $\langle v_y \rangle$ and the deformation induced by the increase in the amplitude of the static component H_x , while keeping constant ω . The observed trend is similar to that of varying ω , since $\langle v_y \rangle$ decreases as H_x increases, figure 2(a). However, as shown in the small schematic in figure 1(a), the field component H_x is also responsible for the degree of alignment of the particle moments, since it determines the cone angle of the precessional motion described by the ellipsoids. At high values of H_x , the average inter particle distance $\langle \delta \rangle$ reduces linearly towards the hard sphere limit $\delta = 1.3 \mu\text{m}$, figure 2(b). A direct consequence of this compression is that the colloidal particles experience stronger dipolar attractions that forces them to rotate in a collective manner. Thus, the colloidal chain assumes a twisted conformation, with groups of particles rotating together. The ellipsoidal shape of the particles allows for characterizing this field induced distortion, and the wavelength of the twist can be measured in terms of the average number of particles contained in a complete turn. This number increases almost linearly with H_x , as δ reduces. For very large field values, all the ellipsoids within the ribbon try to rotate together, and the twisting reaches the size of the entire structure, while $\langle v_y \rangle$ goes to zero. The twisted ribbon resembles the helical ribbon formed by paramagnetic colloids subjected to a precessing magnetic field [42]. However, in our case the pitch remains constant along the chain, and no transversal motion of domain walls was observed as in [42].

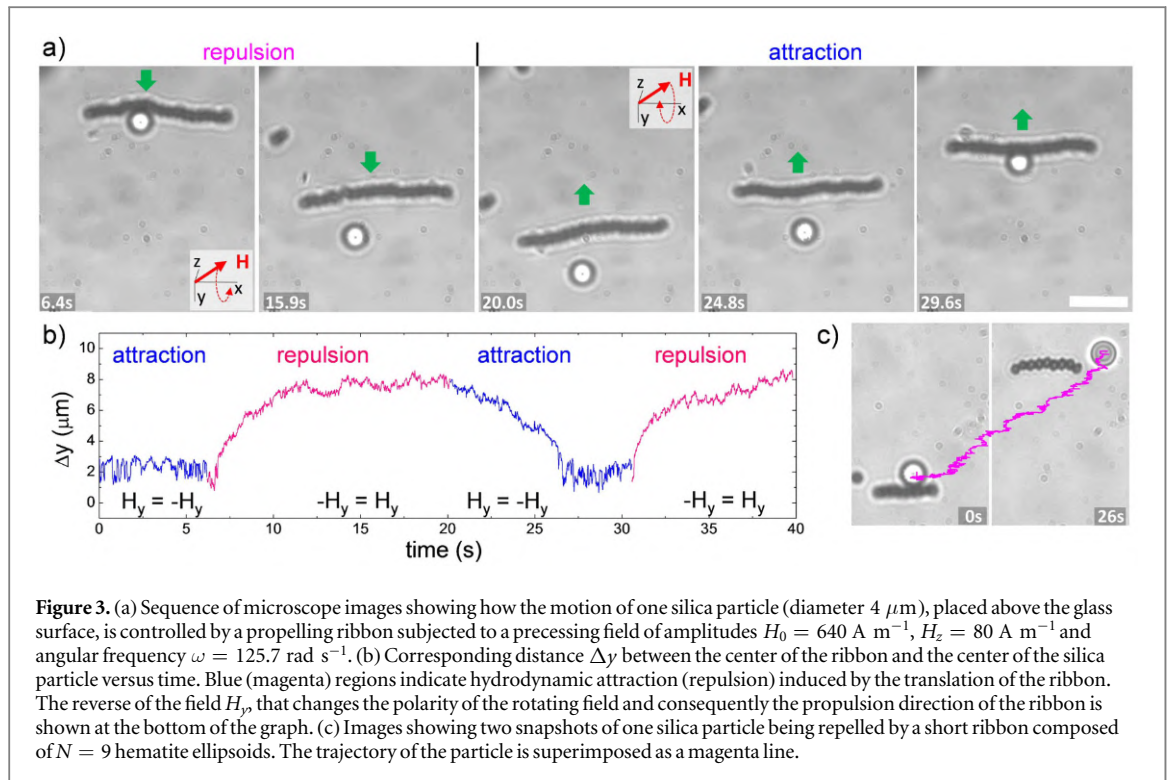


Figure 3. (a) Sequence of microscope images showing how the motion of one silica particle (diameter $4 \mu\text{m}$), placed above the glass surface, is controlled by a propelling ribbon subjected to a precessing field of amplitudes $H_0 = 640 \text{ A m}^{-1}$, $H_z = 80 \text{ A m}^{-1}$ and angular frequency $\omega = 125.7 \text{ rad s}^{-1}$. (b) Corresponding distance Δy between the center of the ribbon and the center of the silica particle versus time. Blue (magenta) regions indicate hydrodynamic attraction (repulsion) induced by the translation of the ribbon. The reverse of the field H_y , that changes the polarity of the rotating field and consequently the propulsion direction of the ribbon is shown at the bottom of the graph. (c) Images showing two snapshots of one silica particle being repelled by a short ribbon composed of $N = 9$ hematite ellipsoids. The trajectory of the particle is superimposed as a magenta line.

4. Transport of non magnetic colloids

The magnetic ribbons can trap and transport non magnetic particles by using the hydrodynamic flow generated by the rotations of the composing particles. We demonstrate this feature in figure 3(a), where we drive a colloidal ribbon close to a large silica particle of $4 \mu\text{m}$ diameter. We find that the non magnetic colloid can be either repelled or attracted when located in front or behind the propelling chain, respectively. Even though the ribbon has a finite extension, this length can be much larger than the silica bead diameter, and the latter can be stably trapped and transported when located close to the central part of the ribbon, see the corresponding supplementary video (see footnote 5). By tracking the relative distance Δy between the particle and the central position of the ribbon, figure 3(b), we observe that in both cases, i.e. when located in front or behind the chain, the silica colloid reaches a constant distance from the center of the ribbon. When attracted, the non magnetic particles reaches the back of the chain and remains there as long as the precessing field is applied. Inverting the polarity of one of the two components of the rotating field, here $H_y = -H_y$, reverses the sense of motion of the ribbon. Now the cargo becomes repelled, moving away from the chain till reaching a mean distance of $\Delta y = 8 \mu\text{m}$. The silica cargo can be further localized in a given place by applying a driving frequency higher than $\omega = 600 \text{ rad s}^{-1}$, so that the chain does not propel but it still generates an attractive flow in its back. An alternative way to trap the non magnetic object without moving it away from the observation area and keeping the frequency constant, would be to periodically switch the sign of H_y . This procedure would allow changing from attraction to repulsion and thus moving the particles back and forth along the same path, confining the colloid along a narrow line. We also find that this hydrodynamic trapping mechanism becomes less stable for shorter ribbons. As shown in figure 3(c), and corresponding VideoS3 (see footnote 5), when transported by a shorter ribbon composed of $N = 9$ particles, the silica colloid eventually escapes from the lateral direction. This indicates that the repulsive hydrodynamic flow is only strictly perpendicular to the ribbon long axis at its center, while it becomes tilted near the edge. This effect can be however minimized by placing the ribbon such that it attracts the non magnetic object at its center.

5. Flow generated by the propelling ribbon

The magnetic ribbon generates a net hydrodynamic flow due to the rotation of the constituent particles. We model this flow by considering the translating chain of ellipsoids as a line of equally spaced particles that rotate close to a solid surface. Direct analytic expressions of the flow produced by this array can be obtained in the Stokes regime, by assuming that each particle has associated an hydrodynamic singularity placed below the solid surface and at the same distance from the solid wall. As described in [43], this singularity is composed by a rotlet,

a stresslet and a source doublet. Thus, the velocity of the flow generated by one colloid rotating at an angular velocity Ω is given by the tensorial equation [43]:

$$\frac{u_i}{a^3} = \frac{\epsilon_{ijk}\Omega_j r_k}{r^3} - \frac{\epsilon_{ijk}\Omega_j R_k}{R^3} + 2h\epsilon_{kij}\Omega_j \left(\frac{\delta_{ik}}{R^3} - \frac{3R_i R_k}{R^5} \right) + 6\epsilon_{kij} \frac{\Omega_j R_i R_k R_z}{R^5}. \quad (1)$$

Here r is the position vector from the center of the particle and R the position of its hydrodynamic image, which has an opposite sense of rotation. In this way the tangential component of the generated flow cancels at the interface. Equation (1) can be extended to derive the flow generated by an array of N rotors, aligned along the \hat{x} direction, and rotating with an angular velocity $\tilde{\Omega}_n \hat{y}$, where the index $n = 1 \dots N$. The rotors are placed at position $(0, \Delta(\frac{N-1}{2} - n), h_n)$, being h_n their elevation from the surface. The velocity field at any point of space (x, y, z) is given by:

$$u_x = \sum_{n=0}^{N-1} a_n^3 \tilde{\Omega}_n \left[\frac{z - h_n}{\left(x^2 + \left(y - \Delta\left(\frac{N-1}{2} - n\right) \right)^2 + (z - h_n)^2 \right)^{3/2}} + \frac{h_n - z}{\left(x^2 + \left(y - \Delta\left(\frac{N-1}{2} - n\right) \right)^2 + (z + h_n)^2 \right)^{3/2}} + \frac{6zx^2}{\left(x^2 + \left(y - \Delta\left(\frac{N-1}{2} - n\right) \right)^2 + (z + h_n)^2 \right)^{5/2}} \right], \quad (2)$$

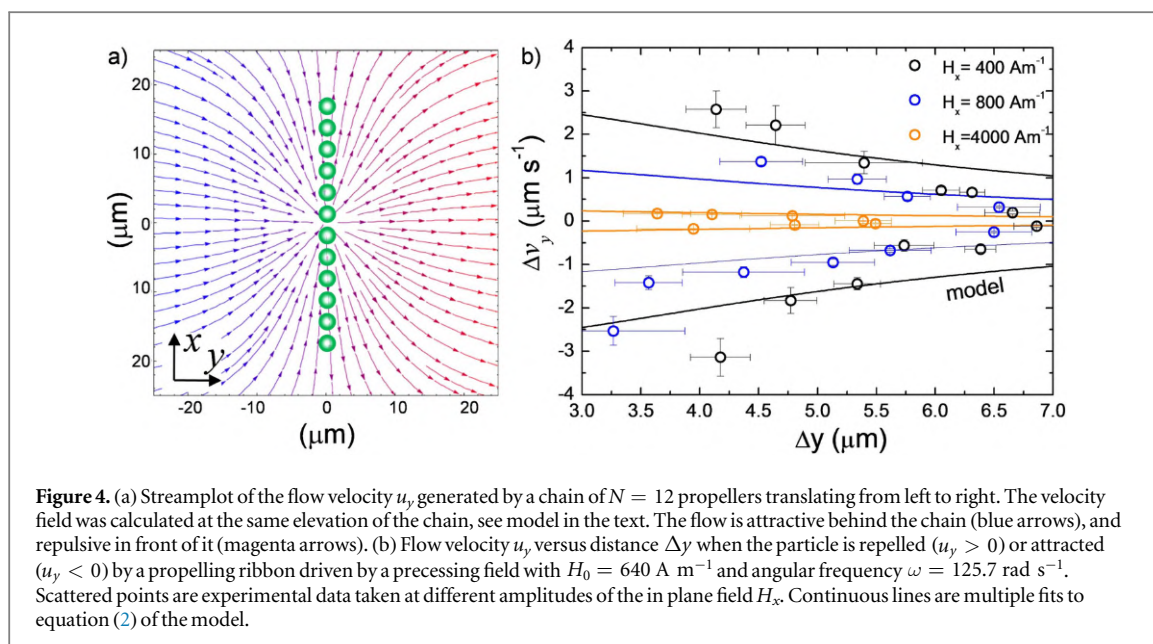
$$u_y = \sum_{n=0}^{N-1} a_n^3 \tilde{\Omega}_n \frac{6zx\Delta\left(\frac{N-1}{2} - n\right)}{\left(x^2 + \left(y - \Delta\left(\frac{N-1}{2} - n\right) \right)^2 + (z + h_n)^2 \right)^{5/2}}, \quad (3)$$

$$u_z = \sum_{n=0}^{N-1} a_n^3 \tilde{\Omega}_n \left[\frac{-x}{\left(x^2 + \left(y - \Delta\left(\frac{N-1}{2} - n\right) \right)^2 + (z - h_n)^2 \right)^{3/2}} + \frac{x}{\left(x^2 + \left(y - \Delta\left(\frac{N-1}{2} - n\right) \right)^2 + (z + h_n)^2 \right)^{3/2}} + \frac{6xz(z + h_n)}{\left(x^2 + \left(y - \Delta\left(\frac{N-1}{2} - n\right) \right)^2 + (z + h_n)^2 \right)^{5/2}} \right]. \quad (4)$$

It should be noted that our theoretical model considers only the hydrodynamic contribution, neglecting any further interaction between the particles. The magnetic interactions are important to assemble the chain of particles and to generate the net torque, but do not have any direct influence on the produced hydrodynamic flow. As a matter of fact, such interactions have been already addressed in a different context [30, 31], and here we assume that the ellipsoids rotate at an average angular velocity $\langle \tilde{\Omega} \rangle$. Using equation (1) it is also possible to determine the average speed for a chain of spherical rotors in a similar way as done in [44], where paramagnetic colloids were magnetically assembled in chains that translated parallel to the surface and along their main axis. However, in our case this calculation may give rise to theoretical values different than the experimental ones due to the non spherical shape of our ellipsoids and the asynchronous rotation resulting from the strong dipolar attraction between the particles.

We test our model by first calculating the flow profile generated by a chain of rotors that moves towards the \hat{y} direction, figure 4(a). As expected from the experimental evidence, the flow profile is attractive behind the propelling chain of particles (blue arrows), and repulsive in front of it (magenta arrows). Moreover, it radially converges toward the center of the chain, sign that tracer particles placed close to the border of the chain migrate toward the chain center when attracted, or are expelled from it when are repelled, as observed in figure 3(c).

A quantitative comparison with the experimental data is shown in figure 4(b), where we measure the average speed of the non magnetic tracer particles as a function of the distance from the center of a ribbon, which is propelled at different speeds obtained by varying the amplitude of H_x . We then perform multiple fits to the experimental data (scattered data in figure 4(b)) by using equation (2) of the model. In all cases, the experimental parameters that we kept fixed are the radius of the rotating particles, $r = 0.65 \mu\text{m}$, their elevation $h = 0.75 \mu\text{m}$, mean distance $\delta = 1.3 \mu\text{m}$ and the elevation of the silica particle $H = 2.1 \mu\text{m}$. We then leave as the only adjustable parameter the average angular rotation of the ellipsoids $\langle \tilde{\Omega} \rangle$, that is induced by the precessing field.



The values of $\langle \tilde{\Omega} \rangle$ obtained from the fits are always smaller than the field frequency ω , confirming the fact that the particles rotates asynchronously with the driving field. For short distances or small speed of the chain (high values of H_x), there is a good agreement with the experimental data, even if the developed model present different approximations. At large separations between the ribbon and the silica particle, some deviations from the theoretical trend become visible. At such distances, thermal fluctuations may be strong enough to perturb the particle trajectory, or the effect of the finite size of the chain may become significant.

6. Conclusions

In this article we have demonstrated a method to trap and transport non magnetic objects in a viscous fluid by using a magnetically assembled and twisted chain of rotating ferromagnetic ellipsoids. The chain propulsion is induced by an external precessing field, that allows for tuning both the chain mean speed and the twisted conformation. We describe the generated hydrodynamic flow as the cooperative flow resulting from a one dimensional ensemble of microscopic rotors. Even though our theoretical approach uses far field approximations, it properly captures the physics behind the hydrodynamic trapping process. Further extension of this study may include the effect of the magnetic interactions between the particles and how these interactions lead to the twisted state. On the application side, our magnetic twisted ribbon may be potentially used in lab on a chip devices where precise transport of non magnetic objects is required for the delivery of drugs or chemicals attached to functionalized particles.

Acknowledgments

HMC and PT acknowledge support from the ERC starting Grant ‘DynaMO’ (No. 335040). FMP acknowledges support from the Ramón y Cajal program (RYC-2015-18495). PT acknowledges support from MINECO (FIS2016-78507-C2-2-P) and DURSI (2014SGR878). EN and IP acknowledge support from MINECO (Spain), Project FIS2016-78507-C2-2-P, DURSI Project 2014SGR-922, and Generalitat de Catalunya under Program ‘ICREA Acadèmia’.

References

- [1] Lutz B R, Chen J and Schwartz D T 2006 Hydrodynamic tweezers: 1. Noncontact trapping of single cells using steady streaming microeddies *Anal. Chem.* **15** 5429–35
- [2] Lin C M, Lai Y S, Liu H P, Chen C Y and Wo A W 2008 Trapping of bioparticles via microvortices in a microfluidic device for bioassay applications *Anal. Chem.* **23** 8937–45
- [3] Schneider T M, Mandre S and Brenner M P 2011 Algorithm for a microfluidic assembly line *Phys. Rev. Lett.* **106** 094503
- [4] Karimi A, Yazdi S and Ardekani A M 2013 Hydrodynamic mechanisms of cell and particle trapping in microfluidics *Biomicrofluidics* **7** 021501
- [5] Tanyeri M and Schroede C M 2013 Manipulation and confinement of single particles using fluid flow *Nano Lett.* **12** 2357–64

- [6] Zhou Y, Basu S, Wohlfahrt K J, Leec S F, Klenerman D, Laue E D and Seshia A A 2016 A microfluidic platform for trapping, releasing and super-resolution imaging of single cells *Sensors Actuators B* **232** 680–91
- [7] Happel J and Brenner H 1973 *Low Reynolds Number Hydrodynamics* (Leiden: Noordhoff)
- [8] Purcell E M 1977 Life at low Reynolds number *Am. J. Phys.* **45** 3
- [9] Petit T, Zhang L, Peyer K E, Kratochvil B E and Nelson B J 2012 Selective trapping and manipulation of microscale objects using mobile microvortices *Nano Lett.* **12** 156–60
- [10] Sing C E, Schmid L, Schneider M F, Franke T and Alexander-Katz A 2010 Controlled surface-induced flows from the motion of self-assembled colloidal walkers *Proc. Natl Acad. Sci. USA* **107** 535–40
- [11] Martinez-Pedrero F and Tierno P 2015 Magnetic propulsion of self-assembled colloidal carpets: efficient cargo transport via a conveyor-belt effect *Phys. Rev. Appl.* **3** 051003
- [12] Driscoll M, Delmotte B, Youssef M, Sacanna S, Donev A and Chaikin P 2017 Unstable fronts and motile structures formed by microrollers *Nat. Phys.* **13** 375–9
- [13] Yellen B B, Hovorka O and Friedman G 2005 Arranging matter by magnetic nanoparticle assemblers *Proc. Natl Acad. Sci. USA* **102** 8860–4
- [14] Tierno P, Reddy S V, Yuan J, Johansen T H and Fischer T M 2007 Transport of loaded and unloaded microcarriers in a colloidal magnetic shift register *J. Phys. Chem. B* **111** 13479–82
- [15] Martinez-Pedrero F, Straube A V, Johansen T H and Tierno P 2015 Functional colloidal micro-sieves assembled and guided above a channel-free magnetic striped film *Lab Chip* **15** 1765–71
- [16] Yang T, Tasci T O, Neeves K B, Ning W N and Marr D W M 2017 Magnetic microlasos for reversible cargo capture, transport and release film *Langmuir* **33** 5932–7
- [17] Howse J R, Jones R A L, Ryan A J, Gough T, Vafabakhsh R and Golestanian R 2007 Self-motile colloidal particles: from directed propulsion to random walk film *Phys. Rev. Lett.* **99** 048102
- [18] Bricard A, Caussin J-B, Desreumaux N, Dauchot O and Bartolo D 2013 Emergence of macroscopic directed motion in populations of motile colloids *Nature* **503** 95
- [19] Wang W, Castro L A, Hoyos M and Mallouk T E 2012 Autonomous motion of metallic microrods propelled by ultrasound *ACS Nano* **6** 6122–32
- [20] Volpe G, Buttini I, Vogt D, Kümmerer H-J and Bechinger C 2011 Microswimmers in patterned environments *Soft Matter* **7** 8810–5
- [21] Dreyfus R, Baudry J, Roper M L, Fermigier M, Stone H A and Bibette J 2005 Microscopic artificial swimmers *Nature* **437** 862
- [22] Snezhko A, Belkin M, Aranson I S and Kwok W K 2009 Self-assembled magnetic surface swimmers *Phys. Rev. Lett.* **102** 118103
- [23] Zhang L, Abbott J J, Dong L, Peyer K E, Kratochvil B E, Zhang H, Bergeles C and Nelson B J 2009 Characterizing the swimming properties of artificial bacterial flagella *Nano Lett.* **9** 3663–7
- [24] Ghosh A and Fischer P 2009 Controlled propulsion of artificial magnetic nanostructured propellers *Nano Lett.* **9** 2243
- [25] Pak O S, Gao W, Wang J and Lauga E 2011 High-speed propulsion of flexible nanowire motors: theory and experiments *Soft Matter* **7** 8169–81
- [26] Lumay G, Obara N, Weyer F and Vandewalle N 2013 Self-assembled magnetocapillary swimmers *Soft Matter* **9** 2420
- [27] Dobnikar J, Snezhko A and Yethiraj A 2013 Emergent colloidal dynamics in electromagnetic fields *Soft Matter* **9** 3693–704
- [28] Tierno P 2014 Recent advances in anisotropic magnetic colloids: realization, assembly and applications *Phys. Chem. Chem. Phys.* **16** 23515
- [29] Sugimoto T, Khan M M and Muramatsu A 1993 Preparation of monodisperse peanut-type alpha-Fe₂O₃ particles from condensed ferric hydroxide gel *Colloids Surf. A* **70** 167
- [30] Martinez-Pedrero F, Cebers A and Tierno P 2016 Dipolar rings of microscopic ellipsoids: magnetic manipulation and cell entrapment *Phys. Rev. Appl.* **6** 034002
- [31] Martinez-Pedrero F, Cebers A and Tierno P 2016 Orientational dynamics of colloidal ribbons self assembled from microscopic magnetic ellipsoids *Soft Matter* **12** 3688–95
- [32] Yan J, Chaudhary K, Chul Bae S, Lewis J A and Granick S 2013 Colloidal ribbons and rings from Janus magnetic rods *Nat. Commun.* **4** 15162
- [33] Laci S, Bacri J C, Cebers A and Perzynski R 1997 Frequency locking and devil's staircase for a two-dimensional ferrofluid droplet in an elliptically polarized rotating magnetic field *Phys. Rev. E* **55** 2640
- [34] Adler R 1946 A study of locking phenomena in oscillators *Proc. IRE* **34** 351
- [35] Tierno P, Claret J, Sagués F and Cebers A 2009 Overdamped dynamics of paramagnetic ellipsoids in a precessing magnetic field *Phys. Rev. E* **79** 021501
- [36] Morimoto H, Ukai T, Nagaoka Y, Grobert N and Maekawa T 2008 Tumbling motion of magnetic particles on a magnetic substrate induced by a rotational magnetic field *Phys. Rev. E* **78** 021403
- [37] Janssen X J, Schellekens A J, van Ommering K, van Ijzendoorn L J and Prins M W 2009 Controlled torque on superparamagnetic beads for functional biosensors *Biosens. Bioelectron.* **24** 1937
- [38] Tierno P, Güell O, Sagués F, Golestanian R and Pagonabarraga I 2010 Controlled propulsion in viscous fluids of magnetically actuated colloidal doublets *Phys. Rev. E* **81** 011402
- [39] Tottori S, Zhang L, Qiu F, Krawczyk K K, Franco-Obregón A and Nelson B J 2012 Magnetic helical micromachines: fabrication, controlled swimming, and cargo transport *Adv. Mater.* **24** 811
- [40] Tasci T O, Herson P S, Neeves K B and Marr D W M 2016 Surface-enabled propulsion and control of colloidal microwheels *Nat. Commun.* **7** 10225
- [41] Cebers A and Kalis H 2011 Dynamics of superparamagnetic filaments with finite magnetic relaxation time *Eur. Phys. J. E* **34** 30
- [42] Casic N, Alvarez-Nodarse R, Mertens F G, Jibuti L, Zimmermann W and Fischer T M 2013 Propulsion efficiency of a dynamic self-assembled helical ribbon *Phys. Rev. Lett.* **110** 168302
- [43] Blake J R and Chwang A T 1974 Fundamental singularities of viscous flow *J. Eng. Math.* **8** 23–9
- [44] Martinez-Pedrero F, Ortiz-Ambriz A, Pagonabarraga I and Tierno P 2015 Colloidal microworms propelling via a cooperative hydrodynamic conveyor belt *Phys. Rev. Lett.* **115** 138301

PUBLICATION 2

Supporting Information

Supporting Information for: Propulsion and hydrodynamic particle transport of magnetically twisted colloidal ribbons

Helena Massana-Cid¹, Fernando Martinez-Pedrero², Eloy

Navarro-Argemí^{1,3}, Ignacio Pagonabarraga Mora^{1,3}, and Pietro Tierno^{1,3,4*}

¹*Departament de Física de la Matèria Condensada, Universitat de Barcelona, Barcelona, Spain.*

²*Departamento de Química Física I, Universidad Complutense de Madrid, Ciudad Universitaria, 28040, Madrid, Spain.*

³*Universitat de Barcelona Institute of Complex Systems (UBICS), Universitat de Barcelona, Barcelona, Spain*

⁴*Institut de Nanociència i Nanotecnologia, IN²UB, Universitat de Barcelona, Barcelona, Spain.*

(Dated: May 29, 2017)

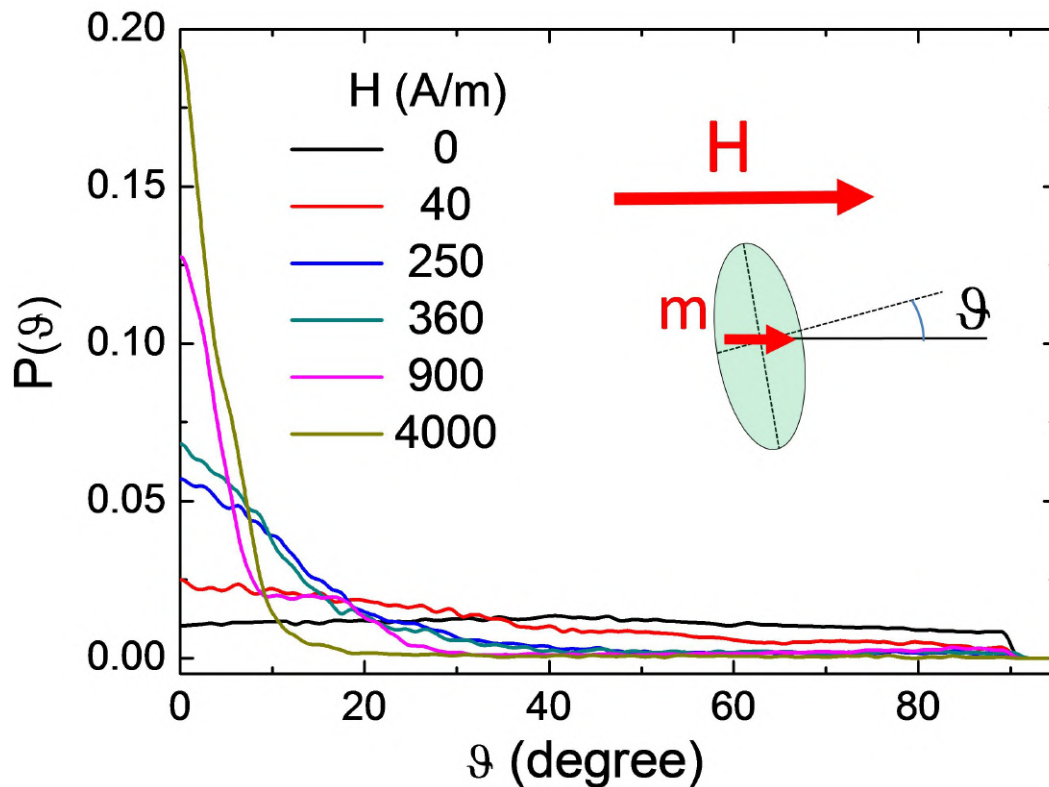


FIG. 1. Distribution of the particle orientation $P(\vartheta)$, for different amplitudes of the static field H . Here ϑ denotes the angle between the applied field and the short axis of the ellipsoid, as shown in the small schematic.

TILT ANGLE OF THE FERROMAGNETIC ELLIPSOIDS

In Fig.1 we measure the tilt angle ϑ that the magnetic moments have in the hematite ellipsoids with respect to their short axis. We have subject different particles in a diluted solution to a static external field H , and measured the angle φ that the long axis of the ellipsoid makes with the field direction, obtaining thus $\vartheta = 90^\circ - \varphi$. As shown from Fig.1, for small applied field thermal fluctuations can easily perturb the particle orientations, and the distribution are broad. However, for $H > 900 \text{ Am}^{-1}$ the distribution becomes narrow and its variance remain constant, demonstrating effectively that the permanent moment within the ellipsoids can have a small tilt up to 10 degrees from the short axis.

SUPPORTING VIDEOS

With the article are 3 videoclips as support of Figs.1(b) and Figs.3(a,c).

- **VideoS1**(.WMV) This videoclip illustrates the transport of a ribbon composed by $N = 38$ hematite ellipsoids and subjected to an external precessing magnetic field with amplitudes $H_0 = 2000 \text{ Am}^{-1}$, $H_x = 460 \text{ Am}^{-1}$, and driving frequency $\omega = 314.2 \text{ rads}^{-1}$. The video corresponds to Fig.1(b) of the article.
- **VideoS2**(.WMV) The video illustrates the controlled trapping of a silica particle of $4 \mu\text{m}$ diameter when placed close to a ribbon propelling due to a precessing field. The field has $H_0 = 640 \text{ Am}^{-1}$, $H_x = 80 \text{ Am}^{-1}$, and driving frequency $\omega = 125.7 \text{ rads}^{-1}$. The sign of the field component H_y is inverted two times such that the ribbon first repel the non-magnetic particle, than attract after 13.6 s since $H_y = -H_y$, and finally at 23.2 s $-H_y = H_y$ and it repels again. The video corresponds to Fig.3(a) of the article.

- **VideoS3**(.WMV) Transport of a silica particle of $4\ \mu\text{m}$ diameter by a shorter chain composed of $N = 9$ hematite ellipsoids. The precessing field has the same parameters as the one used in VideoS3, and after 26 s the silica particle escapes from the hydrodynamic flow of the ribbon due to its tangential nature close to the ribbon boundary. The video corresponds to Fig.3(c) of the article.

* ptierno@ub.edu

- [1] T. Sugimoto and A. Muramatsu, *J. Colloid Interface Sci.*, **184**, 626 (1996).
- [2] F.-M. Pedrero, A. Cebers, and P. Tierno, *Soft Matter*, **12**, 3657 (2016).
- [3] F.-M. Pedrero, A. Cebers, and P. Tierno, *Phys. Rev. Appl.*, **6**, 034002 (2016).
- [4] J. C. Crocker and D. G. Grier, *J. Colloid Interface Sci.*, **179**, 298 (1996).
- [5] F. Perrin, *J. Phys. Radium*, **5**, 497 (1934).

PUBLICATION 3

Leap-frog transport of magnetically driven anisotropic colloidal rotors

The Journal of Chemical Physics **150**, 164901 (2019)

Helena Massana-Cid¹, Eloy Navarro-Argemí^{1,2}, Demian Levis^{1,2,3},
Ignacio Pagonabarraga^{1,2,3}, and Pietro Tierno^{1,2,4}

¹ Departament de Física de la Matèria Condensada,
Universitat de Barcelona, 08028 Barcelona, Spain

² Universitat de Barcelona Institute of Complex Systems
(UBICS), Universitat de Barcelona, 08028 Barcelona, Spain

³CECAM, Centre Européen de Calcul Atomique et Moléculaire,
École Polytechnique Fédérale de Lausanne Batochime,
Avenue Forel 2, 1015 Lausanne, Switzerland

⁴ Institut de Nanociència i Nanotecnologia, IN²UB,
Universitat de Barcelona, 08028 Barcelona, Spain

Leap-frog transport of magnetically driven anisotropic colloidal rotors

Cite as: J. Chem. Phys. 150, 164901 (2019); doi: 10.1063/1.5086280

Submitted: 19 December 2018 • Accepted: 29 March 2019 •

Published Online: 22 April 2019



View Online



Export Citation



CrossMark

Helena Massana-Cid,¹ Eloy Navarro-Argemí,^{1,2} Demian Levis,^{1,2,3}  Ignacio Pagonabarraga,^{1,2,3} 
and Pietro Tierno^{1,2,4,a)} 

AFFILIATIONS

¹Departament de Física de la Matèria Condensada, Universitat de Barcelona, 08028 Barcelona, Spain

²Universitat de Barcelona Institute of Complex Systems (UBICS), Universitat de Barcelona, 08028 Barcelona, Spain

³CECAM, Centre Européen de Calcul Atomique et Moléculaire, École Polytechnique Fédérale de Lausanne, Batochime, Avenue Forel 2, 1015 Lausanne, Switzerland

⁴Institut de Nanociència i Nanotecnologia, IN²UB, Universitat de Barcelona, 08028 Barcelona, Spain

Note: This article is part of the Special Topic “Chemical Physics of Active Matter” in J. Chem. Phys.

^{a)}Electronic mail: ptierno@ub.edu.

ABSTRACT

In this article, we combine experiments and theory to investigate the transport properties of anisotropic hematite colloidal rotors that dynamically assemble into translating clusters upon application of a rotating magnetic field. The applied field exerts a torque to the particles forcing rotation close to a surface and thus a net translational motion at a frequency tunable speed. When approaching, pairs of particles are observed to assemble into stable three-dimensional clusters that perform a periodic leap-frog type dynamics and propel at a faster speed. We analyze the cluster formation and its lifetime and investigate the role of particle shape in the propulsion speed and stability. We show that the dynamics of the system results from a delicate balance between magnetic dipolar interactions and hydrodynamics, and we introduce a theoretical model that qualitatively explains the observed phenomena.

Published under license by AIP Publishing. <https://doi.org/10.1063/1.5086280>

I. INTRODUCTION

Recent years have witnessed a surge of activities in realizing artificial microscopic prototypes that could be remotely guided toward a defined target in a fluid medium.^{1–3} The driving interest arises from both fundamental and technological needs. The physics of artificial microswimmers navigating fluids fascinates scientists due its direct connection with biological systems, such as bacteria, that operate at the low Reynolds number. From the point of view of applications, artificial prototypes demonstrated the capabilities of performing useful tasks in microfluidic chips,^{4–6} in biomedicine,^{7,8} or to transport microscopic cargoes.^{9–15} Thus, the community has been mainly focused on designing individual microswimmers and understanding their principle of propulsion or on analyzing their collective dynamics in high density suspensions.^{16–23,37,38} However, investigating the interactions and dynamics between few micropropellers represents a first step toward understanding the complex

phenomena arising from a collection of them. In particular, the use of colloidal particles as model microswimmers has the advantage that it avoids the intrinsic complexity of biological systems, providing tunable interactions and experimentally accessible length scales.

In this context, we recently realized controllable colloidal rotors that are composed of anisotropic hematite particles and are driven in water by an external rotating magnetic field.²⁴ The particles rotate close to a surface, and the hydrodynamic interaction with the plane rectifies the rotational motion into a net drift velocity.⁴ We find that when two rotors approach each other, they couple forming a dynamic bound state by adjusting their translational speed. The relative orientation of the particles within these states depends on the field parameters: the hematite ellipsoids align side-to-side or tip-to-tip, i.e., with the relative position parallel or perpendicular, respectively, to their long axis. However, in all the observed cases, the bound states remain confined in two dimensions with a

relatively long interparticle distance. Here, by further exploring the space parameter, we discover a new type of cooperative dynamics, where a pair of propellers combines into a rolling three-dimensional cluster that displays a leap-frog type motion while propelling faster than individual rotors. We observe that this bound state can be formed by two or more rotors, and we characterize its stability and dynamics by varying the different field parameters. We complement these experiments with a theoretical model that considers the hydrodynamic interactions between the particles and the bounding plane.

II. EXPERIMENTAL PART

We realize micropropellers by using anisotropic hematite particles that are synthesized via the “sol-gel” technique.²⁵ The particles present a long and a short axis equal to $\alpha = 2.5 \mu\text{m}$ and $\beta = 1.4 \mu\text{m}$, respectively, and a permanent magnetic moment m perpendicular to their long axis, as shown in the schematic of Fig. 1(a). In a previous studies,^{24,39} the magnitude of this moment was measured as $m \simeq 9 \times 10^{-16} \text{ Am}^2$. After synthesis, the particles are diluted in highly deionized water (Milli-Q system, Millipore) and are stabilized by adding sodium dodecyl sulfate (SDS), namely, 0.11 g of SDS for 80 ml of water. This surfactant is used to avoid sticking of the particles due to van der Waals interactions. Before the experiments, the pH of the resulting solution is raised to 9.5 by adding tetramethylammonium hydroxide. The particles sediment on a glass surface, and the balance between gravity and steric interactions due to the SDS confines them on the plane.

The external magnetic field used to propel the particles is generated by using a triaxial magnetic coil system connected to a waveform generator (TGA1244, TTI) feeding a power amplifier (AMP-1800, AKIYAMA or BOP 20-10M, Kepco). A rotating field in a given plane is obtained by passing through two perpendicular coils two sinusoidal currents with 90° phase shift. We then use optical microscopy (Eclipse Ni, Nikon) to record the particle motion with an area-scan camera (scA640-74f, Basler) working

at 50 fps. The videos are then analyzed via particle tracking routines²⁶ to extract the position and the orientation of the hematite particles.

III. DYNAMICS OF AN INDIVIDUAL ROTOR

We start by describing the propulsion of a single rotor and later focus on the emergence of the three-dimensional leap-frog states. The particles are propelled by applying a rotating magnetic field circularly polarized in the (\hat{x}, \hat{z}) plane that is perpendicular to the glass substrate, as shown in Fig. 1(a). The applied field is given by $\mathbf{H} = H_0(\cos(\omega t)\hat{x} - \sin(\omega t)\hat{z})$, being H_0 the amplitude and ω the driving frequency. Figure 1(b) shows two snapshots of a dilute suspension of rotors driven toward the right by the rotating field. Since the permanent moment of the particles is directed along the short axis, Fig. 1(a), during propulsion, the particles keep their long axis always perpendicular to the direction of motion, here given by \hat{x} . From particle tracking, we extract the position of each particle i , $(x_i(t), y_i(t))$, and determine the mean speed of the individual rotors as $\langle v_x \rangle = \frac{1}{N} \sum_i^N \frac{\Delta x_i}{\Delta t}$, where the average $\langle \dots \rangle$ is performed over N different and independent particles. As shown in Fig. 1(c), the particle dynamics is characterized by two regimes of motion, separated by a critical frequency ω_c . The synchronous transport occurs for $\omega < \omega_c$, where the magnetic moment of the particle follows the applied field, and thus, the particle rotational frequency Ω coincides with the driving one, $\Omega = \omega$. In this situation, assuming that the particles have an elevation from the surface equal to $\sim \beta/2$, the net drift velocity is given by $v_x \sim \beta\omega/2$. The dashed lines in Fig. 1(c) show the corresponding fit to the experimental data in this linear regime. For $\omega > \omega_c$, the motion becomes asynchronous, and the phase lag angle between the particle's moment and the field is not constant. This effect induces characteristic back-and-forth oscillations during each field cycle and a consequent reduction of the average particle rotational motion. Neglecting thermal fluctuations, the average speed of the particles can be calculated as²⁷ $v_x \sim \beta\Omega/2$ with

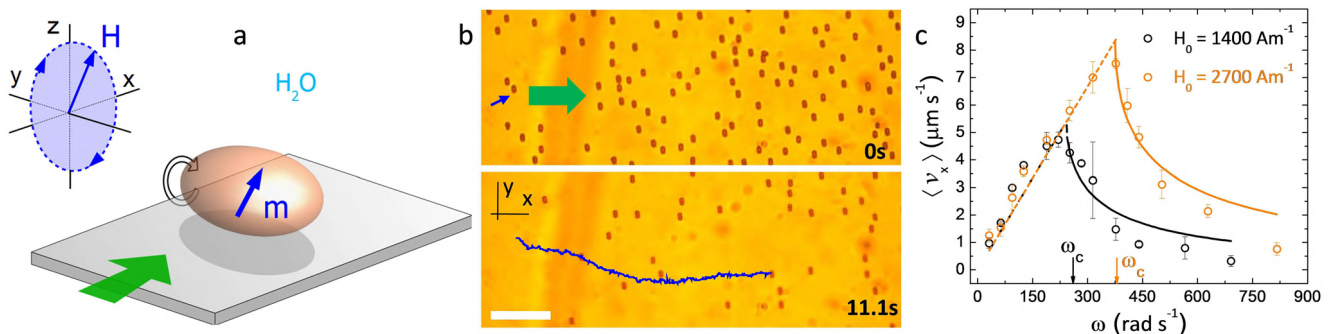


FIG. 1. (a) Schematic illustrating a ferromagnetic hematite ellipsoidal particle propelling in water due to the application of a rotating magnetic field H . Green arrows indicate the direction of propulsion. (b) Sequence of images showing a dilute solution of hematite particles that propel toward the right due to a rotating field with amplitude $H_0 = 2700 \text{ A m}^{-1}$ and angular frequency $\omega = 251.3 \text{ rad s}^{-1}$. In the bottom image, the trajectory of one particle is superimposed and the scale bar is $20 \mu\text{m}$. (c) Average speed $\langle v_x \rangle$ vs driving frequency ω for a single propeller when subjected to a rotating field with amplitudes $H_0 = 1400 \text{ A m}^{-1}$ (black circles) and $H_0 = 2700 \text{ A m}^{-1}$ (orange circles). Dashed (continuous) lines are fit to the synchronous (asynchronous) regime, while ω_c is the critical frequency. Error bars are obtained from the statistical average of different experiments.

$\Omega = \omega - \sqrt{\omega^2 - \omega_c^2}$, as shown by the continuous lines in Fig. 1(c). From the fits to the experimental data, we determine the critical frequencies for the two field amplitudes $\omega_c = 243 \pm 3 \text{ rad s}^{-1}$ for $H_0 = 1400 \text{ A m}^{-1}$ and $\omega_c = 376 \pm 3 \text{ rad s}^{-1}$ for $H_0 = 2700 \text{ A m}^{-1}$, which, as previously observed,²⁷ increase linearly with H_0 . Thus, our hematite rotors display a tunable speed that increases linearly with the driving frequency up to ω_c , while this threshold frequency could be further raised by tuning the field amplitude.

IV. LEAP-FROG DYNAMICS OF ROTORS

At large density of rotors, propelling particles start to interact with each other. Very close hematite rotors may couple their motion forming bound states and altering their translational speed. As shown in the diagram in Fig. 2(a), we observe different situations depending on whether the motion occurs on the same plane or becomes three-dimensional (leap-frog state). For high driving frequencies, we observe that the rotating particles never come too close to generate the leap-frog state, but rather they bound into metastable states confined in the plane of motion (\hat{x}, \hat{y}) . In this situation, the

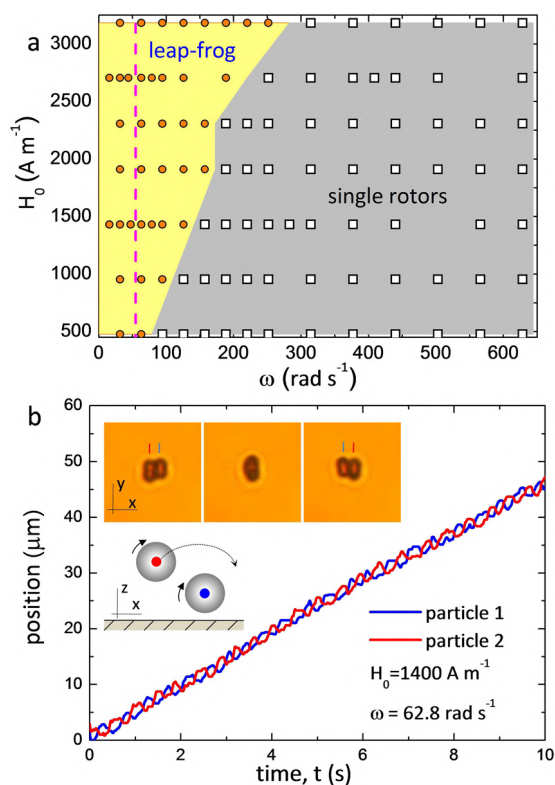


FIG. 2. (a) Diagram in the $(\omega; H_0)$ plane showing the regime where the leap-frog dynamics is observed (yellow region) and where the movement of the hematite particle is limited to a 2D plane (gray region). The magenta dashed line corresponds to $\omega = 54.8 \text{ rad s}^{-1}$. (b) Position vs time of two particles performing the leap-frog dynamics. Insets at the top show experimental images of the hematite particles exchanging their positions during propulsion and the microscope image visualizes the (\hat{x}, \hat{y}) plane at a fixed height. The inset at the bottom shows the corresponding schematic in the (\hat{x}, \hat{z}) plane.

relative particle arrangement is the same to that reported in a previous study²⁴ and thus here will not be described. By contrast, at low frequency, we find that the pair of approaching particles can form three-dimensional leap-frog states, where the hematite ellipsoids roll one on top of each other, periodically exchanging their positions and always keeping their long axis perpendicular to the propulsion direction [Fig. 2(b)].

The resulting dynamics is mainly dictated by the balance between the magnetic dipolar and hydrodynamic interactions. The first type of interaction favors that the particles arrange side by side with their long axis parallel to each other. In this configuration, the permanent moments tend to be aligned along a common direction in order to minimize the magnetic energy of the couple, U_m . If we consider two hematite rotors with moments \mathbf{m}_i , \mathbf{m}_j and at a relative distance $\mathbf{r}_{ij} = |\mathbf{r}_i - \mathbf{r}_j|$, the dipolar interaction between the couple is given by $U_m = \frac{\mu_w}{4\pi} \left(\frac{\mathbf{m}_i \mathbf{m}_j}{r_{ij}^3} - \frac{3(\mathbf{m}_i \cdot \mathbf{r}_{ij})(\mathbf{m}_j \cdot \mathbf{r}_{ij})}{r_{ij}^5} \right)$. Here, $\mu_w \sim \mu_0 = 4\pi \cdot 10^{-7} \text{ H m}$ is the magnetic susceptibility of the medium (water) and \mathbf{r}_i is the position of particle i . Thus, the dipolar potential is maximally attractive (repulsive) for particles with magnetic moments parallel (perpendicular) to \mathbf{r}_{ij} . Since the moment of the particles follows the field that rotates in the (\hat{x}, \hat{z}) plane, the leap-frog motion minimizes the potential U_m . This follows from the fact that the distance between \mathbf{m}_i and \mathbf{m}_j is shorter (longer) when $\mathbf{m}_{i,j} \parallel \mathbf{r}_{ij}$ ($\mathbf{m}_{i,j} \perp \mathbf{r}_{ij}$) during one field cycle. The time average potential between two dipoles performing the leap-frog motion is indeed attractive in the plane (x, z) and given by $\bar{U}_m = -\mu_0 m^2 / (8\pi(x+z)^3)$. In the opposite case, when the particles are aligned tip to tip on the same plane, the moments are always perpendicular to their separation distance, and the potential becomes repulsive $\bar{U}_m = \mu_0 m^2 / (4\pi y^3)$.

This configuration, however, could be perturbed by the hydrodynamic interactions (HIs), which arise from the particle spinning and the generated vortical flow field. The order of magnitude of the two competing interactions can be estimated, in first approximation, by considering the range of forces that act over the pair. The magnetic dipolar forces F_m between two equal dipolar particles of radius a and moment m and located at distance $r = 2a$ is given by $F_m = 3\mu_0 m^2 / (64\pi a^4)$, while the viscous force generated by a single hematite particle is $F_h = 3\pi\eta\Omega h^2 / 4$, being $\eta = 10^{-3} \text{ Pa s}$ the solvent viscosity and $h \sim a$ the particle elevation from the surface. Hence, for $a \sim \beta/2 = 0.7 \mu\text{m}$, we find that when both forces balance, $F_m = F_h$, the angular frequency becomes $\Omega = \mu_0 m^2 / (16\pi^2 \eta a^6) = 54.8 \text{ rad s}^{-1}$, which corresponds to the dashed line in Fig. 2(a). Thus, at low driving frequencies, magnetic interactions dominate over HIs and help keeping the leap-frog stable, as shown in the diagram in Fig. 2(a). However, our simple argument does not explain how the transition region depends on the field amplitude. Indeed, at large values of H_0 , the presence of an induced dipole moment $m_{ind} \sim H_0$ within the particle may lead to strong dipolar interactions and further favor the leap-frog state. While magnetization measurements of similar particles show a negligible value of m_{ind} ,²⁷ its contribution to F_m may become important for large amplitudes, as it grows as $\sim H_0^2$.

In Fig. 3(a), we measure the average speed $\langle v_x \rangle$ of a cluster of hematite particles performing the leap-frog and compare its values to the speed of individual rotors in the synchronous regime. The cluster displays a faster translational motion until it reaches the

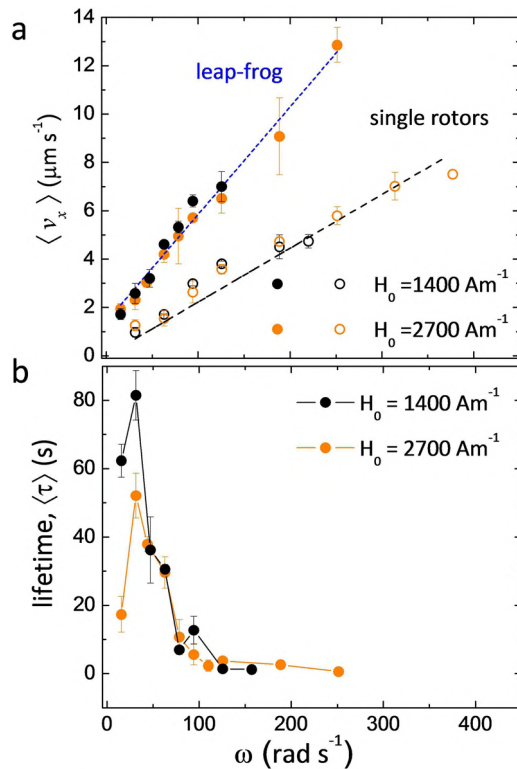


FIG. 3. (a) Average propulsion speed $\langle v_x \rangle$ vs angular driving frequency ω for single rotors (open symbols) and for a leap-frog state (filled symbols). The straight lines are linear fits that serve as guides to the eyes. (b) Average lifetime $\langle \tau \rangle$ vs ω for a bound state performing the leap-frog dynamics for two field amplitudes. In both graphs, the error bars are obtained from the statistical average of different experiments.

critical frequency ω_c , where the two particles enter the asynchronous regime reducing their rotational motion. In this case, the couple easily breaks due to the difference in speeds between the two hematite rotors. Furthermore, we report in Fig. 3(b) the average lifetime $\langle \tau \rangle$ of the observed leap-frog states for two different field amplitudes. The presence of thermal noise or disorder in the experimental system may produce the disassembly of the pair during propulsion, even at frequencies well inside the synchronous regime. The disorder may be due to small polydispersity in the particle shape, in their magnetic moments, or to the presence of surface asperities. These sources of noise can induce variations of the hydrodynamic flow that easily destabilize the propelling cluster. In general, we find that stable clusters with longer $\langle \tau \rangle$ are observed at low frequencies when magnetic dipolar interactions completely overcome the hydrodynamic ones.

V. THEORETICAL MODEL

We describe the HIs between a pair of particles performing the leap-frog state by considering the direct interactions and the presence of the bounding plane. The surface is replaced by a hydrodynamic singularity located below the interface at the same distance

to it as the colloidal particle. The latter image is represented by a particle rotating in the opposite sense that the actuated colloid, and contributing to the flow field with additional stresslet and source doublets.²⁸ We neglect the magnetic dipolar interactions between the pair and assume that the imposed rotating field simply prescribes the angular velocity of the colloid Ω . Thus, in the synchronous regime, the colloids of radius a rotate at $\Omega = \omega$. In the far field, the flow generated by one of them is given by

$$\frac{u_i}{a^3} = \frac{\epsilon_{ijk}\Omega_j r_k}{r^3} - \frac{\epsilon_{ijk}\Omega_j R_k}{R^3} + 2h\epsilon_{kij}\Omega_j \left(\frac{\delta_{ik}}{R^3} - \frac{3R_i R_k}{R^5} \right) + 6\epsilon_{kij} \frac{\Omega_j R_i R_k R_z}{R^5}, \quad (1)$$

where r is the position vector from the center of the particle, R is the position of its image, and the subscripts (i, j, k, z) refer to vector components. From Eq. (1), we can derive analytic expressions for the speeds v_i of the two spheres $i = 1, 2$ rotating with angular speed Ω_i and at elevation h_i ; see the Appendix for the full expressions. To explore the role of anisotropy on the leap-frog state, we perform numerical simulation of single spheres rotating at a common angular velocity and of colloidal dumbbells. We model a dumbbell as a pair of spherical particles linked by a harmonic potential with a stiff spring constant that allows the particle rotation but not separation between the pair. Thus, the dumbbells are made of a pair spheres ($i, i+1$) bounded by a harmonic potential

$$V(r_{i,i+1} = r) = \frac{k}{2}(r - r_0)^2, \quad (2)$$

where r_0 defines the distance between the two composing spheres at rest and k is a spring constant. Thus, each sphere evolves according to an overdamped dynamics

$$\gamma \dot{r}_i = \gamma v_i + f_i, \quad (3)$$

where γ is the viscous friction and $f_i = -\nabla_i V(r_{i,i+1})$ is the spring force. We choose a relatively very stiff spring ($k = 10^3$) that guarantees the dumbbell stability ($k \gg \Omega\gamma a$) avoiding particle separation and set $r_0 = a$.

Figures 4(a)–4(d) show the results of our numerical simulations based on the hydrodynamic model. We start by first calculating the flow profile generated by a pair of spherical rotors that moves toward right along the \hat{x} direction side by side [Fig. 4(a)] and one on top of the other [Fig. 4(b)]. In the first case, the effective flow field induced by the pair creates an elongated dipole with a source corresponding to the front particle and a sink on the back one. When one particle is above the other, the two flow patterns superimpose, creating two lateral swirls with opposite rotational motion. Thus, tracer particles could be easily transported by the propelling pair, being attracted to it when at the back of the pair and pushed when in front of it.

Furthermore, we explore the role of shape anisotropy on the propulsion speed and on the formation of the leap-frog states. As shown in Fig. 4(c), we find that single spheres and dumbbells present almost the same speed that linearly increases with ω . The main difference arises when the pair of spheres or dumbbells performs the leap-frog as we observe a much faster propulsion speed for the latter. However, we find that the normalized velocity $\langle v_x \rangle$ overshoots the experimental data by almost a factor of two. This

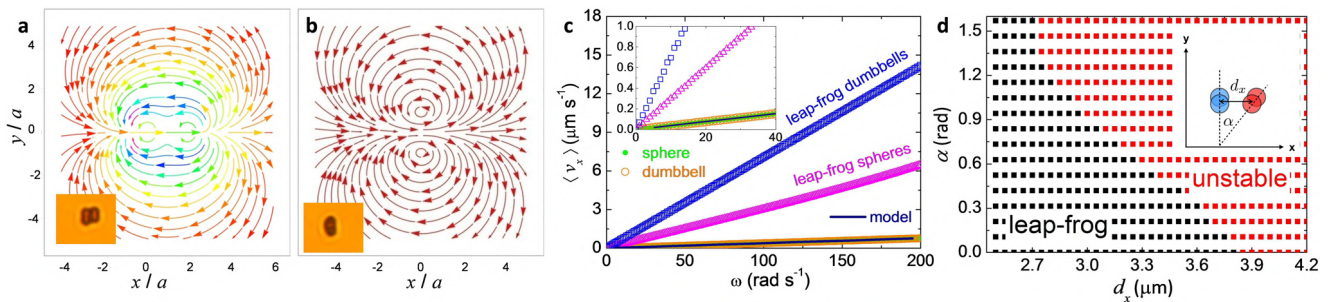


FIG. 4. [(a) and (b)] Plot of the streamlines of the fluid flow velocity \mathbf{u} generated by a pair of spherical rotors performing the leap-frog motion before one particle jumps on top of the other (a) and when the particle sits on top of the other. The (x, y) coordinates are normalized with respect to the particle radius a . The velocity field was calculated in (a) considering both particles at the same elevation ($z_1 = z_2 = 2a$) and in (b) with different elevations ($z_1 = a, z_2 = 3a$) being a the particle radius. The motion of the particles occurs toward the right. (c) Average speed $\langle v_x \rangle$ vs frequency for a single sphere (green filled points) and dumbbell (orange circles) and for a pair of spherical rotors (magenta triangles) and dumbbells (blue squares) performing leap-frog motion. The continuous line is obtained from Eq. (1) in the main text. The inset illustrates enlargement of the main graph. (d) Diagram illustrating the regions where the leap-frog is stable (black squares) and not (red squares) by varying the initial distance d_x and orientation angle α between the two dumbbells. The schematic inset shows α and d_x .

discrepancy could result from the different simplifications used in our model. Specifically, the theoretical model disregards both gravity and magnetic interactions and neglects the homogeneous surface of the particles by considering them as dumbbells. Nevertheless, we find that the leap-frog states could be formed by both spherical and anisotropic rotors, which does not limit our mechanism to magnetic particles with anisotropic shape but also to other types of colloidal systems.²⁹

We also observe that the leap-frog state is much more stable for spherical rotors than for pairs of dumbbells. In the first case, according to the hydrodynamic model, we find that there is no preferred distance between two particles to generate the leap-frog motion. Thus, identical spherical particles will always be coupled, unless thermal dissipation or other types of noise break the bound state. This contrasts with our experimental observation of a finite lifetime [Fig. 3(b)] and can be explained by considering the anisotropic shape of the particles and the presence of a relative orientational motion. In Fig. 4(d), we show the stability of a pair of

dumbbells performing leap-frog by varying their initial distance d_x and orientation angle α . We define the stable leap-frog when it lasts for all the simulation time ($1000 \Omega^{-1}$ with $\Omega = 200 \text{ rad s}^{-1}$) while unstable when it breaks, or does not form at all, as observed for larger distance or angle between the dumbbells. Leap-frog motion might be broken by thermal fluctuations, or other sources noise such as particle inhomogeneities, tumbling induced by particle collision, and substrate roughness. These factors may easily change the distance and relative orientation or even change the particle speed as the cluster of rotors could develop a self-propelling velocity that depends on their elevation (the closer they are, the faster they move).

VI. TRANSPORT OF SEVERAL PARTICLES

The leap-frog state is reminiscent of the walking-like dynamics observed both on dimers^{30,31} and clusters^{32,33} assembled from paramagnetic colloids. However, in contrast to the mentioned studies,

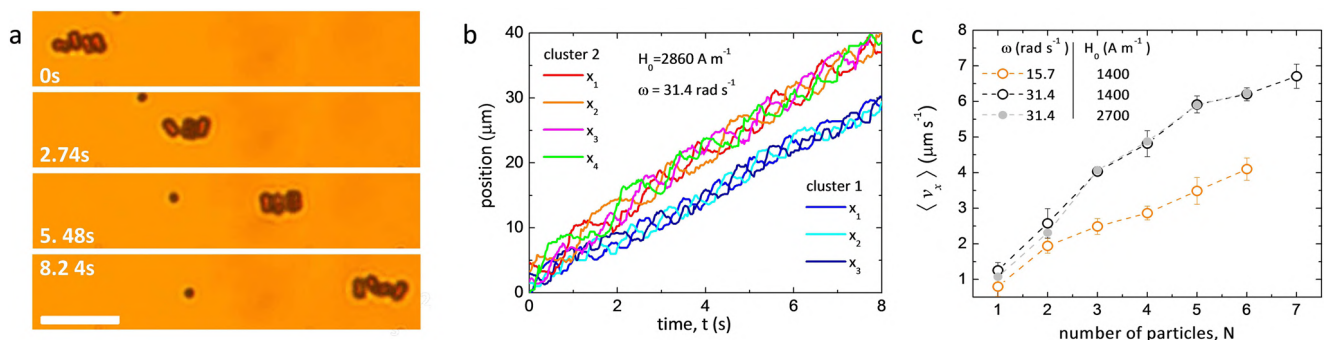


FIG. 5. (a) Sequence of optical microscopy images illustrating the transport of a cluster formed by 4 hematite rotors that move toward the right. The scale bar at the bottom is $10 \mu\text{m}$. (b) Position $\langle \hat{x} \rangle$ vs time of two clusters composed by 3 (cluster 1) and 4 [cluster 2, image (a)] particles propelling toward the right. (c) Average speed $\langle v_x \rangle$ vs number of particles N of a propelling cluster for two different driving frequencies and field amplitudes. The error bars are obtained from the statistical average of different experiments.

here, we find that increasing the number of particles, the leap-frog extends along the \hat{x} direction, thus parallel to the plate, rather than forming tumbling columns perpendicular to it. This situation is illustrated in Fig. 5(a), where a cluster composed by 4 hematite rotors translates toward the right at an average speed of $\langle v_x \rangle = 5 \mu\text{m s}^{-1}$. During propulsion, particles forming the chain are expelled from it to the top, roll on top of the chain, and re-attach at the front of it creating the pair of propelling leap-frog states. This process can be appreciated by tracking the position of the individual particles within smaller clusters, as shown in Fig. 5(b) for two particular cases. If we consider “cluster 2” composed by 4 particles, the positions of each particle periodically alternate with short and long periods where the slope, and thus the velocity, changes or it remains constant, respectively. This indicates that the particles approach the edges of the cluster and slow down, while when they slide above the other 3 particles, they display a constant speed. This process becomes more evident for longer clusters containing more than 6 particles. However, we find that these structures are more difficult to track due to the continuous particle overlapping that impedes the identification of the single elements within a cluster. The average speed along the propulsion direction for different number of particles N is shown in Fig. 5(b). Here, we measure the average speed of the center of symmetry of the cluster that approximately coincides with the center of velocity. We find that larger clusters propel faster until reaching a saturation value for $N \sim 7$. The general trend is similar to that reported for paramagnetic colloids assembled into two-dimensional carpets, where the speed rapidly increases at the beginning and then it saturates at a large value of N . We have explained this behavior in terms of the hydrodynamic coupling among the colloids. Generically, beyond a characteristic length of the chain, the hematite rotors composing the colloidal structure start to be far away, and the relevance of flow additivity vanishes.

VII. CONCLUSIONS

We have investigated the transport properties of anisotropic hematite colloidal rotors that are driven in a viscous fluid via an external rotating magnetic field. We find that close propelling rotors

assemble into rotating clusters performing a leap-frog type dynamics. The clusters display an enhancement of their average speed which arises from the hydrodynamic coupling between the pair. We explain the propulsion using the far field approximation by extending Blake’s tensor formalism to our system.²⁸ We further investigate the role of shape on the dynamics of the pair by comparing numerical simulations of single spheres with dumbbells. We find that while both types of rotors display the leap-frog state, the orientational degrees of freedom of the dumbbells make such a state more unstable.

Our colloidal rollers require a confined geometry to propel and thus could be implemented in microfluidic environments in order to trap, control, and transport micro-objects in a fluid medium. Indeed, previous experimental studies based on paramagnetic colloids,³⁴ hematite-polystyrene composite,³⁵ and ellipsoidal particles³⁶ showed promises in this direction. In our particular case, one could use the pair of rotors to transport a biological cargo entrapped in their vortical flow and then release it by simply varying the frequency of the applied field that allows to tune the lifetime of the leap-frog state. From a more fundamental perspective, our work invites further investigations related to the role of hydrodynamic interactions in synchronization phenomena between emerging suspensions of actuated magnetic colloids.

ACKNOWLEDGMENTS

H.M.-C. and P.T. acknowledge support from the ERC Grant “DynaMO” (No. 335040). E.N.A. and I.P. acknowledge support from MINECO (Grant No. FIS2015-67837-P) and DURSI (Grant No. 2014SGR-922). P.T. acknowledges support from MINECO (Grant Nos. FIS2016-78507-C2-2-P and ERC2018-092827), DURSI (2017SGR1061), and Generalitat de Catalunya under program “Icrea Academia.”

APPENDIX: DETAILS ON THE THEORETICAL MODEL

For two particles of radius a_i located at positions (x_i, y_i, h_i) with an angular velocity $\vec{\Omega}_i = \Omega_i \hat{y}$, the velocities at which they will displace are given by

$$\left\{ \begin{array}{l} v_{x,1} = \frac{\Omega_1 a_1^5}{8h_1^4} + \Omega_2 a_2^3 \left(6h_1 \frac{(x_1 - x_2)^2}{(\Delta^2 + (h_1 + h_2)^2)^{5/2}} + \frac{h_1 - h_2}{(\Delta^2 + (h_1 - h_2)^2)^{3/2}} + \frac{h_2 - h_1}{(\Delta^2 + (h_1 + h_2)^2)^{3/2}} \right), \\ v_{x,2} = \frac{\Omega_2 a_2^5}{8h_2^4} + \Omega_1 a_1^3 \left(6h_2 \frac{(x_1 - x_2)^2}{(\Delta^2 + (h_1 + h_2)^2)^{5/2}} + \frac{h_2 - h_1}{(\Delta^2 + (h_1 - h_2)^2)^{3/2}} + \frac{h_1 - h_2}{(\Delta^2 + (h_1 + h_2)^2)^{3/2}} \right), \\ v_{y,1} = 6h_1 \Omega_2 a_2^3 \frac{(x_2 - x_1)(y_2 - y_1)}{(\Delta^2 + (h_1 + h_2)^2)^{5/2}}, \\ v_{y,2} = 6h_2 \Omega_1 a_1^3 \frac{(x_2 - x_1)(y_2 - y_1)}{(\Delta^2 + (h_1 + h_2)^2)^{5/2}}, \\ v_{z,1} = \Omega_2 a_2^3 \left(\frac{x_2 - x_1}{(\Delta^2 + (h_1 - h_2)^2)^{3/2}} + \frac{x_1 - x_2}{(\Delta^2 + (h_1 + h_2)^2)^{3/2}} + 6h_1 \frac{(x_1 - x_2)(h_1 + h_2)}{(\Delta^2 + (h_1 + h_2)^2)^{5/2}} \right), \\ v_{z,2} = \Omega_1 a_1^3 \left(\frac{x_1 - x_2}{(\Delta^2 + (h_1 - h_2)^2)^{3/2}} + \frac{x_2 - x_1}{(\Delta^2 + (h_1 + h_2)^2)^{3/2}} + 6h_2 \frac{(x_2 - x_1)(h_1 + h_2)}{(\Delta^2 + (h_1 + h_2)^2)^{5/2}} \right), \end{array} \right. \quad (\text{A1})$$

with $\Delta^2 \equiv (x_2 - x_1)^2 + (y_2 - y_1)^2$.

REFERENCES

- ¹M. C. Marchetti, J. F. Joanny, S. Ramaswamy, T. B. Liverpool, J. Prost, M. Rao, and R. A. Simha, *Rev. Mod. Phys.* **85**, 1143 (2013).
- ²C. Bechinger, R. D. Leonardo, H. Löwen, C. Reichhardt, G. Volpe, and G. Volpe, *Rev. Mod. Phys.* **88**, 045006 (2016).
- ³K. Han, W. C. S. IV, and O. D. Velev, *Adv. Funct. Mater.* **28**, 1705953 (2018).
- ⁴P. Tierno, R. Golestanian, I. Pagonabarraga, and F. Sagués, *J. Phys. Chem. B* **112**, 16525 (2008).
- ⁵J. Burdick, R. Laocharoensuk, P. M. Wheat, J. D. Posner, and J. Wang, *J. Am. Chem. Soc.* **130**, 8164 (2008).
- ⁶L. Baraban, D. Makarov, R. Streubel, I. Mönch, D. Grimm, S. Sanchez, and O. G. Schmidt, *ACS Nano* **6**, 3383 (2012).
- ⁷S. Guo, Q. Pan, and M. B. Khamesee, *Microsyst. Technol.* **14**, 307 (2008).
- ⁸B. J. Nelson, I. K. Kaliakatsos, and J. J. Abbott, *Annu. Rev. Biomed. Eng.* **12**, 55 (2010).
- ⁹R. Dreyfus, J. Baudry, M. L. Roper, M. Fermigier, H. A. Stone, and J. Bibette, *Nature* **437**, 862 (2005).
- ¹⁰A. Snezhko and I. S. Aranson, *Nat. Mater.* **10**, 698 (2011).
- ¹¹T. Petit, L. Zhang, K. E. Peyer, B. E. Kratochvil, and B. J. Nelson, *Nano Lett.* **12**, 156 (2012).
- ¹²J. Palacci, S. Sacanna, A. P. Steinberg, D. J. Pine, and P. M. Chaikin, *Science* **339**, 936 (2013).
- ¹³F. Martinez-Pedrero and P. Tierno, *Phys. Rev. Appl.* **3**, 051003 (2015).
- ¹⁴F. Martinez-Pedrero, A. Ortiz-Ambriz, I. Pagonabarraga, and P. Tierno, *Phys. Rev. Lett.* **115**, 138301 (2015).
- ¹⁵H. Massana-Cid, F. Martinez-Pedrero, E. Navarro-Argemí, I. Pagonabarraga, and P. Tierno, *New J. Phys.* **19**, 103031 (2017).
- ¹⁶F. Peruani, A. Deutsch, and M. Bär, *Phys. Rev. E* **74**, 030904 (2006).
- ¹⁷I. Buttinoni, J. Bialké, F. K. ümmel, H. Löwen, C. Bechinger, and T. Speck, *Phys. Rev. Lett.* **110**, 238301 (2013).
- ¹⁸J. Stenhammar, D. Marenduzzo, R. J. Allen, and M. E. Cates, *Soft Matter* **10**, 1489 (2014).
- ¹⁹A. Zöttl and H. Stark, *Phys. Rev. Lett.* **112**, 118101 (2014).
- ²⁰J. Elgeti, R. G. Winkler, and G. Gompper, *Rep. Prog. Phys.* **78**, 056601 (2015).
- ²¹N. Yoshinaga and T. B. Liverpool, *Phys. Rev. E* **96**, 020603 (2017).
- ²²F. Ginot, I. Theurkauff, F. Detcheverry, C. Ybert, and C. Cottin-Bizonne, *Nat. Commun.* **9**, 696 (2018).
- ²³H. Massana-Cid, J. Codina, I. Pagonabarraga, and P. Tierno, *Proc. Natl. Acad. Sci. U. S. A.* **115**, 10618 (2018).
- ²⁴F. Martinez-Pedrero, E. Navarro-Argemí, A. Ortiz-Ambriz, I. Pagonabarraga, and P. Tierno, *Sci. Adv.* **4**, eaap9379 (2018).
- ²⁵S. H. Lee and C. M. Liddell, *Small* **5**, 1957 (2009).
- ²⁶J. C. Crocker and D. G. Grier, *J. Colloid Interface Sci.* **179**, 298 (1996).
- ²⁷F. Martinez-Pedrero, H. Massana-Cid, and P. Tierno, *Small* **13**, 1603449 (2017).
- ²⁸J. R. Blake and A. T. Chwang, *J. Eng. Math.* **8**, 23 (1974).
- ²⁹P. Tierno, *Phys. Chem. Chem. Phys.* **16**, 23515 (2014).
- ³⁰H. Morimoto, T. Ukai, Y. Nagaoka, N. Grobert, and T. Maekawa, *Phys. Rev. E* **78**, 021403 (2008).
- ³¹C. E. S. L. Schmid, M. F. Schneider, T. Franke, and A. Alexander-Katz, *Proc. Natl. Acad. Sci. U.S.A.* **107**, 535 (2010).
- ³²T. O. Tasci, P. S. Herson, K. B. Neeves, and D. W. M. Marr, *Nat. Commun.* **7**, 10225 (2016).
- ³³F. J. Maier, T. Lachner, A. Vilfan, T. O. Tasci, K. B. Neeves, D. W. M. Marr, and T. M. Fischer, *Soft matter* **12**, 9314 (2016).
- ³⁴T. Yang, T. O. Tasci, K. B. Neeves, and D. W. M. Marr, *Langmuir* **33**, 5932 (2017).
- ³⁵M. Driscoll, B. Delmotte, M. Youssef, S. Sacanna, A. Donev, and P. Chaikin, *Nat. Phys.* **13**, 375 (2017).
- ³⁶F. Martinez-Pedrero, A. Cebers, and P. Tierno, *Phys. Rev. Appl.* **6**, 034002 (2016).
- ³⁷A. Bricard, J.-B. Caussin, N. Desreumaux, O. Dauchot, and D. Bartolo, *Nature* **503**, 95 (2013).
- ³⁸J. Yan, M. Han, J. Zhang, E. Luijten, and S. Granick, *Nat. Mater.* **15**, 1095 (2016).
- ³⁹F. Martinez-Pedrero, A. Cebers, and P. Tierno, *Soft Matter* **12**, 3688 (2016).

PUBLICATION 4

Tunable self-healing of magnetically propelling colloidal carpets

Nature Communications **10**, 2444 (2019)

Helena Massana-Cid^{1,7}, Fanlong Meng^{2,3,7}, Daiki Matsunaga^{3,4},
Ramin Golestanian^{2,3} and Pietro Tierno^{1,5,6}

¹ Departament de Física de la Matèria Condensada,
Universitat de Barcelona, 08028 Barcelona, Spain

² Max Planck Institute for Dynamics and Self-Organization
(MPIDS), 37077 Göttingen, Germany

³ Rudolf Peierls Centre for Theoretical Physics,
University of Oxford, Oxford OX13PU, UK

⁴ Division of Bioengineering, Graduate School of Engineering
Science, Osaka University, 5608531 Osaka, Japan

⁵ Institut de Nanociència i Nanotecnologia, IN²UB,
Universitat de Barcelona, 08028 Barcelona, Spain

⁶ Universitat de Barcelona Institute of Complex Systems
(UBICS), Universitat de Barcelona, 08028 Barcelona, Spain

⁷ These authors contributed equally

ARTICLE

<https://doi.org/10.1038/s41467-019-10255-4>

OPEN

Tunable self-healing of magnetically propelling colloidal carpets

Helena Massana-Cid^{1,7}, Fanlong Meng^{2,3,7}, Daiki Matsunaga^{3,4}, Ramin Golestanian^{2,3} & Pietro Tierno^{1,5,6}

The process of crystallization is difficult to observe for transported, out-of-equilibrium systems, as the continuous energy injection increases activity and competes with ordering. In emerging fields such as microfluidics and active matter, the formation of long-range order is often frustrated by the presence of hydrodynamics. Here we show that a population of colloidal rollers assembled by magnetic fields into large-scale propelling carpets can form perfect crystalline materials upon suitable balance between magnetism and hydrodynamics. We demonstrate a field-tunable annealing protocol based on a controlled colloidal flow above the carpet that enables complete crystallization after a few seconds of propulsion. The structural transition from a disordered to a crystalline carpet phase is captured via spatial and temporal correlation functions. Our findings unveil a novel pathway to magnetically anneal clusters of propelling particles, bridging driven systems with crystallization and freezing in material science.

¹Departament de Física de la Matèria Condensada, Universitat de Barcelona, 08028 Barcelona, Spain. ²Max Planck Institute for Dynamics and Self-Organization (MPIDS), 37077 Göttingen, Germany. ³Rudolf Peierls Centre for Theoretical Physics, University of Oxford, Oxford OX1 3PU, UK. ⁴Division of Bioengineering, Graduate School of Engineering Science, Osaka University, 5608531 Osaka, Japan. ⁵Institut de Nanociència i Nanotecnologia, Universitat de Barcelona, Barcelona 08028, Spain. ⁶Universitat de Barcelona Institute of Complex Systems (UBICS), Universitat de Barcelona, Barcelona 08028, Spain. ⁷These authors contributed equally: Helena Massana-Cid, Fanlong Meng. Correspondence and requests for materials should be addressed to R. G. (email: ramin.golestanian@ds.mpg.de) or to P.T. (email: ptierno@ub.edu)

In colloidal science, crystalline order is usually obtained from equilibrium self-assembly, when a system spontaneously forms an organized phase due to specific inter-particle interactions. This general phenomenon has proven to be simple, robust, and scalable, all appealing features that make colloidal crystals ideal candidates for photonic band gap materials, optical switches, or sensors. Investigating the assembly process of tunable colloidal systems may also shed light on fundamental mechanisms underlying melting¹ and crystallization², which are general phenomena occurring in a broad range of systems at different length scales³.

Recent trends in the field are now shifting the focus toward structure formation in systems driven out-of-equilibrium by external fields or forces. Examples are widespread and include the assembly induced by external electric^{4,5}, magnetic^{6,7}, optic⁸ fields, or the organization of active particles^{9–13}. However, an important challenge that still remains to be tackled is whether it is possible to realize perfect crystalline lattices starting from a disordered collection of driven particles, where the individual units display a net propulsive dynamics. Such a feature would be important not only for practical means, i.e., to rapidly realize periodic system on the visible wavelength, but it will also provide a starting point for understanding the fundamental mechanisms behind crystal formation in driven or active out-of-equilibrium systems. We also note that a crystallization process induced by a few active dopants in a bath of passive particles has been demonstrated recently in computer simulation studies^{14,15}. Recent experiments with active particles report melting¹⁶, clustering^{10,13}, or interstitial dynamics¹⁷ but not annealing.

Here we advance in this field by demonstrating a novel field-induced annealing process where an ensemble of propelling particles is able to rapidly form a crystalline lattice upon magnetic command. In particular, we study the dynamics of magnetic colloidal rotors that are assembled into flat, two-dimensional propelling carpets due to external magnetic field modulations. In a previous work¹⁸, we demonstrate that the carpet could be used as an efficient drug-delivery vector for transporting biological cells across its surface. Beyond its technological applications, here we report the discovery that such carpet could be used as a general model system for nonequilibrium crystallization process, by demonstrating a self-healing process that can be controlled by an external magnetic field. We show that by increasing the field amplitude the carpet displays a tread-milling dynamics, where particles detach from the back of the carpet, travel across the lattice, and reattach at the moving front. The dynamic phases of the system may be understood from the delicate balance between magnetism and hydrodynamics. This regrowth process represents a novel annealing process that enables to rapidly regenerate colloidal structures upon magnetic command.

Results

Assembly and propulsion of colloidal carpets. We assemble the colloidal carpets from a dispersion of paramagnetic colloids having radius $a = 1.4 \mu\text{m}$ and subjected to time-dependent external fields. The particles are initially dispersed in water and two-dimensionally confined above a glass substrate due to the balance between gravity and electrostatic interactions (see Methods). Figure 1a–f illustrate the complete process. To realize a propelling carpet we start to apply a rotating magnetic field circularly polarized in the plane of the substrate (\hat{x}, \hat{y}), $\mathbf{B}_1(t) = B_0[\cos(2\pi ft)\hat{x} - \sin(2\pi ft)\hat{y}]$, where B_0 is the field amplitude and f is its frequency. We use a narrow frequency range $f \in [20, 100]\text{Hz}$, far away from resonance frequency ($\sim 400\text{KHz}$) as reported in the past¹⁹. For sufficiently high frequencies, the rotating field induces attractive dipolar interactions that are isotropic when time-averaged¹⁸. The dipolar interaction between two equal dipoles $\mathbf{m}_{i,j}$ at a distance $\mathbf{r}_{ij} = \mathbf{r}_i - \mathbf{r}_j$ is given by

$$U_m = -\mu_0/4\pi\{[3(\mathbf{m}_i \cdot \mathbf{r}_{ij})(\mathbf{m}_j \cdot \mathbf{r}_{ij})/r^5] - (\mathbf{m}_i \cdot \mathbf{m}_j)/r^3\},$$

and becomes maximally attractive (repulsive) for particles with magnetic moments parallel (normal) to \mathbf{r}_{ij} . Performing a time average of the potential gives an effective attractive interaction in this plane $\langle U_m \rangle = -\mu_0 m^2/[8\pi(x+y)^3]$. Thus, a random dispersion of particles that would otherwise perform simple Brownian motion, is forced to assemble into a compact cluster, as shown in Fig. 1a, b. Under the rotating field, the cluster is also observed to perform a spinning motion around its center, since the rotating field applies a magnetic torque, $\mathbf{T}_m \sim B_0^2$, due to the finite internal relaxation time of the particle, see Methods. Once the cluster is formed, propulsion of the carpet is obtained with the following strategy. The rotating in-plane field is transformed in a more complex modulation composed by a field that rotates in the (\hat{x}, \hat{z}) plane plus an oscillating component along the \hat{y} direction with a different frequency f_y . The full expression is given as $\mathbf{B}_2(t) = B_0[\cos(2\pi ft)\hat{x} + \sin(2\pi f_y t)\hat{y} - (B_z/B_0)\sin(2\pi ft)]$, where $f_y = f/2$ (see Fig. 1b, c). The rotating field in the perpendicular plane, (\hat{x}, \hat{z}), is used to induce a magnetic torque on the individual particles, which now rotate close to the glass substrate. As the particles are hydrodynamically coupled to the plane²⁰, this rotational motion is converted into a net translational one. As a consequence, all the cluster elements are now a collection of microscopic rotors that make the whole carpet translating at a constant average speed as shown in Fig. 1e, f (see also Supplementary Movie 1 in the Supplementary Information). On the other hand, the carpet is kept stable by the oscillating component B_y that avoids lateral separation of the rotors due to attractive dipolar interactions.

The carpet speed v_c can be varied mainly by changing the field amplitude B_0 or the number of rotors N . In the latter case it becomes constant above $N \sim 300$, which corresponds to a carpet area $S \sim 1800 \mu\text{m}^2$. Although a previous work¹⁸ analyzed the dependence of v_c on N , here we focus on much larger carpets ($N \geq 1000$ particles) and use only B_0 to tune v_c . Moreover, previously the amplitude of the perpendicular field B_z was always kept below a threshold value, in order to stabilize the structure confined in two dimensions¹⁸. In contrast, here we show a series of remarkable new phenomena that emerge when the propelling carpet is forced to extend toward the third dimension by raising B_z . We also find that, for a certain range of field amplitudes close to the transition region in Fig. 1g, our method allows the relative motion of two lattice planes of colloidal particles. This phenomenon could offer new possibilities in the study of frictional effects at the microscale in the presence of hydrodynamic lubrication.

In Fig. 1g we show the different dynamic states observed in the (B_0, B_z) space, where stable carpets with defects (vacancies) are found at low perpendicular field B_z (“2D carpet”). Increasing B_z forces the carpet to fold into a membrane in the third dimension. However, competition with gravity breaks the monolayer into a series of separate, rolling chains (“broken carpet”), see also Supplementary Movie 2 and Supplementary Movie 3 in the Supplementary Information. Between both dynamic states, we found a stationary phase where particles are transported above the carpet, while the entire structure continues to propel close to the plane (“tread-milling”). We explain the different dynamic phases observed in Fig. 1g by considering the balance between magnetic and hydrodynamic interactions. For a pair of paramagnetic particles located at a distance \mathbf{r} , the dipole–dipole interaction averaged over one period of the rotating field is given by

$$\langle U_m \rangle = \frac{(V\chi B_0)^2}{4\pi\mu_0 r^3} \left[1 - \frac{B_z^2}{B_0^2} - \frac{3}{2} \left(1 - \frac{B_z^2}{B_0^2} \right) \sin^2\theta \right], \quad (1)$$

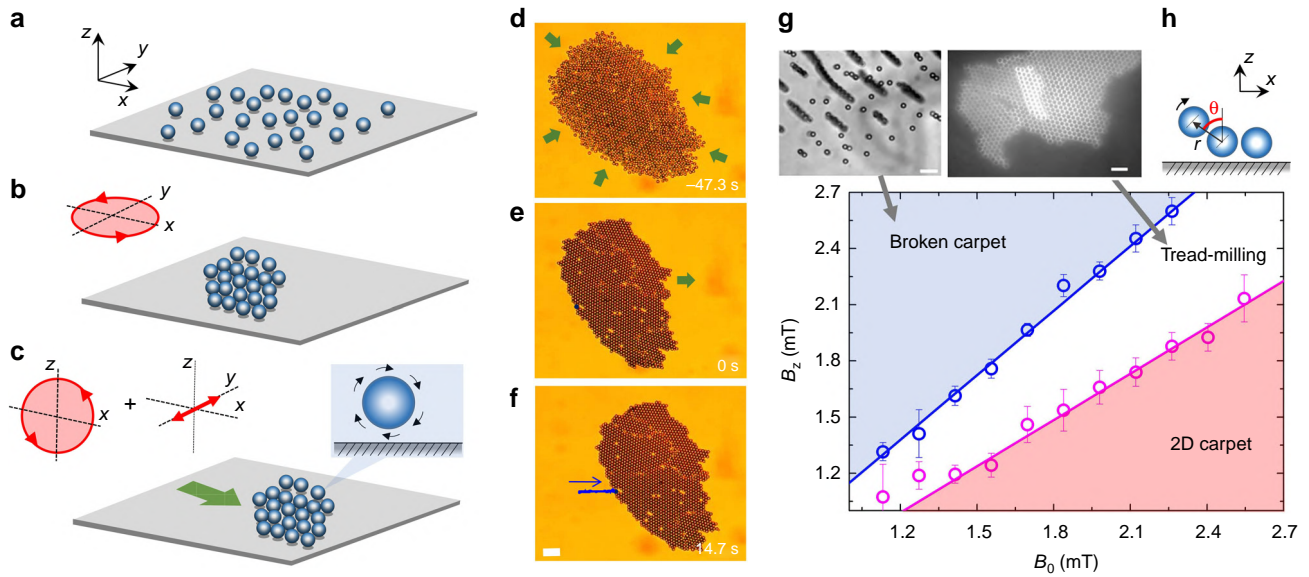


Fig. 1 Realization of a propelling carpet and out-of-equilibrium phase diagram. **a–c** Sequence of schematics showing the formation of a carpet due to a rotating field in the plane (\hat{x}, \hat{y}) (**a, b**) and its propulsion induced by a field rotating in the perpendicular plane (\hat{x}, \hat{z}) plus an oscillating component along the \hat{y} direction (**b, c**). **d–f** Corresponding optical microscope images of a carpet assembled by a rotating field with amplitude $B_0 = 1.6$ mT and frequency $f = 40$ Hz (**d, e**), and transported by a field \mathbf{B}_2 with amplitudes $B_0, B_z = 1.7$ mT, and frequencies $f_x = f_z = f, f_y = f/2$ (**e, f**). In image **f**, the trajectory of one particle is superimposed. Scale bar is 20 μm , see Supplementary Movie 1 in the Supplementary Information. **g** Diagram showing the different assembled structure observed in the (B_0, B_z) plane. The pink region denotes stable propelling structures (“2D carpet”), whereas the white region refers to the situation where the paramagnetic colloids flow above the monolayer (“tread-milling”). The blue region indicates the formation of three-dimensional structures (“broken carpet”). Scattered points are experimental data and continuous lines result from linear stability analysis as described in the text. Error bars are obtained from the statistical average of different experiments. **h** Schematic illustrating the definition of the angle θ and position vector \mathbf{r} . Videos illustrating the tread-milling motion and formation of broken carpets (Supplementary Movie 2 and Supplementary Movie 3) are in the Supplementary Information. Scale bars of the experimental images at the top are 20 μm

where $V = (4/3)\pi a^3$, $\chi = 0.4$ is the magnetic volume susceptibility and $\mu_0 = 4\pi \times 10^{-7}$ Hm. We then assume that the hydrodynamic interactions between the two particles can be cast in terms of an effective energy potential given by

$$U_h = 3\pi\eta a^3 \omega_c \theta, \quad (2)$$

where η the solvent viscosity (water), θ is the angle between the two particles (see Fig. 1h). Here $\omega_c = B_0 B_z \chi \tau_r \omega [6\eta\mu_0(1 + \tau_r^2 \omega^2)] \hat{y}$ is the particle angular velocity, which is in general lower than the driving one, $\omega = 2\pi f$, and τ_r is the magnetic relaxation time of the paramagnetic colloids (see Methods). By combining the contributions from the magnetic dipole–dipole interaction and hydrodynamics, the effective total energy of the colloid that is located at the edge becomes $U_{\text{tot}} = U_m + U_h$. This leads to the dynamic equation for the angle θ as

$$\dot{\theta} = -\frac{1}{4\zeta a^2} \frac{\partial U_{\text{tot}}}{\partial \theta}, \quad (3)$$

where ζ is the friction coefficient, see Methods for a detailed derivation.

From Eq. (3), the condition for obtaining a stable θ is given by:

$$|\sin 2\theta| = \left| \frac{6B_0 B_z}{\chi(B_0^2 - B_z^2)} \frac{\tau_r \omega}{(1 + \tau_r^2 \omega^2)} \right| \leq 1. \quad (4)$$

Equation (4) allows us to understand how the particle behavior changes at the rear edge of the carpet by varying the ratio of field amplitudes, B_z^2/B_0^2 . (1) For small B_z^2/B_0^2 , there is a stable solution $\theta \sim \pi/2$ corresponding to a structure where the colloid at the rear edge tends to lie in the (\hat{x}, \hat{y}) plane; (2) for moderate values of B_z^2/B_0^2 , there is no stable solution of θ and then the

colloid at the rear edge of the carpet is transported toward the front edge (“tread-milling”); (3) for large B_z^2/B_0^2 , there is a solution $\theta \sim 0$ and the colloid at the rear edge “stands up,” giving rise to a structure in the (\hat{y}, \hat{z}) plane (“Broken carpet”). As shown in Fig. 1g, we find that the developed model is in excellent agreement with the experimental data with the following conditions: $B_z/B_0 < 0.84$ for carpet confined in the (\hat{x}, \hat{y}) plane, and $B_z/B_0 > 1.19$ for a disk in (\hat{y}, \hat{z}) plane. The fit to the data are obtained by using as sole adjustable parameter the relaxation time $\tau_r \simeq 10^{-4}$ s, which is in agreement with the value found in separate experiments¹⁸.

Discussion

We next explore in more details the tread-milling phase and how it induces a regeneration of the propelling carpet. By increasing the amplitude of B_z , the particles are forced to detach from the back of the carpet and are transported above the surface by the hydrodynamic flow field. The detached particles move faster than the underlying monolayer, but do not leave the structure when they reach the end, as they remain strongly attracted there by dipolar interactions. Due to this attraction, the particles follow one of the crystallographic axes of the underlying lattice during transport. As shown in Fig. 2a, b, three different situations can be observed, illustrated also in Supplementary Movie 4 in the Supplementary Information. The particles can be adsorbed in the monolayer by filling vacancies that encounter during their excursion, they can change direction when they reach a grain boundary that merges domains with different crystalline orientations, or they can reach the moving front and reattach there. In the latter case, the particles form a growing interface that replicates the carpet wedge and shows no defect or vacancies. This

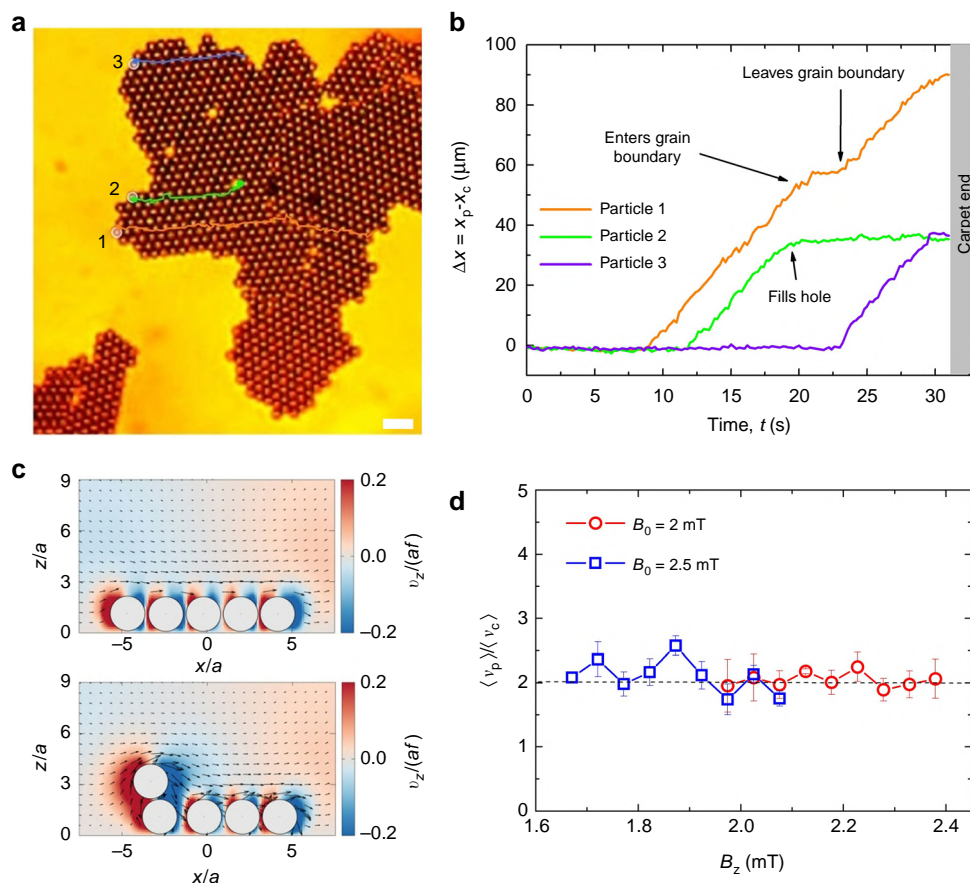


Fig. 2 Tread-milling dynamics: particle flow and speed. **a** Optical microscope image of a traveling carpet with the superimposed trajectories of three particles illustrating the different situations encountered. The carpet translates under the action of a dynamic field with amplitudes $B_0 = 2$ mT, $B_z = 2$ mT, and frequency $f = 40$ Hz. The scale bar is $20 \mu\text{m}$; see Supplementary Movie 4 in the Supplementary Information. **b** Relative distance, $x_p - x_c$ of the three paramagnetic colloids vs. time. Particle 1 enters and leaves a grain boundary above the carpet changing direction but not speed. Particle 2 fills an hole while particle 3 reaches the carpet edge. **c** Calculated flow field around the rotating colloids using boundary element simulation (see Methods). The vectors show the flow direction, while the color map illustrates the \hat{z} -component of velocity. The image shows the process of detachment of one particle at the back of the carpet. **d** Average particle speed $\langle v_p \rangle$ above the colloidal monolayer normalized to the average carpet velocity $\langle v_c \rangle$. Error bars are obtained from the statistical average of different experiments

process can be also appreciated from Supplementary Movie 2 in the Supplementary Information. Furthermore, we calculate the hydrodynamic flow field generated by the particles using a boundary element simulation technique; see Fig. 2c for the corresponding velocity profile and the Methods section for more details. The moving carpet generates a cooperative chiral flow field, which advects continuously the monolayer of particles in a similar way as a hydrodynamic conveyor belt. Although the flow velocity is small below the carpet given the short distance with the surface, it increases significantly close to the edge of the structure and thus forces particle detachment there. The average speed of the particles traveling above the carpet $\langle v_p \rangle$ is twice the carpet speed $\langle v_c \rangle$ as shown in Fig. 2d. This result, which is consistent with the kinematics of rolling motion, is confirmed in the numerical simulation.

The tread-milling phase generates a net colloidal flow above the carpet allowing to completely rebuild its structure in a relatively short time scale. This occurs as the growing front of the carpet crystallizes in a perfect periodic lattice of colloidal rotors, while it smoothen the edge of the structure. The process is illustrated in Fig. 3a, where an initially disordered structure composed by 1045 particles is propelled at a speed of $\langle v_c \rangle = 5.7 \mu\text{m s}^{-1}$ and after $t = 2$ min it has regrown with a perfect crystalline

order. We analyze this process in terms of bond-orientational correlation function

$$g_6(r_{ij}) = \left\langle \Psi_6^*(r_i) \Psi_6(r_j) \right\rangle, \quad (5)$$

where $\Psi_6(r_j) = \left| \frac{1}{N_b} \sum_{k=1}^{nn} e^{6i\theta_{jk}} \right|$, N_b is the number of neighboring particles k , and θ_{kj} is the angle between a fixed axis and the bond joining particles k and j . The initial disordered state results from the assembly of the carpet due to the rotating field and gives rise to a hexatic structure, with an algebraic decay of $g_6(r) \sim r^{-\eta_6}$ that characterizes quasi-long-range order. Here we find an exponent $\eta_6 \sim 0.3$, which is higher than the threshold value $1/4$ as predicted by the KTNHY theory¹ of melting in two-dimensional (2D) at equilibrium. As time advances, the carpet front recrystallizes and the nominal exponent of the correlation function decreases (to values as small as $\eta_6 \sim 0.1$). In this nonequilibrium situation, all rotors are characterized by six nearest neighbors and long-range order develops.

We then monitor the ability of the monolayer to recrystallize or heal itself by varying the carpet speed v_c via the external field amplitudes B_0 and B_z . As shown in Fig. 3c, in order to keep the carpet within the tread-milling phase, we need to simultaneously vary both amplitudes, which allows us to increase v_c from 2.5 to ~

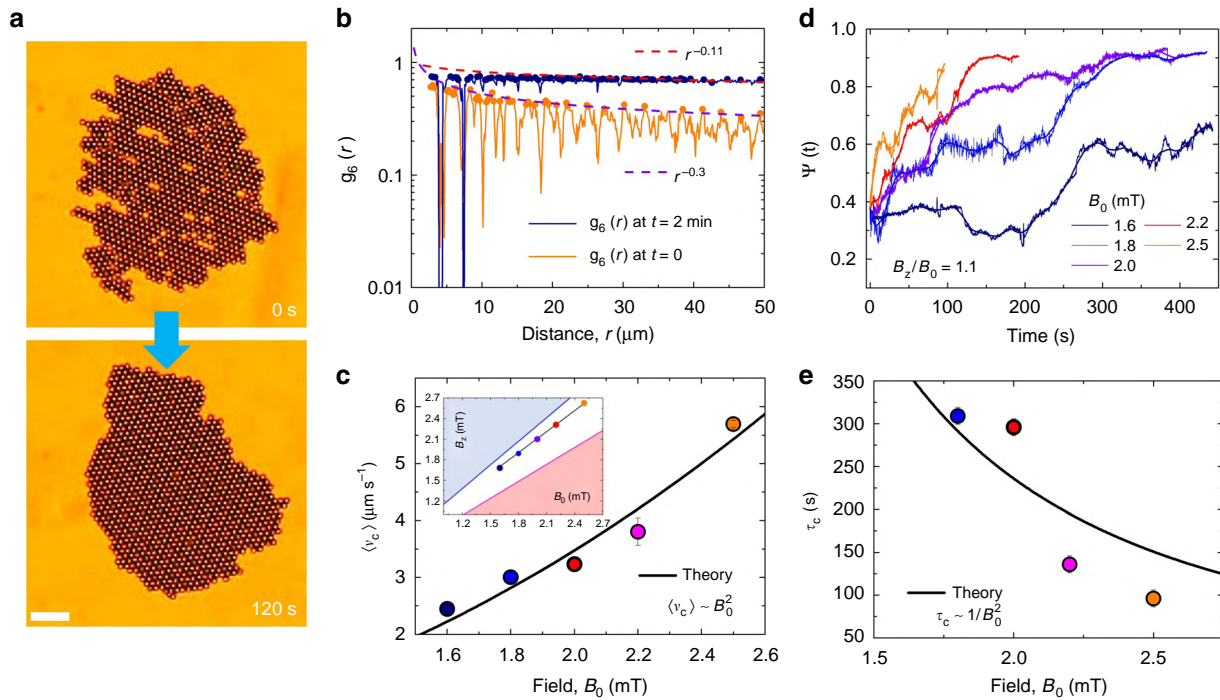


Fig. 3 Annealing of magnetic carpet. **a** Experimental images showing an initial polycrystalline carpet ($t = 0$ s, top) realized with an in-plane rotating field ($B_0 = 2.5$ mT, $f = 40$ Hz), and a monocrystalline carpet obtained after $t = 2$ min of propulsion ($B_0 = 2.5$ mT, $B_z = 2.7$ mT, $f = 40$ Hz). The scale bar is $20 \mu\text{m}$, see Supplementary Movie 5 in the Supplementary Information. **b** Bond-orientational correlation functions $g_6(r)$ of the two carpets with superimposed corresponding peaks as solid disks and fits to an algebraic dependence $g_6(r) \sim r^{-\eta_6}$ as dashed lines. The exponent η_6 can be used to distinguish the crystalline phase ($\eta_6 > 1/4$) from the hexatic one³. **c** Average carpet speed $\langle v_c \rangle$ vs. field amplitude B_0 for different values of B_z . The continuous black line is a fit to the data using Eq. (16), with fixed parameters $l = 3.2 \mu\text{m}$, $\chi = 0.4$, $\omega = 251.3 \text{ rad s}^{-1}$ and $h = 2.6 \mu\text{m}$. The small inset indicates the corresponding location of the experimental points in the diagram in Fig. 1g ($B_0 \sim B_z$ is taken). Error bars are obtained from the statistical average of different experiments. **d** Bond-orientational order parameter $\Psi(t)$ vs. time t for different values of B_0 (thus carpet speed v_c). In the continuous lines in the graph is obtained by averaging the experimental data over a discrete time window. All experiments are conducted for carpets having a similar size of ~ 1000 particles. **e** Annealing time τ_c vs. field amplitude B_0 , with continuous black line is a fit to the data using Eq. (6)

$6 \mu\text{m s}^{-1}$. The carpet speed can be calculated by considering a triangular lattice of surface rotors, with lattice constant l (see Methods section for more details). We can fit the experimental data of Fig. 3c with Eq. (16) using $l \sim 3.2 \mu\text{m}$ with the magnetic relaxation time τ_r as an adjustable parameter. We obtain a value of $\tau_r = 0.3 \times 10^{-4} \text{ s}$ that is consistent with the diagram in Fig. 1g.

The dynamics of the ordering process is then characterized via both the nominal time-dependent exponent η_6 of $g_6(r)$ (see Supplementary Fig. 1 in the Supplementary Information) and the global orientational order parameter averaged over all N particles, $\Psi(t) = \frac{1}{N} \sum_{i=1}^N \Psi_{6,i}$ shown in Fig. 3d. In all cases we find that the increase in the carpet speed boosts the annealing process and allows the carpet to reach the crystalline phase more quickly. We confirm these observations by extracting the annealing time τ_c of the carpet as a function of the applied magnetic field (Fig. 3e). The time to eliminate a single defect in a carpet of area $L_x \times L_y$ can be approximated as $\tau_p \simeq L_y/v_p$, with the tread-milling speed given by $v_p \sim B_0^2 \chi \tau_r \omega a / [6\eta\mu_0(1 + \tau_r^2 \omega^2)]$. For a carpet with N_d defects before annealing, the total annealing time can be approximated as the corresponding annealing time of one colloidal row along the y axis, given by

$$\tau_c = n\tau_p \sim \frac{12N_d L_y \eta \mu_0 (1 + \tau_r^2 \omega^2)}{L_x B_0^2 \chi \tau_r \omega}, \quad (6)$$

where $n = 2N_d a/L_x$ is the number of the defects along one colloidal row. For $L_x \sim L_y$, the annealing time can be simplified as

$\tau_c \sim \frac{12N_d \eta \mu_0 (1 + \tau_r^2 \omega^2)}{B_0^2 \chi \tau_r \omega}$ and can be used to fit the experimental data shown in Fig. 3e.

We also investigate the scalability of the carpet formation (Supplementary Fig. 2 in Supplementary Information), propulsion (Supplementary Fig. 3 in Supplementary Information), and the tread-milling motion (Supplementary Fig. 4 in Supplementary Information). By varying the number of particles in the carpet, we find that the initial self-assembly process could lead to an ordered crystalline structure below $N = 150$ particles, as shown in Supplementary Fig. 2 in the Supplementary Information. Larger carpets assembled by the rotating field display grain boundaries and vacancies that require the tread-milling motion to crystallize. The carpet speed increases with the number of particles, reaching a saturation value above $N \sim 300$ particles, as shown in Supplementary Fig. 3 in the Supplementary Information. Also, we found that the tread-milling behavior can be observed for all the carpet size, and until filling completely the observation area of our experimental system for $N = 4000$ particles (see Supplementary Fig. 4 in Supplementary Information).

In active colloidal systems, increasing particle activity via the propulsion speed leads to an increase in the effective diffusion coefficient or effective temperature of the system, which we might expect to give rise to a reduction of the global order. Here we report exactly the opposite effect: the faster the propelling carpets are, the more rapidly they form ordered structures. Our novel results demonstrate the versatility of our

active magnetic system, as the governing interactions are based on a subtle interplay between hydrodynamics and magnetism

In conclusion, we investigate the collective dynamics of propelling magnetic carpets in a range of field parameters, where the colloidal structures are able to continuously transform into perfect crystalline lattices. The annealing process occurs due to the detachment of individual rotors from the back of the carpet, traveling above the carpet surface following a crystallographic direction, and either filling vacancies or reaching and rejoining the leading edge. We theoretically account for the out-of-equilibrium phase diagram by using a delicate balance between magnetism and hydrodynamics. The mechanism of the motility of our carpets is cooperative and is based on the rectification of the hydrodynamic flow generated by each rotor close to the bounding wall. Moreover, the use of external field allows us to steer and control the colloidal carpet and the corresponding flow of magnetic colloids that dictate the annealing process. From an application point of view, our annealing process could be easily extended to other types of recently engineered microscale particles with heterogeneous and functional properties^{21–23}, or used to entrap, transport, and release non-magnetic particles across the carpet surface¹⁸. All in all, our out-of-equilibrium colloidal model system allows us to investigate crystallization in transported systems and could thus provide deep insight for similar processes occurring in systems at different length and time scales.

Methods

Experimental details. We use paramagnetic colloidal particles (Dynabeads M-270, Invitrogen) with diameter $d = 2.8 \mu\text{m}$, density $\rho = 1.3 \text{ g cm}^{-3}$, and magnetic volume susceptibility $\chi = 0.4$. The particles are coated with surface carboxylic acid group with an active chemical functionality of $150 \mu\text{mol} \times \text{g}^{-1}$ per particle. When dispersed in highly deionized water ($18.2 \text{ M}\Omega \times \text{cm}^{-1}$, MilliQ system), hydrogen ions (H^+) dissociate from such groups, leaving a negative charged surface and inducing the formation of a double layer. The solution containing the particles is introduced by capillarity in a rectangular microtube made of borosilicate glass (inner dimensions $0.1 \times 2.0 \text{ mm}$; CMC Scientific) that is immediately sealed. The particles sediment close to a glass plate, where they remain quasi-2D confined due to gravity, displaying a small thermal motion. The sample is placed in the center of a triaxial coil system arranged on the stage of a light microscope (Eclipse Ni, Nikon). External time-dependent magnetic fields are generated by passing an alternate current through the coils via a waveform generator (TGA1244, TTI) connected to different power amplifiers (AMP-1800, AKIYAMA, and BOP 20-10M, Kepco). The particle position and dynamics are extracted using digital video-microscopy with a charge-coupled device camera (Scout scA640-74fc, Basler) working at 50 frames per second.

Theoretical model. Under a static external magnetic field \mathbf{B} , a paramagnetic colloid of radius a acquires an induced moment $\mathbf{m} = V\chi\mathbf{B}/\mu_0$, where $V = 4\pi a^3/3$ is the particle volume. For a dynamic field, such as the field $\mathbf{B}_1(t)$ rotating in the (\hat{x}, \hat{z}) plane, the paramagnetic colloid experiences a finite magnetic torque²⁴

$$\mathbf{T}_c = \frac{B_0 B_z V \chi \tau_r \omega}{\mu_0 (1 + \tau_r^2 \omega^2)} \hat{y} \quad (7)$$

when the angular frequency of the magnetic field, $\omega = 2\pi f$, is comparable with the inverse of the magnetization relaxation time, $\omega \tau_r \sim 1$. Here, $\tau_r \sim 10^{-4} \text{ s}$ for our paramagnetic colloids¹⁸. Thus, a colloidal particle suspended in a fluid of viscosity η will rotate with angular velocity $\omega_c < \omega$. The hydrodynamic interaction with the substrate induces a translational motion of the particle with velocity $\mathbf{v} \sim \omega_c a$. In the case of translating carpet, the induced moment for the individual colloid is given by,

$$\mathbf{m} = \frac{4}{3\mu_0} \pi a^3 \chi B_0 \left(\cos \omega t, \sin \omega t, -\frac{B_z}{B_0} \sin \omega t \right). \quad (8)$$

The energy due to the magnetic dipole–dipole interaction among the magnetized colloids is:

$$U_m = - \sum_{i,j \neq i} \frac{\mu_0 \left[3(\mathbf{m}_i \cdot \mathbf{r}_{ij})(\mathbf{m}_j \cdot \mathbf{r}_{ij}) - \mathbf{m}_i \cdot \mathbf{m}_j r_{ij}^2 \right]}{4\pi r_{ij}^5}, \quad (9)$$

where \mathbf{r}_{ij} denotes the vector pointing from the i^{th} colloid to the j^{th} one. Due to the employed field strength, we will consider these interactions only at the level of

nearest neighbors. For two close particles as depicted in Fig. 1h, the magnetic dipole–dipole interaction averaged over one period of the rotating magnetic field can be explicitly expressed by Eq. (1), with the vector pointing from one colloid to the other as,

$$\mathbf{r} = r(\sin \theta \cos \phi, \sin \theta \sin \phi, \cos \theta), \quad r \approx 2a. \quad (10)$$

Note that when $B_z \ll B_0$, the averaged magnetic dipole–dipole interaction is attractive in the (\hat{x}, \hat{y}) plane and the particles will form a carpet.

The flow field that the colloids at the edges experience can be approximately by a two-colloid model. Let us denote the colloid at the rear edge as colloid 1 and its nearest neighbor in \hat{x} direction as colloid 2. The rotating colloid 2 induces a flow field around it, which can be approximated by a rotlet. In this case, the flow velocity that colloid 1 (edge colloid) experiences is approximately:

$$\mathbf{v} = \frac{\mathbf{T} \times \mathbf{r}}{8\pi\eta r^3} = \frac{a\omega_c \times \hat{r}}{4} \quad (11)$$

where the distance between the colloids is taken as $r \approx 2a$. As a result, colloid 2 will rotate around 1. Or effectively, it can be considered that there is an effective torque acting on colloid 2 by the rotating colloid 1,

$$\mathbf{T}_h = 3\pi\eta a^3 \omega_c = \frac{\pi a^3 B_0 B_z \chi \tau_r \omega}{2\mu_0 (1 + \tau_r^2 \omega^2)} \hat{y}. \quad (12)$$

We thus write an effective hydrodynamic potential as, $U_h = T_h \theta$ that gives rise to the total potential $U_{\text{tot}} = U_m + U_h$. The dynamic equation in terms of the orientation of the colloid, i.e., Eq. (3) can be expressed as:

$$\dot{\theta} = \frac{1}{4\zeta a^2} \frac{3(V\chi B_0)^2}{64\mu_0 \pi a^3} \left(1 - \frac{B_z^2}{B_0^2} \right) \sin 2\theta - \frac{1}{4\zeta a^2} \frac{\pi a^3 B_0 B_z \chi \tau_r \omega}{2\mu_0 (1 + \tau_r^2 \omega^2)}. \quad (13)$$

Thus, the conditions for obtaining stable θ become:

$$\frac{B_z}{B_0} \leq \frac{-c + \sqrt{c^2 + 4}}{2}, \quad (14)$$

$$\frac{B_z}{B_0} \geq \frac{c + \sqrt{c^2 + 4}}{2}, \quad c = 6\tau_r \omega / [\chi(1 + \tau_r^2 \omega^2)] \quad (15)$$

or alternatively Eq. (4) in the manuscript.

Carpet speed. Here we calculate the mean speed of a carpet composed by a triangular lattice of rotating paramagnetic colloids. An individual particle close to a surface and subjected to a magnetic torque $T_c \mathbf{e}_x$ acquires a propulsion speed $\mathbf{v}_0 = \frac{T_c a^2}{32\pi\eta h} \mathbf{e}_y$, where a is the radius of the particle and h its elevation from the surface. We consider the hydrodynamic interactions of the particle in presence of the surface and extend the calculations in ref. 25 to a 2D triangular lattice. If we consider that the rotating particles form a triangular lattice with lattice constant l , the particle position can be denoted by: $l(i\mathbf{u} + j\mathbf{v})$, $-N \leq i, j \leq N$, where $\mathbf{u} = (1, 0)$ and $\mathbf{v} = (1/2, \sqrt{3}/2)$ are the base unit vectors of the lattice. By treating each rotating colloid as a rotlet, the velocity of the colloid at the lattice center $(0, 0)$ is given by:

$$\mathbf{v} = \mathbf{v}_0 + \sum_{i=-N}^N \sum_{j=-N}^N \left(\frac{a}{h} \right)^{-2} \frac{3\varepsilon^2 (i+j/2)^2}{\{1 + [(i+j/2)^2 + (\sqrt{3}j/2)^2]^{3/2}\}} \mathbf{v}_0 \quad (16)$$

$$\approx T_c \left(\frac{a^2}{32\pi\eta h} + \frac{1}{4\eta l} \right) \mathbf{e}_y.$$

where $\varepsilon = \delta/2h$ with δ being the center-to-center separation between consecutive colloids in the array.

Boundary element simulation. We describe the flow field \mathbf{v} at a given point \mathbf{x} using a boundary integral formulation²⁶, which is a surface integral on the particle surface as

$$\mathbf{v}_i(\mathbf{x}) = -\frac{1}{8\pi\eta} \sum_m \int_{A_m} \mathbf{G}_{ij}(\mathbf{x}, \mathbf{y}) q_j(\mathbf{y}) dA \quad (17)$$

where \mathbf{G} is the Blake tensor²⁷, A_m is the surface of m -th particle, and \mathbf{q} is the viscous traction acting at a point \mathbf{y} on the surface. Integrating the traction force \mathbf{q} over a sphere surface gives the hydrodynamic force \mathbf{F}_h and torque \mathbf{T}_h acting on the particle. As each particle is in force- and torque-free conditions, these satisfy

$$\mathbf{F}_h + \mathbf{F}_m = \int_{A_m} \mathbf{q} dA + \mathbf{F}_m = \mathbf{0}, \quad (18)$$

$$\mathbf{T}_h + \mathbf{T}_m = \int_{A_m} \{\mathbf{q} \times (\mathbf{x} - \mathbf{x}_0)\} dA + \mathbf{T}_m = \mathbf{0} \quad (19)$$

where \mathbf{x}_0 is the hydrodynamic center of the particle, and \mathbf{F}_m and \mathbf{T}_m are external force and torque acting on m -th particle, respectively. The motion of the particles are described by 6 degrees of freedom: i.e., three translational velocities

$\mathbf{U} = (U_x, U_y, U_z)$ and three rotational velocities $\boldsymbol{\Omega} = (\omega_x, \omega_y, \omega_z)$. Therefore, as the boundary condition, a given surface material point \mathbf{x}_s on the particle moves with a velocity

$$\mathbf{v}(\mathbf{x}_s) = \mathbf{U} + \boldsymbol{\Omega} \times (\mathbf{x}_s - \mathbf{x}_0). \quad (20)$$

The surface of each sphere is divided into $N_E = 512$ triangular elements and $N_N = 258$ nodes. According to Eqs. (17) and (20), the i -th node \mathbf{x}_i on the particle surface has to satisfy a boundary condition

$$\mathbf{U} + \boldsymbol{\Omega} \times (\mathbf{x}_i - \mathbf{x}_0) + \frac{1}{8\pi\eta} \sum_m \left\{ \sum_e^{N_E} \mathbf{G}(\mathbf{x}_i, \mathbf{y}_e) \mathbf{q}(\mathbf{y}_e) \Delta A_e \right\} = \mathbf{0} \quad (21)$$

where ΔA is the surface area of the element, subscript e is the index of elements, and \mathbf{y}_e is the position of the element e . The force- and torque-free conditions (18), (19) can be discretized as

$$\sum_e^{N_E} \mathbf{q}(\mathbf{x}_e) \Delta A_e = -\mathbf{F}_m, \quad (22)$$

$$\sum_e^{N_E} \{ \mathbf{q}(\mathbf{x}_e) \times (\mathbf{x}_e - \mathbf{x}_0) \} \Delta A_e = -\mathbf{T}_m. \quad (23)$$

Note that four-point Gaussian quadrature is used to calculate the surface integral over each element. For singular elements, we work in polar coordinates to remove the $1/r$ singularity²⁸.

The external magnetic field is imposed in xz -plane, $\mathbf{B}^{ex}(t) = (B \cos(2\pi ft), 0, -B \sin(2\pi ft))$, and the torque acting on each particle can be obtained as

$$\mathbf{T}_m = \mathbf{m} \times \{ \mathbf{B}^{ex} + \mathbf{B}_m^{dd} \} \quad (24)$$

where \mathbf{B}^{dd} is the magnetic field that is created by other particle:

$$\mathbf{B}_m^{dd} = \sum_{j \neq m} \frac{\mu_0}{4\pi r^3} \{ 3(\mathbf{m}_j \cdot \mathbf{n})\mathbf{n} - \mathbf{m}_j \} \quad (25)$$

where μ_0 is the vacuum permeability, r is the particle distance, and \mathbf{n} is the normal vector pointing from particle m to j . We have three components for the external force: the gravitational force \mathbf{F}_m^g , the magnetic dipolar force \mathbf{F}_m^{dd} , and the repulsive force \mathbf{F}_m^{rep} , as follows

$$\mathbf{F}_m^g = -\frac{4}{3}\pi a^3 \Delta \rho g \hat{\mathbf{z}}, \quad (26)$$

$$\mathbf{F}_m^{dd} = \sum_{j \neq m} \frac{3\mu_0}{4\pi r^4} \{ 5(\mathbf{m}_j \cdot \mathbf{n})(\mathbf{m}_m \cdot \mathbf{n})\mathbf{n} - (\mathbf{m}_m \cdot \mathbf{n})\mathbf{m}_j - (\mathbf{m}_j \cdot \mathbf{n})\mathbf{m}_m - (\mathbf{m}_m \cdot \mathbf{m}_j)\mathbf{n} \}, \quad (27)$$

$$\mathbf{F}_m^{rep} = \sum_{r < r_0} k(r - r_0)\mathbf{n} \quad (28)$$

where $\hat{\mathbf{z}}$ is a normal vector pointing $+z$ direction, k is the spring constant, and r_0 is the natural length. The repulsive force is introduced in order to avoid overlap between sphere–sphere and sphere–wall, and the force is present only when the distance is less than the natural length.

The velocities are obtained by solving the linear equations $\mathbf{A}\mathbf{x} = \mathbf{b}$ with a known vector $\mathbf{b} = \{\mathbf{v}^\infty, -\mathbf{F}_m, -\mathbf{T}_m\}$ and an unknown vector $\mathbf{x} = \{\mathbf{q}, \mathbf{U}, \boldsymbol{\Omega}\}$, where \mathbf{A} is the dense matrix of size $M(3N_N + 6)$ based on Eqs. (21)–(23). For details, see previous works^{26,29,30}.

Data availability

The data that support the findings of this study are available from the corresponding author upon reasonable request (ptierno@ub.edu).

Received: 20 January 2019 Accepted: 26 April 2019

Published online: 04 June 2019

References

- Strandburg, K. J. Two-dimensional melting. *Rev. Mod. Phys.* **60**, 161 (1988).
- Cheng, Z., Russel, W. B. & Chaikin, P. M. Controlled growth of hard-sphere colloidal crystals. *Nature* **401**, 893–895 (1999).
- Li, B., Zhou, D. & Han, Y. Assembly and phase transitions within colloidal crystals. *Nat. Rev. Mater.* **1**, 15011 (2016).
- Vissers, T., van Blaaderen, A. & Imhof, A. Band formation in mixtures of oppositely charged colloids driven by an ac electric field. *Phys. Rev. Lett.* **106**, 228303 (2011).
- Yan, J. et al. Reconfiguring active particles by electrostatic imbalance. *Nat. Mater.* **15**, 1095–1099 (2016).

- Erb, R. M., Son, H. S., Samanta, B., Rotello, V. M. & Yellen, B. B. Magnetic assembly of colloidal superstructures with multipole symmetry. *Nature* **457**, 999–1002 (2009).
- Yan, J., Bloom, M., Bae, S. C., Luijten, E. & Granick, S. Linking synchronization to self-assembly using magnetic Janus colloids. *Nature* **491**, 578–581 (2012).
- Aubret, A., Youssef, M., Sacanna, S. & Palacci, J. Targeted assembly and synchronization of self-spinning microgears. *Nat. Phys.* **14**, 1114–1118 (2018).
- Bialké, J., Speck, T. & Löwen, H. Crystallization in a dense suspension of self-propelled particles. *Phys. Rev. Lett.* **108**, 168301 (2012).
- Palacci, J., Sacanna, S., Steinberg, A. P., Pine, D. J. & Chaikin, P. M. Living crystals of light-activated colloidal surfers. *Science* **339**, 936–940 (2013).
- Soto, R. & Golestanian, R. Self-assembly of catalytically active colloidal molecules: tailoring activity through surface chemistry. *Phys. Rev. Lett.* **112**, 068301 (2014).
- Menzel, A. M., Takao, O. & Löwen, H. Active crystals and their stability. *Phys. Rev. E* **89**, 022301 (2014).
- Ginot, F., Theurkauff, I., Detcheverry, F., Ybert, C. & Cottin-Bizonne, C. Aggregation-fragmentation and individual dynamics of active clusters. *Nat. Commun.* **9**, 696 (2017).
- Ni, R., Cohen, A. C. S. & Dijkstra, M. Pushing the glass transition towards random close packing using self-propelled hard spheres. *Nat. Commun.* **4**, 2704 (2013).
- Ni, R., Cohen, A. C. S., Dijkstra, M. & Bolhuis, P. G. Crystallizing hard-sphere glasses by doping with active particles. *Soft Matter* **10**, 6609–6613 (2013).
- Kümmel, F., Shabestari, P., Lozano, C., Volpe, G. & Bechinger, C. Formation, compression and surface melting of colloidal clusters by active particles. *Soft Matter* **11**, 6187 (2015).
- Dietrich, K. et al. Active atoms and interstitials in two-dimensional colloidal crystals. *Phys. Rev. Lett.* **120**, 268004 (2018).
- Martinez-Pedrero, F. & Tierno, P. Magnetic propulsion of self-assembled colloidal carpets: efficient cargo transport via a conveyor-belt effect. *Phys. Rev. Appl.* **3**, 051003 (2015).
- Janssen, X. J. A., Schellekens, A. J., van Ommering, K., van Ijzendoorn, L. J. & Prins, M. J. Controlled torque on superparamagnetic beads for functional biosens. *Biosens. Bioelectron.* **24**, 1937 (2009).
- Goldman, A. J., Cox, R. G. & Brenner, H. Slow viscous motion of a sphere parallel to a plane wall-I motion through a quiescent fluid. *Chem. Eng. Sci.* **22**, 637 (1967).
- Zerrouki, D., Baudry, J., Pine, D., Chaikin, P. & Bibette, J. Chiral colloidal clusters. *Nature* **455**, 380 (2008).
- Sinn, I. et al. Magnetically uniform and tunable Janus particles. *Appl. Phys. Lett.* **98**, 024101 (2011).
- Zhou, R., Bai, F. & Wang, C. Magnetic separation of microparticles by shape. *Lab. Chip.* **17**, 401 (2017).
- Cebers, A. & Kalis, H. Dynamics of superparamagnetic filaments with finite magnetic relaxation time. *Eur. Phys. J. E* **34**, 1292 (2011).
- Martinez-Pedrero, F., Ortiz-Ambriz, A., Pagonabarraga, I. & Tierno, P. Colloidal microworms propelling via a cooperative hydrodynamic conveyor belt. *Phys. Rev. Lett.* **115**, 138301 (2015).
- Pozrikidis, C. *Boundary integral and singularity methods for linearized viscous flow* (Cambridge Univ. Press, 1992).
- Blake, J. R. A note on the image system for a stokeslet in a no-slip boundary. *Math. Proc. Camb.* **70**, 303–310 (1971).
- Pozrikidis, C. Finite deformation of liquid capsules enclosed by elastic membranes in simple shear flow. *J. Fluid. Mech.* **297**, 123–152 (1995).
- Ishikawa, T. T., Simmonds, M. P. & Pedley, T. J. Hydrodynamic interaction of two swimming model micro-organisms. *J. Fluid. Mech.* **568**, 119–160 (2006).
- Matsunaga, D., Meng, F., Zöttl, A., Golestanian, R. & Yeomans, J. M. Focusing and sorting of ellipsoidal magnetic particles in microchannels. *Phys. Rev. Lett.* **119**, 198002 (2017).

Acknowledgements

We acknowledge Fernando Martinez-Pedrero for initial experiments. This project has received funding from the European Unions Horizon 2020 research and innovation program under Grant Agreement number 665440. H.M. and P.T. acknowledge support from the ERC Grant “ENFORCE” (Number 811234). P.T. acknowledges support from from MINECO (FIS2016-78507-C2, ERC2018-092827), DURSI (2017SGR1061), and Generalitat de Catalunya under Program “ICREA Acadèmia”.

Author contributions

H.M.-C. performed the experiments. F.M. and D.M. conducted the theoretical and computational part of the work. H.M.-C., F.M., D.M., R.G., and P.T. wrote the paper, discussed, and interpreted the results.

Additional information

Supplementary Information accompanies this paper at <https://doi.org/10.1038/s41467-019-10255-4>.

Competing interests: The authors declare no competing interests.

Reprints and permission information is available online at <http://npg.nature.com/reprintsandpermissions/>

Journal peer review information: *Nature Communications* thanks Maximilian Wolff and other anonymous reviewer(s) for their contribution to the peer review of this work. Peer reviewer reports are available.

Publisher's note: Springer Nature remains neutral with regard to jurisdictional claims in published maps and institutional affiliations.



Open Access This article is licensed under a Creative Commons Attribution 4.0 International License, which permits use, sharing, adaptation, distribution and reproduction in any medium or format, as long as you give appropriate credit to the original author(s) and the source, provide a link to the Creative Commons license, and indicate if changes were made. The images or other third party material in this article are included in the article's Creative Commons license, unless indicated otherwise in a credit line to the material. If material is not included in the article's Creative Commons license and your intended use is not permitted by statutory regulation or exceeds the permitted use, you will need to obtain permission directly from the copyright holder. To view a copy of this license, visit <http://creativecommons.org/licenses/by/4.0/>.

© The Author(s) 2019

PUBLICATION 4

Supporting Information

Supplementary Information

Tunable self-healing of magnetically propelling colloidal carpets

Helena Massana-Cid¹ Fanlong Meng^{2,3} Daiki Matsunaga,^{4,3} Ramin Golestanian,^{2,3} Pietro Tierno^{1, 5, 6}

¹Departament de Física de la Matèria Condensada, Universitat de Barcelona, 08028 Barcelona, Spain

²Max Planck Institute for Dynamics and Self-Organization (MPIDS), 37077 Gottingen, Germany

³Rudolf Peierls Centre for Theoretical Physics, University of Oxford, Oxford OX1 3PU, United Kingdom

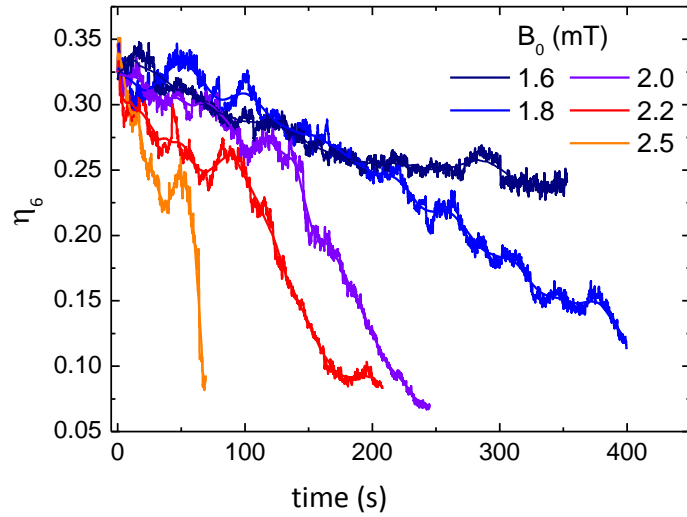
⁴Division of Bioengineering, Graduate School of Engineering Science, Osaka University, 5608531 Osaka, Japan

⁵Institut de Nanociència i Nanotecnologia, Universitat de Barcelona, Barcelona, Spain

⁶Universitat de Barcelona Institute of Complex Systems (UBICS), Universitat de Barcelona, Barcelona, Spain

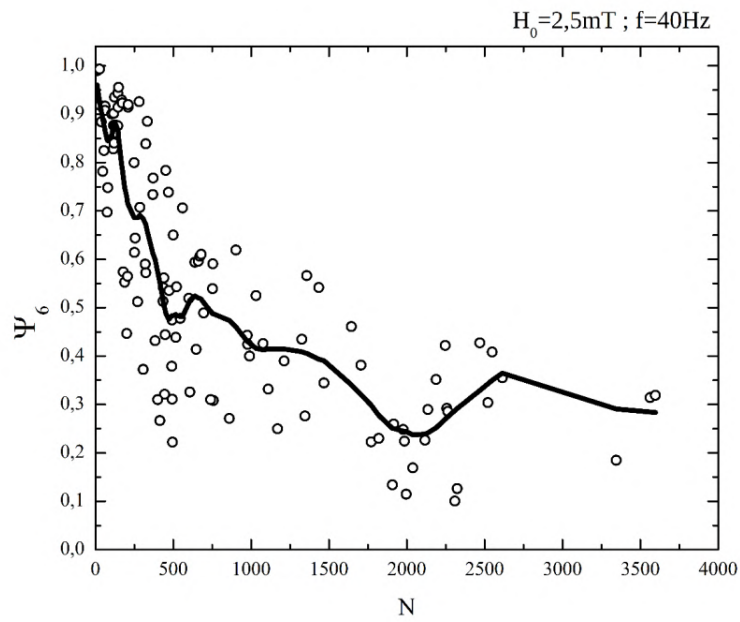
Supplementary Figures

Supplementary Figure 1



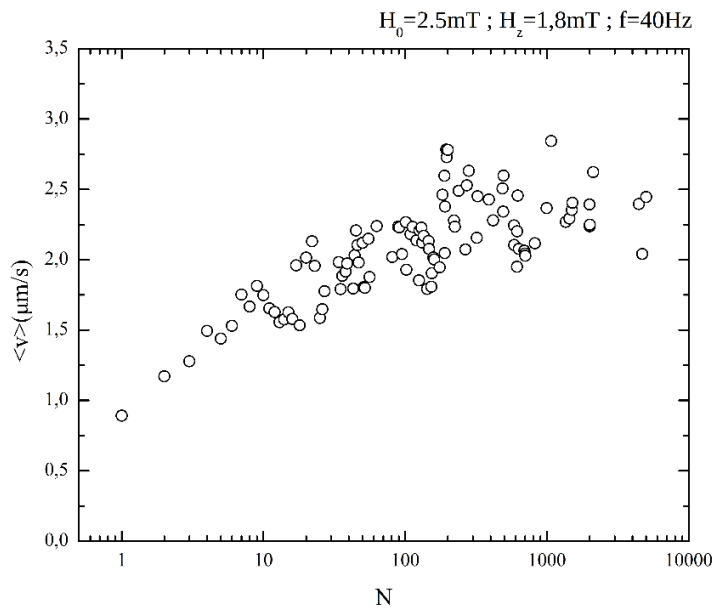
Caption Supplementary Figure 1. Exponent η_6 of the correlation function $g_6(r)$ versus time for different values of the magnetic field B_0 , and hence carpet speed v_c .

Supplementary Figure 2



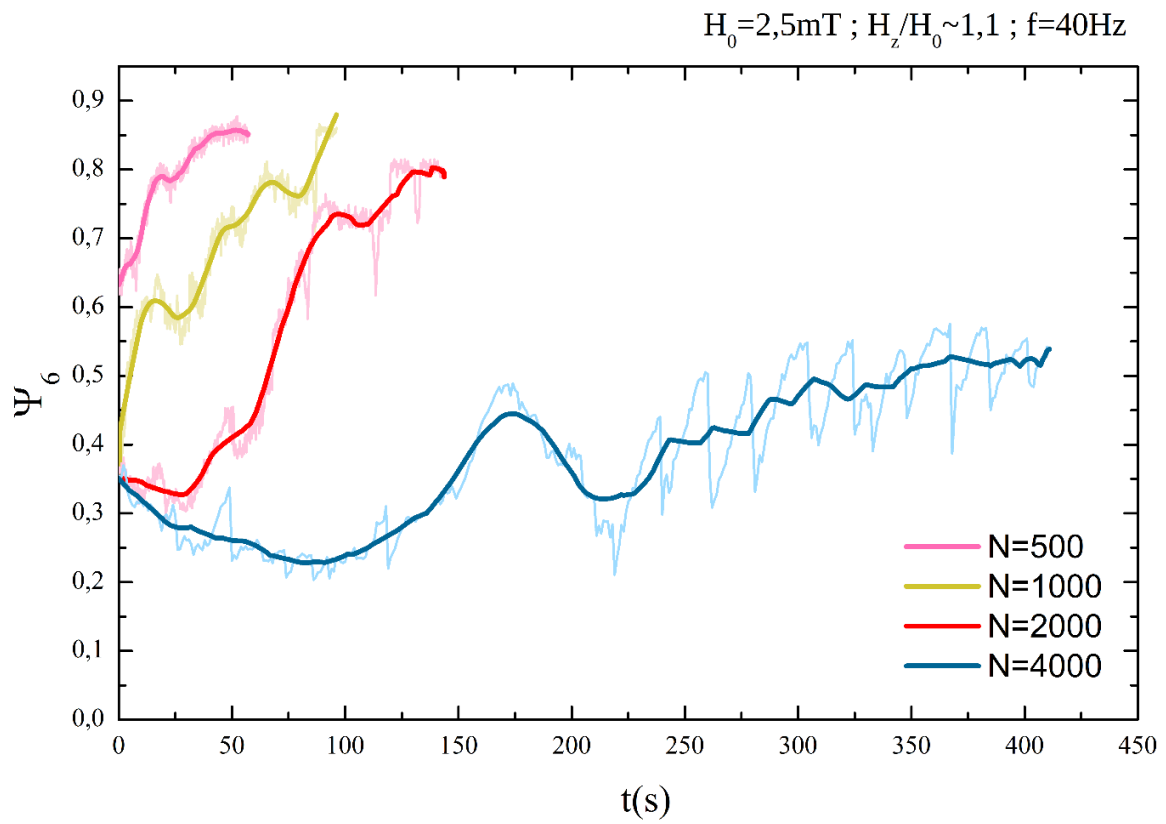
Caption Supplementary Figure 2. Bond orientational order parameter Ψ_6 versus the number of particles within the carpet in the assembly stage. The continuous black line is an average of the experimental data, which are the scattered open circles. The applied rotating field has amplitude $B_0=2.5\text{ mT}$ and frequency $f = 40\text{ Hz}$.

Supplementary Figure 3



Caption Supplementary Figure 3. Average speed of the carpet versus the number of particles N for a carpet driven by a time dependent field with amplitudes $B_0=2.5\text{ mT}$, $B_z=1.8\text{ mT}$ and frequency $f=40\text{ Hz}$.

Supplementary Figure 4



Caption Supplementary Figure 4. Bond orientational order parameter versus time for four different carpet sizes.

Description of Additional Supplementary Files

File Name: Supplementary Movie 1

Description: This videoclip illustrates the assembly of paramagnetic colloids in a two-dimensional carpet via a rotating magnetic field with amplitude $B_0 = 1.6$ mT and frequency $f = 40$ Hz. The carpet is later transported to the right via the application of a rotating field perpendicular to the plane of the particles with amplitudes $B_0 = 1.6$ mT and $B_z = 1.7$ mT, and frequency $f = 40$ Hz. The oscillating component applied along the y -axis has amplitude $B_y = B_0$ and frequency $f_y = f/2$. The video correspond to the Figs.1(d,e,f) of the article.

File Name: Supplementary Movie 2

Description: This videoclip illustrates the breakage of a two-dimensional carpet when the amplitude of the perpendicular component of the rotating field is raised above a limiting value; here $B_z = 2.2$ mT. The remaining field parameters are $B_0 = 1.17$ mT, $f = 40$ Hz and $f_y = f/2$. The video corresponds to the first of the two micrographs at the top of Fig.1(g) in the manuscript.

File Name: Supplementary Movie 3

Description: Generation of the colloidal flow above the carpet in the tread-milling regime. The video shows the motion of paramagnetic colloids above the carpet and was obtained by using the optical microscope in the reflection mode rather than the transmission one. The applied field parameters are $B_0 = 2.2$ mT, $B_z = 1.8$ mT, $f = 40$ Hz and $f_y = f/2$. The video corresponds to Fig.2(a) in the manuscript.

File Name: Supplementary Movie 4

Description: This video illustrates the three different possibilities that the particles propelling above the carpet have in the treadmilling phase: (i) filling one hole, (ii) traveling across the whole carpet, (iii) change direction due to a grain boundary. The applied field parameters are $B_0 = 2$ mT, $B_z = 2$ mT, $f = 40$ Hz and $f_y = f/2$. The video corresponds to the second of the two micrographs at the top of Fig.1(g).

File Name: Supplementary Movie 5

Description: Videos showing the transformation of a carpet composed by 1045 particles from a disordered phase with one grain boundary to a perfect crystalline lattice after 2 min of propulsion in the tread-milling phase. The applied field parameters are $B_0 = 2.5$ mT, $B_z = 2.7$ mT, $f = 40$ Hz and $f_y = f/2$. The video corresponds to the second of the two micrographs at the top of Fig.3(a) of the article.

PUBLICATION 5

Bidirectional particle transport and size selective sorting of Brownian particles in a flashing spatially periodic energy landscape

Physical Chemistry Chemical Physics **18**, 26353 (2016)

Fernando Martinez-Pedrero¹, Helena Massana-Cid¹, Till Ziegler²,
Tom H. Johansen^{3,4}, Arthur V. Straube⁵ and Pietro Tierno^{1,6,7}

¹ Departament de Física de la Matèria Condensada,
Universitat de Barcelona, 08028 Barcelona, Spain

² Department of Physics, Humboldt-Universität zu Berlin,
Newtonstr. 15, 12489 Berlin, Germany

³ Department of Physics, The University of Oslo,
P.O. Box 1048 Blindern, 0316 Oslo, Norway

⁴ Institute for Superconducting and Electronic Materials,
University of Wollongong, Wollongong, New South Wales 2522, Australia

⁵ Department of Mathematics and Computer Science,
Freie Universität Berlin, Arnimallee 6, 14195, Berlin, Germany

⁶ Institut de Nanociència i Nanotecnologia, IN²UB,
Universitat de Barcelona, 08028 Barcelona, Spain

⁷ Universitat de Barcelona Institute of Complex Systems
(UBICS), Universitat de Barcelona, 08028 Barcelona, Spain

CrossMark
click for updatesCite this: *Phys. Chem. Chem. Phys.*,
2016, **18**, 26353Received 12th August 2016,
Accepted 6th September 2016

DOI: 10.1039/c6cp05599k

www.rsc.org/pccp

Bidirectional particle transport and size selective sorting of Brownian particles in a flashing spatially periodic energy landscape†

Fernando Martinez-Pedrero,^a Helena Massana-Cid,^a Till Ziegler,^b
Tom H. Johansen,^{cd} Arthur V. Straube^{ae} and Pietro Tierno^{*afg}

We demonstrate a size sensitive experimental scheme which enables bidirectional transport and fractionation of paramagnetic colloids in a fluid medium. It is shown that two types of magnetic colloidal particles with different sizes can be simultaneously transported in opposite directions, when deposited above a stripe-patterned ferrite garnet film subjected to a square-wave magnetic modulation. Due to their different sizes, the particles are located at distinct elevations above the surface, and they experience two different energy landscapes, generated by the modulated magnetic substrate. By combining theoretical arguments and numerical simulations, we reveal such energy landscapes, which fully explain the bidirectional transport mechanism. The proposed technique does not require pre-imposed channel geometries such as in conventional microfluidics or lab-on-a-chip systems, and permits remote control over the particle motion, speed and trajectory, by using relatively low intense magnetic fields.

The nonequilibrium dynamics of particles driven above periodic potentials are common to different physical and biological systems, from vortices in superconductors,¹ to charge density waves,² frictional surfaces,³ cell migration⁴ and molecular motors.⁵ On the technological side, periodic potentials generated by patterned substrates have been successfully used in the past to transport and

separate microscopic particles dispersed in a fluid medium. It is possible to direct different particle species along separate paths under similar experimental conditions, when the interaction of the particles with the imposed landscape depends on their particular properties, such as their size, electric, magnetic susceptibility or surface charge. Particle sorting has been demonstrated in the past *via* electric,^{6–8} magnetic^{9–12} and optic^{13–15} fields among other types of driving mechanisms.^{16,17} In most of the cases, the colloidal species are deflected from the periodic potential, and the degree of deflection is used to transport different particles towards different locations. A smaller number of experimental realizations have demonstrated the possibility to use an external field to direct the particles in opposite directions. In this context, most of the examples have been obtained by driving the particles with an electric field, in presence of a periodic pattern,^{6,8,18} or using binary mixtures of oppositely charged particles.^{19,20} This task is even more challenging if the particles are driven with a magnetic field. In this case the periodic potential is usually generated by a structured magnetic substrate, and unless a proper strategy to steer polarizable particles is designed,^{10,12} the magnetic particles typically exhibit a unidirectional transport.

In this article we report on the controlled transport and separation of paramagnetic colloidal particles driven by an externally modulated spatially periodic energy landscape, generated across the surface of a structured magnetic substrate. We demonstrate *via* real-time experiments that colloidal particles of different sizes can be transported in opposite directions at a well defined speed, the latter being mainly controlled by the driving frequency of the applied field. The mechanism behind the bidirectional transport is rather robust, and it is fully determined by the different shapes that the magnetic potential adopts at the different particle elevations. We use theoretical arguments to assess the shape of these energy landscapes, finding a good agreement between the experimental data and the numerical simulations performed using these potentials. Extending our procedure to a polydisperse colloidal system, we determine the sensitivity to sorting colloidal species when transported across the magnetic substrate.

^a *Departament de Física de la Matèria Condensada, Universitat de Barcelona, Av. Diagonal 647, 08028, Barcelona, Spain. E-mail: ptierno@ub.edu; Tel: +34 9340 934034031*

^b *Department of Physics, Humboldt-Universität zu Berlin, Newtonstr. 15, 12489 Berlin, Germany*

^c *Department of Physics, The University of Oslo, P.O. Box 1048 Blindern, 0316 Oslo, Norway*

^d *Institute for Superconducting and Electronic Materials, University of Wollongong, Wollongong, New South Wales 2522, Australia*

^e *Department of Mathematics and Computer Science, Freie Universität Berlin, Arnimallee 6, 14195, Berlin, Germany*

^f *Institut de Nanociència i Nanotecnologia, IN²UB, Universitat de Barcelona, Av. Diagonal 647, 08028, Barcelona, Spain*

^g *Universitat de Barcelona Institute of Complex Systems (UBICS), Universitat de Barcelona, Barcelona, Spain*

† Electronic supplementary information (ESI) available: Two video clips illustrating the dynamics of the magnetic colloids. See DOI: 10.1039/c6cp05599k

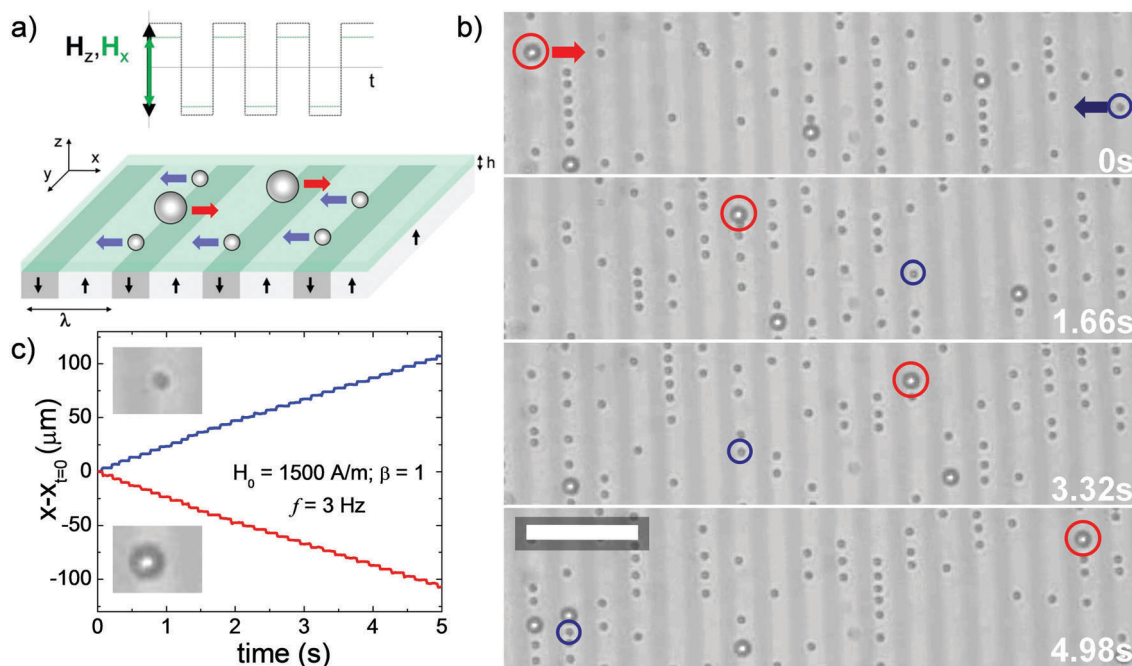


Fig. 1 (a) Schematic showing a binary mixture of paramagnetic colloids deposited above a ferrite garnet film, characterized by parallel stripes with spatial periodicity $\lambda = 6.8 \mu\text{m}$. The two applied field modulations are characterized by strengths H_x and H_z of zero phase lag. (b) Sequence of microscope images showing the bidirectional transport of a large particle (moving to the right, size $2.8 \mu\text{m}$, red circle) and a small particle (moving to the left, size $1.0 \mu\text{m}$, blue circle). The applied field has amplitude $H_0 = 1500 \text{ A m}^{-1}$, anisotropy $\beta = 1$ and frequency $f = 3 \text{ Hz}$. The corresponding video-clip can be found in the ESI† (Video S1). (c) Displacements along the x -axis versus time of the large (red) and small (blue) particle.

Fig. 1(a) shows a sketch of the experimental system. The substrate potential is generated by the stray field of a bismuth substituted ferrite garnet film (FGF), of composition $\text{Y}_{2.5}\text{Bi}_{0.5}\text{Fe}_{5-q}\text{Ga}_q\text{O}_{12}$ ($q = 0.5-1$). The FGF is grown by dipping liquid phase epitaxy, and is characterized by parallel ferromagnetic domains with alternating up and down magnetization and a spatial periodicity of $\lambda = 6.8 \mu\text{m}$.²¹ Bridging the magnetic domains are Bloch walls (BW), *i.e.* $\sim 20 \text{ nm}$ narrow transition regions where the magnetization vector rotates by 180 degrees. The position of the BWs can be easily manipulated with the aid of a relatively low (few mT) external field, a feature which is used to modify the magnetic stray field of the film. We demonstrate the bidirectional transport by dispersing small (s) and large (L) paramagnetic colloids above the FGF, with diameters $d_s = 1.0 \mu\text{m}$ (Dynabeads Myone, Dynal) and $d_L = 2.8 \mu\text{m}$ (Dynabeads M-270, Dynal), and magnetic volume susceptibilities $\chi_s = 1$ and $\chi_L = 0.4$, respectively.^{22,23} Both types of particles are composed of a crosslinked polystyrene matrix with surface COOH groups and are diluted in highly deionized water (MilliQ) before being deposited above the FGF surface.

Once above the FGF, the particles sediment due to density mismatch, and are attracted by the stray field \mathbf{H}^{sub} of the film, which confines them to the horizontal plane. To avoid particle sticking and reduce the strong attraction of the FGF, we coat the latter with a uniform layer (thickness h) of a positive photoresist AZ-1512 (Microchem, Newton, MA) *via* standard spin coating and UV photo-crosslink.²⁴ Due to weak residual electrostatic repulsive interaction, particles hover slightly above the coating layer without mechanically touching it. Under no applied field, the FGF generates a one-dimensional $\lambda/2$ -periodic magnetic landscape. The particles

are attracted to the minima of the landscape located above the BWs and stay at fixed elevations, z_s for the small or z_L for the large particles. The external fields are applied with a custom-made triaxial coil system connected to a wave generator (TTi-TGA1244, TTi) feeding a power amplifier (IMG STA-800, Stage Line). The particle dynamics are visualized with an upright optical microscope (Eclipse Ni, Nikon) equipped with a CCD camera (Scout scA640-74f, Basler) operating at 60 frames per second.

As shown in Fig. 1(a), we transport the magnetic colloids above the FGF film upon application of a square-wave magnetic field, $\mathbf{H}^{\text{ac}} \equiv [H_x \text{sgn}(\cos(2\pi ft)), 0, H_z \text{sgn}(\cos(2\pi ft))]$, where $\text{sgn}(x)$ is the signum function and f denotes the driving frequency. The field strength can be described in terms of the amplitude $H_0 = \sqrt{(H_x^2 + H_z^2)}/2$ and the field anisotropy $\beta = H_x/H_z$. The applied field modulates the magnetic domains such that the potential is switched between two states every half ($T/2$) a period, $T = 1/f$, inducing a net particle current above the FGF. Before discussing in detail the resulting potential, we will describe the main experimental observations. As shown in Fig. 1(b), we find that for a certain range of field amplitudes and anisotropies, particles of different size are transported in opposite directions above the FGF surface. In particular, the series of polarization microscopy images in Fig. 1(b) show one large particle (highlighted by the red circle) and a small particle (highlighted by the blue circle), which completely exchange their positions after 4.98 s. Both particles display step-like trajectories reflecting the discontinuous nature of the driving field, see Fig. 1(c) and ESI† (Video S1). The particle motion proceeds through a series of successive steps: every half a

period ($T/2$), when the oscillating field changes sign, the particles start to move towards the nearest energy minimum (steep part of the trajectory) at a distance of one magnetic domain ($\lambda/2$), reach it and wait (flat part of the trajectory) for a next change of sign. This movement leads to an average speed $\langle v_j \rangle = \pm \lambda f$ with $j = \{s, L\}$. In a more concentrated system, particles propelling in opposite directions might accidentally collide. In this case, the small particles usually slide over the surface of the large ones and continue further almost unperturbed. Thus, for the discontinuous magnetic modulation used here, the magnetic dipolar interactions between particles of different sizes are irrelevant, as recently observed for a binary mixture of particles driven unidirectionally by a continuous modulation.²⁵ In contrast, the pair interactions between similar particles are non-negligible, as discussed in a previous work.²⁶ However, for the measurements of average speed, we avoid chain formation by using low concentrations of particles, such that the pair interactions do not affect the particle motion. We also note that the bidirectional transport observed for the square-wave modulation was not found for other types of magnetic driving, such as linear oscillating²⁷ or rotating magnetic fields.²⁸

In order to understand the mechanism behind the bidirectional transport, we calculate the magnetic energy landscape generated by the FGF surface under the influence of an external field. We consider two paramagnetic colloidal particles having different diameters d_j , volumes $V_j = \pi d_j^3/6$, and effective magnetic volume susceptibilities χ_j . Under a magnetic field \mathbf{H} the particles acquire a dipole moment $\mathbf{m}_j = V_j \chi_j \mathbf{H}(x, z_j, t)$, and an energy $U_j(x, t) = \frac{1}{2}(\mu_0 V_j \chi_j) \mathbf{H}^2(x, z_j, t)$. Here, $\mu_0 = 4\pi \times 10^{-7} \text{ H m}^{-1}$ is the magnetic permeability of the free space, and the global magnetic field $\mathbf{H} = \mathbf{H}^{\text{ac}} + \mathbf{H}^{\text{sub}}$ is the sum of the external modulation \mathbf{H}^{ac} and the substrate field \mathbf{H}^{sub} expressed as²⁹

$$\mathcal{H}^{\text{sub}} = -\frac{2M_s}{\pi} \log\left(\frac{1-u_-}{1-u_+}\right), \quad (1)$$

with $H_x^{\text{sub}} = \text{Re}\{\mathcal{H}^{\text{sub}}\}$ and $H_z^{\text{sub}} = -\text{Im}\{\mathcal{H}^{\text{sub}}\}$. Here, $u_{\pm} = e^{-kz} e^{ik(x \pm \Delta)}$ with $k = \frac{2\pi}{\lambda}$ the wave number, M_s is the saturation magnetization, and $\Delta(t) = \varepsilon H_z^{\text{ac}}(t)/2$ is the displacement of BWs *via* the external field, where ε is a prefactor which determines the amplitude of such displacement. Fig. 2 shows the magnetic energy landscape for the two particles calculated at two different time steps, separated by half a period of the driving field. The modulation switches the potential between two states, which are represented by the λ -periodic profiles in the top (state 1) and bottom (state 2) panels of the image. Because of exponentially strong dependence on the elevation in eqn (1), small differences in the particle size significantly affect the shape of the potential seen by the two types of particles. As shown in Fig. 2, the potential for a small particle has a more complex shape as compared to the magnetic landscape of the large one. This shape results from higher order harmonic terms in the Fourier expansion of eqn (1) which decrease with the elevation, thus remaining non-negligible for the small particle but becoming less relevant for the large one. In both cases, a particle in state 1 appears close to a maximum when the switching to state 2 occurs and tends towards the

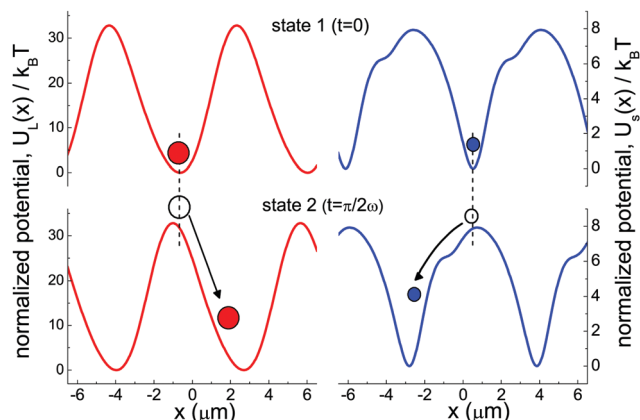


Fig. 2 Normalized magnetic potential $U_j(x)/k_B T$, $j = \{s, L\}$ illustrating the mechanism of bidirectional transport of the large ($2.8 \mu\text{m}$, red left panels) and the small ($1.0 \mu\text{m}$, blue right panels) particles, as described in the text. Top panels show two states of the flashing potential plotted at $t = 0$ and bottom panels after half a period at $t = T/2 = \pi/2\omega$.

nearest minimum. The crucial point is that the emerging maximum is always slightly displaced with respect to the minimum, to the left for the large and to the right for the small particles, forcing the two species to move in opposite directions.³⁰ At low frequencies (such that a particle has enough time to reach its target minimum within the time $T/2$), its average speed $\langle v_j \rangle = \pm \lambda f$, as discussed above. In contrast, when the switching between the two states is too fast, the particle is unable to reach the minimum in such brief period of time and gets trapped, moving back and forth between the two minima in states 1 and 2. As a consequence, at high frequencies the average speed vanishes for both types of particles.

In order to probe these theoretical arguments, we next perform a series of experiments and measure the average speed $\langle v_j \rangle$ of the two types of driven particles, varying the frequency and keeping constant the amplitude and the anisotropy of the applied field. The experimental data in Fig. 3 (the filled symbols) show the speeds having different signs for the two types of particles. In both cases, the motion is characterized by two well defined regimes, as described above. At low frequencies, the particles display net motion with the average speed $\langle v_j \rangle$ increasing almost linearly with f . In contrast, beyond a critical value ($f_s^c = 14.2 \text{ Hz}$ for the small particles and $f_L^c = 30 \text{ Hz}$ for the large ones), the beads cannot follow the flashing minimum, showing a gradual decrease of $\langle v_j \rangle$ with f . To achieve a quantitative agreement with the experiment, we simulate the individual dynamics of particles in the magnetic potential based on eqn (1) with account of thermal fluctuations, as described by the equation

$$\zeta_j \frac{dx_j}{dt} = -\frac{\partial U_j(x_j, t)}{\partial x} + \sqrt{2\zeta_j k_B T} \xi_j(t), \quad j = \{s, L\}. \quad (2)$$

Here, $\zeta_j = 3\pi\eta d_j$ is the viscous friction coefficient, $\eta = 10^{-3} \text{ Pa s}$ is the dynamic viscosity of the solvent, $k_B T$ is the thermal energy, and $\xi_j(t)$ is a Gaussian white noise with zero mean and unit covariance. The results of the numerical simulations, shown as empty symbols in Fig. 3, agree well with the experimental data for all the range of frequencies explored. In the numerical simulation

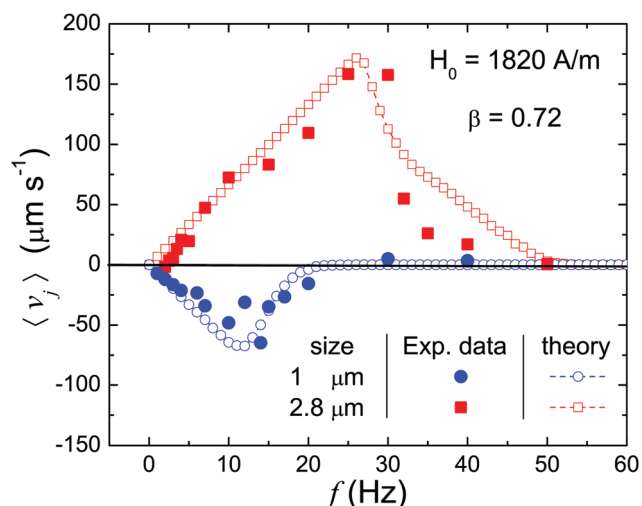


Fig. 3 Average speed $\langle v_j \rangle$ versus field frequency f for a large (red) and small (blue) colloidal particle driven above the FGF. The magnetic modulation is characterized by $H_0 = 1820 \text{ A m}^{-1}$, and $\beta = 0.72$. Filled points denote experimental data, while open symbols connected by dashed lines are from the numerical simulations.

we fixed the elevation of the particles as $z_s = 0.9 \mu\text{m}$ ($z_L = 1.8 \mu\text{m}$) for the small (large) particle, considering that the thickness of the polymer film covering the FGF surface is $h = 0.4 \mu\text{m}$. We used the corresponding experimental values for the field amplitude $H_0 = 1820 \text{ A m}^{-1}$ and the anisotropy $\beta = 0.72$. The saturation magnetization was a free parameter and we find the best agreement with $M_s = 27 \text{ kA m}^{-1}$.

We now explore the sorting capability of our system by changing the size of the employed paramagnetic particles. We deposit on the FGF a polydisperse suspension composed of particles having 7 different sizes, from 270 nm to $10 \mu\text{m}$. The corresponding average speeds for a suspension subjected to a field with amplitude $H_0 = 4300 \text{ A m}^{-1}$, frequency $f = 12 \text{ Hz}$ and anisotropy $\beta = 1.12$, are shown in Fig. 4. Particles having size $d \leq 1 \mu\text{m}$ display a positive velocity, while larger particles are transported in opposite direction. We note that the largest particle ($d = 10 \mu\text{m}$) is unable to move on average. For such long distance to the particle center, the landscape gets perfectly symmetric, and the potential switches between two inverted states, which forbids any net motion.³¹ Moreover, because of stronger thermal fluctuations, smaller nano-particles exhibit a lower speed as compared to the paramagnetic colloids having $d = 1 \mu\text{m}$ size. Fig. 4 makes it evident that the threshold for the magnetic separation depends crucially on the distance between the particle center and the FGF, assuming that each particle is doped by the same fraction of magnetic content. One thus can increase or reduce the thickness of the polymer film deposited above the FGF in order to tune this threshold, allowing to efficiently sort magnetic colloids with different sizes.

To summarize, we have experimentally demonstrated and theoretically explained a novel method to control and transport paramagnetic colloids in opposite directions. We note that an earlier study using a different FGF film showed an apparently similar size-based particle separation method.²⁷ In that work, bidirectional motion of a bidisperse mixture of particles was

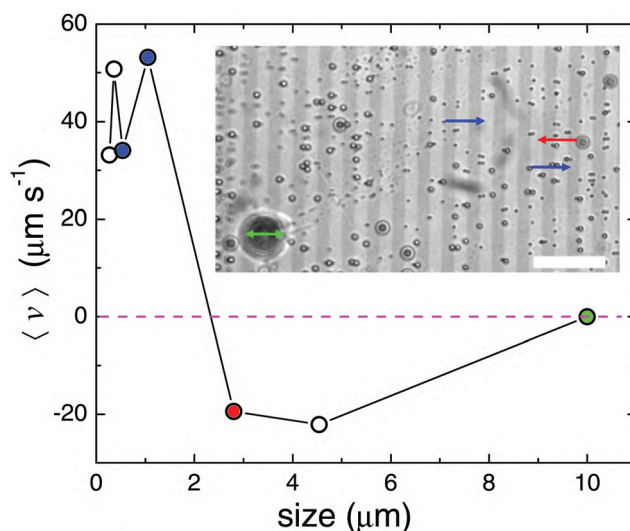


Fig. 4 Average speed $\langle v \rangle$ versus size of different paramagnetic colloids driven above the FGF upon application of a square-wave magnetic field with amplitude $H_0 = 4300 \text{ A m}^{-1}$, anisotropy $\beta = 1.12$ and driving frequency $f = 12 \text{ Hz}$. Inset shows a snapshot of the FGF with all types of particles, where only three are highlighted by arrows. In particular, the arrows indicate the direction of motion of particles having sizes $1.0 \mu\text{m}$ (blue arrow, to the right), $2.8 \mu\text{m}$ (red arrow, to the left) and $10 \mu\text{m}$ (green double arrow, no average motion). Scale bar is $20 \mu\text{m}$. The corresponding video-clip (Video S2) can be found in the ESI.†

induced by applying a rather complicated Lissajous-like magnetic modulation, characterized by two different driving frequencies. In contrast, here we straightforwardly use one driving frequency and a switching field which simultaneously generates different energy landscapes depending on the elevation. The transport method proves robust over a wide range of field parameters, allowing one to reach an unprecedented difference in the speed between particles of different sizes, as high as $|\langle v^L \rangle - \langle v^S \rangle| = 80 \mu\text{m s}^{-1}$. As for fundamental implications of our work, the realization of a flashing potential able to simultaneously generate opposite particle fluxes may prompt further extensions of previously developed ratchet models.^{31,32} In this context, an intriguing aspect would be the role of the thermal fluctuations in the process, which are negligible for the large particles used in the present study, but become increasingly important while reducing the size of the particles down to the nanoscale. On the technological side, our work could provide a method to fractionate magnetic microspheres in a channel-free microfluidic environment, since it does not require the presence of hard walls to confine the motion of micro-particles. Furthermore, paramagnetic particles can be easily functionalized in order to target and bind specific biological or chemical agents, which could be then transported on command by the applied field. This feature opens up the possibility for novel applications in micro- and nanofluidic systems.

We thank L. Schimansky-Geier and I. M. Sokolov for valuable discussions. F. M. P., H. M. C. and P. T. acknowledge support from the ERC Starting Grant ‘‘DynaMO’’ (Proj. No. 335040). P. T. acknowledges support from Mineco (No. FIS2013-41144-P) and AGAUR (Grant No. 2014SGR878). A. V. S. and P. T. acknowledge support from a bilateral German-Spanish program of DAAD

(project no. 57049473) via the Bundesministerium für Bildung und Forschung (BMBF).

References

- 1 L. F. Cohen and H. J. Jensen, *Rep. Prog. Phys.*, 1997, **60**, 1581.
- 2 G. Grüner, *Rev. Mod. Phys.*, 1988, **60**, 1129.
- 3 T. Bohlein, J. Mikhael and C. Bechinger, *Nat. Mater.*, 2012, **11**, 126.
- 4 G. Mahmud, C. J. Campbell, K. J. M. Bishop, Y. A. Komarova, O. Chaga, S. Soh, S. Huda, K. Kandere-Grzybowska and B. A. Grzybowski, *Nat. Phys.*, 2009, **5**, 606.
- 5 F. Julicher, A. Ajdari and J. Prost, *Rev. Mod. Phys.*, 1997, **69**, 1269.
- 6 J. Regtmeier, R. Eichhorn, T. T. Duong, P. Reimann, D. Anselmetti and A. Ros, *Eur. Phys. J. E: Soft Matter Biol. Phys.*, 2007, **22**, 335.
- 7 U. Kim, J. Qian, S. A. Kenrick, P. S. Daugherty and H. T. Soh, *Anal. Chem.*, 2008, **80**, 8656.
- 8 L. Bogunovic, R. Eichhorn, J. Regtmeier, D. Anselmetti and P. Reimann, *Soft Matter*, 2012, **8**, 3900.
- 9 O. H. B. B. Yellen and G. Friedman, *Proc. Natl. Acad. Sci. U. S. A.*, 2005, **102**, 8860.
- 10 K. Gunnarsson, P. E. Roy, S. Felton, J. Pihl, P. Svedlindh, S. Berner, H. Lidbaum and S. Oscarsson, *Adv. Mater.*, 2005, **17**, 1730.
- 11 D. Robert, N. Pamme, H. Conjeaud, F. Gazeau, A. Iles and C. Wilhelm, *Lab Chip*, 2011, **11**, 1902.
- 12 B. Lim, V. Reddy, X. Hu, K. Kim, M. Jadhav, R. Abedini-Nassab, Y.-W. Noh, Y. T. Lim, B. B. Yellen and C. Kim, *Nat. Commun.*, 2014, **5**, 3846.
- 13 K. Xiao and D. G. Grier, *Phys. Rev. E: Stat., Nonlinear, Soft Matter Phys.*, 2010, **82**, 051407.
- 14 M. P. MacDonald, G. C. Spalding and K. Dholaki, *Nature*, 2013, **426**, 421.
- 15 O. Brzobohatý, V. Karásek, M. Siler, L. Chvátal, T. Čížmár and P. Zemánek, *Nat. Photonics*, 2013, **7**, 123.
- 16 X. g. Ma, P.-Y. Lai, B. J. Ackerson and P. Tong, *Soft Matter*, 2015, **11**, 1182.
- 17 K. J. Morton, K. Louthback, D. W. Inglis, O. K. Tsui, J. C. Sturm, S. Y. Chou and R. H. Austin, *Lab Chip*, 2008, **105**, 7434.
- 18 R. Eichhorn, J. Regtmeier, D. Anselmetti and P. Reimann, *Soft Matter*, 2010, **6**, 1858.
- 19 T. Vissers, A. Wysocki, M. Rex, H. Löwen, P. Royall, A. Imhof and A. van Blaaderen, *Soft Matter*, 2011, **7**, 2352.
- 20 T. Vissers, A. van Blaaderen and A. Imhof, *Phys. Rev. Lett.*, 2011, **106**, 228303.
- 21 P. Tierno, F. Sagués, T. H. Johansen and T. M. Fischer, *Phys. Chem. Chem. Phys.*, 2009, **11**, 9615.
- 22 L. Clime, B. L. Drogoff and T. Veres, *IEEE Trans. Magn.*, 2007, **43**, 2929.
- 23 L. E. Helseth, *J. Phys. D: Appl. Phys.*, 2007, **40**, 3030.
- 24 P. Tierno, *Soft Matter*, 2012, **8**, 11443.
- 25 P. Tierno and A. V. Straube, *Eur. Phys. J. E: Soft Matter Biol. Phys.*, 2016, **39**, 54.
- 26 A. V. Straube and P. Tierno, *Soft Matter*, 2014, **10**, 3915.
- 27 P. Tierno, S. V. Reddy, M. G. Roper, T. H. Johansen and T. M. Fischer, *J. Phys. Chem. B*, 2008, **112**, 3833.
- 28 P. Tierno, *Phys. Rev. Lett.*, 2012, **109**, 198304.
- 29 A. V. Straube and P. Tierno, *Europhys. Lett.*, 2013, **103**, 28001.
- 30 J.-F. Chauwin, A. Ajdari and J. Prost, *EPL*, 1994, **27**, 421.
- 31 P. Reimann, *Phys. Rep.*, 2002, **57**, 361.
- 32 P. Hänggi and F. Marchesoni, *Rev. Mod. Phys.*, 2009, **81**, 387.

PUBLICATION 5

Supporting Information

Supporting Information for the article:

Bidirectional particle transport and size selective sorting of Brownian particles in a flashing spatially periodic energy landscape

Fernando Martinez-Pedrero,¹ Helena Massana-Cid,¹ T. Ziegler,² Tom H. Johansen,³ Arthur V. Straube^{1,4} Pietro Tierno^{1,5,}*

¹Departament de Física de la Matèria Condensada, Universitat de Barcelona, Av.Diagonal 647, 08028, Barcelona, Spain.

E-mail: ptierno@ub.edu

² Department of Physics, Humboldt-Universität zu Berlin, Newtonstr. 15, 12489 Berlin, Germany.

³ Department of Physics, The University of Oslo, P.O. Box 1048 Blindern, 0316 Oslo, Norway.

⁴Department of Mathematics and Computer Science, Freie Universität Berlin, Arnimallee 6, 14195 Berlin, Germany

⁵Institut de Nanociència i Nanotecnologia, IN2UB, Universitat de Barcelona, Av. Diagonal 647, 08028, Barcelona, Spain.

*Email: ptierno@ub.edu

SUPPORTING VIDEO FILES.

With the article 2 video clips are included in support of Fig.1 and Fig. 4.

VideoS1(.WMV): This videoclip shows the controlled bidirectional transport of two types of paramagnetic colloidal particles with size $d=2.8 \mu\text{m}$ and $d=1.0 \mu\text{m}$ driven above the FGF film. The applied field has amplitude $H_0=1500 \text{ A/m}$, anisotropy $\beta = 0$ and angular frequency $f = 3\text{Hz}$. The videoclip corresponds to Fig.1(b) in the article.

VideoS2(.WMV): This videoclip shows the fractionation of a polydisperse suspension of paramagnetic colloids having 7 different sizes. The applied field has amplitude $H_0=4300 \text{ A/m}$, anisotropy $\beta = 1.12$ and angular frequency $f = 12\text{Hz}$. This videoclip corresponds to the inset of Fig.4 of the article.

PUBLICATION 6

Assembly and Transport of Microscopic Cargos via Reconfigurable Photoactivated Magnetic Microdockers

Small **13**, 1603449 (2017)

Fernando Martinez-Pedrero¹, Helena Massana-Cid¹ and Pietro Tierno^{1,2,3}

¹ Departament de Física de la Matèria Condensada,
Universitat de Barcelona, 08028 Barcelona, Spain

² Institut de Nanociència i Nanotecnologia, IN²UB,
Universitat de Barcelona, 08028 Barcelona, Spain

³ Universitat de Barcelona Institute of Complex Systems
(UBICS), Universitat de Barcelona, 08028 Barcelona, Spain

Assembly and Transport of Microscopic Cargos via Reconfigurable Photoactivated Magnetic Microdockers

Fernando Martinez-Pedrero, Helena Massana-Cid, and Pietro Tierno*

The realization of micromotors able to dock and transport microscopic objects in a fluid medium has direct applications toward the delivery of drugs and chemicals in small channels and pores, and the realization of functional wireless microrobots in lab-on-a-chip technology. A simple and general method to tow microscopic particles in water by using remotely controllable light-activated hematite microdockers is demonstrated. These anisotropic ferromagnetic particles can be synthesized in bulk and present the remarkable ability to be activated by light while independently manipulated via external fields. The photoactivation process induces a phoretic flow capable to attract cargos toward the surface of the propellers, while a rotating magnetic field is used to transport the composite particles to any location of the experimental platform. The method allows the assembling of small colloidal clusters of various sizes, composed by a skeleton of mobile magnetic dockers, which cooperatively keep, transport, and release the microscopic cargos. The possibility to easily reconfigure in situ the location of the docker above the cargo is demonstrated, which enables optimize transport and cargo release operations.

1. Introduction

The realization of propelling microdevices able to navigate and transport objects in a fluid medium plays a crucial role in the miniaturization of many basic processes in physics, biology and analytical science. From a fundamental point of view, the development of strategies to design efficient

prototypes in viscous fluids is related with our understanding of the physics of locomotion at such scale,^[1,2] which is common to many biological systems, such as bacteria. When reducing the size to the microscale, inertia is negligible (low Reynolds number), and the corresponding hydrodynamic laws become time-reversible. As a consequence, swimming by reciprocal motion, i.e., based purely on symmetric backward and forward body distortions, does not lead to net translation, as described in the Purcell seminal work.^[3] Different experimental prototypes capable to attain directed motion at low Reynolds number have been proposed in the past, being powered by electric,^[4,5] optic,^[6,7] acoustic,^[8,9] or magnetic^[10–15] fields, or via a chemical reaction. In the latter case, a common strategy relies on the use of hydrogen peroxide as fuel, catalytically decomposed by platinum located only on one side of the propeller. Since its proof-of-concept realization via microscopic boats,^[16] this actuation scheme has been further extended to different systems, including nanoscale platinum–gold nanorods,^[17] Janus colloids half coated with Pt,^[18] dimer particles,^[19] and many others.^[20–24] The field has recently evolved beyond the use of hydrogen peroxide, by designed reaction schemes which could dramatically improve the motor propulsion efficiency,^[25] developing novel

Dr. F. Martinez-Pedrero, H. Massana-Cid, Prof. P. Tierno
Departament de Física de la Matèria Condensada
Universitat de Barcelona
Avinguda Diagonal 647, 08028 Barcelona, Spain
E-mail: ptierno@ub.edu



Dr. F. Martinez-Pedrero, H. Massana-Cid,
Prof. P. Tierno
Institut de Nanociència i Nanotecnologia
IN2UB

Universitat de Barcelona
08028 Barcelona, Spain

Dr. F. Martinez-Pedrero, H. Massana-Cid, Prof. P. Tierno
Universitat de Barcelona Institute of Complex Systems (UBICS)
Universitat de Barcelona
08028 Barcelona, Spain

DOI: 10.1002/sml.201603449

prototypes able to move in nontoxic environments,^[26] or via a biochemical reaction.^[27]

A major effort in the field relies on the design of micromotors featuring the possibility to transport and release a cargo on command. This ability has direct applications in biomedicine^[28,29] targeted drug delivery,^[30] and microfluidics,^[31] when there is the need to pick-up, transport, and release^[32] a microscopic cargo at a defined location in a vein^[33] or a microfluidic network.^[34] External fields can provide an efficient way to steer and guide micromotors during the transportation of a given cargo, since the applied field determines the path to travel, avoiding the trajectory randomization that arises from rotational diffusion or fuel consumption when the propeller is powered by a chemical reaction. Alternatively, recent advances with lithographic patterning showed that also boundaries^[35] and topographic pathways^[36] could provide a steering mechanism for chemically powered Janus particles.

Magnetic propellers are usually actuated by an oscillating or rotating external field: for large enough field strengths, the propulsion speed can be well controlled by the driving frequency, allowing speeding up or slowing down the prototype by varying this sole control parameter. Time dependent magnetic fields have been used to date for disparate applications like to self-assemble and transport ferromagnetic particles,^[37] artificial helical swimmers,^[38] nanowires,^[39] Janus micromotors,^[40] or DNA flagellar bundles.^[41] Nevertheless, realizations which can combine magnetic and chemical actuation schemes could give rise to a higher level of functionality.^[42] For example, a composite system formed by a microscopic cargo chemically bound to the magnetic motor could be propelled by an external field and later released by a different chemical reaction when entering another region of the experimental platform. Another possibility would be to power the prototype via a chemical reaction, if it guarantees a faster transportation mechanism, and use the applied field either to steer the micromotor, or as a complementary mean of transport when reaching the full consumption of the catalysts. In this context, some of us demonstrated in the past that catalytically driven anisotropic paramagnetic microellipsoids could be steered in a hydrogen peroxide (H_2O_2) aqueous solution by using a static magnetic field.^[43] The field oriented the particles due to their magnetic anisotropy allowing to precisely guide them to a given location. However, the applied field did not provide the propulsion mechanism, which was only due to the decomposition of hydrogen peroxide. Moreover, these prototypes were not tested for microscopic cargo loading/delivery, but it was only demonstrated the possibility to steer them by means of a constant magnetic field.

Other more recent works showed that hematite microparticles in the form of cubes^[44] or peanuts,^[45] represent versatile prototypes where both, chemical propulsion and magnetic steering could be independently and simultaneously achieved. When dispersed in a solution of water and H_2O_2 , the hematite particles were activated by blue light, which triggered the photocatalytic decomposition of H_2O_2 and produced self-propulsion. These microdockers were able to transport large cargos attached due to an imbalanced osmotic flow, and were guided along straight paths using either a constant magnetic field or microscopic tracks embedded in a polydimethylsiloxane (PDMS) substrate.^[45]

We introduce here an alternative and general method to manipulate and transport hematite ellipsoidal micropellers, activated by light but transported and fully controlled via time dependent magnetic fields. We use a rotating magnetic field to translate these particles at a well-defined speed, and to easily set the direction of motion by changing the field orientation or its sense of rotation. This feature provides the possibility to surpass obstacles via magnetic guiding and thus to react to environmental changes. The unique ability to independently actuate over the light-induced phoretic attraction and field induced actuation allows to precisely dock, transport, and release microscopic objects on command. We use this method to assemble small active colloidal clusters which are transported by the cooperative rotational motion of several magnetic inclusions. Finally we show the possibility to reconfigure in situ the relative location of the docker above the cargo, a feature which enables the optimization of transportation and cargo release via magnetic command.

2. Results and Discussion

We synthesize hematite ellipsoids by using the “gel-sol” technique,^[46] more details are given in the Experimental Section. The process allows producing monodisperse ferromagnetic microparticles with different shapes, such as cubes, peanuts, or spheres, at a relative high yield. We focus here on particles with ellipsoidal shape, since the magnetic properties and the corresponding propulsion speed can be well described theoretically and easily characterized using video-microscopy. Particle inspection via scanning electron microscopy (SEM), **Figure 1a**, reveals that the synthesized ellipsoids have a rather uniform shape, with an average major and minor axes of length $a = 1.80 \pm 0.11 \mu\text{m}$ and $b = 1.31 \pm 0.12 \mu\text{m}$, respectively, see also Figure S1 in the Supporting Information for the EDX spectra. The particles are characterized by a small permanent moment $m = 2 \times 10^{-16} \text{Am}^2$, which was previously measured by following the particle reorientation under a static field.^[47] A major difference with other anisotropic magnetic colloids is that the hematite ellipsoids present the permanent moment perpendicular to their long axis, as shown in the schematic of Figure 1b. This peculiarity results from the magnetic structure of hematite, which crystallizes in the corundum form.^[48] In this configuration, the Fe cations are antiferromagnetically aligned along the c axis, and above the Morin temperature ($T_m \approx 263 \text{K}$) the hematite becomes weakly ferromagnetic, with the magnetic spins lying mostly in the basal plane, and thus perpendicular to the long axis. From SQUID measurements (see Figure S1 in the Supporting Information), we find that, in the range of field used, the induced magnetization is negligible (<5%) compared with the remanent magnetization. Hence the orientation and dynamics of the hematite particles under the external field can be well described by considering only the particle's permanent magnetic moment.

Once dispersed in a mixture of water and H_2O_2 (9 vol%), the ellipsoids sediment close to a glass-substrate, where they remain 2D confined, displaying a small thermal motion. As shown in Figure 1b,c, the particles are propelled by a uniform

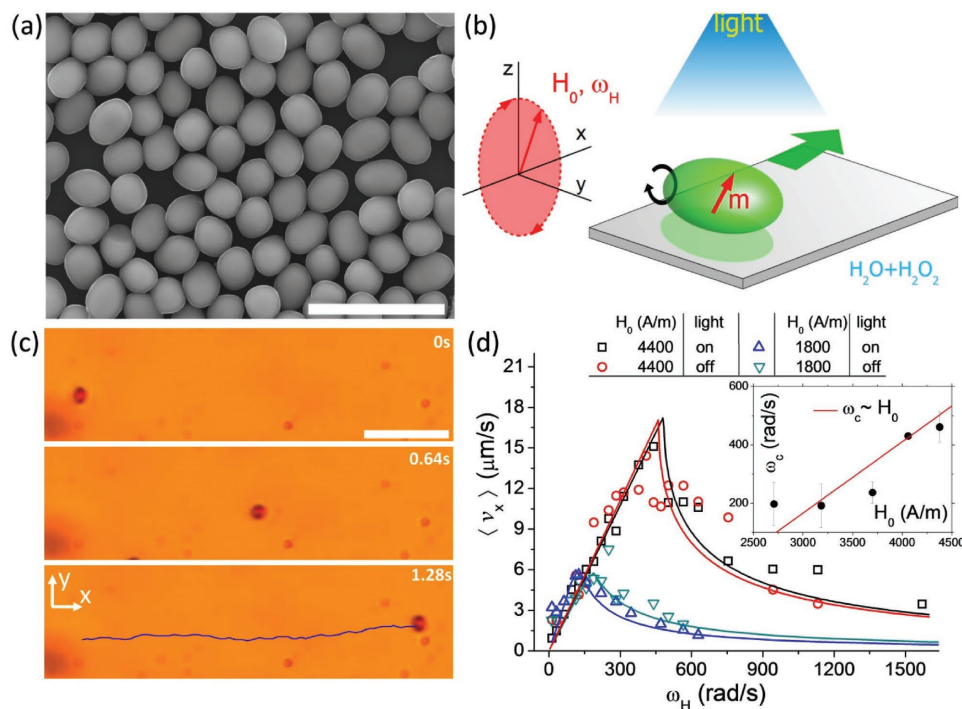


Figure 1. a) Scanning electron microscopy (SEM) image showing the monodisperse hematite ellipsoids. Scale bar is 5 μm. b) Schematic illustrating one ellipsoid propelling in H₂O + H₂O₂ solution due to the application of a rotating magnetic field of amplitude H_0 and angular frequency ω_H . The ellipsoid displays a small permanent moment m , perpendicular to its long axis. c) Sequence of images showing one propelling microellipsoid translating at a speed $\langle v_x \rangle = 15.6 \mu\text{m s}^{-1}$ due to the application of a rotating field with amplitude $H_0 = 4400 \text{ A m}^{-1}$ and frequency $\omega_H = 502.6 \text{ rad s}^{-1}$, in absence of light. Scale bar is 5 μm (Video S1, Supporting Information). d) Average speed versus frequency of one microdocking at two different field amplitudes with and without illumination. Continuous lines are fits obtained from the model, see text. Inset shows the critical frequency ω_c versus amplitude H_0 . The continuous red line is a fit to the data following $\omega_c \sim H_0$.

rotating magnetic field circularly polarized in the plane perpendicular to the wall (x, z) with amplitude H_0 and angular frequency ω_H , namely $\vec{H} = H_0(\cos(\omega_H t), 0, -\sin(\omega_H t))$. The magnetic field applies a net torque $\vec{\tau}$ to the particles, and the torque induces the rotational motion of the ellipsoids around their long axis with an average angular velocity $\langle \omega_r \rangle$, being $\vec{\tau} = \mu_0 \vec{m} \times \vec{H}$ and $\mu_0 = 4\pi \times 10^{-7} \text{ H m}^{-1}$. This rotational motion is translated into a net drift velocity due to the hydrodynamic interaction with the substrate.^[49] The particle velocity is given by $\langle v \rangle = b f_r \langle \omega_r \rangle / 2$, being f_r a correction factor which takes into account the proximity of the wall.^[50] The average speed of one magnetic propeller versus the driving frequency is shown in Figure 1d, in absence and in presence of blue light ($\lambda = 450\text{--}490 \text{ nm}$) irradiated at a power $P = 1.04 \text{ mW}$ and for two field strengths. The similarity between the curves with and without illumination suggests that the photoinduced decomposition of H₂O₂ does not affect significantly the propulsion speed, while being crucial for the docking process as we discuss later. In all the cases analyzed in Figure 1d, the average speed of the microdocking shows two distinct regimes of motion. Below a critical frequency ω_c , the magnetic moment of the particle is able to follow synchronously the field rotation, and $\langle \omega_r \rangle = \omega_H$. As a consequence, the ellipsoids translate along the substrate at a constant average speed proportional to the driving frequency. Above ω_c , the magnetic field becomes too fast, and the magnetic torque is unable to balance the viscous one arising due to the particle rotation in the dissipative medium. Thus, the phase lag between

the permanent moment and the field increases, showing a characteristic “back-and-forth” motion during each cycle of the magnetic field. The average rotational motion of the docker decreases with ω_H , following the relationship $\langle \omega_r \rangle = \omega_H - \sqrt{\omega_H^2 - \omega_c^2}$,^[51] continuous lines in Figure 1d. As a consequence, the speed of the microdockers also decreases, vanishing at very high frequencies and reducing the efficiency of these propellers as cargo transporters. From the fits to the experimental data in Figure 1d, we determine the correction factor f_r , which allows estimating the elevation h of the surface of the microdocking from the boundary wall. We find that in absence and in presence of light, the microdocking translates very close from the surface at an elevation $h = 0.042$ and $0.040 \mu\text{m}$, respectively. We also find that the critical frequency increases linearly with the amplitude of the applied field, as shown in the small inset in Figure 1d.

To carry out tasks as microtransporters, the hematite particles require an effective interaction field which could be used to attract a cargo on command, without interfering with their rotational motion. When exposed to blue light, the surface of the hematite particles starts the decomposition of the H₂O₂ in solution as, $2\text{H}_2\text{O}_2(l) \rightarrow \text{O}_2(g) + 2\text{H}_2\text{O}(l)$. Thus, the particles generate an unbalanced osmotic flow which pushes them toward the bottom surface, slightly reducing their diffusive motion. The generated osmotic flow is also able to attract other particles located nearby, as shown in **Figure 2a,b**, opening the possibility to use these particles as microdockers. The attraction is long ranged, extended over

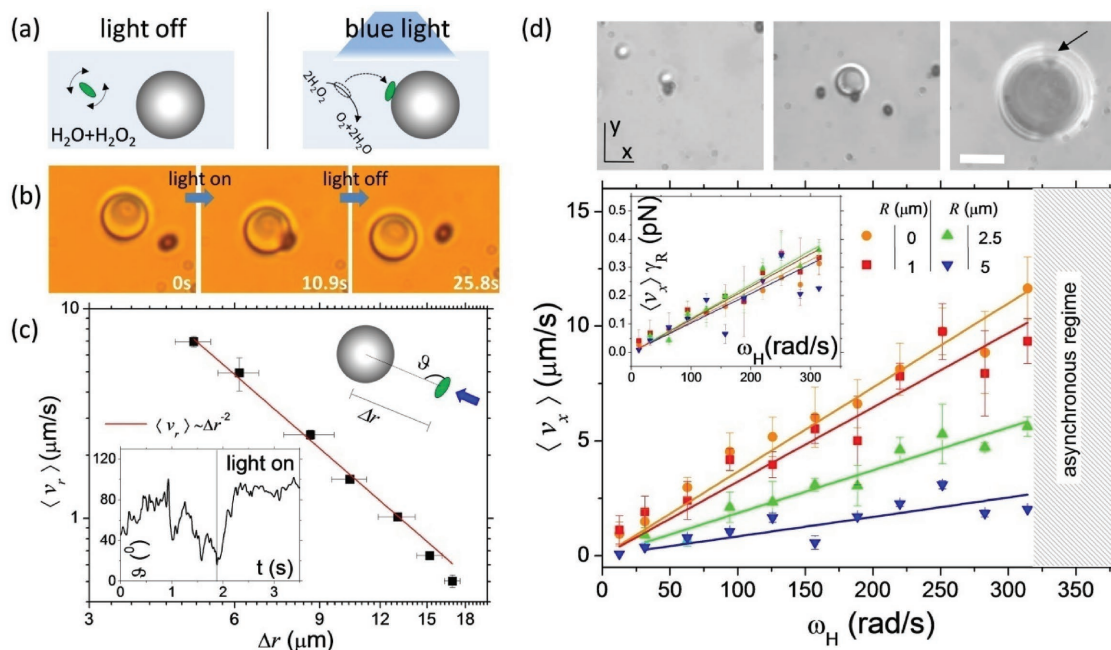


Figure 2. a) Schematics showing the attraction induced by blue light. b) Snapshots illustrating the consecutive binding (light on at $t = 6.38$ s) and unbinding (light off at $t = 18.3$ s) of one hematite ellipsoid close to a $5 \mu\text{m}$ SiO_2 particle (Video S2, Supporting Information). c) Log–log plot of the average speed of the hematite particle versus distance Δr from the cargo, see schematic. The continuous red line is a quadratic fit ($\sim \Delta r^{-2}$), assuming an attractive phoretic potential. Bottom inset shows the orientational angle θ of the microdocked (in degrees) with respect to the surface of the cargo. d) Average speed $\langle v_x \rangle$ versus driving frequency ω_H for the hematite propellers subjected to a rotating field with amplitude $H_0 = 4400 \text{ A m}^{-1}$. Orange disks indicate propellers without cargo, red squares with a cargo of radius $R = 1 \mu\text{m}$, first image on the top; green up-triangles, a cargo of radius $R = 2.5 \mu\text{m}$, middle image on the top; blue down-triangles, a cargo of radius $R = 5 \mu\text{m}$, last image on the top. In the last case, the arrow indicates the docker position, scale bar is $5 \mu\text{m}$. Continuous lines are linear fits, while the gray region in the graph represents the asynchronous regime of the magnetic propeller. Small inset at the top left shows the propulsion forces $\langle v_x \rangle \cdot \gamma_R$ versus ω_H .

several micrometers, and it is quantified in Figure 2c. There, we measure the average speed of the hematite particles when attracted toward a large polystyrene (PS) cargo having a radius of $R = 5 \mu\text{m}$. By using cubic-shape particles, it was already shown that this complex hydrodynamic attraction can be approximated by an effective potential scaling as r^{-2} , as expected for phoretic attraction from a reaction site.^[44] The continuous line in Figure 2c confirms this tendency also for our hematite ellipsoids. In these measurements, we avoid the effect of Brownian motion by measuring the attraction toward cargos which were previously irreversible stuck to the surface of the substrate. Moreover we restrict our measurements to distances shorter than $15 \mu\text{m}$, where the effect of Brownian fluctuations on the trajectory is negligible. As shown in the inset in Figure 2c, the long axis of the microdockers faces toward the surface of the large silica particle during the last stages of the binding process. Moreover, the binding–unbinding is completely reversible since, when switching off the illumination, the dockers immediately detach from the cargo surface due to their diffusive motion, Figure 2b. To avoid irreversible binding via van der Waals interaction, the dockers were previously coated with an anionic surfactant (sodium dodecyl sulfate). This surfactant creates a protective shell that produces steric repulsion and avoids the close contact with the cargo surface during application of light. We also notice that, once the particles are attached to the colloid cargo, sometimes they display a small self-propulsion induced by the chemical reaction. This behavior arises from

the Janus-like morphology of the composite particles, since the osmotic flow generated by the hematite particles is attenuated on the side occupied by the colloidal cargo, see Figure S2 in the Supporting Information for more details. In a previous work^[45] the peanuts particles were etched with hydrochloric acid before being immersed in the water H_2O_2 solution, in order to roughen their surface and enhance further their mobility. We avoid this step to not alter the magnetic properties of the propellers.

We use the phoretic attraction to dock colloidal cargos of different sizes, which can be later released by switching off the illumination. Then, the rotating magnetic field is applied as an independent mean to propel the whole composite structure. Figure 2d shows the average translational speed of one magnetic microdocked pulling different colloidal cargos with radii ranging from $R = 1$ to $5 \mu\text{m}$, with the corresponding microscope images showed at the top. All measurements are taken in the synchronous regime, i.e., when the propeller speed grew linearly with the driving frequency. Thus, for a transported colloidal cargo with radius $R = 2.5 \mu\text{m}$, the composite cluster could reach an average speed of $\langle v_x \rangle = 5.8 \mu\text{m s}^{-1}$ for $\omega_H = 314.8 \text{ rad s}^{-1}$, much higher than the value reached by the chemically driven one $\langle v_x \rangle = 0.22 \mu\text{m s}^{-1}$ (Figure S2, Supporting Information). Although the latter could be increased by roughening the surface of the hematite particle,^[45] the magnetic actuation scheme provides a full control over particle direction and a constant velocity over time, not perturbed by the fuel concentration in the environment.

The decrease in the slope of the curves in Figure 2d is primarily due to the additional drag coefficient γ experienced by the microdocking, which also grows linearly with the size of the transported cargo. Here $\gamma = 6 \pi \eta R$ and $\eta = 10^{-3}$ Pa·s is the viscosity of water. We demonstrate this point in the inset of Figure 2d by multiplying the experimental data and also the linear fits by γ_R , being $\gamma_R = \gamma_0 + 6 \pi \eta R$ and $\gamma_0 = 3 \pi \eta b$ the friction coefficient of a single microdocking. The product $\langle v_x \rangle \gamma_R$ gives the net propulsion force of the composite particle, that also grows linearly with the driving frequency ω_H . All data in the inset fall on the same line, with small deviations that could be a result of the neglect of the differences in the correction factor due to the interaction with the wall.

Even if the microdocking speed decreases with the cargo size, one could clearly use more magnetic particles to speed up the motion of the assembled structure. This feature is demonstrated in **Figure 3**, which shows different active colloidal clusters composed by different number of microdockers and SiO₂ cargos, Figure 3a, with their corresponding average speeds reported in Figure 3b. These examples represent only few of the several possible configurations observed, but they can be used to illustrate the assembly pathway of the smaller units. When many ellipsoids bind to one cargo, the particles also slightly attract each other due to the phoretic flow, tending to cover the SiO₂ cargo by aligning tip to tip around its surface. The cluster speed increases linearly with the

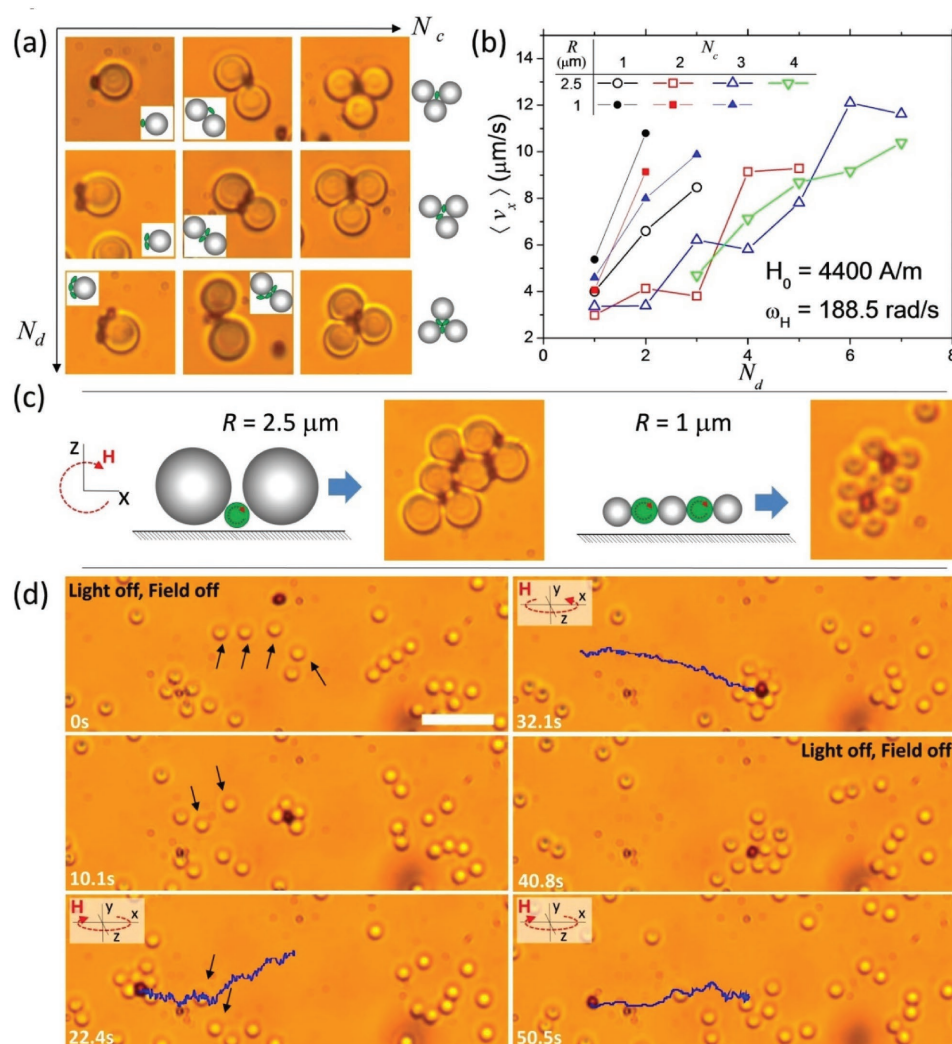


Figure 3. a) Images of different clusters composed by magnetic microdockers and SiO₂ particles ($R = 2.5 \mu\text{m}$) assembled via blue light ($P = 9.94$ mW, $\lambda = 450\text{--}490$ nm). Schematics indicating the number of ellipsoids and their location within the cluster. b) Average translational speed versus number of attached dockers (N_d) for the colloidal clusters composed by small cargos ($R = 1 \mu\text{m}$, filled symbols) and large cargos ($R = 2.5 \mu\text{m}$, empty symbols). N_c denotes the number of cargos present in the cluster. c) Schematics with experimental images illustrating the position of the ellipsoids in the assembled clusters. d) Sequence of images showing the cluster assembly via application of blue light, (from $t = 0$ s to $t = 22.4$ s), transport of the cargo toward left (from $t = 10.1$ s to $t = 22.4$ s), right ($t = 32.1$ s), the cluster disassembly by turning off the illumination ($t = 40.8$ s) and the final propulsion of the sole magnetic dockers toward left ($t = 50.5$ s). Arrows in the first three images mark the colloidal cargos (radius $R = 1 \mu\text{m}$) that are finally attracted to the magnetic dockers. Schematics on the top right of third, fourth, and sixth image display the sense of rotation of the field applied in the (x, z) plane with frequency $\omega_H = 125.6$ rad s⁻¹ and amplitude $H_0 = 4400$ A m⁻¹. Scale bar in first image is $10 \mu\text{m}$ (Video S4, Supporting Information).

number of attached dockers N_d , as shown by the empty circles in Figure 3b. However, we find that for a high number of cargos, the average speed increases slower since it is affected by the additional drag exerted by the attached particles. As shown in Video S3 in the Supporting Information, clusters of dimers or trimers propelled by the rotating field could display an additional rotational motion in their linear path, which does not affect significantly their translational speed. The clusters composed of large cargos are usually formed by a skeleton of magnetic ellipsoids located in the interstitial regions of a compact triangular lattice, Figure 3c. The situation is different when the cargos have a size similar to the dockers, since the magnetic inclusions become part of the packed structure, as shown on the right side of Figure 3c. Given the radial symmetry of the photoactivated osmotic flow, the dockers attract particles nearby rapidly, forcing them to pack into a compact cluster which completely encircles the magnetic inclusions. However, the phoretic attraction represents not only a reversible but also a rather flexible bond, since it allows the magnetic particles to rotate within the structure.

The sequence of images in Figure 3d illustrates the high maneuverability of such composite structures, when subjected to the rotating field. We assemble via blue light a small colloidal tetramer that afterward is translated by the rotating field first toward the left, and later toward the right, just by inverting the chirality of the applied field. During these

operations the illumination is always on, in order to preserve the cluster. The composite structure grows when it approaches to other colloidal cargos, which are attracted by the phoretic flow, reaching its final size at $t = 32.1$ s. Switching off the blue light melts the cluster, dispersing the cargos evenly above the plane. At the end of the process, the microdoker is propelled to a different region to eventually dock and transport back other particles. Besides the basic trajectories shown in Figure 3c, more complex paths can be equally obtained by adjusting on the fly the orientation and direction of the driving field. Drug delivery operations could be performed by using colloidal cargos functionalized with specific chemical agents able to bind and transport functional molecules.

Many microswimmers can be classified as pushers or pullers depending whether the generated flow is outward or inward the axis of net swimming.^[52] When transporting a given cargo, a swimmer can also act as a “pusher” or a “puller”, depending on if it drags the cargo directly in front or behind it. In the last case, transport could occur only if the cargo is bound to the swimmer via a certain interaction but not via the sole mechanical contact of the two surfaces. A lingering question which naturally arises is whether being in front of the transported particle (puller) or behind it (pusher) implies a significant difference in the transport velocity. To answer this question, in Figure 4a we report the translational speed of a towed PS cargo ($R = 5 \mu\text{m}$) versus

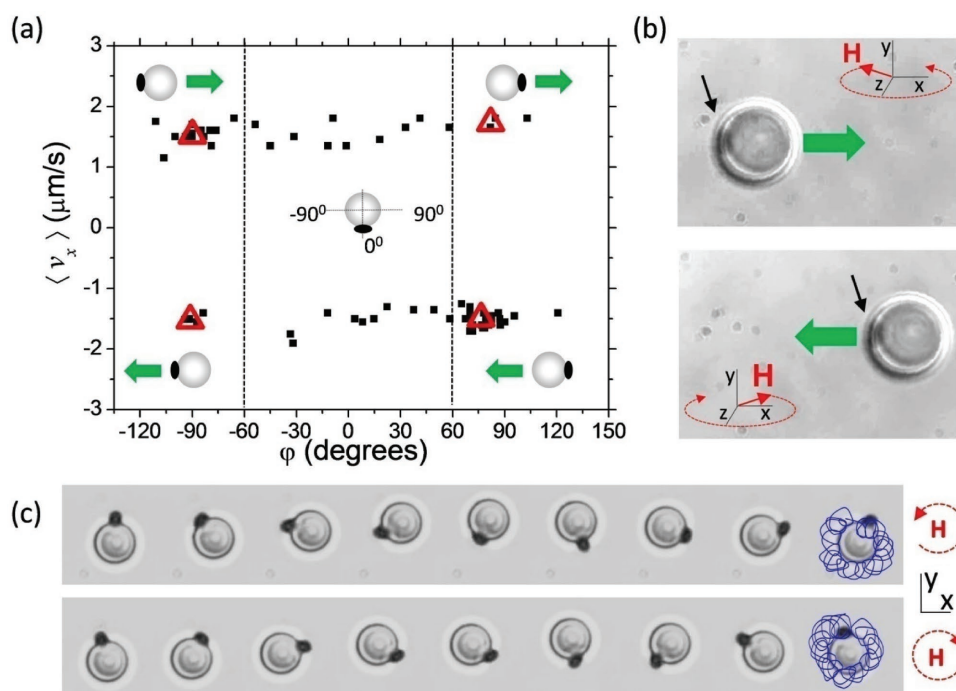


Figure 4. a) Average speed of a microdoker transporting a $10 \mu\text{m}$ PS colloidal cargo versus the angle ϕ formed by the y -axis and the line joining the centers of the particles. The red triangles represent the mean velocity, averaged excluding all velocities corresponding to configurations with angles $-60^\circ < \phi < 60^\circ$. In all measurements the applied field has a frequency of $\omega_H = 125.6 \text{ rad s}^{-1}$ and an amplitude of $H_0 = 4400 \text{ A m}^{-1}$. b) Two images corresponding to the data in (a) showing the “pusher” (top) and the “puller” (bottom) configurations. The sense of rotation of the magnetic field (see small schematics) is opposite in the two images. Green arrows in (a) and (b) indicate the direction of propulsion of the colloidal assembly. c) Rotational motion of one magnetic microdoker above a $5 \mu\text{m}$ SiO_2 colloidal cargo. The applied field is circularly polarized in the (x, y) plane with amplitude $H_0 = 2900 \text{ A m}^{-1}$ and frequency $\omega_H = 125.6 \text{ rad s}^{-1}$. Top panel refers to counterclockwise rotation while bottom panel to clockwise. The last snapshots in both cases display the epitrochoid-like trajectory of one tip of the particle above the colloidal cargo (Video S5, Supporting information). The trajectory can be matched by using the parametric equations: $x = (R_c + R_d)\cos(t) - \delta\cos((R_c + R_d)/R_d t)$; $y = (R_c + R_d)\sin(t) - \delta\sin((R_c + R_d)/R_d t)$; where $R_c = 2.5 \mu\text{m}$ and $R_d = 0.3 \mu\text{m}$ are geometrical radii of the trajectories described by the cargo and doker, and $\delta = 0.1 \mu\text{m}$ is a fitting parameter.

the relative angle φ , which is the angle between the y axis and the line joining the centers of the two particles. This angle is defined in the schematic in Figure 4a. The sign of the speed of the microdocking and the angle φ are used to determine if the propeller tows the cargo in a pusher or a puller configuration. From the experimental data, we do not observe significant differences of the speed when being in one of the two configurations. However, the relative position can be essential during the process of cargo release: if the docker is placed behind the cargo, then the cargo could be released faster without entering into the region where the cargo could react.

The manipulation via rotating field also allows controlling the position of the docker around the cargo as demonstrated in Figure 4c. When subjected to a rotating in-plane field, $\vec{H} = H_0(\cos(\omega_H t), \sin(\omega_H t), 0)$, the hematite particle performs rotational motion close to the surface of the silica particle, remaining attached to the cargo due to the phoretic attraction. The trajectory traced by the tip of the microdocking around the cargo equator is an epitrochoid, as shown in the last two microscope images in Figure 4c. The docker does not roll along the cargo surface, but rather performs a “walking”-like motion, since the combination of osmotic flow and the magnetic torque lift the hematite particle during its excursion around the cargo equator. One can easily control the direction of rotation of the hematite particle by changing the sense of rotation of the applied field. The driving frequency controls the period of the epitrochoid and thus the average circulation speed $\langle \omega \rangle$ of the microdocking around the cargo. In the range of frequencies used, $\omega_H \in [20, 300]$ rad s⁻¹, the rotating docker follows synchronously the applied field and thus $\langle \omega \rangle$ is proportional to the driving frequency $\langle \omega \rangle = \alpha \omega_H$, as shown in Figure S3 in the Supporting Information. These features enable a selective control and reorganization of the bound couple microdocking/cargo on the fly, optimizing the potential shipping and final delivery of any drug transported by the cargo.

3. Conclusion

In summary, we investigated the transport properties and versatility of ferromagnetic hematite microdockers towing microscopic cargos and being powered by an external rotating magnetic field. The colloidal cargos can be reversibly bound to these microdockers via photoinduced decomposition of H₂O₂ in water, and can be picked up, transported, and released on command in any place of the experimental platform. Since the proposed method works well for both cases, one could envisage switching from a chemically based driving mechanism to a magnetic one in order to optimize the towing process or reduce the consumption of fuel within the medium. The possibility of varying the driving frequency of the applied field allows for tuning the speed of the prototype in order to fasten or slow down the delivery of a given cargo in a fluidic based microdevice. Moreover, the use of a time dependent magnetic field allows us to vary the relative position of carrier and cargo, in order to change at will the towing scheme from a pusher to a puller, depending on the defined need. While the amount of H₂O₂ required to

trigger the cluster assembly excludes, for the moment, direct biological applications, our method can be improved in the future by contemplating different and more biocompatible reaction schemes. Finally, in absence of catalytic agents, the sole magnetic dockers can be used to drag biological species via the hydrodynamic flow field generated by their coupled rotational–translational motion. A similar feature indeed was demonstrated for isotropic particles driven above a magnetic substrate.^[53]

4. Experimental Section

Particle Synthesis and Procedures: Monodisperse hematite (α -Fe₂O₃) ellipsoids were synthesized via a co-precipitation of FeCl₃ and NaOH solutions, followed by a hydrothermal treatment of the slurry in the presence of potassium sulfate as an additive. A sodium hydroxide solution (21.64 g of NaOH in 90 mL of high deionized water) was slowly mixed with an iron chloride hexahydrate solution (54.0 g FeCl₃·6H₂O in 100 mL of high deionized water) at room temperature. During the mixing process, which lasted 5 min, both solutions were vigorously stirred, giving rise to an iron hydroxide gel submerged in an acid environment. After this stage, a 10 mL aqueous solution containing 0.29 g of potassium sulfate (K₂SO₄) was added, and the resulting dark brown mixture was stirred for another 5 min. Then, the mixture was hermetically sealed and left unperturbed in an oven at 100 °C for 8 days. After 8 days, a dense aqueous suspension composed of monodisperse ellipsoids together with rod-like nanoparticles made of akaganeite was obtained. The ellipsoids were recovered by diluting the suspension with high deionized water, letting the particles sediment and removing the resulting yellowish-brown supernatant, a procedure that was repeated several times. The hematite ellipsoids were finally functionalized with sodium dodecyl sulfate (SDS). The surfactant was grafted on the particle surface by dispersing the ellipsoids in an aqueous solution containing 0.12 g of SDS in 80 mL of high deionized water. Finally, the pH of the resulting solution was adjusted to 8.5–9.5 by adding tetramethylammonium hydroxide (TMAH). The authors used TMAH since in basic conditions (pH ≈ 9.5) the hematite particles display a negative phoresis, i.e., they are able to attract colloidal particles made by PS or silica, as previously reported.^[54] In contrast, the authors also found that a small positive phoresis (repulsion of the cargos from the dockers) appeared when the pH was adjusted to 6.5.

Particle size and shape were analyzed by SEM (Quanta 200 FEI, XTE 325/D8395). The nonmagnetic samples employed in this study were commercial aqueous suspensions of monodisperse particles based on silicon dioxide (44054 Sigma-Micro), that are 1–5 μm in size, and commercial aqueous suspensions of polystyrene particles (C37259, Thermo Fisher) 10 μm in size. The use of two types of particles (PS and Si) having different density and surface charges, demonstrated the generality of the proposed approach, which could be applicable to a large variety of microscale cargos.

Observation of the Particles: The solution containing the magnetic dockers and the colloidal cargos was introduced by capillarity in a rectangular microtube made of borosilicate glass (inner dimensions 0.1 × 2.0 mm, CMC scientific) that was immediately sealed. The dynamics of the microdockers were investigated determining

the motion of the colloidal particles with a CCD camera (Basler Scout scA640-74f, Basler), at a frame rate of 50 Hz, mounted on top of a light microscope (Eclipse Ni, Nikon), equipped with high magnification objectives.

Magnetic Coils Systems: The external magnetic field was provided by using two pairs of custom-made coils arranged in an Helmholtz-like configuration and having a common axis aligned along the x and y directions. These custom made coils were composed each one by $N = 1100$ turns of a 0.4 mm thin copper wire, and they were able to generate a uniform magnetic field on the sample plane. A fifth coil was located under the sample cell to provide a perpendicular field along the z direction. AC fields were obtained by connecting the coils to a wave generator (TTI-TGA1244, TTI) feeding a power amplifier (IMG STA-800, stage line or BOP 10-20 M, KEPCO). Under AC field the field amplitudes at different frequencies were calibrated via a Teslometer (FM 205, Projekt Elektronik GmbH).

Illumination Set-Up: The illumination was provided via a commercial mercury-fiber illuminator system (C-HGFI Intensilight, Nikon) connected to an upright optical microscope via an epifluorescent tower. Blue light was obtained via a fluorescent filter cube with excitation wavelength between 450 and 490 nm. The optical power was measured at the sample plane with a power meter (PM200, Thorlabs) equipped with a photodiode sensor (400–1100 nm, S121C, Thorlabs).

Supporting Information

Supporting Information is available from the Wiley Online Library or from the author.

Acknowledgements

The authors acknowledge stimulating discussions with Ignacio Pagonabarraga Mora, Andrej Vilfan, and Igor M. Aronson. The authors acknowledge support from the European Research Council (Project No. 335040). P.T. acknowledges support from Mineco (No. FIS2013-41144-P) and AGAUR (Grant No. 2014SGR878).

- [1] A. Najafi, R. Golestanian, *J. Phys.: Condens. Matter* **2005**, *17*, S1203.
- [2] E. Lauga, T. R. Powers, *Rep. Prog. Phys.* **2009**, *72*, 096601.
- [3] E. M. Purcell, *Am. J. Phys.* **1977**, *45*, 3.
- [4] S. Hernández-Navarro, P. Tierno, J. Ignés-Mullol, F. Sagués, *Soft Matter* **2013**, *9*, 7999.
- [5] F. Ma, S. Wang, D. T. Wu, N. Wu, *Proc. Natl. Acad. Sci. USA* **2015**, *112*, 6307.
- [6] G. Volpe, I. Buttinoni, D. Vogt, H.-J. Kümmerer, C. Bechinger, *Soft Matter* **2011**, *7*, 8810.
- [7] S. Palagi, A. G. Mark, S. Y. Reigh, K. Melde, T. Qiu, H. Zeng, C. Parmeggiani, D. Martella, A. Sanchez-Castillo, N. Kapernaum, F. Giesselmann, D. S. Wiersma, E. Lauga, P. Fischer, *Nat. Mater.* **2016**, *15*, 647.
- [8] R. J. Dijkink, J. P. van der Dennen, C. D. Ohl, A. Prosperetti, *J. Micromech. Microeng.* **2006**, *16*, 1653.
- [9] W. Wang, L. A. Castro, M. Hoyos, T. E. Mallouk, *ACS Nano* **2012**, *6*, 6122.
- [10] R. Dreyfus, J. Baudry, M. L. Roper, M. Fermigier, H. A. Stone, J. Bibette, *Nature* **2005**, *437*, 862.
- [11] L. Zhang, J. J. Abbott, L. Dong, K. E. Peyer, B. E. Kratochvil, H. Zhang, C. Bergeles, B. J. Nelson, *Nano Lett.* **2009**, *9*, 3663.
- [12] A. Ghosh, P. Fischer, *Nano Lett.* **2009**, *9*, 2243.
- [13] P. Tierno, R. Golestanian, I. Pagonabarraga, F. Sagués, *Phys. Rev. Lett.* **2008**, *101*, 218304.
- [14] A. Snezhko, M. Belkin, I. S. Aranson, W.-K. Kwok, *Phys. Rev. Lett.* **2009**, *102*, 118103.
- [15] O. S. Pak, W. Gao, J. Wang, E. Lauga, *Soft Matter* **2011**, *7*, 8169.
- [16] R. F. Ismagilov, A. Schwartz, N. Bowden, G. M. Whitesides, *Angew. Chem. Int. Ed.* **2002**, *41*, 652.
- [17] W. F. Paxton, K. C. Kistler, C. C. Olmeda, A. Sen, S. K. S. Angelo, Y. Cao, T. E. Mallouk, P. E. Lammert, V. H. Crespi, *J. Am. Chem. Soc.* **2004**, *126*, 13424.
- [18] J. R. Howse, R. A. L. Jones, A. J. Ryan, T. Gough, R. Vafabakhsh, R. Golestanian, *Phys. Rev. Lett.* **2007**, *99*, 048102.
- [19] L. F. Valadares, Y.-G. Tao, N. S. Zacharia, V. Kitaev, F. Galembeck, R. Kapral, G. A. Ozin, *Small* **2010**, *4*, 565.
- [20] W. Gao, J. Wang, *Nanoscale* **2014**, *6*, 10486.
- [21] W. Duan, W. Wang, S. Das, V. Yadav, T. E. Mallouk, A. Sen, *Annu. Rev. Anal. Chem.* **2015**, *8*, 311.
- [22] H. Wang, M. Pumera, *Chem. Rev.* **2015**, *115*, 8704.
- [23] X. Lin, Z. Wu, Y. Wu, M. Xuan, Q. He, *Adv. Mater.* **2016**, *28*, 1060.
- [24] S. J. Ebbens, *Curr. Opin. Coll. Interface Sci.* **2016**, *21*, 14.
- [25] W. Gao, A. Pei, R. Dong, J. Wang, *J. Am. Chem. Soc.* **2014**, *136*, 2276.
- [26] W. Gao, A. Uygun, A. J. Wang, *J. Am. Chem. Soc.* **2012**, *134*, 897.
- [27] R. A. Pavlick, S. Sengupta, T. McFadden, H. Zhang, A. Sen, *Angew. Chem. Int. Ed.* **2011**, *50*, 9374.
- [28] S. Guo, Q. Pan, M. B. Khamesee, *Microsyst. Technol.* **2008**, *14*, 307.
- [29] B. J. Nelson, I. K. Kaliakatsos, J. J. Abbott, *Annu. Rev. Biomed. Eng.* **2010**, *12*, 55.
- [30] S. Kim, F. Qiu, S. Kim, A. Ghanbari, C. Moon, L. Zhang, B. J. Nelson, H. Choi, *Adv. Mater.* **2013**, *25*, 5863.
- [31] S. Sanchez, A. A. Solovev, S. M. Harazim, O. G. Schmidt, *J. Am. Chem. Soc.* **2011**, *133*, 701.
- [32] S. Sundararajan, P. E. Lammert, A. W. Zudans, V. H. Crespi, A. Sen, *Nano Lett.* **2008**, *8*, 1271.
- [33] J. Burdick, R. Laocharoensuk, P. M. Wheat, J. D. Posner, J. Wang, *J. Am. Chem. Soc.* **2008**, *130*, 8164.
- [34] C. Peters, M. Hoop, S. Pané, B. J. Nelson, C. Hierold, *Adv. Mater.* **2016**, 28533.
- [35] S. Das, A. Garg, A. I. Campbell, J. R. Howse, A. Sen, D. Velegol, R. Golestanian, S. J. Ebbens, *Nat. Commun.* **2015**, *6*, 8999.
- [36] J. Simmchen, J. Katuri, W. E. Uspal, M. N. Popescu, M. Tasinkevych, S. Sánchez, *Nat. Commun.* **2016**, *7*, 10598.
- [37] A. Snezhko, I. S. Aranson, *Nat. Mater.* **2011**, *10*, 698.
- [38] S. Tottori, L. Zhang, K. E. Peyer, B. J. Nelson, *Nano Lett.* **2013**, *13*, 4263.
- [39] L. Zhang, T. Petit, Y. Lu, B. E. Kratochvil, K. E. Peyer, R. Pei, J. Lou, B. J. Nelson, *ACS Nano* **2010**, *4*, 6228.
- [40] L. Baraban, R. Streubel, D. Makarov, L. Han, D. Karnausenko, O. G. Schmidt, G. Cuniberti, *ACS Nano* **2013**, *7*, 1360.
- [41] A. M. Maier, C. Weig, P. Oswald, E. Frey, P. Fischer, T. Lied, *Nano Lett.* **2016**, *16*, 906.
- [42] T. R. Kline, W. F. Paxton, T. E. Mallouk, A. Sen, *Angew. Chem. Int. Ed.* **2005**, *44*, 744.
- [43] P. Tierno, R. Albalat, F. Sagués, *Small* **2010**, *6*, 1749.
- [44] J. Palacci, S. Sacanna, A. P. Steinberg, D. J. Pine, P. M. Chaikin, *Science* **2013**, *339*, 936.
- [45] J. Palacci, S. Sacanna, A. Vatchinsky, P. M. Chaikin, D. J. Pine, *J. Am. Chem. Soc.* **2013**, *135*, 15978.

- [46] T. Sugimoto, M. M. Khan, M. Muramatsu, *Colloids Surf., A* **1993**, 70, 167.
- [47] F. Martinez-Pedrero, A. Cebers, P. Tierno, *Soft Matter* **2016**, 12, 3688.
- [48] S. H. Lee, C. M. Liddell, *Small* **2009**, 5, 1957.
- [49] A. J. Goldmann, R. G. Cox, H. Brenner, *Chem. Eng. Soc.* **1967**, 22, 637.
- [50] Assuming that the translational motion of the ellipsoids is due to the sole rotation induced by the applied field, we find that, $f_r = f_{rot}/f_{trans}$, being $f_{rot} = \frac{2}{15} \log\left(\frac{b}{2h}\right) - 0.2526$, and $f_{trans} = \left(\frac{8}{15} + \frac{32}{375} \frac{h}{b}\right) \left(\log\left(\frac{b}{h}\right) + 0.58461\right)$ as derived in the lubrication limit and for a small distance h between the surface of a particle of radius $b/2$ and the wall. We use the expression derived in [49] for a spherical particle given the small aspect ratio of our ellipsoids.
- [51] A. Cebers, M. Ozols, *Phys. Rev. E* **2006**, 73, 021505.
- [52] M. T. Downton, H. Stark *J. Phys.: Condens. Matter* **2009**, 21, 204101.
- [53] P. Tierno, S. V. Reddy, J. Yuan, T. H. Johansen, T. M. Fischer, *J. Phys. Chem. B* **2007**, 111, 13479.
- [54] a) J. Palacci, S. Sacanna, D. J. Pine, P. Chaikin, P. Michael, *US Patent Application* num. 14/759910, **2016**; b) J. Palacci, S. Sacanna, S.-H. Kim, G.-R. Yi, D. J. Pine, P. M. Chaikin, *Phil. Trans. A* **2014**, 372, 20130372.

Received: October 14, 2016
Revised: January 13, 2017
Published online: March 15, 2017

PUBLICATION 6

Supporting Information



Supporting Information

for *Small*, DOI: 10.1002/sml.201603449

Assembly and Transport of Microscopic Cargos via
Reconfigurable Photoactivated Magnetic Microdockers

*Fernando Martinez-Pedrero, Helena Massana-Cid, and Pietro
Tierno**

Supporting Information

Assembly and Transport of Microscopic Cargos via Reconfigurable Photoactivated Magnetic Microdockers

Fernando Martinez-Pedrero, Helena Massana-Cid and Pietro Tierno

Supplementary Figure 1S.

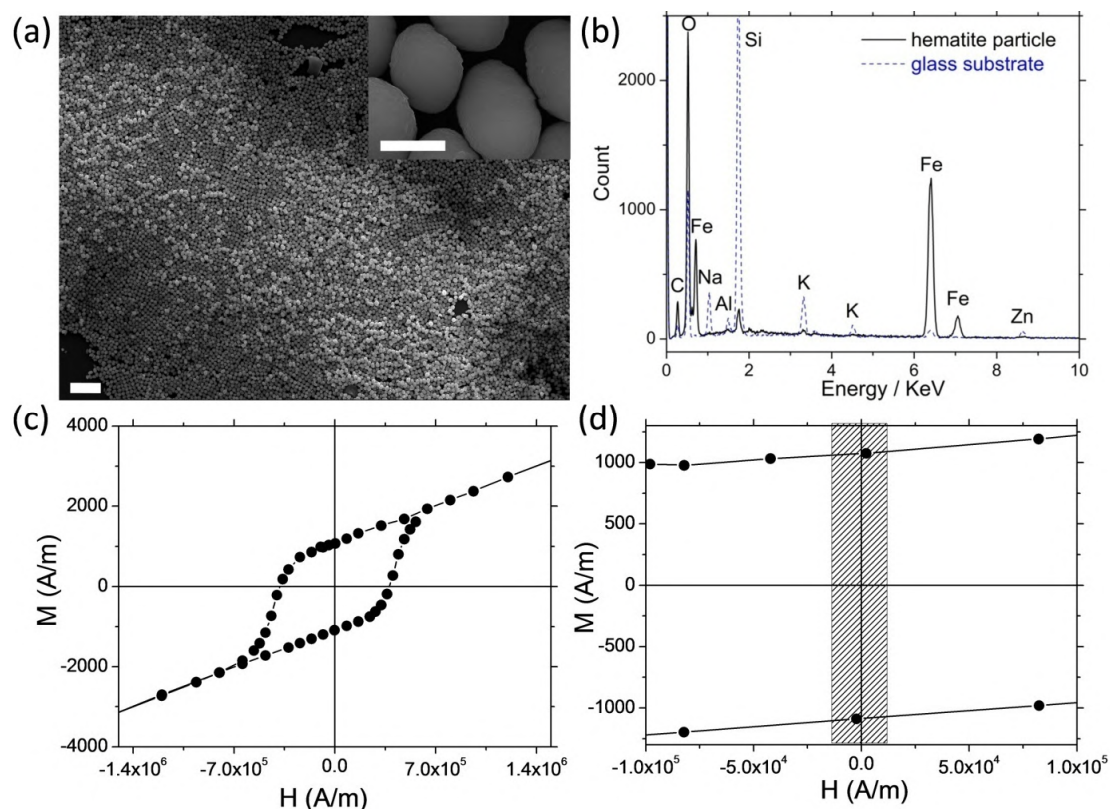


Figure 1S. (a) Scanning electron microscopy image showing the monodisperse hematite ellipsoids, with an enlargement on the top-right inset. Scale bar is 10 μm (1 μm for the inset). (b) Corresponding energy-dispersive X-ray spectroscopy (EDX) of the hematite ellipsoids (continuous black line) and of the sample holder (dashed blue lines) composed by a borosilicate glass. The peaks at 0.71, 6.41 and 7.05 KeV denote the location of Fe, at 0.52 KeV of Oxygen while 1.74 KeV of Si, the latter being present due to the sample holder. (c) SQUID magnetization curve of a dry sample of hematite particles and (d) enlargement of the central section, which displays the range of field used in the propulsion experiments (shaded region). The almost constant slope of M in the shaded region demonstrates the small contribution of the induced moment as compared to the permanent one.

Supplementary Figure 2S.

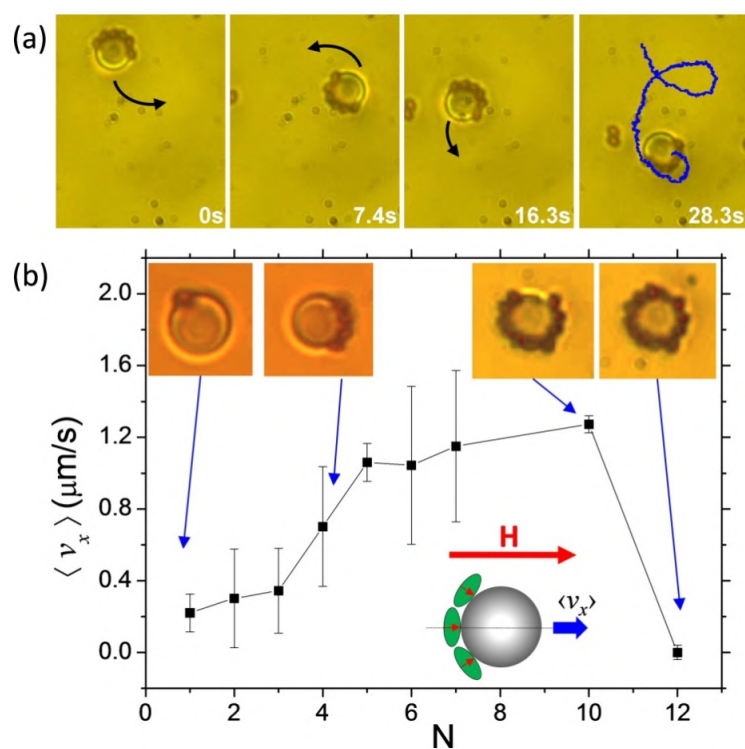


Figure 2S. (a) Optical microscope images showing the active motion of a 5 μm SiO₂ particle decorated by 6 hematite ellipsoids under a constant blue light illumination. (b) Average translational speed measured in presence of a small DC field for a 5 μm SiO₂ decorated with a different number of hematite particles. Schematic on the bottom shows the geometry of one cargo propelled chemically by three microdocks while the composite particle is oriented by a static magnetic field \mathbf{H} , oriented along the x-axis.

Supplementary Figure 3S.

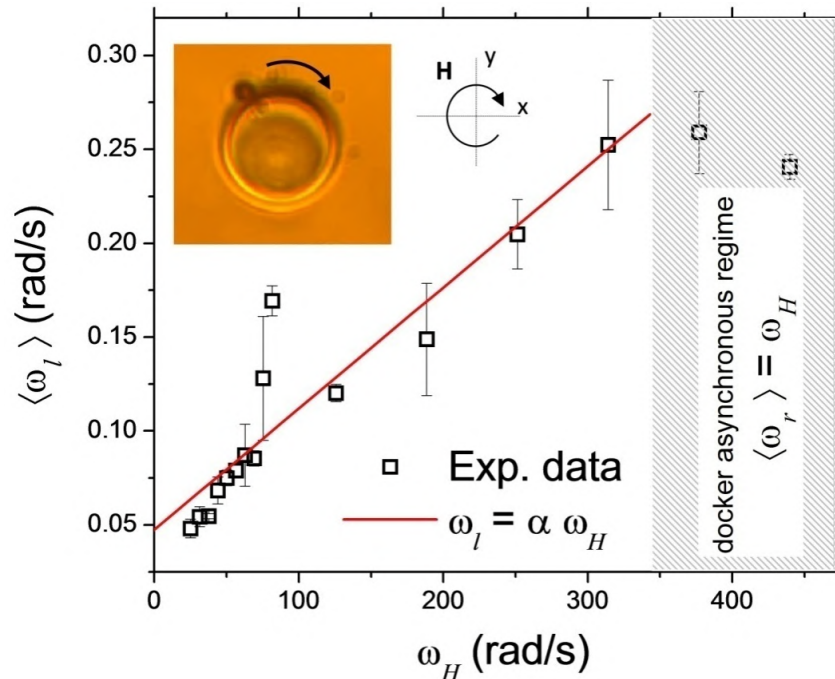


Figure 3S. Average circulation frequency of an hematite microdocked around a 10 μm polystyrene particle, on a plane parallel to the glass surface, versus driving frequency ω_H . The hematite particle was subjected to a rotating magnetic field in the particle plane (x, y) with amplitude $H_0=2700$ A/m. The empty symbols denote the experimental data, while the linear fit emphasizes the fact that in the range of frequency used the motion occurs in the "synchronous" regime of the microdocked, where $\langle \omega_r \rangle = \omega_H$. Top inset shows an optical microscope snapshot illustrating the microdocked and the polystyrene cargo with the corresponding schematic of the rotating magnetic field \mathbf{H} .

Supplementary text: Chemically powered motion.

In **Figure 2S** we analyze the average speed of the microdockers due to the sole chemical reaction when carrying a microcargo. The average speed of the transported cargo can be increased by enhancing the number of hematite particles attached to it. Fig.2S(a) shows a typical particle trajectory of a 5 μm silica bead covered by 6 hematite microdockers and subjected to a constant illumination, via blue light. When binding to the cargo due to the phoretic interaction, the ellipsoids also slightly attract each other, and thus they tend to align close to each other on the particle surface. The microdockers form a protective "hand", which drags the cargo along a randomized path. The random trajectory could result either from small differences in the chemical propulsion of the attached particles, or due to the rotational diffusive motion of the composite cluster. In Fig.2S(b) we show how the average propulsion speed depends on the number of attached particles. Here, we use a small uniform magnetic field for steering the composite micro-object along a linear path. The chemical powered motion displays a translational speed which almost grows linearly with the number N of the attached hematite particles. A higher number of hematite ellipsoids indeed enlarges the area of the composite cluster able to generate osmotic flow, reaching a maximum speed of $\langle v_x \rangle = 1.2 \mu\text{m/s}$ for $N=9$ attached dockers. When the microdockers encircle completely the colloidal cargo, the chemical gradient is symmetric and the translational speed vanishes, since now the whole perimeter surrounding the cargo generates osmotic flow. As a consequence, the encircled particle performs an enhanced diffusive motion, but does not show any net drift.

Supplementary Movie legends

Video1S(.MPEG1): Single particle propulsion. Hematite microellipsoids transported above a glass substrate upon application of an external rotating magnetic field with amplitude $H_0=4400$ A/m and frequency $\omega_H = 502.6$ rad/s. The movie is in real time and it corresponds to Fig.1(c) in the main article.

Video2S(.MPEG1): Reversible binding-unbinding via light activation. Video illustrating the phoretic attraction induced by blue light ($\lambda=450-490$ nm, $P = 1.04$ mW) applied after $t = 6.38$ s on a field of view that encloses a docker and a large PS cargo (radius $R=2.5$ μm) suspended in a solution of 9%-by-volume H_2O_2 in water. After $t = 18.3$ s, the light is switched off and the particles is dispersed back by random fluctuations. The movie is in real time and it corresponds to Fig.2b in the main article.

Video3S(.MPEG1): Transport of colloidal clusters composed by $N_c = 1$ SiO_2 cargo (radius $R=2.5$ μm) and $N_d= 3$ magnetic dockers (top row); $N_c = 3$ and $N_d= 3$ (middle row); $N_c = 7$ and $N_d= 7$ (bottom row). The rotating magnetic field used to transport these structures was circularly polarized with an amplitude $H_0=4400$ A/m and frequency $\omega_H=188.5$ rad/s. The movies are in real time.

Video4S(.MPEG1): Video illustrating the formation of a cluster upon illumination via blue light. The assembly is transported towards the left and right via application of a rotating magnetic field with frequency $\omega_H=125.6$ rad/s and amplitude $H_0=4400$ A/m. After $t=47.1$ s the illumination and the rotating field are switched off, and the cargos are released. Then the magnetic field is switched on again, and the particle is transported toward right. The movie is in real time and corresponds to the sequence of images in Fig.3(d) in the main article.

Video5S(.MPEG1): Rotation and transport above the cargo. The video illustrates the different operation of binding (via blue light), rotation above the silica colloidal cargo (radius $R=2.5$ μm) and transport via magnetic field. The rotation was powered by a circularly polarized rotating field in the (x,y) plane with amplitude $H_0=2900$ A/m and frequency $\omega_H=125.6$ rad/s. Reversing the sense of rotation of the field inverts the angular rotation of the magnetic microdocker which now moves around the cargo in the opposite sense. Top panel refers to counterclockwise rotation while bottom panel to clockwise. The movie is in real time and it corresponds to Fig.4c of the main article.

PUBLICATION 7

Active apolar doping determines routes to colloidal clusters and gels

Proceedings of the National Academy of Sciences **115**, 10618-10623
(2018)

Helena Massana-Cid^{1,5}, Joan Codina^{1,2,5}, Ignacio Pagonabarraga^{1,2,3} and Pietro Tierno^{1,2,4}

¹ Departament de Física de la Matèria Condensada,
Universitat de Barcelona, 08028 Barcelona, Spain

² Universitat de Barcelona Institute of Complex Systems
(UBICS), Universitat de Barcelona, 08028 Barcelona, Spain

³CECAM, Centre Européen de Calcul Atomique et Moléculaire,
École Polytechnique Fédérale de Lausanne Batochime,
Avenue Forel 2, 1015 Lausanne, Switzerland

⁴ Institut de Nanociència i Nanotecnologia, IN²UB,
Universitat de Barcelona, 08028 Barcelona, Spain

⁵ These authors contributed equally



Active apolar doping determines routes to colloidal clusters and gels

Helena Massana-Cid^{a,1}, Joan Codina^{a,b,1}, Ignacio Pagonabarraga^{a,b,c}, and Pietro Tierno^{a,b,d,2}

^aDepartament de Física de la Matèria Condensada, Universitat de Barcelona, 08028 Barcelona, Spain; ^bUniversitat de Barcelona Institute of Complex Systems, Universitat de Barcelona, 08028 Barcelona, Spain; ^cCentre Européen de Calcul Atomique et Moléculaire, École Polytechnique Fédérale de Lausanne, 1015 Lausanne, Switzerland; and ^dInstitut de Nanociència i Nanotecnologia, Universitat de Barcelona, 08028 Barcelona, Spain

Edited by Michael L. Klein, Temple University, Philadelphia, PA, and approved September 7, 2018 (received for review June 29, 2018)

Collections of interacting active particles, self-propelling or not, have shown remarkable phenomena including the emergence of dynamic patterns across different length scales, from animal groups to vibrated grains, microtubules, bacteria, and chemical- or field-driven colloids. Burgeoning experimental and simulation activities are now exploring the possibility of realizing solid and stable structures from passive elements that are assembled by a few active dopants. Here we show that such an elusive task may be accomplished by using a small amount of apolar dopants, namely synthetic active but not self-propelling units. We use blue light to rapidly assemble 2D colloidal clusters and gels via nonequilibrium diffusiophoresis, where microscopic hematite dockers form long-living interstitial bonds that strongly glue passive silica microspheres. By varying the relative fraction of doping, we uncover a rich phase diagram including ordered and disordered clusters, space-filling gels, and bicontinuous structures formed by filamentary dockers percolating through a solid network of silica spheres. We characterize the slow relaxation and dynamic arrest of the different phases via correlation and scattering functions. Our findings provide a pathway toward the rapid engineering of mesoscopic gels and clusters via active colloidal doping.

active systems | colloids | gels

Active colloids constitute an emergent class of autonomous, motile elements that display fascinating collective behavior evoking that of active biological systems (1–8). Given the experimental accessible time/length scales, these artificial prototypes represent a laboratory-scale model system for self-organization under out-of-equilibrium conditions with the possibility of describing them in terms of simplified potentials and interactions. While densely packed passive colloids have been used as a reference system to analyze the formation of gels (9), glasses (10), or jammed phases (11), active systems may provide a faster route toward their formation, and richer phenomenologies, due to the emergent dynamics intrinsic to their nonequilibrium nature. However, at low or moderate concentrations, active particles displaying self-propulsion have been unable to form stable and long-living structures due to the presence of a net drift velocity that gives rise to collisional dynamics. Recent experiments (12–15) and simulations (16–22) have reported the formation of clusters from mixtures of active–passive systems, but at moderate concentrations such structures were found to be dynamic in nature, i.e., continuously breaking and reforming over time.

We show here that more routes toward the formation of 2D clusters and gels may be uncovered by using a few active apolar colloidal dopants that are dispersed in a population of inert passive particles. The activity and interactions between the synthetic dopants are controlled by light, and the absence of self-propulsion makes them ideal dockers for the formation of stable and strong bonds that chemophoretically glue different inert particles, creating solid, space-filling networks. This contrasts with previous works based on active polar, i.e., self-propelling, units that were activated by external fields or chemical reactions. By

varying the fraction of doping, we show different types of gels where either the active particles localize in the interstitial regions of large clusters or they assemble into percolating structures that surround the passive spheres, forming a protective, structural scaffold. Computer simulations complement our experiments and allow us to explore in depth the structural relaxation of the identified phases.

To realize gels and clusters via external command, we use a mixture of passive and apolar colloidal particles. The former are silica microspheres (diameter $\sigma_p = 4 \mu\text{m}$) that present simple Brownian fluctuations in the dispersing medium, here presented by a mixture of water and 9% hydrogen peroxide (H_2O_2). The apolar particles are ferromagnetic hematite ellipsoids with a long (short) axis equal to $a = 1.8 \mu\text{m}$ ($b = 1.3 \mu\text{m}$) (Fig. 1A). The particles are characterized by a small, permanent dipole moment $m = 2 \times 10^{-16} \text{Am}^2$ in the direction of the particle short axis (23). The presence of this moment adds a further degree of functionality to the system, since external magnetic fields can be used as an independent tool to manipulate the inclusions outside or within the formed clusters. The hematite magnetic dipole can also be used as an additional means to manipulate the morphology of the emerging structures, since the magnetic anisotropy favors the initial chaining of the hematite ellipsoids. Hence, both the hematite chain orientation and the associated structure kinetics may be controlled by an external field.

Once dispersed in water and sedimented above the surface, the system is globally in a liquid phase, with both types of particles performing simple Brownian diffusion (Fig. 1B). Illumination with blue light activates only the hematite ellipsoids that start

Significance

Collections of polar active particles have been unable to form stable and long-living structures due to the presence of self-propulsion. We solve this timely issue by introducing the concept of “active doping” and show that a few light-activated apolar, i.e., non-self-propelling, units can be used to rapidly trigger the formation of solid clusters and gels composed of passive colloidal particles. Our active doping can be used to assemble disparate microscopic objects, including synthetic or biological ones, paving the way toward the extension of fundamental concepts of gel and glass formation to active out-of-equilibrium systems.

Author contributions: I.P. and P.T. designed research; H.M.-C. and J.C. performed research; H.M.-C. and J.C. contributed new reagents/analytic tools; H.M.-C., J.C., I.P., and P.T. analyzed data; and P.T. wrote the paper.

The authors declare no conflict of interest.

This article is a PNAS Direct Submission.

This open access article is distributed under [Creative Commons Attribution-NonCommercial-NoDerivatives License 4.0 \(CC BY-NC-ND\)](https://creativecommons.org/licenses/by-nc-nd/4.0/).

¹H.M.-C. and J.C. contributed equally to this work.

²To whom correspondence should be addressed. Email: ptierno@ub.edu.

This article contains supporting information online at www.pnas.org/lookup/suppl/doi:10.1073/pnas.1811225115/-/DCSupplemental.

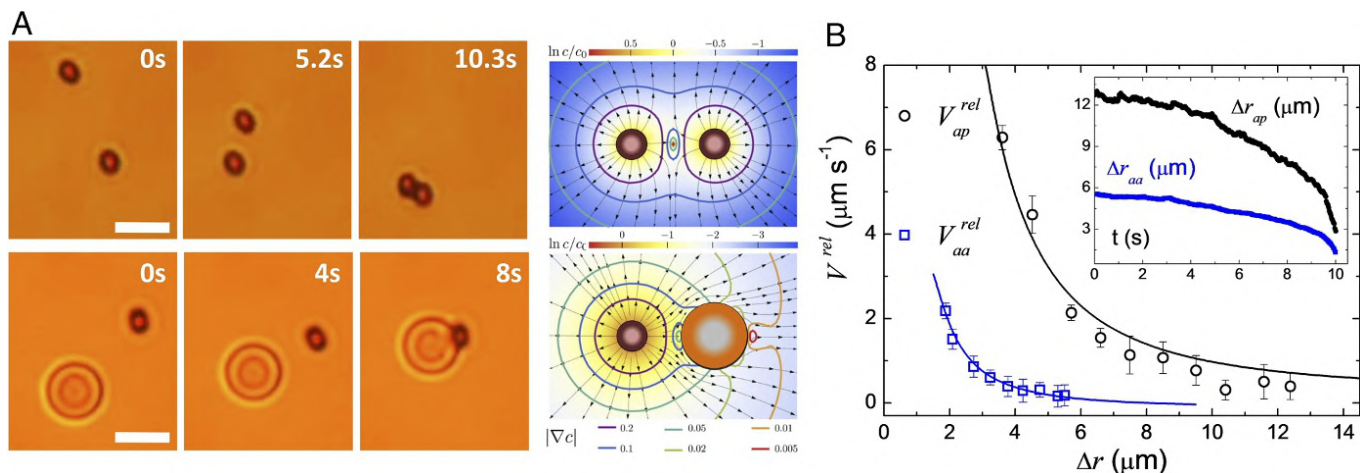


Fig. 2. (A, Left) Microscope images showing the light-induced attraction between two active–active (aa) particles (Top) and an active–passive (ap) pair (Bottom). A, Right shows the color-coded logarithm of the chemical-field concentration around the aa (Top) and ap (Bottom) pair. The vector field denotes at each point the direction of the diffusiophoretic speed, while the level curves are the absolute value of the velocity-field module. (B) Relative particle speed V^{rel} of an ap pair (black circles) and of an aa pair (blue squares) vs. relative distance Δr . Solid lines are fitted to the data following the model in the main text. B, Inset shows the corresponding distances Δr vs. time.

r. In a first approximation, an active spherical particle of diameter σ_a , acting as a source, generates an isotropic, monopolar, chemical field, $c(r) = c_0 + \alpha\sigma_a^2/(4D_c r)$, where D_c is the diffusion constant of the chemical product, and α is the production/consumption rate of the chemical per unit area (28, 29). A probe particle of diameter σ at a distance d from the source experiences a concentration difference δ across its size of magnitude proportional to $\delta \propto \alpha c'(d) \propto \alpha/d^2$. To the lowest order, this concentration gradient on the probe particle can be described by a dipolar chemical field. This chemical gradient induces a diffusiophoretic velocity of the probe particle, $\mathbf{v} = \mu\nabla_{\parallel} c$, where μ is a mobility, and forces motion of the embedding fluid (Fig. 2A). Integration of the surface velocity over the surface of the probe particle results in a net diffusiophoretic velocity with dominant magnitude $v \propto d^{-2}$. Specifically, the relative speed between pairs of active and passive particles of radii, σ_a and σ_p , respectively, reads as

$$V_{ap}^{rel} = V_0 \left[\bar{\mu} \left(\frac{\sigma_a}{d} \right)^2 + \frac{1}{4} \left(\frac{\sigma_p}{\sigma_a} \right)^3 \left(\frac{\sigma_a}{d} \right)^5 \right], \quad [1]$$

$$V_{aa}^{rel} = 2V_0 \left[\left(\frac{\sigma_a}{d} \right)^2 + \frac{1}{4} \left(\frac{\sigma_a}{d} \right)^5 \right], \quad [2]$$

where $V_0 = \mu_a \sigma_a^2 / (12D_c)$ is the characteristic chemical diffusiophoretic velocity for an active pair, and $\bar{\mu} = \mu_p / \mu_a$ is the ratio between mobilities of the two types of particles (*Materials and Methods*). The first terms on the right-hand side of Eqs. 1 and 2 describe the direct interaction between two particles, while the second terms result from the reflection of the chemical concentration produced by an active particle on the receptor one.

Due to their permanent magnetic moment, the hematite ellipsoids will attract magnetically at short distances, forming ribbon-like structures where they assemble side by side to minimize their magnetic energy. For parallel aligned magnetic particles, such interactions contribute to the relative speed with a term of smaller magnitude, $2V_m(d_a/r)^4$. Here $V_m = 3\mu_0 m^2 / (4\pi^2 \eta d_p^5)$, with μ_0 the permittivity of vacuum and η the kinematic viscosity of the dispersing medium. Thus, two apolar particles will approach with a total relative velocity $V_{aa} = V_{aa}^{rel} + V_m$. As shown in Fig. 2B, we validate the derived functional dependence

of the interaction velocity for a pair of particles vs. Δr by fitting Eqs. 1 and 2 to the experimental data. We then use the result to calibrate the magnitudes of V_0 and $\bar{\mu}$ for the numerical simulation. At parity of light power and H_2O_2 concentration, we find a stronger attraction between ap particles than between two active ones. The attractive phoretic flow generated by one active particle can easily drag a passive sphere nearby, while two activated dopants have to adjust their relative orientation to assemble side by side (Fig. 2A). When in close contact, the magnetic dipolar interaction becomes dominant and promotes chain formation. We note that the magnetic interactions are shorter range compared with the phoretic ones. In fact, for distances of $r \sim 1 \mu\text{m}$ they become of the order of thermal energy $U_m \sim k_B T$, being $T = 293 \text{ K}$, the ambient temperature.

We next characterize the assembly process in a mixture of hematite and silica particles, by varying the relative surface fraction covered by the two active and passive particles, quantified by $\Phi_a = N_a \pi a b / (4L^2)$ and $\Phi_p = N_p \pi \sigma_p^2 / (4L^2)$, respectively. Here L is the lateral size of the observation area and N_a, N_p the number of particles of a given type. The emerging stationary phases are shown in Fig. 3A, while the diagram in Fig. 3B reports their location in the (Φ_a, Φ_p) plane. The system is activity quenched from a homogeneous distribution of silica particles and hematite ellipsoids. We observe the appearance of a rich phase behavior after a fast aggregation process, with different types of clusters and space-filling structures. In the first case, the clusters may be either composed of a triangular lattice of silica colloids glued together by a few interstitial dopants ($\Phi_a \leq 0.06, \Phi_p < 0.4$, cluster I) or composed of a more disordered morphology ($0.09 < \Phi_a < 0.2$ and $\Phi_p < 0.25$, cluster II). Here an entangled cluster-percolating network of active particles destroys the hexagonal structure of the silica clusters and slows down its dynamics, as shown in Fig. 4. At a larger surface fraction of ellipsoidal particles, $\Phi_a > 0.2$, chains of active particles completely surround the silica clusters, forming a continuous gel-like structure (gel II). Another way to create an arrested gel is by increasing the concentration of silica particles Φ_a . Above $\Phi_p = 0.35$ ($0 < \Phi_a < 0.15$), only the silica particles form a percolating network, while few ellipsoids that assemble the structure remain separated within its interstitial region (gel I). In contrast, for $\Phi_a > 0.15$ the active colloids form a percolating network that now completely scaffolds the silica spheres (gel III), preventing the collapse into a compact aggregate. Here the percolation of

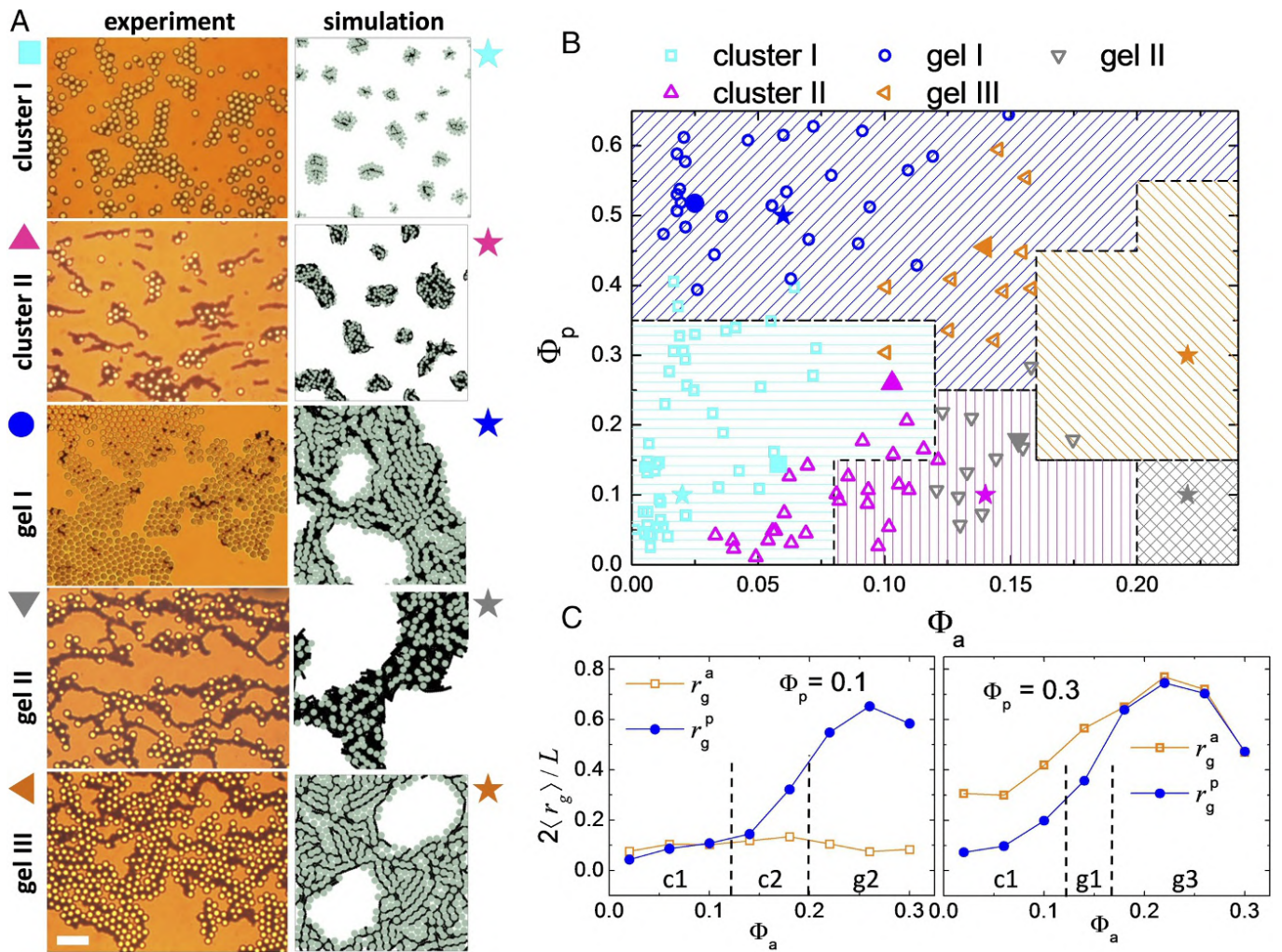


Fig. 3. (A) Sequence of images showing the five different morphologies observed. *Left* column displays experimental images. (Scale bar, 20 μm for all images.) *Right* column shows small snapshots from numerical simulations. See corresponding videos ([Movies S2–S6](#)). (B) Phase diagram in the (Φ_a, Φ_p) plane combining experimental points (open symbols) and simulation results (regions with solid lines). Solid symbols indicate the location of the experimental (symbols) and simulation (stars) images shown in A. (C) Normalized average radius of gyration $\langle r_g \rangle$ vs. fraction Φ_a for different densities of passive particles, $\Phi_p = 0.1$ (*Left* graph) and $\Phi_p = 0.3$ (*Right* graph). Here we define $\langle r_g \rangle = 1/N \sum_k n_k [1/n_k \sum_j (r_j^k - r_{cm}^k)]^{1/2}$, with N the total number of particles, n_k the number of particles that belong to the k th cluster, and r_j^k the position of the j th particle in the k th cluster with center of mass located at position r_{cm}^k .

hematite particles is different from that of the silica ones, as their dipolar attraction leads to a preferential linear growth, giving a certain degree of directionality in the formed structures. The emergence of gel structures is also seen in the low- q divergence of the structure factors $S(q) \sim q^{-D}$, as shown in [SI Appendix, Fig. S1](#).

To reproduce numerically the main features observed in the experimental system, we have set up a simulation code based on the pair interactions between the different colloidal units ([SI Appendix](#)). The phase diagram summarized in [Fig. 3B](#) and the snapshots of the different morphologies in [Fig. 3A](#), *Right* column show that the computational model captures satisfactorily the experimentally observed self-assembled structures. To classify them we calculate the radius of gyration $\langle r_g \rangle$ from the particle positions (30) ([Fig. 3C](#)). From these measurements we distinguish between cluster and percolating structures by identifying a relative percolation threshold for the passive particles, $r_p^* \sim 0.5$, and active inclusions, $r_a^* \sim 0.4$. Cluster phases occur when the emerging structures stay below the percolation thresholds, $\langle r_g^p \rangle < r_p^*$ and $\langle r_g^a \rangle < r_a^*$, and thus type I (II) occurs for $\langle r_g^a \rangle < \langle r_g^p \rangle$ ($\langle r_g^p \rangle < \langle r_g^a \rangle$). We note here that the observed clus-

ters represent a stable stationary phase, as they were found to not coalesce over the whole experimental/simulation time. Further, above the respective percolation thresholds gels I ($\langle r_g^a \rangle < r_a^*$, $\langle r_g^p \rangle > r_p^*$), II ($\langle r_g^a \rangle > r_a^*$, $\langle r_g^p \rangle < r_p^*$), and III ($\langle r_g^a \rangle > r_a^*$, $\langle r_g^p \rangle > r_p^*$) were observed. The presence of a magnetic interaction competing against the attractive interaction of chemical origin gives an internal structure and slows the size growth of the system below $R \sim t^{1/4}$ and arrests the structures in the gel phases. When comparing the images in [Fig. 3](#), one can note a more anisotropic shape for the clusters obtained in the experiments than the one from the simulations. While it could be considered an effect of hydrodynamic interactions (31), it arises from the presence of a small bias field that results from an imperfect balance of the Earth's magnetic field. This field induces initial particle chaining and a more anisotropic growth of the structures.

We characterize the structural arrest of the observed gels both through the dynamic scattering function $F_q(t_0, \Delta t)$ that describes the relaxation of the density field $\rho(\mathbf{r})$ and through the bond-orientational correlation function $C_\Psi(t_0, \Delta t)$, which quantifies the evolution of the local hexatic ordering in the

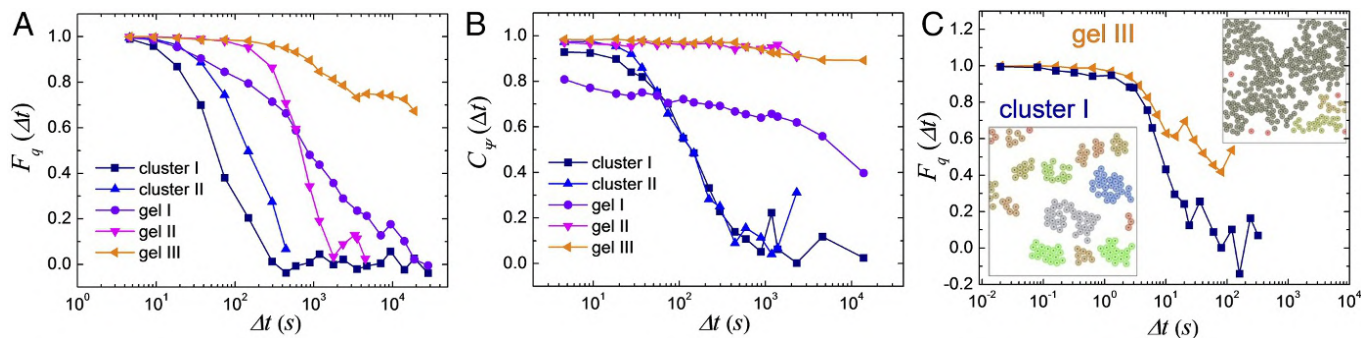


Fig. 4. Numerical simulations. (A and B) Dynamic scattering function $F_q(t)$ (A) and self-correlation function of the bond orientational order $C_\psi(t)$ (B) vs. time calculated for the different assembled structures. Here the wave vector is $|q| = 2\pi/\sigma_p$, being $\sigma_p = 4 \mu\text{m}$ the diameter of the passive spheres. Experiments in C show scattering function from the experimental data obtained for the cluster I ($\Phi_p = 0.22$, $\Phi_a = 0.03$) and gel III phases ($\Phi_p = 0.421$, $\Phi_a = 0.105$). C, Insets show color-coded clusters analyzed from the particle position in the experimental system.

system. Both quantities, defined in *SI Appendix*, are shown in Fig. 4 A and B for the different phases obtained from the computational model. In all cases, we find that the slow dynamics of our systems do not display any intermediate plateaus and thus particle localization, in agreement with what is theoretically predicted for 2D systems (32). While cluster phases rapidly relax toward equilibrium, where F_q vanishes, gel phases display a very slow decay of F_q over all time scales, corresponding to a long subdiffusive regime of the passive particles, as also confirmed by measuring their mean-square displacement. The decay of the bond orientational correlation function identifies more clearly the slow relaxation associated to the gels in contrast with a fast relaxation process for cluster phases. Despite the difficulties in maintaining stable experimental conditions over sufficiently long times for large concentrations of chemically reacting hematite particles, we succeeded in measuring the intermediate dynamic scattering function for the cluster I and gel III phases (Fig. 4C). In agreement with the computational predictions, in the cluster I phase F_q shows a smooth decay for large values of the wave vector q . As we move to small wave vectors, the system decorrelates at longer time scales, while for gel III we observe an initial decay that subsequently slows down.

In conclusion, we have shown that a few active apolar dopants are enough to rapidly engineer large-scale space-filling 2D gels or clusters composed of passive microscopic particles. Thus, we have demonstrated how active doping may be used for the realization of amorphous soft–solid materials. Moreover, we also uncovered a rich scenario for arrested systems that may have distinctive properties emerging from their intrinsic nonequilibrium nature, tunable upon external command. We note that our structures are the result of nonequilibrium interactions that arise solely from the activated hematite particles. Thus, in contrast to clusters and gels realized via attractive interactions such as polymer depletion (9, 10, 33), our particles are subjected to interactions that favor the formation of anisotropic clusters of bicontinuous structures (gel II and gel III). This is not possible via simple attractive interactions such as the ones in a polymer–colloidal mixture (34). It would be interesting to explore how the reported structure changes upon further variation of the density and size of the colloidal dopants. In the first case, we limit to a maximum density of active particles $\Phi_a = 0.17$, to avoid bubble generation and the appearance of artifacts in the experimental system. In the second case, increasing the size of the hematite ellipsoids would favor disorder, as the active particles would not be able to fit within the interstitial region of the passive spheres. Thus, we expect that this could produce a change in the phase diagram in Fig. 3A, with the appearance of more disordered clusters. Our colloidal model system

bridges gels and glass formation with active systems allowing us to investigate on exceptionally short time scales exciting scenarios when driven by nonequilibrium forces. All in all our findings may be extended to other arrested systems and states or more complex environments spanning living and nonliving artificial systems.

Materials and Methods

Experimental Details. Monodisperse hematite ellipsoids are synthesized following the “gel-sol” technique (35). Typically, an iron chloride hexahydrate solution (54.00 g $\text{FeCl}_3 \cdot 6\text{H}_2\text{O}$ in 100 mL of high deionized H_2O) is gradually added to a sodium hydroxide mixture (19.48 g of NaOH in 90 mL of H_2O) and stirred at room temperature. After 5 min, we add to the stirring solution 10 mL of H_2O containing 0.29 g of potassium sulfate (K_2SO_4). The resulting mixture, after being stirred for 5 min, is hermetically sealed and left to age at 100°C for 8 d. After synthesis, the ellipsoids are stabilized with SDS in a highly deionized H_2O (milliQ; Millipore) solution containing also hydrogen peroxide (H_2O_2). We add 0.11 g of SDS and 11 g of H_2O_2 for 80 mL of H_2O . The pH is adjusted to 9.5 by adding tetramethylammonium hydroxide. As passive microspheres we use monodisperse particles of $4 \mu\text{m}$ based on silicon dioxide (44054; Sigma-Micro). Particle size and shape were analyzed by SEM (Quanta 200 FEI, XTE 325/D8395).

The solution containing the magnetic ellipsoids and the SiO_2 particles is introduced by capillarity in a rectangular microtube made of borosilicate glass (inner dimensions $0.1 \times 2.0 \text{ mm}$; CMC Scientific) that is immediately sealed. The particles sediment close to a glass plate, where they remain quasi-2D confined due to gravity, displaying a small thermal motion. The illumination is provided via a commercial mercury fiber illuminator system (C-HGFI Intensilight; Nikon) connected to an upright optical microscope via an epifluorescent tower. Blue light is obtained via a fluorescent filter cube with excitation wavelength between 450 nm and 490 nm. The optical power is measured at the sample plane with a power meter (PM200; Thorlabs) equipped with a photodiode sensor (S121C; Thorlabs). We irradiated at a power $P = 1.04 \text{ mW}$. The dynamics of the particles are monitored with a CCD camera (Basler Scout scA640-74f), at a frame rate of 50 fps, mounted on top of a light microscope (Eclipse Ni; Nikon) equipped with high-magnification objectives.

Theoretical Model. We model active and passive particles as spheres of size σ_a and σ_p , respectively, immersed in a concentration field with Neumann boundary conditions $D_c \partial_r c(r)|_\sigma \propto \alpha$ on each particle, where α is the production/consumption rate of the chemical, and D_c its diffusion constant; for passive particles $\alpha = 0$. We consider the production and consumption to be small compared with the provided reactant and hence disregard fuel depletion.

The concentration field around an active particle, i , located in the origin in the presence of a second one, j , a distance $d = |\mathbf{r}_i - \mathbf{r}_j|$ away from each other, with the center-to-center direction parallel to $\hat{\mathbf{z}}$, can be expressed as

$$c_i(r, d, \theta) = \frac{\alpha_i \sigma_i^2}{4D_c} \frac{1}{r} + c_{ij}(r, d, \theta), \quad [3]$$

where the first term on the right-hand side corresponds to the corresponding production of chemicals, and the second term gives the disturbance of the chemical concentration produced by the j th particle to guarantee the boundary condition in the i th particle. The disturbance term c_{ij} can be expanded as a multipolar series with the axis of symmetry along \hat{z} .

The first contribution on particle i created by a particle j , $c_{ij}^{(1)}(r, d, \theta)$, corresponds to a dipole and depends on the activity α_j of the j th particle, and the distance between the pair,

$$c_{ij}^{(1)}(r, d, \theta) = -\frac{1}{2} \left(\frac{\sigma_j}{2} \right)^3 \frac{1}{d^2} \frac{\alpha_j \sigma_j^2 \cos \theta}{4D_c r^2}. \quad [4]$$

The second dipolar contribution on particle i appears only on active particles. The monopolar field generated by i is reflected on particle j and gives, on i the dipolar term, $c_{ij}^{(2)}$. As expected it depends on α_i as

$$c_{ij}^{(2)}(r, d, \theta) = -\frac{1}{2} \left(\frac{\sigma_i}{2} \right)^3 \left(\frac{\sigma_j}{2} \right)^3 \frac{1}{d^5} \frac{\alpha_i \sigma_i^2 \cos \theta}{4D_c r^2}. \quad [5]$$

The gradient of the chemical concentration on the surface of a sphere generates a tangential diffusiophoretic velocity, $\mathbf{v} = \mu_d \nabla_{\parallel} c(r)$, of the fluid at the particle interface. Momentum conservation leads to a particle velocity,

$$\mathbf{v} = \frac{-1}{\pi \sigma^2} \int d\Omega \mathbf{v}(r, \theta) = (\pi \sigma^2)^{-1} \mu_d \int d\Omega \nabla_{\parallel} c(r, \theta). \quad [6]$$

The integration of $\nabla_{\parallel} c$ for a multipolar expansion of the form $c(\theta, r) = \sum_l B_l P_l(\cos \theta) r^{-(l+1)}$ on a spherical shell of diameter σ results in a velocity in \hat{z} , the symmetry axis of the system:

$$\mathbf{v} = \frac{2}{3} \mu_d \left(\frac{2}{\sigma} \right)^3 B_1 \hat{z}. \quad [7]$$

Introducing Eqs. 4 and 5 into Eq. 7, we recover the relative velocities Eqs. 1 and 2, with a characteristic velocity $V_0 = \alpha \sigma_a^2 / (12D_c)$. We have taken into account that active and passive particles have different diffusiophoretic mobilities, $\mu_d^{(a)}$, $\mu_d^{(p)}$, and have introduced their ratio, $\mu = \mu_d^{(p)} / \mu_d^{(a)}$.

ACKNOWLEDGMENTS. We acknowledge Fernando Martinez-Pedrero for initial experiments and Walter Kob for stimulating discussions. H.M.-C. and P.T. acknowledge support from the Starting Grant "DynaMO" (335040) from the European Research Council. J.C. is supported by the Spanish MEDC Fellowship Grant FPU13/01911 from Ministerio de Educación Cultura y Deporte. J.C. and I.P. acknowledge support from Grant FIS2015-67837-P from Ministerio de Ciencia, Innovación y Universidades and Grant 2017SGR844 from Generalitat de Catalunya. P.T. acknowledges support from Grant FIS2016-78507-C2 from Ministerio de Ciencia, Innovación y Universidades and Grant 2014SGR878 from Generalitat de Catalunya.

- Marchetti MC, et al. (2013) Hydrodynamics of soft active matter. *Rev Mod Phys* 85:1143–1189.
- Bechinger C, et al. (2016) Active particles in complex and crowded environments. *Rev Mod Phys* 88:045006.
- Bricard A, Caussin JB, Desreumaux N, Dauchot O, Bartolo D (2013) Emergence of macroscopic directed motion in populations of motile colloids. *Nature* 503: 95–98.
- Snezhko A, Aranson IS (2011) Magnetic manipulation of self-assembled colloidal asters. *Nat Mater* 10:698–703.
- Yan J, Han M, Zhang J, Luijten E, Granick S (2016) Reconfiguring active particles by electrostatic imbalance. *Nat Mater* 15:1095–1099.
- Palacci J, Sacanna S, Steinberg AP, Pine DJ, Chaikin PM (2013) Living crystals of light-activated colloidal surfers. *Science* 339:936–940.
- Han M, Yan J, Granick S, Luijten E (2017) Effective temperature concept evaluated in an active colloid mixture. *Proc Natl Acad Sci USA* 114:7513–7518.
- Kokot G, et al. (2017) Active turbulence in a gas of self-assembled spinners. *Proc Natl Acad Sci USA* 114:12870–12875.
- Zaccarelli E (2007) Colloidal gels: Equilibrium and non-equilibrium routes. *J Phys Condens Matter* 19:323101.
- Hunter GL, Weeks ER (2012) The physics of the colloidal glass transition. *Rep Prog Phys* 75:066501.
- Liu AJ, Nagel SR (1998) Jamming is not just cool any more. *Nature* 396:21–22.
- Kümmel F, Shabestari P, Lozano C, Volpe G, Bechinger C (2015) Formation, compression and surface melting of colloidal clusters by active particles. *Soft Matter* 11:6187–6191.
- Zhang J, Yan J, Granick S (2016) Directed self-assembly pathways of active colloidal clusters. *Angew Chem Int Ed* 55:5166–5169.
- Singh DP, Choudhury U, Fischer P, Mark AG (2017) Non-equilibrium assembly of light-activated colloidal mixtures. *Adv Mater* 29:1701328.
- Ginot F, Theurkauff J, Detcheverry F, Ybert C, Cottin-Bizonne C (2017) Aggregation-fragmentation and individual dynamics of active clusters. *Nat Commun* 9:696.
- Ni R, Cohen ACS, Dijkstra M (2013) Pushing the glass transition towards random close packing using self-propelled hard spheres. *Nat Commun* 4:2704.
- Ni R, Cohen ACS, Dijkstra M, Bolhuis PG (2013) Crystallizing hard-sphere glasses by doping with active particles. *Soft Matter* 10:6609–6613.
- Hinz DF, Panchenko A, Kim T-Y, Fried E (2014) Motility versus fluctuations in mixtures of self-motile and passive agents *Soft Matter* 10:9082–9089.
- Takatori SC, Brady JF (2016) A theory for the phase behavior of mixtures of active particles. *Soft Matter* 11:7920–7931.
- Stenhammar J, Wittkowski R, Marenduzzo D, Cates ME (2016) Light-induced self-assembly of active rectification devices *Sci Adv* 2:e1501850.
- Wysocki A, Winkler RG, Gompper G (2016) Propagating interfaces in mixtures of active and passive Brownian particles *New J Phys* 18:123030.
- Wittkowski R, Stenhammar J, Cates ME (2017) Nonequilibrium dynamics of mixtures of active and passive colloidal particles *New J Phys* 19:105003.
- Martinez-Pedrero F, Cebers A, Tierno P (2016) Orientational dynamics of colloidal ribbons self assembled from microscopic magnetic ellipsoids. *Soft Matter* 12: 3688–3695.
- Anderson JL (1989) Colloid transport by interfacial forces. *Annu Rev Fluid Mech* 21: 61–99.
- Hastings MB, Olson Reichhardt CJ, Reichhardt C (2003) Depinning by fracture in a glassy background. *Phys Rev Lett* 90:098302.
- Palacci J, Sacanna S, Vatchinsky A, Chaikin PM, Pine DJ (2013) Photoactivated colloidal dockers for cargo transportation. *J Am Chem Soc* 135:15978–15981.
- Martinez-Pedrero F, Massana-Cid H, Tierno P (2017) Assembly and transport of microscopic cargos via reconfigurable photoactivated magnetic microdockers. *Small* 13:1603449.
- Golestanian R, Liverpool TB, Ajdari A (2007) Designing phoretic micro- and nano-swimmers. *New J Phys* 9:126.
- Soto R, Golestanian R (2014) Self-assembly of catalytically active colloidal molecules: Tailoring activity through surface chemistry. *Phys Rev Lett* 112:068301.
- Baumgartl J, Dullens RP, Dijkstra M, Roth R, Bechinger C (2007) Experimental observation of structural crossover in binary mixtures of colloidal hard spheres. *Phys Rev Lett* 98:198303.
- Tanaka H, Araki T (2000) Simulation method of colloidal suspensions with hydrodynamic interactions: Fluid particle dynamics. *Phys Rev Lett* 85:1338.
- Flenner E, Szamel G (2015) Fundamental differences between glassy dynamics in two and three dimensions. *Nat Commun* 6:392.
- Sciortino F, Tartaglia P (2005) Glassy colloidal systems. *Adv Phys* 54:471–524.
- Feng L, Laderman B, Sacanna S, Chaikin PM (2015) Re-entrant solidification in polymer-colloid mixtures as a consequence of competing entropic and enthalpic attractions. *Nat Mater* 14:61–65.
- Sugimoto T, Muramatsu A (1996) Formation mechanism of monodispersed alpha-Fe₂O₃ particles in dilute FeCl₃ solutions. *J Colloid Interf Sci* 184:626.

PUBLICATION 7

Supporting Information

Supporting Information for the Article: Active apolar doping determines novel routes to colloidal clusters and gels

Helena Massana-Cid^{1,*}, Joan Codina^{1,2,*}, Ignacio Pagonabarraga^{1,2,3}, and Pietro Tierno^{1,2,4†}

¹*Departament de Física de la Matèria Condensada, Universitat de Barcelona, Barcelona, Spain.*

²*Universitat de Barcelona Institute of Complex Systems (UBICS),*

Universitat de Barcelona, 08028 Barcelona, Spain

³*CECAM, Centre Européen de Calcul Atomique et Moléculaire,*

École Polytechnique Fédérale de Lausanne, Batochime, Avenue Forel 2, 1015 Lausanne, Switzerland

⁴*Institut de Nanociència i Nanotecnologia, IN²UB,*

Universitat de Barcelona, 08028 Barcelona, Spain.

(Dated: September 6, 2018)

NUMERICAL SIMULATION

We model silica particles as diffusive discs of diameter σ_p , and centre of mass at positions $\{\mathbf{R}_i\}$. To account for their ellipsoidal shape, active particles are modeled as dimers with beads of diameter σ_a at positions $\{\mathbf{q}_i^a\}$, and $\{\mathbf{q}_i^b\}$ in the direction of the orientation vector $\{\hat{\mathbf{n}}_i\}$. The particles are connected by a restoring force, $\{\mathbf{F}_i^h\}$, with rest length r_0 , and elastic constant k . We introduce $\sigma_a = 1.3\mu\text{m}$ and $r_0 = 0.5\mu\text{m}$ to model the aspect ratio of the experimental ellipsoids, $1.3 \times 1.5\mu\text{m}$.

Particles follow an overdamped Langevin dynamics with mobilities μ_t for the beads of the dimers, and $\sigma_p/\sigma_a\mu_t$ for passive particles,

$$\dot{\mathbf{q}}_i^a = \mathbf{v}_i^a + \mu_t (\mathbf{F}_i^h \hat{\mathbf{n}}_i + \mathbf{F}_i^{c,a} + \mathbf{F}_i^{m,a}) + \sqrt{2D_t} \boldsymbol{\xi}_i \quad (1)$$

$$\dot{\mathbf{q}}_i^b = \mathbf{v}_i^b + \mu_t (-\mathbf{F}_i^h \hat{\mathbf{n}}_i + \mathbf{F}_i^{c,b} + \mathbf{F}_i^{m,b}) + \sqrt{2D_t} \boldsymbol{\xi}_i \quad (2)$$

$$\dot{\mathbf{R}}_i = \mathbf{V}_i + \mu_t \frac{\sigma_a}{\sigma_p} \mathbf{F}_i^c + \sqrt{2D_t \sigma_a / \sigma_p} \boldsymbol{\xi}_i \quad (3)$$

with the diffusiophoretic velocities \mathbf{v}_i^α for the active beads, and \mathbf{V}_i for passive particles, as derived in the previous section. For the relative velocity between an active and a passive pair we consider the symmetrized relative velocity that ensures that action-reaction is fulfilled. Excluded volume is introduced by the repulsive WCA force, $\{\mathbf{F}_i^{c,\alpha}\}$, $\alpha = a, b$, with $\sigma = \sigma_a$ for aa interactions, $\sigma = \sigma_p$ for pp interactions, and $\sigma = (\sigma_a \sigma_p)^{1/2}$ for ap interactions, and characteristic energy $\epsilon = 24k_B T$. The choice of σ for ap interactions corresponds to the centre-to-centre distance for two touching spheres lying on the same surface.

Active particles have a permanent magnetic moment in the direction of their short axis, a vector $\hat{\mathbf{t}}$ in the plane perpendicular to $\hat{\mathbf{n}}$. We introduce relative magnetic interactions, body force and torque, on each bead $\{\mathbf{F}_i^{m,\alpha}\}$, $\alpha = a, b$.

The last term in Eq. (1-3) accounts for thermal diffusion, D_t , for active beads, and $\sigma_p/\sigma_a D_t$ for passive

colloids, respectively, with random Gaussian vectors $\boldsymbol{\xi}$ with zero mean and unit variance.

ORDER PARAMETERS

We define the particle density in Fourier space $\rho_{\mathbf{q}}(t)$ as the discrete Fourier transform of the real density $\rho(\mathbf{r}; t) = \sum_j \delta(\mathbf{r} - \mathbf{r}_j)$ at time t ,

$$\rho_{\mathbf{q}}(t) = \sum_j \exp(i\mathbf{q} \cdot \mathbf{r}_j(t)), \quad (4)$$

We decompose the domain in \mathbf{q} in elements of size $dq = 2\pi/L$, where L is the system size. From the structure factors, $S(q)$ (see Supporting Information), we identify the position of q_{max} , corresponding to a characteristic maximum of $S(q)$. For passive particles $q_{max} \approx 2\pi/\sigma_p \approx 1.57$, while for active particles $q_{max} \approx 2\pi/\sigma_a$. To study the relaxation of the density field in Fourier space, $\rho_{\mathbf{q}}$, at different times we measure the dynamic structure factor [1, 2] relative to an initial time t_0 from the activity quench,

$$F_q(t_0, \Delta t) = \frac{\langle \sum_i \rho_{\mathbf{q}}(t_0) \rho_{\mathbf{q}}^\dagger(t_0 + \Delta t) \rangle}{\langle \sum_i \rho_{\mathbf{q}}(t_0) \rho_{\mathbf{q}}^\dagger(t_0) \rangle} \quad (5)$$

which we compute for the values of the wave vector $|\mathbf{q}| = q_{max} \pm \Delta q$ of modulus q_{max} in a shell of thickness $\Delta q \approx 0.1[3]$. We identify t_0 when the system is arrested, or in a steady state and measure the dynamic structure factor.

To describe the relaxation of the local orientation of particles we define the local hexagonal order on each particle as,

$$\Psi_6^n = \frac{1}{n_b} \sum_{j \in \{neigh\}}^{n_b} \exp(i6\theta_{nj}(t)) \quad (6)$$

Where n_b is the number of neighbors of a particle that satisfy $r < r_c = 1.5\sigma_p$. A structured hexagonal pattern gives $\Phi_6 = \sum_i N^{-1} \Psi_6^n = 1$. θ_{nj} is the angle formed by

the center-to-center vector between neighboring particles n and j , with the \hat{x} axis – the choice of axis is not relevant as long as it is kept fixed for all j neighbors of n .

$$\theta_{nj} = \arctan\left(\frac{\mathbf{r}_{nj} \cdot \hat{\mathbf{y}}}{\mathbf{r}_{nj} \cdot \hat{\mathbf{x}}}\right), \quad |\mathbf{r}_{nj}| < r_{cut} \quad (7)$$

The temporal evolution of the local hexatic order parameter defines the self-correlation function $C_\Psi(t_0, \Delta t)$

$$C_\Psi(t_0, \Delta t) = \frac{\langle \sum_n \Psi_6^*(t_0) \Psi_6(t_0 + \Delta t) \rangle}{\langle \sum_n \Psi_6^*(t_0) \Psi_6(t_0) \rangle} \quad (8)$$

SUPPORTING VIDEOS

With the article there are 6 videoclips as supplements of the figures in the main text.

- **MovieS1(.WMF)**: Formation of a colloidal gel via doping of passive silica particles (diameter $\sigma_p = 4\mu\text{m}$) with hematite ellipsoids (short and long axis equal to $b = 1.3\mu\text{m}$ and $a = 1.8\mu\text{m}$ resp.). Both particles are suspended in a water solution of H_2O_2 (9% in Vol) and subjected to blue light ($\lambda = 450 - 490\text{nm}$, $P = 1.04\text{mW}$) that induces the phoretic attraction. The corresponding process is illustrated in Fig. 1(b,c,d) of the article.
- **MovieS2(.WMF)**: Formation of the cluster I phase via application of blue light. Left video corresponds to the experimental system ($\Phi_a = 0.01$, $\Phi_p = 0.04$) while right video results from numerical simulations ($\Phi_a = 0.02$, $\Phi_p = 0.1$). The illustrated process corresponds to the first row Fig. 2(a) of the manuscript.
- **MovieS3(.WMF)**: Formation of the cluster II phase via application of blue light. Left video corresponds to the experimental system ($\Phi_a = 0.06$, $\Phi_p = 0.04$) while right video results from numerical simulation ($\Phi_a = 0.1$, $\Phi_p = 0.14$). The illustrated process corresponds to the second row Fig. 2(a) of the manuscript.

- **MovieS4(.WMF)**: Formation of the gel I phase via application of blue light. Left video corresponds to the experimental system ($\Phi_a = 0.05$, $\Phi_p = 0.51$) while right video results from numerical simulations ($\Phi_a = 0.55$, $\Phi_p = 0.5$). The illustrated process corresponds to the third row Fig. 2(a) of the manuscript.
- **MovieS5(.WMF)**: Formation of the gel II phase via application of blue light. Left video corresponds to the experimental system ($\Phi_a = 0.15$, $\Phi_p = 0.17$) while right video results from numerical simulation ($\Phi_a = 0.25$, $\Phi_p = 0.1$). The illustrated process corresponds to the fourth row Fig. 2(a) of the manuscript.
- **MovieS6(.WMF)**: Formation of the gel III phase via application of blue light. Left video corresponds to the experimental system ($\Phi_a = 0.14$, $\Phi_p = 0.45$) while right video results from numerical simulation ($\Phi_a = 0.25$, $\Phi_p = 0.3$). The illustrated process corresponds to the last row Fig. 2(a) of the manuscript.

SUPPORTING IMAGE

* These authors equally contributed to the work

† ptierno@ub.edu

- [1] Berne BJ, Pecora R (2000) Dynamic light scattering: with applications to chemistry, biology, and physics. Courier Corporation.
- [2] Sciortino F, Tartaglia P. (2005) Glassy colloidal systems. *Adv. Phys.*, 54:471-524.
- [3] Testard V, Berthier L, Kob W (2014) Intermittent dynamics and logarithmic domain growth during the spinodal decomposition of a glass-forming liquid. *J. Chem. Phys.*, 140:16.

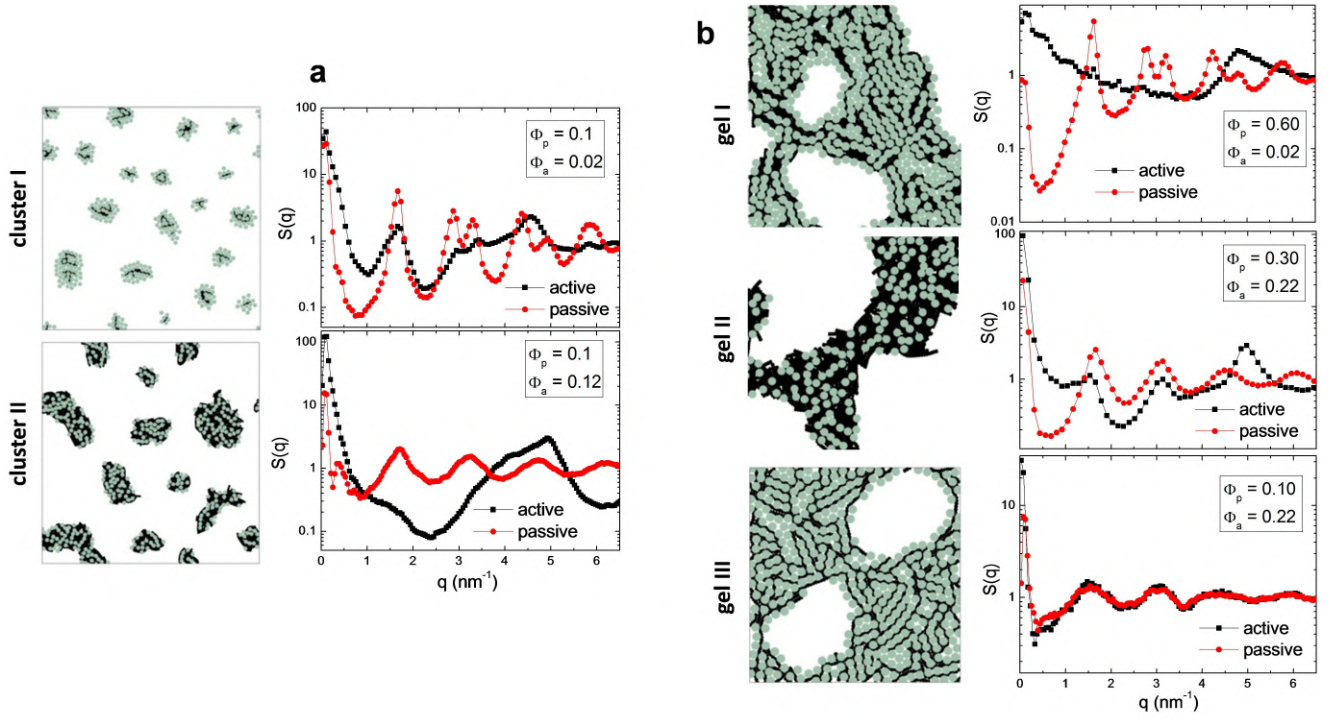


FIG. 1. (a,b) Images from numerical simulations (left) and corresponding static structure factor $S(q)$ (right) calculated for the different assemblies observed in the diagram showed in Fig.3(b) of the main article. Fig.(a) shows the cluster I (top) and the cluster II (bottom) phases, Fig.(b) the cluster phases *I* to *III* from top to bottom.

PART V

CONCLUSIONS

CHAPTER 9

CONCLUSIONS AND PERSPECTIVES

This thesis has focused on the dynamics of out-of-equilibrium driven and active magnetic colloidal systems and on their individual and collective effects. We applied external magnetic fields to control and manipulate these particles and, in some cases, exploited the activity of hematite colloids. We observed the dynamics of these systems in real-time using video microscopy. Our experiments were compared and contrasted both with analytical models and simulations.

We studied the assembly of ferromagnetic ellipsoidal particles into elongated ribbons that could transport cargos using the hydrodynamic flow they create. Changing the parameters of the applied field, these types of particles assembled into dynamically bound three-dimensional clusters. Furthermore, when activated by blue light, the magnetic ellipsoids could transform into dockers that were able to move around the experimental platform, trapping, transporting and releasing cargos. Their chemical activity also induced the formation of dynamically arrested two-dimensional gels, bicontinuous structures and clusters. Additionally, when we fine-tuned the parameters of an external field, paramagnetic particles assembled into two-dimensional propelling crystals were able to self-heal. On the other hand, we demonstrated the bidirectional transport of paramagnetic particles on top of magnetic substrates, where smaller and larger particles moved towards opposite directions.

In conclusion, we found novel approaches to tune the interactions of magnetic colloids on an external command in order to drive and engineer a rich variety of microstructures. Colloids are an excellent model system to investigate collective processes that are more difficult to observe and control, such as those in atomic and living systems. Furthermore, they are a useful test-bed that helps to understand microscale fluid dynamics, which has applications in miniaturization processes that are essential for lab-on-a-chip studies and biomedicine. This work gets us one step further into finding an optimal microdevice based on colloidal particles to manipulate, transport and control processes at such scales. Therefore, this thesis is of great interest for both fundamental and technological reasons.

As for future perspectives, one open question relates to how chains of hematite particles would behave when activated. Enhancing the activity of some of the colloids by increasing the intensity of applied light, we expect to obtain self-propulsion of individual asymmetric clusters. Moreover, the propelling carpets could be studied further in order to understand the fluctuations of their shape during the self-healing process. The evolution of their edges' roughness and the deposition procedure could provide insight into the process of surface growth. Additionally, the collective effects of denser solutions of ellipsoids under external magnetic fields, such as cluster formation, could be explored in future research. We also observed highly surprising phenomena when paramagnetic particles were confined in a cell of a thickness of the order of their diameter under a time-dependent magnetic field. This gave rise to the emergence of colloidal currents in the absence of external gradients and to the formation of bimodal lattices and rotating dimers. Exploring further this system is an exciting future perspective.

BIBLIOGRAPHY

1. S. R. Nagel. Experimental soft-matter science. *Reviews of Modern Physics* **89** (2017).
2. R. J. Hunter & L. R. White. *Foundations of Colloid Science Volume 1* (Clarendon Press, 1987).
3. M. Kerker. Classics and classicists of colloid and interface science. *Journal of Colloid and Interface Science* **116**, 296–299 (1987).
4. I. Asimov. *Words of Science and the History Behind Them* (Riverside Press, 1959).
5. H. Freundlich. *Colloid and Capillary Chemistry* (Methuen, 1926).
6. J. Perrin. *Brownian Movement and Molecular Reality* (London : Taylor and Francis, 1910).
7. A. Einstein. Über die von der molekularkinetischen Theorie der Wärme geforderte Bewegung von in ruhenden Flüssigkeiten suspendierten Teilchen. *Annalen der Physik* **322**, 549–561 (1905).
8. A. Einstein. Eine neue Bestimmung der Moleküldimensionen. *Annalen der Physik* **19**, 289–306 (1906).
9. E. J. W. Verwey & J. T. G. Overbeek. *Theory of the Stability of Lyophobic Colloids* (Elsevier, 1948).
10. W. D. Harkins. A General Theory of the Mechanism of Emulsion Polymerization. *Journal of the American Chemical Society* **69**, 1428–1444 (1947).
11. P. N. Pusey. *Liquids, freezing and the glass transition* (eds J. P. Hansen, D. Levesque & J. Zinn-Justin) chap. Colloidal Suspensions (North Holland, 1991).
12. W. C. K. Poon & P. N. Pusey. *Observation, prediction and simulation of phase transitions in complex fluids* (eds M. Baus, L. F. Rull & J. P. Ryckaert) chap. Phase transition of spherical colloids (Springer Netherlands, 1995).
13. R. J. Hunter. *Introduction to Modern Colloid Science* (Oxford University Press, 1993).
14. M. D. Haw. *Middle World* (Macmillan, 2006).
15. H. Mollet & A. Grubennann. *Formulation Technology: Emulsions, Suspensions, Solid Foams* (Wiley-VCH, 2001).

16. S. Auer & D. Frenkel. Prediction of absolute crystal-nucleation rate in hard-sphere colloids. *Nature* **409**, 1020–1023 (2001).
17. A. L. Thorneywork, J. L. Abbott, D. G. Aarts & R. P. Dullens. Two-Dimensional Melting of Colloidal Hard Spheres. *Physical Review Letters* **118**, 1–5 (2017).
18. E. R. E. Weeks, J. C. Crocker, A. C. A. Levitt, A. Schofield & D. A. Weitz. Three-Dimensional Direct Imaging of Structural Relaxation Near the Colloidal Glass Transition. *Science* **287** (2000).
19. K. N. Pham *et al.* Multiple glassy states in a simple model system. *Science* **296**, 104–106 (2002).
20. W. C. K. Poon. Colloidal Glasses. *MRS Bulletin*, 96–99 (2004).
21. P. Pusey & W. van Megen. Phase behaviour of concentrated suspensions of nearly hard colloidal spheres. *Nature* **320**, 340–342 (1986).
22. G. L. Hunter & E. R. Weeks. The physics of the colloidal glass transition. *Reports on Progress in Physics* **75**. ISSN: 00344885 (2012).
23. T. Palberg. Crystallization kinetics of repulsive colloidal spheres. *Journal of Physics: Condensed Matter* **11**, R323–R360 (1999).
24. J. Bergenholtz. Theory of rheology of colloidal dispersions. *Current Opinion in Colloid and Interface Science* **6**, 484–488 (2001).
25. J. Mewis & N. J. Wagner. *Colloidal Suspension Rheology* (Cambridge University Press, 2011).
26. P. Habdas & E. R. Weeks. Video microscopy of colloidal suspensions and colloidal crystals. *Current Opinion in Colloid and Interface Science* **7**, 196–203 (2002).
27. M. S. Elliot & W. C. K. Poon. Conventional optical microscopy of colloidal suspensions. *Advances in Colloid and Interface Science* **92**, 133–194 (2001).
28. V. Prasad, D. Semwogerere & E. R. Weeks. Confocal microscopy of colloids. *Journal of Physics Condensed Matter* **19**, 1–25 (2007).
29. M. D. Haw. Colloidal suspensions, Brownian motion, molecular reality: a short history. *Journal of Physics: Condensed Matter* **14**, 7769–7779 (2002).
30. J. Perrin. *Les atomes* (F. Alcan, 1914).
31. E. Nelson. *Dynamical Theories of Brownian Motion* (Princeton University Press, 1973).
32. S. Lindsay. *Introduction to Nanoscience* (OUP Oxford, 2009).
33. W. C. K. Poon. *The Oxford Handbook of Soft Condensed Matter* (eds E. Terentjev & D. Weitz) chap. Colloidal Suspensions (Oxford University Press, 2015).
34. R. Kimmich. *Principles of Soft-Matter Dynamics* chap. 2 (Springer, 2012).

35. T. Li & M. G. Raizen. Brownian motion at short time scales. *Annalen der Physik* **525**, 281–295 (2013).
36. R. Huang *et al.* Direct observation of the full transition from ballistic to diffusive Brownian motion in a liquid. *Nature Physics* **7**, 576–580 (2011).
37. F. Perrin. Mouvement brownien d'un ellipsoïde - I. Dispersion diélectrique pour des molécules ellipsoïdales. *Le Journal de Physique et le Radium* **5**, 497 (1934).
38. Y. Han *et al.* Brownian Motion of an Ellipsoid. *Science* **314**, 626–630 (2006).
39. R. Grima & S. N. Yaliraki. Brownian motion of an asymmetrical particle in a potential field. *The Journal of Chemical Physics* **127**, 084511 (2007).
40. O. Guell, P. Tierno & F. Sagués. Anisotropic diffusion of a magnetically torqued ellipsoidal microparticle. *The European Physical Journal Special Topics* **187**, 15–20 (2010).
41. W. L. Fan, O. S. Pak & M. Sandoval. Ellipsoidal Brownian self-driven particles in a magnetic field. *Physical Review E* **95**, 032605 (2017).
42. J. N. Israelachvili. *Intermolecular and Surface Forces* 3rd ed. (Academic Press, 2011).
43. R. F. Probstein. *Physicochemical Hydrodynamics: An Introduction* (1994).
44. W. Ninham. On progress in forces since the DLVO theory. *Advances in Colloid and Interface Science* **83**, 1–17 (1999).
45. W. C. K. Poon, E. R. Weeks & C. P. Royall. On measuring colloidal volume fractions. *Soft Matter* **8**, 21–30 (2012).
46. W. Zhu, C. Wang, G. Dong, Y. Wu & M. Zhang. Fabrication of Large-area 3-D Ordered Silver-coated Colloidal Crystals and Macroporous Silver Films Using Polystyrene Templates. *Nano-Micro Letters* **5**, 182–190 (2013).
47. J. Vanderhoff, H. Van den Hul, R. Tausk & J. T. G. Overbeek. Clean surfaces: their preparation and characterization for interfacial studies. *Marcel Dekker, New York*, 15 (1970).
48. J. Goodwin, J. Hearn, C. Ho & R. Ottewill. The preparation and characterisation of polymer latices formed in the absence of surface active agents. *British polymer journal* **5**, 347–362 (1973).
49. S. H. Behrens & D. G. Grier. The charge of glass and silica surfaces. *The Journal of Chemical Physics* **115**, 6716 (2001).
50. L. M. Liz-Marzan & P. V. Kamat. *Nanoscale materials* chap. 18 (Springer, 2004).
51. J. Yan, S. C. Bae & S. Granick. Rotating crystals of magnetic Janus colloids. *Soft Matter* **11**, 147–153 (2015).
52. P. J. Lu & D. A. Weitz. Colloidal Particles: Crystals, Glasses, and Gels. *Annual Review of Condensed Matter Physics* **4**, 217–233 (2013).

53. A. van Blaaderen, R. Ruel & P. Wiltzius. Template-directed colloidal crystallization. *Nature* **385**, 321–324 (1997).
54. F. Li, D. P. Josephson & A. Stein. Colloids Colloidal Assembly : The Road from Particles to Colloidal Molecules and Crystals *Angewandte Chemie International Edition* **50**, 360–388 (2011).
55. G. M. Whitesides & B. Grzybowski. Self-Assembly at All Scales. *Science* **295**, 2418–2422 (2002).
56. J. D. Joannopoulos, P. R. Villeneuve & S. H. Fan. Photonic crystals: Putting a new twist on light. *Nature* **386**, 143–149 (1997).
57. G. Pan, R. Kesavamoorthy & S. A. Asher. Optically Nonlinear Bragg Diffracting Nanosecond Optical Switches. *Physical Review Letters* **78**, 3860–3863 (1997).
58. J. H. Holtz & S. A. Asher. Polymerized colloidal crystal hydrogel films as intelligent chemical sensing materials. *Nature* **389**, 829–832 (1997).
59. J. Dobnikar, A. Snezhko & A. Yethiraj. Emergent colloidal dynamics in electromagnetic field. *Soft Matter* **9**, 3693–3704 (2013).
60. E. V. Yakovlev *et al.* Tunable two-dimensional assembly of colloidal particles in rotating electric fields. *Scientific Reports*, 1–10 (2017).
61. K. J. Strandburg. Two-dimensional melting. *Reviews of Modern Physics* **60**, 161–207 (1988).
62. A. Van Blaaderen & A. Yethiraj. A colloidal model system with an interaction tunable from hard sphere to soft and dipolar. *Nature* **421**, 513–517 (2003).
63. H. Sedgwick, S. U. Egelhaaf & W. C. Poon. Clusters and gels in systems of sticky particles. *Journal of Physics Condensed Matter* **16**. ISSN: 09538984 (2004).
64. E. Zaccarelli. Colloidal gels: Equilibrium and non-equilibrium routes. *Journal of Physics Condensed Matter* **19** (2007).
65. P. Tierno, R. Muruganathan & T. M. Fischer. Viscoelasticity of Dynamically Self-Assembled Paramagnetic Colloidal Clusters. *Physical Review Letters* **98**, 028301 (2007).
66. F. Martinez-Pedrero, A. Ortiz-Ambriz, I. Pagonabarraga & P. Tierno. Colloidal Microworms Propelling via a Cooperative Hydrodynamic Conveyor Belt. *Physical Review Letters* **115**, 138301 (2015).
67. F. Martinez-Pedrero, A. Cebers & P. Tierno. Orientational dynamics of colloidal ribbons self-assembled from microscopic magnetic ellipsoids. *Soft Matter* **12**, 3688–3695 (2016).
68. S. Chikazumi. *Physics of Magnetism* 1st ed. (John Wiley & Sons, Inc., 1964).

69. U. Jeong, X. Teng, Y. Wang, H. Yang & Y. Xia. Superparamagnetic colloids: Controlled synthesis and niche applications. *Advanced Materials* **19**, 33–60 (2007).
70. D. L. Leslie-Pelecky & R. D. Rieke. Magnetic properties of nanostructured materials. *Chemistry of Materials* **8**, 1770–1783 (1996).
71. L. Néel. Influence des fluctuations thermiques sur l'aimantation de grains ferromagnétiques très fins. *Comptes rendus de l'Académie des Sciences* **228**, 664 (1949).
72. M. A. M. Gijs. Magnetic bead handling on-chip: New opportunities for analytical applications. *Microfluidics and Nanofluidics* **1**, 22–40 (2004).
73. N. A. Frey, S. Peng, K. Cheng & S. Sun. Magnetic nanoparticles: Synthesis, functionalization, and applications in bioimaging and magnetic energy storage. *Chemical Society Reviews* **38**, 2532–2542 (2009).
74. Q. A. Pankhurst, J. Connolly, S. K. Jones & J. Dobson. Applications of magnetic nanoparticles in biomedicine. *Journal of Physics D: Applied Physics* **36**, 167–181 (2003).
75. M. Colombo *et al.* Biological applications of magnetic nanoparticles. *Chemical Society Reviews* **41**, 4306–4334 (2012).
76. T. Sugimoto. Preparation of monodispersed colloidal particles. *Advances in Colloid and Interface Science* **28**, 65–108 (1987).
77. E. Matijevic. Production of Monodispersed Colloidal Particles. *Annual Review of Materials Science* **15**, 483–516 (1985).
78. M. Haruta & B. Delmon. Preparation of homodisperse solids. *Journal de Chimie Physique* **83**, 859–868 (1986).
79. E. Matijevic. Preparation and properties of uniform size colloids. *Chemistry of Materials* **5**, 412–426 (1993).
80. P. Tierno. Recent advances in anisotropic magnetic colloids: realization, assembly and applications. *Physical Chemistry Chemical Physics* **16**, 23515–23528 (2014).
81. H. Löwen *et al.* Colloidal layers in magnetic fields and under shear flow. *Journal of Physics Condensed Matter* **17** (2005).
82. P. Tierno, J. Claret, F. Sagués & A. Cebers. Overdamped dynamics of paramagnetic ellipsoids in a precessing magnetic field. *Physical Review E* **79**, 1–6 (2009).
83. F. Martinez-Pedrero, E. Navarro-Argemí, A. Ortiz-Ambriz, I. Pagonabarraga & P. Tierno. Emergent hydrodynamic bound states between magnetically powered micropellers. *Science Advances* **4**, 1–8 (2018).
84. X. J. A. Janssen, A. Schellekens, K. van Ommering, L. J. van Ijzendoorn & M. W. J. Prins. Controlled torque on superparamagnetic beads for functional biosensors. *Biosensors and Bioelectronics* **24**, 1937–1941 (2009).

85. A. Cebers & H. Kalis. Dynamics of superparamagnetic filaments with finite magnetic relaxation time. *The European Physical Journal E* **34**, 30 (2011).
86. J. Yan, K. Chaudhary, S. Chul Bae, J. A. Lewis & S. Granick. Colloidal ribbons and rings from Janus magnetic rods. *Nature Communications* **4**, 1516–1519 (2013).
87. F. Vereda, J. De Vicente & R. Hidalgo-Alvarez. Physical properties of elongated magnetic particles: magnetization and friction coefficient anisotropics. *ChemPhysChem* **10**, 1165–1179 (2009).
88. S. Guo, Q. Pan & M. B. Khamesee. Development of a novel type of microrobot for biomedical application. *Microsystem Technologies* **14**, 307–314 (2008).
89. S. Sundararajan, P. E. Lammert, A. W. Zudans, V. H. Crespi & A. Sen. Catalytic Motors for Transport of Colloidal Cargo. *Nano Letters* **8**, 1271–1276 (2008).
90. B. J. Nelson, I. K. Kaliakatsos & J. J. Abbott. Microrobots for Minimally Invasive Medicine. *Annual Review of Biomedical Engineering* **12**, 55–85 (2010).
91. S. Sanchez, A. A. Solovev, S. M. Harazim & O. G. Schmidt. Microbots Swimming in the Flowing Streams of Microfluidic Channels. *Journal of the American Chemical Society* **133**, 701–703 (2011).
92. S. Kim *et al.* Fabrication and Characterization of Magnetic Microrobots for Three-Dimensional Cell Culture and Targeted Transportation. *Advanced Materials* **25**, 5863–5868 (2013).
93. C. Peters, M. Hoop, S. Pané, B. J. Nelson & C. Hierold. Degradable Magnetic Composites for Minimally Invasive Interventions: Device Fabrication, Targeted Drug Delivery, and Cytotoxicity Tests. *Advanced Materials* **28**, 533–538 (2016).
94. Y. Tu, F. Peng & D. A. Wilson. Motion Manipulation of Micro- and Nanomotors. *Advanced Materials* **29**, 1–20 (2017).
95. X. Z. Chen *et al.* Small-Scale Machines Driven by External Power Sources. *Advanced Materials* **30**, 1–22 (2018).
96. E. Lauga & T. R. Powers. The hydrodynamics of swimming microorganisms. *Reports on Progress in Physics* **72**, 096601 (2009).
97. J. Happel & H. Brenner. *Low Reynolds Number Hydrodynamics* (Noordhoff, Leiden, 1973).
98. G. Taylor. Analysis of the swimming of microscopic organisms. *Proceedings of the Royal Society of London, Series A* **209**, 447–461 (1951).
99. A. M. Purcell. Life at Low Reynolds Number. *American Journal of Physics* **45**, 3–11 (1977).
100. H. C. Berg & R. A. Anderson. Bacteria Swim by Rotating their Flagellar Filaments. *Nature* **245**, 380–382 (1973).

101. M. C. Marchetti *et al.* Hydrodynamics of soft active matter. *Reviews of Modern Physics* **85**, 1143–1189 (2013).
102. H. C. Berg. *Random Walks in Biology* (Princeton University Press, 1983).
103. K. M. Ehlers, A. D. Samuel, H. C. Berg & R. Montgomery. Do cyanobacteria swim using traveling surface waves? *Proceedings of the National Academy of Sciences* **93**, 8340–8343 (1996).
104. H. C. Berg. The Rotary Motor of Bacterial Flagella. *Annual Review of Biochemistry* **72**, 19–54 (2003).
105. X. Lin, Z. Wu, Y. Wu, M. Xuan & Q. He. Self-Propelled Micro- Nanomotors Based on Controlled Assembled Architectures. *Advanced Materials* **28**, 1060–1072 (2016).
106. T. Qiu *et al.* Swimming by reciprocal motion at low Reynolds number. *Nature Communications* **5**, 5119 (2014).
107. J. Elgeti, R. G. Winkler & G. Gompper. Physics of microswimmers - Single particle motion and collective behavior: A review. *Reports on Progress in Physics* **78** (2015).
108. L. E. Becker, S. A. Koehler & H. A. Stone. On self-propulsion of micro-machines at low Reynolds number: Purcell's three-link swimmer. *Journal of Fluid Mechanics* **490**, 15–35 (2003).
109. D. Tam & A. E. Hosoi. Optimal Stroke Patterns for Purcell's Three-Link Swimmer. *Physical Review Letters* **98**, 068105 (2007).
110. A. Najafi & R. Golestanian. Simple swimmer at low Reynolds number: Three linked spheres. *Physical Review E* **69**, 062901 (2004).
111. R. Golestanian & A. Ajdari. Mechanical Response of a Small Swimmer Driven by Conformational Transitions. *Physical Review Letters* **100**, 038101 (2008).
112. S. Camalet, F. Jülicher & J. Prost. Self-Organized Beating and Swimming of Internally Driven Filaments. *Physical Review Letters* **82**, 1590–1593 (1999).
113. C. P. Lowe. A hybrid particle/continuum model for micro-organism motility. *Future Generation Computer Systems* **17**, 853–862 (2001).
114. E. Gauger & H. Stark. Numerical study of a microscopic artificial swimmer. *Physical Review E* **74**, 021907 (2006).
115. H. Shum. Microswimmer propulsion by two steadily rotating helical flagella. *Micromachines* **10**, 1–13 (2019).
116. E. Lauga. Floppy swimming: Viscous locomotion of actuated elastica. *Physical Review E* **75**, 041916 (2007).
117. M. J. Lighthill. On the squirming motion of nearly spherical deformable bodies through liquids at very small reynolds numbers. *Communications on Pure and Applied Mathematics* **5**, 109–118 (1952).

118. J. R. Blake. A spherical envelope approach to ciliary propulsion. *Journal of Fluid Mechanics* **46**, 199 (1971).
119. M. T. Downton & H. Stark. Simulation of a model microswimmer. *Journal of Physics: Condensed Matter* **21**, 204101 (2009).
120. H. Wang & M. Pumera. Fabrication of Micro/Nanoscale Motors. *Chemical Reviews* **115**, 8704–8735 (2015).
121. P. Illien, R. Golestanian & A. Sen. 'Fuelled' motion: Phoretic motility and collective behaviour of active colloids. *Chemical Society Reviews* **46**, 5508–5518 (2017).
122. S. J. Ebbens & J. R. Howse. In pursuit of propulsion at the nanoscale. *Reports on Progress in Physics* **6**, 726–738 (2010).
123. F. Ma, S. Wang, D. T. Wu & N. Wu. Electric-field-induced assembly and propulsion of chiral colloidal clusters. *Proceedings of the National Academy of Sciences* **112**, 6307–6312 (2015).
124. S. Palagi *et al.* Structured light enables biomimetic swimming and versatile locomotion of photoresponsive soft microrobots. *Nature Materials* **15**, 647–653 (2016).
125. B. Behkam & M. Sitti. Bacterial flagella-based propulsion and on/off motion control of microscale objects. *Applied Physics Letters* **90**, 023902 (2007).
126. W. Gao & J. Wang. Synthetic micro/nanomotors in drug delivery. *Nanoscale* **6**, 10486–10494 (2014).
127. W. Duan *et al.* Synthetic Nano- and Micromachines in Analytical Chemistry: Sensing, Migration, Capture, Delivery, and Separation. *Annual Review of Analytical Chemistry* **8**, 311–333 (2015).
128. X. Z. Chen *et al.* Recent developments in magnetically driven micro- and nanorobots. *Applied Materials Today* **9**, 37–48 (2017).
129. R. Dreyfus *et al.* Microscopic artificial swimmers. *Nature* **437**, 862–865 (2005).
130. H. Morimoto, T. Ukai, Y. Nagaoka, N. Grobert & T. Maekawa. Tumbling motion of magnetic particles on a magnetic substrate induced by a rotational magnetic field. *Physical Review E* **78**, 021403 (2008).
131. P. Tierno, R. Golestanian, I. Pagonabarraga & F. Sagués. Controlled Swimming in Confined Fluids of Magnetically Actuated Colloidal Rotors. *Physical Review Letters* **101**, 218304 (2008).
132. S. Tottori, L. Zhang, K. E. Peyer & B. J. Nelson. Assembly, disassembly, and anomalous propulsion of microscopic helices. *Nano Letters* **13**, 4263–4268 (2013).
133. A. Snezhko & I. S. Aranson. Magnetic manipulation of self-assembled colloidal asters. *Nature Materials* **10**, 698–703 (2011).

134. M. Roper *et al.* On the dynamics of magnetically driven elastic filaments. *Journal of Fluid Mechanics* **554**, 167–190 (2006).
135. O. S. Pak, W. Gao, J. Wang & E. Lauga. High-speed propulsion of flexible nanowire motors: Theory and experiments. *Soft Matter* **7**, 8169–8181 (2011).
136. A. M. Maier *et al.* Magnetic Propulsion of Microswimmers with DNA-Based Flagellar Bundles. *Nano Letters* **16**, 906–910 (2016).
137. L. Zhang *et al.* Characterizing the Swimming Properties of Artificial Bacterial Flagella. *Nano Letters* **9**, 3663–3667 (2009).
138. A. Ghosh & P. Fischer. Controlled Propulsion of Artificial Magnetic Nanostructured Propellers. *Nano Letters* **9**, 2243–2245 (2009).
139. A. J. Goldman, R. G. Cox & H. Brenner. Slow viscous motion of a sphere parallel to a plane wall—I Motion through a quiescent fluid. *Chemical Engineering Science* **22**, 637–651 (1967).
140. A. M. J. Davis, M. T. Kezirian & H. Brenner. On the Stokes-Einstein Model of Surface Diffusion along Solid Surfaces: Slip Boundary Conditions. *Journal of Colloid and Interface Science* **165**, 129–140 (1994).
141. L. Zhang *et al.* Controlled propulsion and cargo transport of rotating nickel nanowires near a patterned solid surface. *ACS Nano* **4**, 6228–6234 (2010).
142. E. Lauga, W. R. DiLuzio, G. M. Whitesides & H. A. Stone. Swimming in Circles: Motion of Bacteria near Solid Boundaries. *Biophysical Journal* **90**, 400–412 (2006).
143. C. Bechinger *et al.* Active particles in complex and crowded environments. *Reviews of Modern Physics* **88** (2016).
144. J. Anderson. Colloid Transport By Interfacial Forces. *Annual Review of Fluid Mechanics* **21**, 61–99 (1989).
145. S. J. Ebbens. Active colloids: Progress and challenges towards realising autonomous applications. *Current Opinion in Colloid and Interface Science* **21**, 14–23 (2016).
146. Y. Wang *et al.* Bipolar electrochemical mechanism for the propulsion of catalytic nanomotors in hydrogen peroxide solutions. *Langmuir* **22**, 10451–10456 (2006).
147. W. F. Paxton *et al.* Catalytic Nanomotors: Autonomous Movement of Striped Nanorods. *Journal of the American Chemical Society* **126**, 13424–13431 (2004).
148. R. Golestanian. Debut of a hot “fantastic voyager”. *Physics* **3**, 8–10 (2011).
149. W. F. Paxton, A. Sen & T. E. Mallouk. Motility of catalytic nanoparticles through self-generated forces. *Chemistry - A European Journal* **11**, 6462–6470 (2005).
150. S. Hernández-Navarro, P. Tierno, J. Ignés-Mullol & F. Sagués. AC electrophoresis of microdroplets in anisotropic liquids: transport, assembling and reaction. *Soft Matter* **9**, 7999–8004 (2013).

151. D. Rings, R. Schachoff, M. Selmke, F. Cichos & K. Kroy. Hot Brownian Motion. *Physical Review Letters* **105**, 090604 (2010).
152. H. R. Jiang, N. Yoshinaga & M. Sano. Active motion of a Janus particle by self-thermophoresis in a defocused laser beam. *Physical Review Letters* **105**, 1–4 (2010).
153. L. Baraban *et al.* Fuel-free locomotion of janus motors: Magnetically induced thermophoresis. *ACS Nano* **7**, 1360–1367 (2013).
154. R. Golestanian, T. B. Liverpool & A. Ajdari. Propulsion of a molecular machine by asymmetric distribution of reaction products. *Physical Review Letters* **94**, 220801 (2005).
155. G. Volpe, I. Buttioni, D. Vogt, H. J. Kümmerer & C. Bechinger. Microswimmers in patterned environments. *Soft Matter* **7**, 8810–8815 (2011).
156. J. R. Howse *et al.* Self-Motile Colloidal Particles: From Directed Propulsion to Random Walk. *Physical Review Letters* **99**, 048102 (2007).
157. J. Zhang, X. Zheng, H. Cui & Z. Silber-Li. The self-propulsion of the spherical Pt-SiO₂ Janus micro-motor. *Micromachines* **8**, 1–17 (2017).
158. J. Palacci, S. Sacanna, A. Vatchinsky, P. M. Chaikin & D. J. Pine. Photoactivated colloidal dockers for cargo transportation. *Journal of the American Chemical Society* **135**, 15978–15981 (2013).
159. W. Gao, S. Sattayasamitsathit, J. Orozco & J. Wang. Highly efficient catalytic micro-engines: Template electrosynthesis of polyaniline/platinum microtubes. *Journal of the American Chemical Society* **133**, 11862–11864 (2011).
160. R. F. Ismagilov, A. Schwartz, N. Bowden & G. M. Whitesides. Autonomous Movement and Self-Assembly. *Angewandte Chemie International Edition* **41**, 652–654 (2002).
161. A. A. Solovev *et al.* Self-propelled nanotools. *ACS Nano* **6**, 1751–1756 (2012).
162. S. Sanchez, A. N. Ananth, V. M. Fomin, M. Viehrig & O. G. Schmidt. Superfast motion of catalytic microjet engines at physiological temperature. *Journal of the American Chemical Society* **133**, 14860–14863 (2011).
163. W. Gao, A. Pei, R. Dong & J. Wang. Catalytic Iridium-Based Janus Micromotors Powered by Ultralow Levels of Chemical Fuels. *Journal of the American Chemical Society* **136**, 2276–2279 (2014).
164. W. Gao, A. Uygun & J. Wang. Hydrogen-Bubble-Propelled Zinc-Based Microrockets in Strongly Acidic Media. *Journal of the American Chemical Society* **134**, 897–900 (2012).
165. R. A. Pavlick, S. Sengupta, T. McFadden, H. Zhang & A. Sen. A Polymerization-Powered Motor. *Angewandte Chemie International Edition* **50**, 9374–9377 (2011).
166. P. Tierno, R. Albalat & F. Sagués. Autonomously moving catalytic microellipsoids dynamically guided by external magnetic fields. *Small* **6**, 1749–1752 (2010).

167. S. A. Mallory, C. Valeriani & A. Cacciuto. An Active Approach to Colloidal Self-Assembly. *Annual Review of Physical Chemistry* **69**, 59–79 (2018).
168. J. Palacci, S. Sacanna, A. P. Steinberg, D. J. Pine & P. M. Chaikin. Living Crystals of Light-Activated Colloidal Surfers. *Science*, 936–939 (2013).
169. I. Buttinoni *et al.* Dynamical Clustering and Phase Separation in Suspensions of Self-Propelled Colloidal Particles. *Physical Review Letters* **238301**, 238301 (2013).
170. A. P. Petroff, X. L. Wu & A. Libchaber. Fast-moving bacteria self-organize into active two-dimensional crystals of rotating cells. *Physical Review Letters* **114**, 1–6 (2015).
171. Z. Lin, C. Gao, M. Chen, X. Lin & Q. He. Collective motion and dynamic self-assembly of colloid motors. *Current Opinion in Colloid & Interface Science* **35**, 51–58 (2018).
172. M. E. Cates & J. Tailleur. Motility-Induced Phase Separation. *Annual Review of Condensed Matter Physics* **6**, 219–244 (2015).
173. I. Theurkauff, C. Cottin-Bizonne, J. Palacci, C. Ybert & L. Bocquet. Dynamic clustering in active colloidal suspensions with chemical signaling. *Physical Review Letters* **108**, 1–5 (2012).
174. F. Schmidt, B. Liebchen, H. Löwen & G. Volpe. Light-controlled assembly of active colloidal molecules. *Journal of Chemical Physics* **150** (2019).
175. H. Stark. Artificial Chemotaxis of Self-Phoretic Active Colloids: Collective Behavior. *Accounts of Chemical Research* **51**, 2681–2688 (2018).
176. F. Kümmel, P. Shabestari, C. Lozano, G. Volpe & C. Bechinger. Formation, compression and surface melting of colloidal clusters by active particles. *Soft Matter* **11**, 6187–6191 (2015).
177. R. Di Leonardo *et al.* A bacterial ratchet motor. *Proceedings of the National Academy of Sciences* **107**, 9541–9545 (2010).
178. D. P. Singh, U. Choudhury, P. Fischer & A. G. Mark. Non-Equilibrium Assembly of Light-Activated Colloidal Mixtures. *Advanced Materials* **29**, 1–7 (2017).
179. S. Ramananarivo, E. Ducrot & J. Palacci. Activity-controlled annealing of colloidal monolayers. *Nature Communications* **10**. ISSN: 2041-1723 (2019).
180. D. F. Hinz, A. Panchenko, T. Y. Kim & E. Fried. Motility versus fluctuations in mixtures of self-motile and passive agents. *Soft Matter* **10**, 9082–9089 (2014).
181. W. Yang, V. R. Misko, K. Nelissen, M. Kong & F. M. Peeters. Using self-driven microswimmers for particle separation. *Soft Matter* **8**, 5175–5179 (2012).
182. X.-L. Wu & A. Libchaber. Particle Diffusion in a Quasi-Two-Dimensional Bacterial Bath. *Physical Review Letters* **84**, 3017 (2000).

183. F. A. Lavergne, H. Wendehenne, T. Bäuerle & C. Bechinger. Group formation and cohesion of active particles with visual perception-dependent motility. *Science* **364**, 70–74. ISSN: 10959203 (2019).
184. T. Bäuerle, A. Fischer, T. Speck & C. Bechinger. Self-organization of active particles by quorum sensing rules. *Nature Communications* **9**, 1–8 (2018).
185. T. Vicsek, A. Czirok, E. Ben-Jacob, I. Cohen & O. Shochet. Novel Type of Phase Transition in a System of Self-Driven Particles. *Physical Review Letters* **75**, 1226–1229 (1995).
186. A. Czirók, H. E. Stanley & T. Vicsek. Spontaneously ordered motion of self-propelled particles. *Journal of Physics A: Mathematical and General* **30**, 1375–1385 (1997).
187. T. Sugimoto, M. M. Khan & A. Muramatsu. Preparation of monodisperse peanut-type α -Fe₂O₃ particles from condensed ferric hydroxide gel. *Colloids and Surfaces A: Physicochemical and Engineering Aspects* **70**, 167–169 (1993).
188. T. Sugimoto, M. M. Khan, A. Muramatsu & H. Itoh. Formation mechanism of monodisperse peanut-type α -Fe₂O₃ particles from condensed ferric hydroxide gel. *Colloids and Surfaces A: Physicochemical and Engineering Aspects* **79**, 233–247 (1993).
189. R Ottewill. Adsorption from solution (1983).
190. Y. W. Choi, H. Lee, Y. Song & D. Sohn. Colloidal stability of iron oxide nanoparticles with multivalent polymer surfactants. *Journal of Colloid and Interface Science* **443**, 8–12 (2015).
191. L. Rossi. *Colloidal Superballs* PhD thesis (2012).
192. S. H. Lee & C. M. Liddell. Anisotropic Magnetic Colloids: A Strategy to Form Complex Structures Using Nonspherical Building Blocks. *Small* **5**, 1957–1962 (2009).
193. G. Fonnum, C. Johansson, A. Molteberg, S. Mørup & E. Aksnes. Characterisation of Dynabeads® by magnetization measurements and Mössbauer spectroscopy. *Journal of Magnetism and Magnetic Materials* **293**, 41–47 (2005).
194. D. T. Grob, N. Wise, O. Oduwole & S. Sheard. Magnetic susceptibility characterisation of superparamagnetic microspheres. *Journal of Magnetism and Magnetic Materials* **452**, 134–140 (2018).
195. L. E. Helseth. Paramagnetic particles as sensitive force detectors in liquids. *Journal of Physics D: Applied Physics* **40**, 3030–3037 (2007).
196. L. Clime, B. Le Drogoff & T. Veres. Dynamics of superparamagnetic and ferromagnetic nano-objects in continuous-flow microfluidic devices. *IEEE Transactions on Magnetics* **43**, 2929–2931 (2007).
197. P. Tierno, F. Sagués, T. H. Johansen & T. M. Fischer. Colloidal transport on magnetic garnet films. *Physical Chemistry Chemical Physics* **11**, 9615 (2009).

198. L. E. Helseth, T. M. Fischer & T. H. Johansen. Paramagnetic beads surfing on domain walls. *Physical Review E* **67**, 4 (2003).
199. A. V. Straube & P. Tierno. Synchronous vs. asynchronous transport of a paramagnetic particle in a modulated ratchet potential. *EPL (Europhysics Letters)*, 28001 (2013).
200. P. Tierno & A. V. Straube. Transport and selective chaining of bidisperse particles in a travelling wave potential. *European Physical Journal E* **39**, 1–7 (2016).
201. J. C. Crocker & D. G. Grier. Methods of Digital Video Microscopy for Colloidal Studies. *Journal of Colloid and Interface Science* **310**, 298–310 (1996).
202. D. Blair & E. Dufresne. The matlab particle tracking code repository. *Particle-tracking code available at <http://physics.georgetown.edu/matlab>* (2008).
203. F. Martinez-Pedrero & P. Tierno. Magnetic Propulsion of Self-Assembled Colloidal Carpets: Efficient Cargo Transport via a Conveyor-Belt Effect. *Physical Review Applied* **3**, 1–6 (2015).

LIST OF PUBLICATIONS

- H. Massana-Cid, F. Meng, D. Matsunaga, R. Golestanian, and P. Tierno. Tunable self-healing of magnetically propelling colloidal carpets. *Nature Communications* **10**, (2019) 2444
- H. Massana-Cid, E. Navarro-Argemí, D. Levis, I. Pagonabarraga, and P. Tierno. Leap-frog transport of magnetically driven anisotropic colloidal rotors. *The Journal of Chemical Physics* **150**, (2019) 164901
- H. Massana-Cid, J. Codina, I. Pagonabarraga, and P. Tierno. Active apolar doping determines novel routes to colloidal clusters and gels. *Proceedings of the National Academy of Sciences* **115**, (2018) 10618-10623
- H. Massana-Cid, F. Martinez-Pedrero, E. Navarro-Argemí, I. Pagonabarraga and P. Tierno. Propulsion and hydrodynamic particle transport of magnetically twisted colloidal ribbons. *New Journal of Physics* **19** (2017) 103031
- H. Massana-Cid, F. Martinez-Pedrero, A. Cebers and P. Tierno. Orientational dynamics of fluctuating dipolar particles assembled in a mesoscopic colloidal ribbon. *Physical Review E* **96** (2017) 012607
- F. Martinez-Pedrero, H. Massana-Cid and P. Tierno. Assembly and Transport of Microscopic Cargos via Reconfigurable Photoactivated Magnetic Microdockers. *Small* **13** (2017) 1603449
- F. Martinez-Pedrero, H. Massana-Cid, T. Ziegler, T. H. Johansen, A. V. Straube and P. Tierno. Bidirectional particle transport and size selective sorting of Brownian particles in a flashing spatially periodic energy landscape. *Physical Chemistry Chemical Physics* **18**, (2016) 26353

Not included in this thesis:

- H. Massana-Cid, A. Ortiz-Ambriz, A. Vilfan and P. Tierno. Emergent colloidal edge currents generated via exchange dynamics in a broken dimer state. *Submitted*
- H. Massana-Cid, A. Ernst, D. De Las Heras, A. Jarosz, M. Urbaniak, F. Stobiecki, A. Tomita, R. Huhnstock, I. Koch, A. Ehresmann, D. Holzingerd and T. M. Fischer. Edge transport at the boundary between topologically equivalent lattices. *Soft Matter* **15**, (2019) 1539-1550¹

¹This publication was done during my visit to Thomas M. Fischer's group in the University of Bayreuth (Germany).

RESUM EN CATALÀ

En aquesta tesi hem investigat la dinàmica fora de l'equilibri de col·loides magnètics i el seu comportament individual i col·lectiu sota camps externs. Explico com els vam manipular per construir microdispositius nedadors capaços de transportar altres materials i formar cadenes, agrupacions, gels, i cristalls amb l'habilitat de reordenar-se.

Una suspensió col·loïdal és una barreja de partícules insolubles de mida nanomètrica o microscòpica dispersades en un altre medi, com un fluid. Hi ha molts exemples de col·loides en la vida quotidiana, com ara la pasta de dents, la llet i la pintura. En aquest treball quan parlem de col·loides ens referim a micropartícules sòlides disperses en una solució líquida. A causa de la seva mida, els col·loides són fàcilment accessibles experimentalment i es poden observar amb microscopis òptics tradicionals. A més, s'ha demostrat que poden ser sistemes model excel·lents per estructures amb diferents escales de longitud, que van des de sistemes atòmics a matèria biològica. D'altra banda, poden ser útils per entendre la hidrodinàmica a la microescala i per formar micromàquines de transport que són essencials per a processos de miniaturització.

L'objectiu principal d'aquesta tesi és investigar sistemes de matèria tova a través de la manipulació de col·loides magnètics per tal de trobar maneres de propulsar microdispositius i per formar diferents tipus d'estructures. Per aconseguir-ho, vam controlar les interaccions presents en col·leccions de partícules utilitzant camps magnètics externs, substrats magnètics i l'activitat química de col·loides especialment sintetitzats. Tot això serveix per entendre les propietats fonamentals d'aquests sistemes microscòpics i per trobar nombroses aplicacions.

Aquesta tesi està estructurada en cinc parts. Després d'una breu introducció ([primera part](#)), explico alguns fonaments que ajuden a entendre millor els principis bàsics que intervenen en aquest treball ([segona part](#)). El [Capítol 2](#) es dedica a la ciència col·loïdal. Explico l'analogia de col·loides com a àtoms, descriu les seves interaccions principals i algunes de les estructures que aquestes partícules poden formar. La ciència col·loïdal ha guanyat més atenció durant les últimes dècades gràcies al desenvolupament de tècniques i eines experimentals que permeten fabricar, manipular i observar partícules microscòpiques i nanoscòpiques amb alta precisió.

Al [Capítol 3](#) parlo de micropartícules i nanopartícules magnètiques, esmentant les

interaccions que intervenen quan els col·loides magnètics es sotmeten a camps externs. Aquests camps es poden utilitzar per induir interaccions en una col·lecció de partícules. L'amplitud del camp defineix la força de la interacció mentre la seva direcció controla si aquesta és atractiva o repulsiva. Això dona lloc a la formació de diferents tipus d'estructures i a l'aparició d'una gran varietat de fenòmens.

El [Capítol 4](#) tracta de les peculiaritats de la dinàmica de fluids a la microescala i introdueix alguns dels últims desenvolupaments que s'han fet en sistemes de partícules actives i de micropropulsors magnètics. Quan s'estudia la dinàmica de suspensions col·loïdals és essencial entendre la hidrodinàmica a baix nombre de Reynolds. Les equacions relatives al flux es converteixen en reversibles en el temps i el moviment recíproc no indueix translació. Els camps magnètics externs poden ajudar a aconseguir propulsió en cossos magnètics. Per altra banda, les partícules actives, capaces d'agafar energia del seu entorn i convertir-la en moviment dirigit, també són candidates excel·lents per aconseguir translació en ambients microfluidics.

A la [tercera part](#) parlo dels materials i dels mètodes utilitzats en aquest treball. Al [Capítol 5](#) detallo els col·loides emprats en aquesta tesi, principalment col·loides paramagnètics i ferromagnètics, i explico com vam preparar les nostres mostres. Vam sintetitzar el·lipsoides ferromagnètics d'hematites amb dues mides diferents utilitzant un mètode sol-gel i vam utilitzar col·loides paramagnètics esfèrics comercials. També els vam barrejar amb col·loides no magnètics i vam utilitzar substrats magnetitzats per canviar les seves interaccions.

El [Capítol 6](#) descriu el nostre muntatge experimental, el qual ens va permetre aplicar camps magnètics externs constants i dependents del temps in situ, mentre observàvem l'evolució de la mostra a temps real amb tècniques de videomicroscopia. Vam analitzar els vídeos resultants per obtenir informació sobre la dinàmica fora d'equilibri dels sistemes estudiats.

La [quarta part](#) inclou tots els resultats obtinguts. El [Capítol 7](#) els resumeix i el [Capítol 8](#) conté totes les publicacions. A les Publicacions 1-5 vam utilitzar camps magnètics per organitzar i conduir partícules magnètiques i les estructures que formen. Vam poder traslladar cadenes i agrupacions de partícules al llarg del pla bidimensional de la mostra. A més, vam observar transport bidireccional de col·loides sobre un substrat magnètic. A les Publicacions 6 i 7 vam introduir activitat química al nostre sistema, format per una barreja de partícules col·loïdals actives apolars i partícules passives. Aquesta activitat indueix mecanismes difusorètics que permeten acoblar cossos a les partícules magnètiques actives, que poden transportar-se mitjançant un camp extern. A més, vam utilitzar les mateixes partícules com a dopants per la formació de diferents estructures, com gels bidimensionals. Els nostres experiments es van comparar i contrastar amb models analítics i simulacions.

Finalment, a la [cinquena part](#) resumeixo les conclusions obtingudes i afegeixo algunes

perspectives futures. Ajustant les interaccions de sistemes col·loïdals mitjançant camps externs vam trobar noves maneres de transportar i formar una gran varietat de microestructures. A més, els col·loïdes ens van ajudar a comprendre la dinàmica de fluids a baix nombre de Reynolds, el que té aplicacions en estudis de microfluídica. Aquest treball és un pas més que ens acosta a trobar un microdispositiu òptim basat en partícules col·loïdals per manipular, transportar i controlar processos a aquestes escales. Una qüestió que encara roman oberta és com es comportarien les cadenes de partícules d'hematites en presència d'activitat química. A més, augmentant l'activitat d'alguns dels col·loïdes canviant la potència de la llum aplicada esperariem obtenir autopropulsió de cossos asimètrics. També es podrien estudiar les fluctuacions en les partícules constituents de les estructures propulsors bidimensionals, així com l'evolució de la rugositat de les seves vores. Per altra banda, hem observat fenòmens sorprenents quan partícules paramagnètiques estan sota un camp magnètic dependent del temps i són confinades en una cel·la d'un gruix de l'ordre del seu diàmetre. Hem vist corrents col·loïdals, la formació de xarxes bimodals i dímers rotatius. Explorar més aquest sistema és una altra perspectiva emocionant.

LIST OF FIGURES

2.1 Colloidal phases.	8
2.2 Schematic of different interactions between colloids	10
2.3 DLVO interaction	11
2.4 Image of polystyrene colloids	12
2.5 Colloidal crystals	13
2.6 Colloidal gels	14
3.1 Types of coupling in magnetic materials	16
3.2 Hysteresis loops and dependence of the coercivity on particle size	17
3.3 Schematic illustrating two interacting magnetic particles	18
3.4 Confined paramagnetic colloids under an external magnetic field	19
3.5 Anisotropic magnetic colloids	20
4.1 Scallop theorem illustration	22
4.2 Biological swimmers	23
4.3 Theoretical proposals of swimmers.	23
4.4 Magnetic micropropellers	24
4.5 Phoretic swimmers	26
4.6 Self-propelled bodies	27
4.7 Clusters formed in active systems	28
4.8 Collective phenomena in a mixture of active and passive particles	29
5.1 SEM image of the hematite ellipsoids	34
5.2 Permanent magnetic moment orientation in the hematite particles	35
5.3 Paramagnetic Dynabeads	36
5.4 Ferrite garnet films	37
6.1 Experimental set-up	40
7.1 Orientational dynamics of ellipsoidal dipolar particles in a ribbon	45
7.2 Propulsion and hydrodynamic particle transport of magnetic ribbons	46

7.3	Leap-frog transport of magnetically driven anisotropic colloidal rotors . . .	46
7.4	Assembly and self-healing of magnetically propelling colloidal carpets . . .	47
7.5	Bidirectional transport of paramagnetic particles on top of a FGF	48
7.6	Assembly and transport of cargos by activated magnetic dockers	49
7.7	Colloidal gel assembled by active apolar doping	50

LIST OF SYMBOLS AND ABBREVIATIONS

SYMBOLS

k_B	Boltzmann constant
T	Temperature
Δr	Average displacement
t	Time
D	Diffusion coefficient
R	Radius
γ	Drag coefficient
τ_B	Brownian time
ϕ	Volume fraction
V	Volume
N	Number of particles
M	Magnetisation
H	Magnetic field
M_S	Saturation magnetisation
H_c	Coercivity field
χ	Volumetric magnetic susceptibility
m	Magnetic moment
μ_0	Permeability of free space
μ_m	Permeability of the medium
U_d	Dipolar interaction
Ω	Angular velocity
T_m	Magnetic torque
T_v	Viscous torque
ζ_r	Rotational friction coefficient
τ_r	Relaxation time
τ_{int}	Internal relaxation time
η	Dynamic viscosity of the medium
u	Flow field

ρ	Density
p	Pressure
Re	Reynolds number
L	Characteristic length scale
U	Characteristic velocity scale
a	Major ellipsoid axis
b	Minor ellipsoid axis
d	Diameter

ABBREVIATIONS

EDL	Electrical Double Layer
PS	Polystyrene
PMMA	Polymethymethacrylate
MIPS	Motility Induced Phase Separation
SDS	Sodium Dodecyl Sulfate
TMAH	Tetramethylammonium Hydroxide
SEM	Scanning Electron Microscopy
SQUID	Superconducting Quantum Interference Devices
NP	Nanoparticles
FGF	Ferrite Garnet Film
BW	Bloch Wall
AC	Alternating Current
DC	Direct Current